博士論文

Ph.D. Dissertation

Simultaneous Optimization of Flight Trajectory and Robust Controller and its Application to Hypersonic Aircraft

(飛行軌道とロバスト制御則の同時最適化と極超音速機への適用)

Masaharu Hiruma

晝間 正治

Department of Aeronautics and Astronautics

School of Engineering

The University of Tokyo

Dissertation Committee in Charge

Takeshi Tsuchiya　(土屋武司)
Supervisor
Professor
Department of Aeronautics and Astronautic, School of Engineering,
The University of Tokyo

Junichiro Kawaguchi　(川口淳一郎)
Professor
Department of Space Flight Systems, Institute of Space and Astronautical Science,
Japan Aerospace Exploration Agency

Shinichi Nakasuka　(中須賀真一)
Professor
Department of Aeronautics and Astronautic, School of Engineering,
The University of Tokyo

Kojiro Suzuki　(鈴木宏二郎)
Professor
Department of Aeronautics and Astronautic, School of Engineering,
The University of Tokyo

Hideyuki Taguchi　(田口秀之)
Researcher
Hypersonic Passenger Aircraft Technology Section, Aeronautical Technology Directorate,
Japan Aerospace Exploration Agency

Abstract

For hypersonic aircraft, significant amount of flight trajectory and control system integration is necessary in order to achieve requisite system stability and performance. This is due to the dynamic coupling between flight path and attitude being more prevalent at hypersonic speed. Furthermore, the operating flight conditions will vary significantly and the ability to predict the aerodynamic characteristics can be marginal at best. To compensate for flight condition changes as well as uncertainties in the system, a robust controller can be suggested. However, the coupling between flight path and attitude still needs to be resolved in terms of generating a control-oriented trajectory. Therefore, for hypersonic aircraft as well as any vehicle with the aforementioned coupling, a simultaneous design method of trajectory and robust controller is proposed by designing a control-oriented trajectory minimizing tracking error and controller robust against flight condition changes as well as to the trajectory.

Simultaneous design of trajectory and robust controller is achieved by converting the trajectory into a transfer function at each discretized segment of the trajectory and incorporating the identified trajectory transfer function to the structured H_∞ controller design at each iteration of the optimization. Maximum tracking error tolerance was specified and placed as the nonlinear inequality constraint of the nonlinear programming problem solved by sequential quadratic programming. Maximum tracking error for tracking reference trajectory is obtained by closed loop nonlinear simulation calculated at each iteration. The novel method was tested on two example optimal control problem one in the field of aerospace and one outside of aerospace field. The results are compared to the method where the trajectory and robust controller are obtained separately and with the proposed method, objective function showed improved results as well as the maximum tracking error decreasing while adding robustness to the trajectory compared to the separated method. Finally, the proposed method was applied to the Hypersonic Experimental Aircraft problem and successfully obtained a control-oriented trajectory and robust controller for accomplishing mission requirements. The obtained trajectory and robust controller was tested via Monte Carlo simulation for robustness against state uncertainties present during separation from the rocket and the mission success rate was identified as well as valuable insights for increasing technical maturity.

Table of Contents

List of Figures

List of Tables

Chapter 1

Introduction

1.1 Research Background

As the market for commercial flight has seen increase over the years, 20 years into the future the number is expected to double with passenger traffic expected to grow by an average rate of 4.6% [13]. Within the growing commercial market, the consortium HIKARI (HIgh speed Key technologies for future Air transport - Research and Innovation cooperation scheme) has addressed a possible market (long range routes with sufficient business and first class passenger traffic to sustain high speed operations) for high speed travel [11]. To meet the expectations of the rising demand for intercontinental travel, Japan Aerospace Exploration Agency (JAXA) is currently researching a hypersonic transport aircraft in pursuit for faster and reliable flight system [75]. The aircraft is planned to be equipped with a hypersonic pre-cooled turbo jet engine (PCTJ) under research and its target speed region is from take-off to Mach 5. To make hypersonic flight of practical use, JAXA has set a hypersonic flight experiment concept for the goal of realizing hypersonic transport aircraft. The concept consists of a series of autonomous flight experiments using a launch vehicle to demonstrate key hypersonic technologies.

The road map is broken into four stages of autonomous flight tests. The first stage is the unmanned experimental launch vehicle, High Mach Integrated Control Experiment (HIMICO), and its experiment objective is to test engine and aircraft system integration. The second stage is the unmanned experimental launch vehicle, Hypersonic Experimental Aircraft [42], and its experiment objective is to test for hypersonic cruise capability through autonomous flight. Two PCTJ engines around 3[m] in length are placed on both sides of the fuselage each producing roughly 1[kN] of thrust. The aircraft will be attached to the fuselage of the NAL735 rocket. It will reach 100[km] altitude and detach from the rocket. Through suborbital flight, the aircraft will accelerate until 50[kPa] of dynamic pressure is achieved for

engine test conditions. Then, the aircraft will pitch up and will begin its hypersonic cruise experiment at Mach 5. After the hypersonic experiment has been conducted, the aircraft will descend to a lower altitude for subsonic flight. The third stage is the scaled up hypersonic UAV and its objective is to test for intercontinental flight and the final stage is to introduce the aircraft for commercial flight.

Autonomous flight will generally track a preplanned trajectory and the trajectory and controller are designed separately offline which can then be evaluated for desired controller performances preflight [29]. Knowing the control system behavior preflight through a series of simulations is critical for determining the mission success in the presence of disturbances or uncertainties and improves accuracy as well as confidence for the flight test. This was also the case for experimental launch vehicles researched in the past and of the numerous vehicles, NEXST[69] and X-43A[71] are well-known experimental launch vehicles which conducted unmanned flight tests.

1. **NEXST** [69]
   NEXST (National EXperimental Supersonic Transport) is a supersonic experimental aircraft built for the purpose of improving advanced aerodynamic design technologies. Three objectives were placed where one was to evaluate supersonic CFD analysis tools to experimental data used for designing the natural laminar flow wing for the aircraft. Second was to establish cranked-arrow wing, area-ruled fuselage, and warped wing design methods. Third was to obtain knowledge and experience on unmanned aircraft flight testing. A solid rocket booster NAL-735 was developed and used to carry the airplane on the fuselage of the rocket to the target height and velocity. A total of two flight test were conducted of which the first flight test failed due to electrical short on the rocket causing the aircraft to separate from the rocket at ground level. The second flight test was a success and the intended aerodynamic, structural, and flight dynamics data were obtained.

2. **X-43A** [71]
   X-43A is the first hypersonic aircraft to demonstrate airframe-integrated, scramjet-powered sustained hypersonic flight. The objective of the experimental flight test was to demonstrate and validate tools, test, and analysis techniques as well as to obtain design methodologies of scram-jet powered hypersonic vehicles and data for aerodynamics and flight control research. A total of three flight tests were conducted where the first flight test ended in failure due to control system failure during the accelerated pull-up trajectory. The failure was caused by excess control system gain inefficient for the preplanned

trajectory resulting in divergent roll oscillation. Second flight test was a successful Mach 7 cruise and the third flight test being a successful Mach 10 cruise.

In this dissertation, the focus is on trajectory and controller design of the unmanned second stage Hypersonic Experimental Aircraft. Although the target aircraft is the Hypersonic Experimental Aircraft, it should be noted that the novel design method which will be introduced in this dissertation can be applied to any unmanned vehicles and is not restricted in the field of aerospace (i.e. naval architecture, etc.) since trajectory and controller design are common technologies needed for realizing unmanned operations. This will be shown by applying the proposed method to a speed boat problem (modified Zermelo's problem).

When designing a trajectory for autonomous vehicles, general problem formulation includes minimizing a cost function (e.g. tracking error, time, fuel consumption) while subject to constraints (e.g. dynamic pressure, static margin) [19] and tracking performance for the controller is verified subsequently. After obtaining reference trajectory the general design method is to design a controller and based on the design points selected by the control system designer, the nonlinear dynamics are linearized by, for example, perturbation method assuming steady-state flight (i.e. nonlinear dynamics are usually linearized at there cruising conditions). From there, the controller is designed to stabilize the closed-loop system under a given set of requirements such as robustness against flight condition changes, parameter uncertainties, gain and phase margins, rise time and overshoot tolerance, etc. One possible method for attaining stability under flight condition changes and uncertainty is by utilizing a robust controller and H_∞ robust controller design has been shown to be robust for flight condition changes as well as against uncertainties [25]. For this research, the emphasis is placed on designing a controller with robustness against flight condition changes and therefore the H_∞ controller design is one possible method to be considered. After the linearized controller is obtained, the controller is verified for performance via nonlinear simulation of tracking the generated reference trajectory. Since the controller is linearized at the their design conditions, depending on the trajectory the performance of tracking the reference trajectory may decrease. Even with the robust controller the tracking performance can differ depending on the flight condition and thus a redesign of the trajectory as well as the robust controller design may be needed summarized in Fig.1.1. This calls for integrating the design process of trajectory and controller via simultaneously designing the controller during trajectory optimization for generating a control-oriented trajectory for autonomous vehicles. The same may apply for autonomous hypersonic vehicles however, further evaluation is needed to verify the interaction between trajectory and controller design.

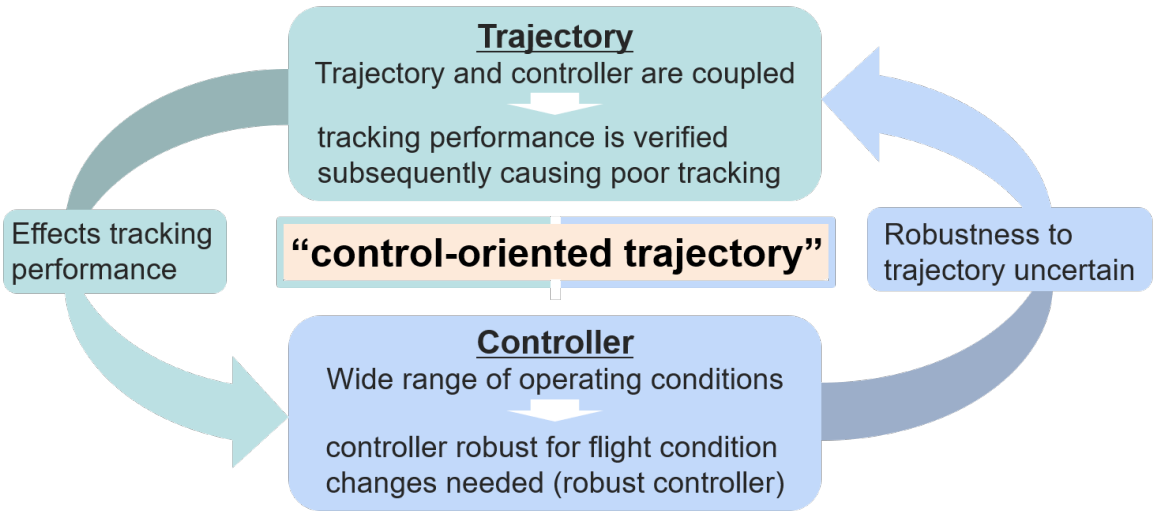

Fig. 1.1 Trajectory and Controller Design Problem.

1.2 Previous Works and Research Issues

In this section, a brief explanation of previous works regarding trajectory and controller design method for hypersonic vehicles will be discussed to identify possible research issues that arises during conventional method of designing trajectory and controller separately.

1.2.1 Case Studies on Hypersonic Experimental Aircraft

It is worth noting that the trajectory and controller design can differ depending on the aircraft configuration (e.g. aerodynamic characteristics) and so a case study to evaluate the descent trajectory for tracking performance was needed for hypersonic vehicles. In order to verify the coupling between trajectory and controller for the Hypersonic Experimental Aircraft, two case studies were conducted of the first case being a sensitivity analysis on trajectory generation [36] and PID controller performance and second case on designing a robust controller [38].

In the first case study of trajectory generation (flight path angle), the objective of the paper was to evaluate the flight trajectory of the Hypersonic Experimental Aircraft during descent for sensitivities to tracking performance. Furthermore, the flight trajectory with the smallest fuel consumption over downrange ratio was analysed through parametric study with the flight path angle γ being the parametric variable ($\gamma = [-2, -4, -6, -8, -10]$). (See Appendix A for complete analysis). The conditions for the aircraft cruising at Mach 5 is trim angle of 1.4[deg] and the altitude 25[km]. The target flight profile is to descend and pitch up from cruising altitude of Mach 5 at 25[km] to Mach 0.8 at 6[km]. The controller for tracking

γ was tuned through trial and error for high tracking performance. The reference trajectoy was given in the form of a Bessel function where pitch down and pitch up duration were tuned to meet the cruising conditions after descent. From the results, $\gamma = -4$ had minimum fuel consumption per kilometer. When comparing the trajectory of $\gamma = -4$ and $\gamma = -10$ shown in Fig.1.2 and Fig.1.3 respectively, the tracking performance for tracking γ decreased during descent as the flight path for descent became steeper. Here, the blue line represents the system output, orange line is the reference input, black line represents steady-state flight before the descent, green line is the descent duration for $\gamma = -4$, and red line is the constraint placed on state variables. Based on the results, the controller can be tuned to meet controller design requirements but the tracking performance was effected greatly by the reference trajectory due to the angle of attack constraint placed on the system to prevent stall and excess loading. Therefore, it was verified that interaction between flight path and attitude control were significant for the Hypersonic Experimental Aircraft and depending on the trajectory controller performance decreased.

In the second case study, a robust controller design for the Hypersonic Experimental Aircraft model was conducted to evaluate the controller for stability and robustness against flight condition changes in the assumed descent trajectory phase taken from the previous case study (See Appendix B for complete analysis). For the controller design, the nonlinear dynamic equations were linearized at steady-state flight conditions for each flight Mach number in the descent trajectory. The constructed control system for tracking the reference flight path angle for the Hypersonic Aircraft Model is shown in Fig.1.4. The system is an SISO with the angle of attack as its command input u, e as error between output γ of y and reference γ, W_e is the weighting function placed on the sensitivity function, K is the controller, P is the plant model, and Δe is a fictitious uncertainty block placed only to close the loop. The plant models used for the control design are the LTI models obtained linearized at steady-state flight conditions from Mach 5 to 2. From the results, a controller robust to flight Mach number of 5 to 2 was designed and verified by having a stable doublet response shown in Fig.1.5. However, as can be seen from the doublet response, the controller performs differently at each Mach number where the overshoot becomes greater as the Mach number increases. With the robust controller, robustness against flight condition changes is obtained, but the performance can deviate significantly. The controller was designed separately without considering the trajectory and depending on the trajectory tracking performance can decrease as was seen in the previous case study. Therefore, integrating the robust controller design method to have robustness against the trajectory was needed to generate a trajectory oriented towards control (i.e. minimizing tracking error).

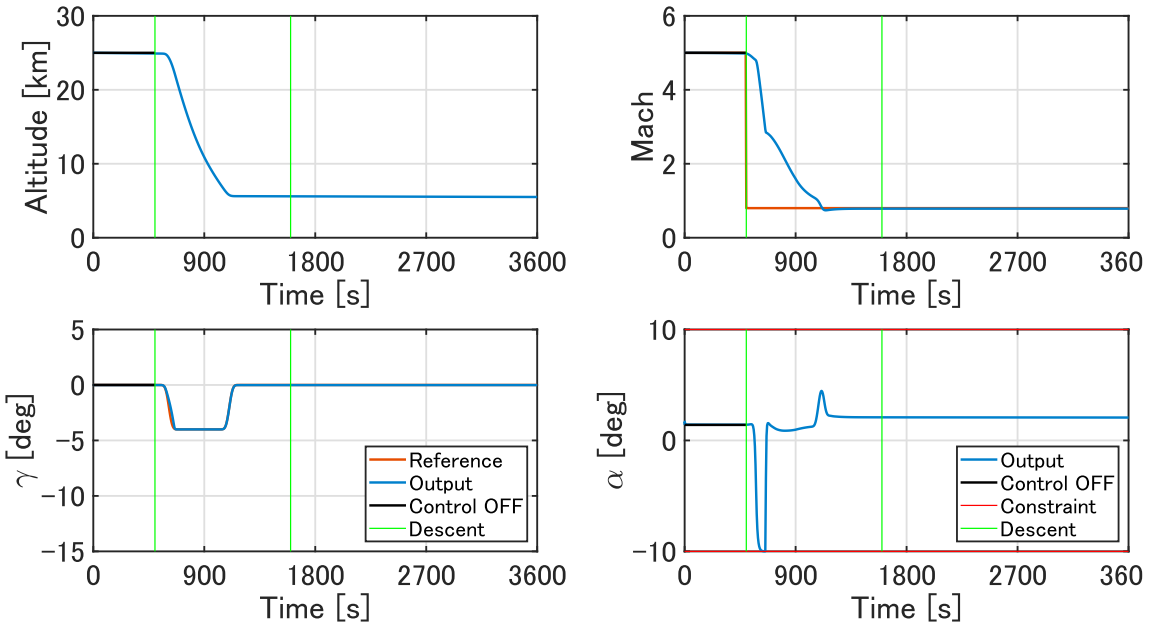

Fig. 1.2 $\gamma = -4$ [deg] Trajectory Generation Result.

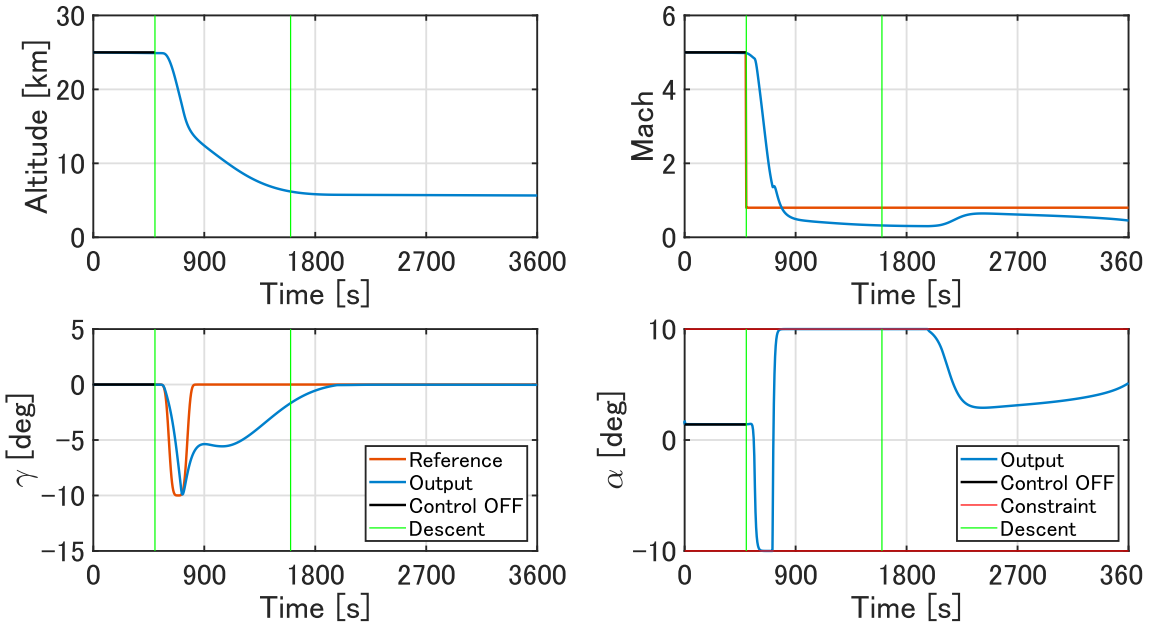

Fig. 1.3 $\gamma = -10$ [deg] Trajectory Generation Result.

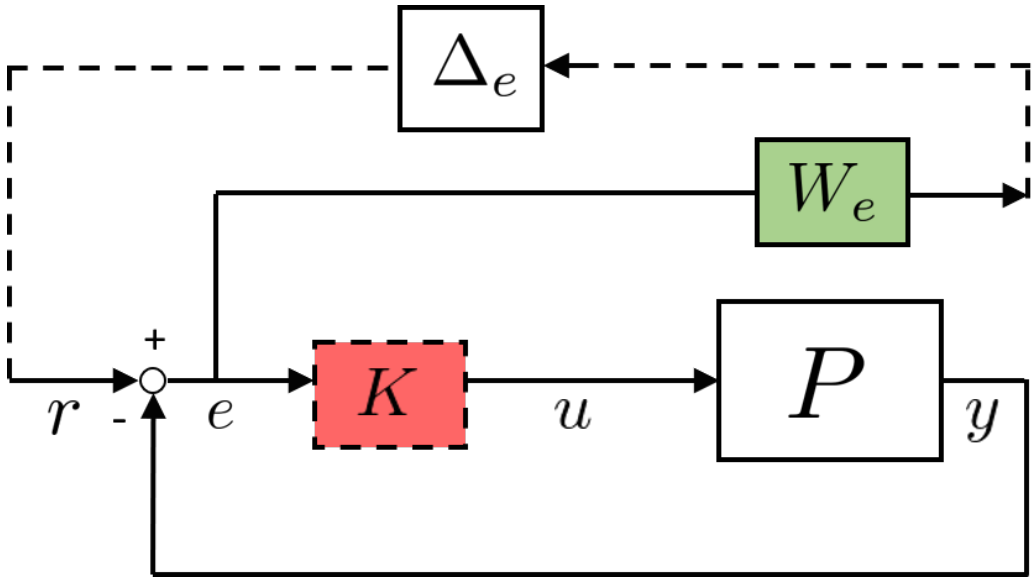

Fig. 1.4 Block Diagram of the Robust Controller Design.

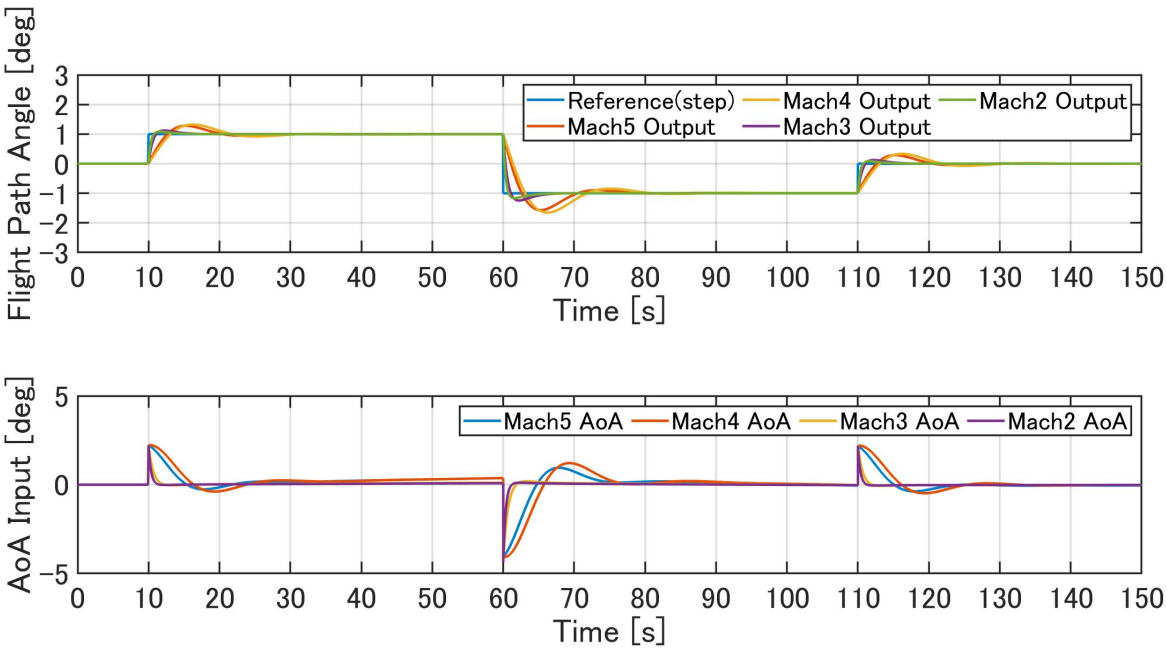

Fig. 1.5 Doublet Response to Multiple Inputs.

From the two case studies conducted on generating reference trajectory and designing a robust controller, conventional design process of trajectory and robust controller design for the Hypersonic Experimental Aircraft had the following characteristics:

a. Verified through nonlinear simulation that interaction between flight path and attitude control are significant for the Hypersonic Experimental Aircraft as well and depending on the flight path angle, severe overshoot can cause the performance of the controller to decrease.

b. The robust controller was designed separately without considering the trajectory and depending on the trajectory tracking performance may decrease verified through a doublet response.

Therefore, it can be said that interaction between trajectory and controller performance is prevalent for the hypersonic vehicle and simultaneously designing the controller during trajectory optimization for generating a control-oriented trajectory has a possibility to improve tracking performance.

1.2.2 Trajectory and Robust Controller Design of Hypersonic Vehicle

For a hypersonic aircraft it has been noted that intensive coupling between trajectory and controller performance is present as mentioned in Ref.[65] where significant amount of guidance and control system integration is necessary in order to achieve requisite system stability and performance. This is due to the dynamic coupling between flight path and attitude being more prevalent at hypersonic speed. The dynamic coupling is closely related to the high dynamic pressure during hypersonic flight which causes exponential fluctuations in the aerodynamic forces and moments of the vehicle. The prevalent interaction between the trajectory and controller performance is a significant research issue when performing hypersonic flight test. The trajectory and controller coupling was also the factor for the flight test failure for the first flight of the X-43A flight test [79]. The X-43A Mishap Investigation Board had the following statement:

Root Cause:
The X-43A HXLV failed because the vehicle control system design was deficient for the trajectory flown due to inaccurate analytical models

As was the case for the X-43A, there is an limit on predicting the amount of uncertainties the mission holds being in the states and analytical models since prediction of the control system

deficiency was not possible in the preflight analyses. From the root cause of the failure, it can be interpreted that depending on the trajectory flown the deficiency of the control system could have been mitigated. The controller design impacts the final mission success rate as with any other disciplines however, for hypersonic vehicles and with other vehicles with a strong coupling between trajectory and controller, the burden on the controller can be mitigated by considering a trajectory oriented towards controllability (control-oriented trajectory). From this, a control-oriented trajectory with the least tracking error can lead to higher tracking performance of the reference trajectory which is essential given that unpredicted uncertainties can rise during actual flight test and can be a possible solution for preventing control system failures as was seen for the X-43A. For a vehicle with intensive coupling between flight path and attitude control, there is a possibility to increase tracking performance through the simultaneous design of trajectory and controller generating a control-oriented trajectory. There has been substantial research on designing a robust controller separately from trajectory generation before flight with controller performance evaluations [56, 70, 15]. Additionally, substantial research has been done generating optimal trajectories separately from the controller design as well [12, 19, 10]. Few have integrated the design process of trajectory generation and robust controller design, but was done using a online design method [15]. Online method such as model predictive control poses a stability issue for system in that it can ensure stability for a finite time (horizon) whereas stability for a closed-loop system is only ensured for a infinite time system [60].

Therefore, continuing from previous studies as well as the case studies an offline method to simultaneously design the trajectory and robust controller design for a control-oriented trajectory can be effective in a scenario where intensive coupling between trajectory and controller performance exists (i.e. trajectory minimizing tracking error and controller having robustness against flight condition changes as well as to the trajectory). To incorporate the trajectory details into the robust controller design to have robustness against the generated trajectory, a method to transcribe the trajectory into a transfer function is needed. In H_∞ controller design, the controller gains are optimized to minimize the H_∞ norm of the system for all frequencies. In the time domain, a step input can be expressed as an input of all frequencies since the infinite sum of all frequencies of sinusoidal waves constitutes a step wave form through Fourier series [62]. Therefore by applying a step input as the input command and taking the trajectory flight path angle as the output, the trajectory can be expressed as a transfer function through system identification and robust against flight trajectory can be obtained as well. However, an approach for the simultaneous design of trajectory and robust controller design utilizing the described system identification method has not been conducted in previous works and development of such method is needed.

Additionally, the vehicle flight profile typically has a wide velocity range from hypersonic to subsonic. When designing a controller for hypersonic aircrafts, it has been stated by Ref. [65] that the wide range of operating conditions calls for a controller robust for flight condition changes and against aerodynamic uncertainties. The operating flight conditions will vary and poses a heavy burden on the controller since the dynamics of the model differ significantly with flight conditions. The controller needs to be able to handle model differences accordingly to the reference trajectory however, the ability to predict the analytical models (flight condition changes, aerodynamics, mass, vehicle configuration, structural dynamics, actuators, sensors, etc) can be marginal at best. There exists model uncertainties in almost every analytical model and for the controller to be robust or stable against these uncertainties can be challenging since there is a trade-off between stability and performance [34]. Designing a controller to be robust against large uncertainties usually decreases the performance of the controller in that uncertainties can limit the frequencies in which the controller is able to be tuned for high tracking performance [16]. To compensate for the coupling between the trajectory and controller as well as the limit on performance a controller can exhibit in the presence of uncertainties, physical optimization needs to be considered regarding the sizing of the control surface. Controller can only perform under the existing control surface thus control surface sizing can dramatically impact performance for tracking reference trajectory. Providing robustness against flight condition changes and uncertainties can lead to performance degradation which can be compensated by the physical modelling of the control surface sizing.

Therefore, research issue of designing a trajectory and controller for hypersonic vehicle can be summarized by the following:

1. **Significant Coupling between Trajectory and Robust Controller:**
   Trajectory and robust controller design needs to be integrated due to the intensive coupling arising from the high dynamic pressure during hypersonic flight as well as the need for robust controller design due to the presence of significant flight condition changes where the vehicle transitions from hypersonic to subsonic speed.

2. **Sizing of Control Surface Needed for Increasing Tracking Performance:**
   Robustness against flight condition changes and uncertainties comes at the expense of controller performance of tracking the reference trajectory. Therefore, physical modelling of control surface sizing needs to be conducted to ensure satisfactory performance on controller performance for the Hypersonic Experimental Aircraft as well.

Generating a optimal trajectory for the Hypersonic Experimental Aircraft consisting of rocket launch, suborbital flight, hypersonic flight test, and descent through suborbital flight

utilizing a simultaneous design method of trajectory and robust controller while optimizing the control surface sizing for increasing controller performance, no examples of such has been confirmed by the author. Therefore, obtaining a optimal solution to the problem and gaining knowledge for the possibility of the design method as well as an insight on the issues involved from the obtained results will contribute greatly to future research regarding hypersonic flight tests and testing for vehicles with strong coupling between trajectory and controller.

1.3 Research Objectives

Considering the research issues described in Section 1.2 where possible research area is defined, the research objectives of the dissertation is divided into two points summarized below of proposing a simultaneous design method for solving the coupling between flight path and attitude and applying the novel method to the Hypersonic Experimental Aircraft problem.

1. **Development of Simultaneous Design Method of Trajectory and Robust Controller:** Propose a novel method to simultaneously design the trajectory and robust controller by converting the trajectory into a transfer function at each discretized segment of the trajectory and incorporating each identified transfer function to the H_∞ controller design. The proposed method is validated by successfully applying to 2 well-known optimal control problems of which one is aerospace related and another being outside the field of aerospace for showing applicability outside of aerospace field. The results are then compared to the conventional method where the trajectory and robust controller are obtained separately.

2. **Application to Hypersonic Experimental Aircraft with Control Surface Sizing:** For hypersonic aircrafts, a strong coupling between trajectory and controller performance exists as stated in the Section 1.2. Therefore, by using the novel method and incorporating sizing problem of the control surface to the optimization, a reference trajectory and robust controller as well as optimal sizing of the control surface will be obtained for the Hypersonic Experimental Aircraft. The obtained trajectory and controller is evaluated via Monte Carlo simulation of the uncertainties present during separation from the launch vehicle.

1.4 Layout of this Dissertation

This dissertation is organized as follows:

Chapter 1 provides the overview of the trajectory and controller design for unmanned vehicles and addressing previous research as well as research issues in simultaneously designing both trajectory and controller to provide the objective for this dissertation.

Chapter 2 describes the novel method of simultaneous design optimization of trajectory and robust controller as well as key concepts of the proposed method.

Chapter 3 tests the proposed method against a aerospace related problem of simple rocket launch problem and the Zermelo's boat problem outside of the aerospace field. The validity of the proposed method is illustrated through solving these example problem.

Chapter 4 applies the novel method developed in Chapter 2 to the Hypersonic Experimental Aircraft problem where a control-oriented trajectory and a controller robust against flight condition changes as well as to trajectory will be generated.

Chapter 5 evaluates the obtained trajectory and robust controller performance to state uncertainties which is present during the separation stage between the rocket and the aircraft. The trajectory and controller are tested for robustness against state uncertainties.

Finally, Chapter 6 provides the conclusion and summary of the results obtained in each chapter as well as recommendations for future work.

Chapter 2

Simultaneous Optimization of Flight Trajectory and Robust Controller

In this chapter, in order to satisfy the first objective of developing a simultaneous design method of trajectory and robust controller a novel method is presented with advantages and limitations. The proposed method is based on the combination of 1) a gradient-based optimization method, 2) linear regression modeling, and 3) structured H_∞ controller design. The formulation of the optimal control problem and transformation into nonlinear programming problem is described in Section 2.1. The system identification of each discretized trajectory into its relevant transfer function is described in Section 2.2. Section 2.3 details the robust controller design procedures for obtaining a controller robust against flight condition changes and to the trajectory.

2.1 Method Outline

Simultaneous design of trajectory and robust controller is performed by handling the trajectory as a transfer function to be implemented into the robust PI controller design. The diagram for the overview of the proposed method (simultaneous system) is shown in Fig.2.1 and the flowchart of the optimization process is shown in Table 2.1.

The simultaneous method consists of nonlinear trajectory optimization, linear regression modelling for converting the trajectory into a transfer function, and linear robust controller design. The concept of nonlinear trajectory optimization is explained briefly in Section 2.2, for linear regression modelling in Section 2.3, and for linear robust controller design in Section 2.4. With the obtained robust controller, nonlinear simulation of tracking the reference trajectory r will be conducted at every iteration of solving the nonlinear optimization

problem. The simultaneous system for tracking optimal trajectory is shown in Fig.2.2. Here, u and P represents the control input and plant model respectively. The red blocks indicate the optimization variable. The maximum error e from the nonlinear simulation will be evaluated against the maximum error requirement placed as the nonlinear inequality constraint. With the simultaneous method, a robust controller for flight condition changes and to the trajectory can be obtained by the simultaneous design of trajectory optimization and controller design.

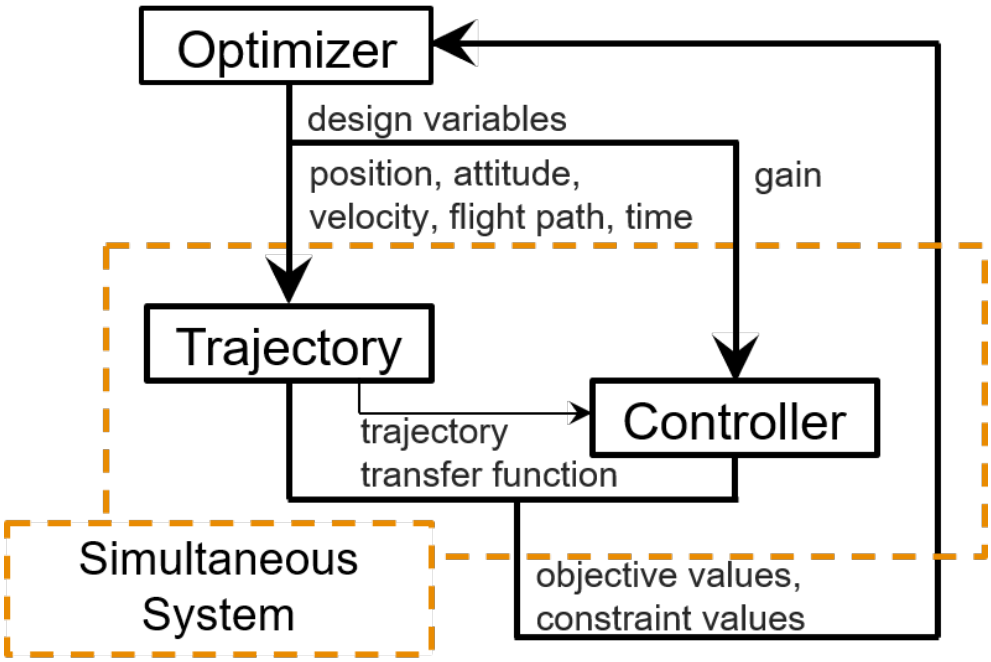

Fig. 2.1 Simultaneous Method Overview.

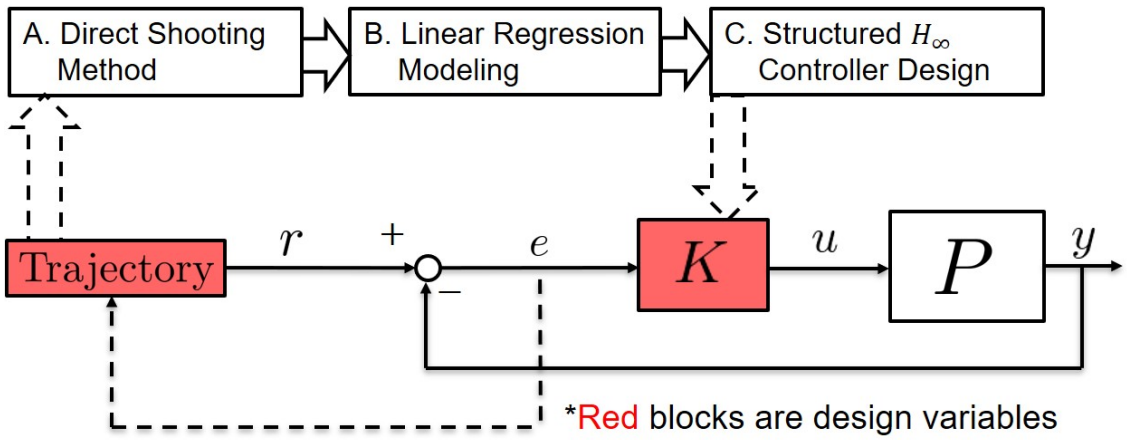

Fig. 2.2 Nonlinear Trajectory Tracking System for Obtaining Maximum Tracking Error.

Table 2.1 Flowchart of the Proposed Method.

A. Nonlinear Trajectory Design
1) Transcribe optimal control problem to NLP problem with the maximum tracking error of closed-loop system placed as a nonlinear inequality constraint
2) Discretize the trajectory into segments through direct shooting method
3) Solve the iteration of the NLP by SQP method
B. Linear Regression Modeling
4) Convert each segment of the trajectory to first order transfer function through linear regression
C. Linear Robust Controller Design
5) Add converted transfer function after the reference input of the SISO system
6) Obtain LTI model for each n th Segment of the trajectory
7) Design structured H_∞ controller for flight condition changes and to the trajectory
8) Obtain maximum error from tracking reference trajectory (Fig.2.2)
9) If the convergence criteria are not met, iterate from step 3)

2.2 Nonlinear Trajectory Design

For generating a optimal trajectory for a given object, the general method is to classify the nonlinear trajectory design as a nonlinear optimal control problem. The nonlinear optimal control problem uses nonlinear dynamics to represent the motion of the object and seeks to find a control input to minimize a objective function under arbitrary constraints [10, 60, 47].

The general nonlinear optimal control problem can be solved by either indirect or direct method. Indirect method is based on Pontryagin's Maximum Principle (general form of calculus of variations to be applicable for control problems) and optimized in a continuous time or infinite-dimensional function space. From the Maximum principle, the conditions for optimal control are obtained analytically, and solving for the state and control variables to meet the maximum principle by numerical method yields the optimal solution. The obtained results yield highly accurate solutions for the optimal control problem since no approximation of the state and control functions were conducted [47]. However, the disadvantages are that necessary conditions for optimality needs to be derived analytically which cannot be fully automated and in most cases unpractical where state and control variables ranges in significant number. On the other hand, by using a direct method, the problem will be solved numerically without the use of the Maximum Principle and optimized in a discretized or finite-dimensional function space. The discretized problem can be solved through nonlinear programming (NLP) and can be automated to solve for a large number of state and control

variables. Also, direct methods have better convergence to local optimum which is more practical for complex problem and therefore, a direct method will be used.

Problem formulation for a general nonlinear optimal control problem [47, 60] is shown in Eq.(2.1) with the trajectory assumed to have M number of phases $t \in [t_0^k, t_f^k](k = 1, \cdots, M)$ to represent discontinuity in state equation or constraints in the trajectory. Therefore, at the phase boundaries, $t_f^{l-1} = t_0^l (l = 2, \cdots, M)$ are satisfied with the state variable $\boldsymbol{x}(t) \in \mathbb{R}^{n_x}$ at $t \in [t_0, t_f]$, control input as $\boldsymbol{u}(t) \in \mathbb{R}^{n_u}$,and time-independent static variable as $\boldsymbol{p} \in \mathbb{R}^{n_p}$ (e.g. vehicle design variables).

$$
\begin{aligned}
&\text{objective function} && J(\boldsymbol{x}(t^k), \boldsymbol{u}(t^k), \boldsymbol{p}, t^k) \\
&\text{state equation} && \dot{\boldsymbol{x}}(t) = f^k(\boldsymbol{x}(t), \boldsymbol{u}(t), \boldsymbol{p}, t) \\
&\text{equality boundary constraints at } t \in [t_0, t_f] && \boldsymbol{r}_{eq}^k(\boldsymbol{x}(t^k), \boldsymbol{u}(t^k), \boldsymbol{p}, t^k) = 0 \\
&\text{inequality boundary constraints at } t \in [t_0, t_f] && \boldsymbol{r}_{in}^k(\boldsymbol{x}(t^k), \boldsymbol{u}(t^k), \boldsymbol{p}, t^k) \leq 0 \\
&\text{linear/nonlinear equality constraints} && \boldsymbol{C}^k(\boldsymbol{x}(t), \boldsymbol{u}(t), \boldsymbol{p}, t) = 0 \\
&\text{linear/nonlinear inequality constraints} && \boldsymbol{S}^k(\boldsymbol{x}(t), \boldsymbol{u}(t), \boldsymbol{p}, t) \leq 0
\end{aligned}
\tag{2.1}
$$

Solving for $\boldsymbol{x}(t^k), \boldsymbol{u}(t^k), \boldsymbol{p}, t^k$ which minimizes a Mayer type objective function will be the nonlinear optimal control problem used for this study.

2.2.1 Direct Shooting Method

There are a variety of transcription methods to discretize the nonlinear optimal control problem introduced in Eq.(2.1) to a nonlinear programming problem (NLP). Of the numerous transcription methods, direct multiple shooting method [12] has been applied to numerical examples of constrained and unconstrained two point boundary value problems [53] as well as real world applications such as for two body orbit transfers or for projectile guidance using a direct multiple shooting method [77, 68]. In this paper, a method of direct single shooting method (DSS) and direct multiple shooting method (DMS) is applied for discretizing the optimal trajectory. DSS integrates along a single segment while DMS integrates along multiple segments simultaneously and is considered to be more flexible to complex problems. When compared against direct collocation methods, at each iteration of the optimization collocation methods approximates the trajectory into piecewise polynomials and is then discretized to meet the dynamics [45], while the DSS and DMS integrates the dynamic equation to piece together the trajectory at each iteration. The DSS and DMS satisfies the dynamic equation constraints at each iteration by using sub-intervals to integrate the dynamics in between discretized segments. This is preferred since the maximum error of tracking the trajectory at each iteration of the optimization process will be evaluated and the

trajectory should be physically feasible to attain (identification method explained in Section 2.3).

In Eq.(2.1), the state variables $\boldsymbol{x}(t)$ and control inputs $\boldsymbol{u}(t)$ are a function of t which cannot be formulated into NLP. Discretization of $\boldsymbol{u}(t)$ is conducted by first equally dividing the continuous time into N segments as shown in Eq.(2.2).

$$t_0^k < t_1^k < \cdots < t_{N-1}^k < t_N^k = t_f^k \tag{2.2}$$

On each segment $[t_i, t_{i+1}]$ $(0 \leq i \leq N-1)$, the control input is denoted as $\boldsymbol{u}_i(t)$ shown in Eq.(2.3).

$$\boldsymbol{u}_i(t^k) = [u_{i0}^k, u_{i1}^k, \cdots, u_{ij}^k, \cdots, u_{in}^k,] \tag{2.3}$$

Where j $(0 \leq j \leq n)$ represents the sub-segments at each segment. It should be noted that a simplified version of DMS known as direct single shooting (DSS) method can be expressed in the same context as DMS where DSS has only a single segment $N = 1$ with n sub-segments. The control input can be defined as piecewise constant control ($j = 1$), piecewise linear controls or piecewise cubic spline controls ($j > 1$).

The state variables are obtained by integrating Eq.(2.4) for the corresponding $u_i(t^k), p$ using 4^{th} order Runge-Kutta method [7].

$$\dot{\boldsymbol{x}}_i(t) = f^k(\boldsymbol{x}_i(t), \boldsymbol{u}_i(t), \boldsymbol{p}, t) \quad t \in [t_i^k, t_{i+1}^k],\ 0 \leq i \leq N-1 \tag{2.4}$$

In order to ensure continuity of the obtained state variables $\boldsymbol{x}_i(t)$, Eq.(2.5) of initial value problem (IVP) is introduced.

$$\boldsymbol{x}_i(t_{i+1}^k; \boldsymbol{u}_i(t^k), \boldsymbol{p}, t_i^k) - \boldsymbol{x}_{i+1}^k = 0 \quad 0 \leq i \leq N-1 \tag{2.5}$$

Here, $\boldsymbol{x}_i(t_{i+1}; \boldsymbol{u}_i(t), \boldsymbol{p}, t_i)$ denotes the final value $\boldsymbol{x}(t_{i+1})$ obtained as the solution to the IVP on the segment $[t_i, t_{i+1}]$ when starting at the initial value $\boldsymbol{x}(t_i)$ and applying the control input $\boldsymbol{u}_i(t)$ on $[t_i, t_{i+1}]$. As noted by Eq.(2.1), when different phases are introduced to the trajectory, $t_f^{l-1} = t_0^l (l = 2, \cdots, M)$ needs to be satisfied to ensure continuity which is summarized in Eq.(2.6).

$$\boldsymbol{x}_0(t_0^l; \boldsymbol{u}_0(t^l), \boldsymbol{p}, t_0^l) - \boldsymbol{x}_f(t_f^{l-1}; \boldsymbol{u}_f(t^{l-1}), \boldsymbol{p}, t_f^{l-1}) = 0 \quad (l = 2, \cdots, M) \tag{2.6}$$

The boundary constraints from Eq.(2.1) is discretized into segments shown in Eq.(2.7) at $t \in [t_0, t_f]$.

$$\begin{aligned} &\text{equality boundary constraints} \quad \boldsymbol{r}^k_{eq_i}(\boldsymbol{x}_i(t^k),\boldsymbol{u}_i(t^k),\boldsymbol{p},t^k_i)=0 \quad 0\le i\le N \\ &\text{inequality boundary constraints} \quad \boldsymbol{r}^k_{in_i}(\boldsymbol{x}_i(t^k),\boldsymbol{u}_i(t^k),\boldsymbol{p},t^k_i)\le 0 \quad 0\le i\le N \end{aligned} \tag{2.7}$$

The nonlinear boundary constraints from Eq.(2.1) is discretized into segments shown in Eq.(2.8) at $t \in [t_0, t_f]$.

$$\begin{aligned} &\text{linear/nonlinear equality constraints} \quad \boldsymbol{C}^k_i(\boldsymbol{x}_i(t),\boldsymbol{u}_i(t),\boldsymbol{p},t_i)=0 \quad 0\le i\le N \\ &\text{linear/nonlinear inequality constraints} \quad \boldsymbol{S}^k_i(\boldsymbol{x}_i(t),\boldsymbol{u}_i(t),\boldsymbol{p},t_i)\le 0 \quad 0\le i\le N \end{aligned} \tag{2.8}$$

The optimal control problem from Eq.(2.1) resulting from application of the direct multiple shooting discretization reads Eq.(2.9).

$$\begin{aligned} &\text{find} \quad \boldsymbol{X}=\boldsymbol{x}^k_i(t),\boldsymbol{u}_i(t^k),\boldsymbol{p},t^k\in[t^k_0,t^k_f] \\ &\text{min.} \quad F(\boldsymbol{X})=\sum_N^{i=0} J_i(\boldsymbol{X}) \\ &\text{s.t.} \quad G(\boldsymbol{X})=\begin{bmatrix} \boldsymbol{r}^k_{eq_i}(\boldsymbol{x}_i(t^k),\boldsymbol{u}_i(t^k),\boldsymbol{p},t^k_i) \\ \boldsymbol{C}^k_i(\boldsymbol{x}_i(t),\boldsymbol{u}_i(t),\boldsymbol{p},t_i) \\ \boldsymbol{x}_i(t^k_{i+1};\boldsymbol{u}_i(t^k),\boldsymbol{p},t^k_i)-\boldsymbol{x}^k_{i+1} \\ \boldsymbol{x}_0(t^l_0;\boldsymbol{u}_0(t^l),\boldsymbol{p},t^l_0)-\boldsymbol{x}_f(t^{l-1}_f;\boldsymbol{u}_f(t^{l-1}),\boldsymbol{p},t^{l-1}_f) \end{bmatrix}=0 \\ &\qquad H(\boldsymbol{X})=\begin{bmatrix} \boldsymbol{r}^k_{in_i}(\boldsymbol{x}_i(t^k),\boldsymbol{u}_i(t^k),\boldsymbol{p},t^k_i) \\ \boldsymbol{S}^k_i(\boldsymbol{x}_i(t),\boldsymbol{u}_i(t),\boldsymbol{p},t_i) \end{bmatrix}\le 0 \end{aligned} \tag{2.9}$$

Here, $\boldsymbol{X}\in\mathbb{R}^n$ is the design variables, $F(\boldsymbol{X})\in R$ is the objective function, $G(\boldsymbol{X})\in R^{m_E}$ is the linear and nonlinear equality constraints, and $H(\boldsymbol{X})\in R^{m_I}$ is the linear and nonlinear inequality constraints.

The key approach taken in the novel simultaneous method is that the maximum error obtained from the tracking error using the controller obtained from the structured H_∞ controller design and is placed as a nonlinear inequality constraint. The NLP is solved by sequential quadratic problem (SQP) algorithm and will be explained briefly in the next section.

2.2.2 Sequential Quadratic Programming Method

The sequential quadratic programming method (SQP) is a class of method to solve a nonlinear programming by obtaining a local optimum and has arguably been considered one of the most successful method for solving nonlinear constrained optimization problem [14]. The

method uses the second-order Taylor approximation of the Lagrange function around a local point to find a feasible point for the next iteration of the optimization [60]. The objective function is transcribed into a quadratic programming (QP) problem at each iteration and easily solved through the Karsh-Kuhn-Tucker (KKT) condition sequentially thus the name. The algorithm can be summarized in which it applies the Newton's method to solve the KKT equations. When solving for the Hessian, it is approximated through Quasi-Newton method of Broyden-Fletcher-Goldfarb-Shanno (BFGS) method which ensures the second-order sufficient condition of optimality since the approximated Hessian will be positive definite [60]. Consider now the optimization problem discretized by DMS from Eq.(2.9). Eq.(2.9) is solved using *fmincon* MATLAB function available with comprehensive online documentation.

The algorithm for the SQP is described as follows:

Step 1. **Initialize:**
Provide initial guess of $\boldsymbol{X}^{(0)}$ as well as for the Lagrange multipliers $\lambda_{E_i}^{(0)} \in \mathbb{R}^{m_E} (i = 1, \cdots, m_E)$, $\lambda_{I_j}^{(0)} \in \mathbb{R}^{m_I} (j = 1, \cdots, m_I)$. Here, set the iteration count K as 0 for initial condition. The initial values for $\boldsymbol{X}^{(0)}$ are given by the user and the initial value for the Lagrange multipliers are generally zero vectors. For Eq.(2.9), the Lagrangian function is given by Eq.(2.10) referenced from [60].

$$L(\boldsymbol{X}^{(K)}, \lambda_{E_i}^{(K)}, \lambda_{I_j}^{(K)}) = F(\boldsymbol{X}^{(K)}) + \lambda_{E_i}^{(K)^T} G_i(\boldsymbol{X}^{(K)}) + \lambda_{I_j}^{(K)^T} H_j(\boldsymbol{X}^{(K)}) \tag{2.10}$$

Step 2. **Evaluate Gradients:**
From Step 2, the iteration of SQP begins. First, obtain the objective function value at $F(\boldsymbol{X}^{(K)})$ and the equality and inequality constraint value at $G_i(\boldsymbol{X}^{(K)})$ and $H_j(\boldsymbol{X}^{(K)})$. Next, obtain the gradients of the objective function, the Jacobian matrices $\nabla G_i(\boldsymbol{X}^{(K)})$ and $\nabla H_i(\boldsymbol{X}^{(K)})$. Finally, calculate the gradient of the Lagrangian function shown in Eq.(2.11).

$$\nabla L(\boldsymbol{X}^{(K)}, \lambda_{E_i}^{(K)}, \lambda_{I_j}^{(K)}) = \nabla F(\boldsymbol{X}^{(K)}) + \lambda_{E_i}^{(K)^T} \nabla G_i(\boldsymbol{X}^{(K)}) + \lambda_{I_j}^{(K)^T} \nabla H_j(\boldsymbol{X}^{(K)}) \tag{2.11}$$

Step 3. **Assess Convergence:**
Based on the assessment of whether the $F(\boldsymbol{X}^{(K)})$ has reached a local optimum and has converged, iteration will terminate. Assessment of local optimum is based on the first order necessary conditions of optimality referred to as the KKT conditions of Eq.(2.12) referenced from [60] (The second order sufficient condition for optimality will be discussed in Step 4). When the first order necessary conditions and second

order sufficient conditions are met at $\boldsymbol{X}^{(K)}, \lambda_{E_i}^{(K)}, \lambda_{I_j}^{(K)}$, then the the local optimum is achieved at $\boldsymbol{X}^{(K)}$ for each iteration.

$$\begin{aligned} \nabla L(\boldsymbol{X}^{(K)}, \lambda_{E_i}^{(K)}, \lambda_{I_j}^{(K)}) &= 0 \\ \nabla G_i(\boldsymbol{X}^{(K)}) &= 0 \\ \nabla H_j(\boldsymbol{X}^{(K)}) &\leq 0 \\ \lambda_{I_j}^{(K)^T} H_j(\boldsymbol{X}^{(K)}) &= 0 \quad (j = 1, \cdots, m_I) \\ \lambda_{I_j}^{(K)^T} &\geq 0 \end{aligned} \tag{2.12}$$

When the KKT equations shown in Eq.(2.12) are satisfied as well as the conditions shown in Eq.(2.13) are satisfied, then the optimization has converged with local optimum obtained at $\boldsymbol{X}^{(K)}, \lambda_{E_i}^{(K)}, \lambda_{I_j}^{(K)}$ is achieved.

$$\begin{aligned} \|G_i(\boldsymbol{X}^{(K)})\|_\infty &< \varepsilon_{con} \\ \|H_j(\boldsymbol{X}^{(K)})\|_\infty &< \varepsilon_{con} \end{aligned} \tag{2.13}$$

Here, $\|\cdot\|_\infty$ represents the infinity norm of a matrix. The optimization converges when the step length and constraint tolerance ε_{con} was below 1×10^{-15} and 1×10^{-2} respectively. Step length will be explained in Step 6.

Step 4. **Update Hessian:**

The second order sufficient condition for optimality is that the Hessian matrix be positive definite. The Hessian $\boldsymbol{H}^{(K)}$ in this study is approximated using BFGS Hessian approximation known for producing positive definite Hessian approximation [60] and is obtained by Eq.(2.14). For the initial iteration, unit matrix is used for $\boldsymbol{H}^{(0)}$.

$$\begin{aligned} \boldsymbol{H}^{(K)} &= \boldsymbol{H}^{(K-1)} + \frac{q^{(K)}(q^{(K)})^T}{(q^{(K)})^T s^{(K)}} - \frac{(\boldsymbol{H}^{(K-1)} s^{(K)})(\boldsymbol{H}^{(K-1)} s^{(K)})^T}{(s^{(K)})^T \boldsymbol{H}^{(K-1)} s^{(K)}} \\ q^{(K)} &= \nabla L(\boldsymbol{X}^{(K)}, \lambda_{E_i}^{(K)}, \lambda_{I_j}^{(K)}) - \nabla L(\boldsymbol{X}^{(K-1)}, \lambda_{E_i}^{(K-1)}, \lambda_{I_j}^{(K-1)}) \\ s^{(K)} &= \boldsymbol{X}^{(K)} - \boldsymbol{X}^{(K-1)} \end{aligned} \tag{2.14}$$

Step 5. **Solve QP problem:**

The second-order Taylor approximation of the Lagrange function around $\boldsymbol{X}^{(K)}$ is conducted to find the step direction $d^{(K)}$ as well as $\lambda_{E_i}^{(K)}, \lambda_{I_j}^{(K)}$ for $\boldsymbol{X}^{(K+1)}$ in the

next iteration. Using the second-order approximation, the quadratic problem (QP) subproblem for obtaining $d^{(K)}$ is represented in Eq.(2.15).

$$\begin{aligned} &\text{find} && d^{(K)} \\ &\text{min.} && \nabla F(\boldsymbol{X}^{(K)})d^{(K)} + \frac{1}{2}d^{(K)^T}\boldsymbol{H}^{(K)}d^{(K)} \\ &\text{s.t.} && G_i(\boldsymbol{X}^{(K)}) + \nabla G_i(\boldsymbol{X}^{(K)})d^{(K)} = 0 \quad (i = 1, \cdots, m_E) \\ & && H_j(\boldsymbol{X}^{(K)}) + \nabla H_j(\boldsymbol{X}^{(K)})d^{(K)} = 0 \quad (j = 1, \cdots, m_I) \end{aligned} \tag{2.15}$$

Step 6. **Perform Line Search:**
The solution to the QP subproblem produces a vector $d^{(K)}$, which is used to form $\boldsymbol{X}^{(K+1)}$ of Eq.(2.16).

$$\boldsymbol{X}^{(K+1)} = \boldsymbol{X}^{(K)} + \alpha^{(K)}d^{(K)} \tag{2.16}$$

Here, to find the step length $\alpha^{(K)}$ to obtain $\boldsymbol{X}^{(K+1)}$, another optimization is necessary to find a sufficient decrease in the penalty function. The penalty function used by [30, 63] are used shown in Eq.(2.17).

$$F_p(\boldsymbol{X}^{(K)}) = F(\boldsymbol{X}^{(K)}) + r_j \left[\sum_{m_E}^{i=1} G_i(\boldsymbol{X}^{(K)}) + \sum_{m_I}^{j=1} \max(0, H_j(\boldsymbol{X}^{(K)})) \right] \tag{2.17}$$

Here, r_j is derived by Eq.(2.18) which was referenced from [63].

$$r_j = (r_{K+1})_j = \max_j \left(\lambda_j, \frac{(r_K)_j + \lambda_j)}{2} \right) \quad (j = 1, \cdots, m_I) \tag{2.18}$$

For the initial value, the penalty parameter r_{0_j} is initially set to Eq.(2.19) where $\|\cdot\|$ denotes the Euclidean norm.

$$r_{0_j} = \frac{\|\nabla F(\boldsymbol{X}^{(K)})\|}{\|H_j(\boldsymbol{X}^{(K)}))\|} \tag{2.19}$$

By solving the optimization problem of Eq.(2.20), step length $\alpha^{(K)}$ is obtained.

$$\begin{aligned} &\text{find} && \alpha^{(K)} \\ &\text{min.} && F_p(\boldsymbol{X}^{(K)} + \alpha^{(K)}d^{(K)}) \\ &\text{s.t.} && 0 \leq \alpha^{(K)} \leq 1 \end{aligned} \tag{2.20}$$

Once the value of $d^{(K)}$ and $\alpha^{(K)}$ are obtained, $\boldsymbol{X}^{(K+1)}$ for the next iteration is defined. The SQP algorithm is repeated from Step.2 until the convergence criteria are met at Step.3

2.3 Linear Regression Modeling

For the coupling between trajectory optimization and robust controller design, a method to convert the trajectory into a transfer function was needed. In H_∞ controller design, the controller gains are optimized to minimize the H_∞ norm of the system for all frequencies. In the time domain, a step input can be expressed as an input of all frequencies since the infinite sum of all frequencies of sinusoidal waves constitutes a step wave form through Fourier series [62]. Therefore by applying a step input as the input command $u(k)$ and taking the trajectory flight path angle as the output, the trajectory can be expressed as a transfer function through system identification. The process is depicted in Fig.2.3 where the left box indicated as *A* and right box indicated as *B* represents Step A and B from Table 2.1 respectively. As shown in Fig.2.3, a linear regression estimation method was used for the sample points in the discretized n segment trajectory to a first order transfer function.

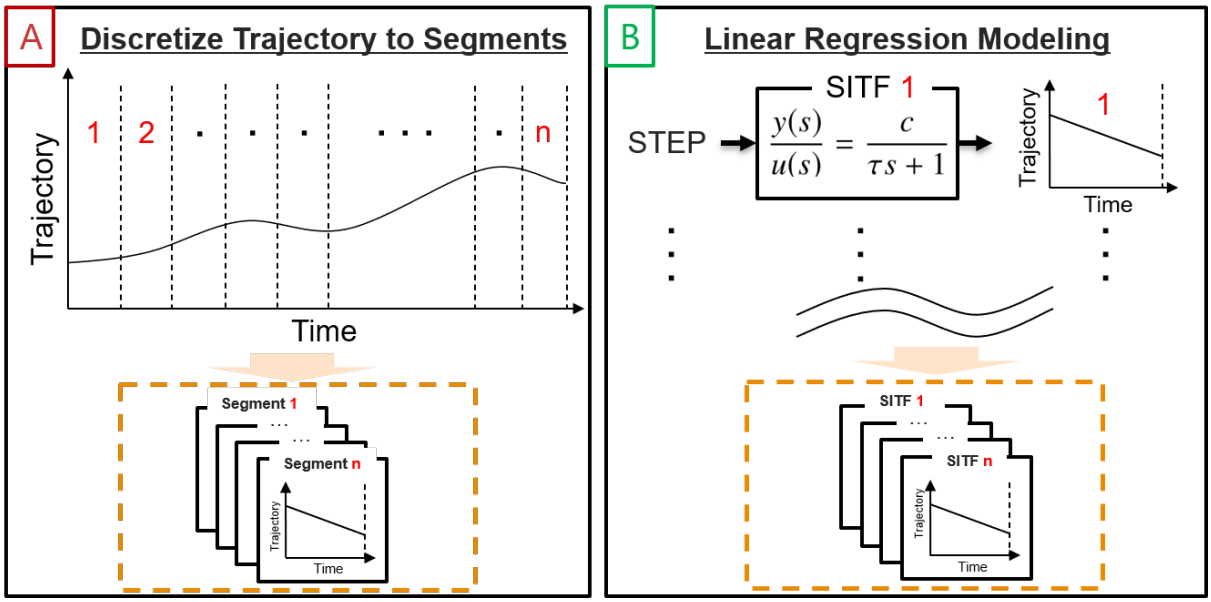

Fig. 2.3 Linear Regression Modeling for the Discretized Trajectory.

The problem formulation for single input single output system without noise of a system with the response of y to input u is shown below [80].

$$y(z^{-1}) = \frac{A(z^{-1})}{B(z^{-1})} u(z^{-1}) \tag{2.21}$$

Here, $A(z^{-1})$ and $B(z^{-1})$ form the numerator and denominator for the transfer function to be estimated. z^{-1} is the backward shift operator in the z domain. $A(z^{-1})$ and $B(z^{-1})$ are the following polynomials in z domain [80]:

$$\begin{cases} A(z^{-1}) = 1 + a_1 z^{-1} + \cdots + a_n z^{-n} \\ B(z^{-1}) = b_0 + b_1 z^{-1} + \cdots + b_{m-1} z^{-m+1} \end{cases} \tag{2.22}$$

Here, the order of the numerator and denominator of the transfer function is denoted by n and m. For first order systems where $n = 0$ and $m = 2$, Eq.(2.21) can be rewritten in the following form:

$$\frac{y(z^{-1})}{u(z^{-1})} = \frac{A(z^{-1})}{B(z^{-1})} = \frac{\frac{a_0}{b_1}}{\frac{b_0}{b_1} z^{-1} + 1} \tag{2.23}$$

Eq.(2.23) can be converted into to following form by applying inverse z transform [61]:

$$y(k) = \frac{a_0}{b_1} u(k) - \frac{b_0}{b_1} y(k+1) \tag{2.24}$$

Here, k represents the sample points which are normalized by the maximum number to represent a step input of 1 (i.e. $u(k)$ is all 1 while $y(k)$ is the trajectory normalized by the maximum number since step response is not affected by scaling).

Eq.(2.24) can then be written in the following linear regression form (i.e. similar method can be found in [81, 46]):

$$y(k) = \begin{bmatrix} u(k) & y(k+1) \end{bmatrix} \begin{bmatrix} \frac{a_0}{b_1} \\ -\frac{b_0}{b_1} \end{bmatrix} \tag{2.25}$$

Where the transfer function coefficients can be obtained by solving Eq.(2.25) for $\frac{a_0}{b_1}$ and $-\frac{b_0}{b_1}$. By substituting $\frac{a_0}{b_1}$ and $-\frac{b_0}{b_1}$ back to Eq.(2.23), the discrete time transfer function is obtained shown in Eq.(2.26).

$$\frac{y(z^{-1})}{u(z^{-1})} = \frac{\frac{a_0}{b_1}}{-\frac{b_0}{b_1} z^{-1} + 1} \tag{2.26}$$

After obtaining the linear regression model in discrete time, by using bilinear transformation shown in Eq.(2.27) to substitute s for z^{-1}, the transfer function is converted into continuous time transfer function [61].

$$s = \frac{2(z^{-1}-1)}{T(z^{-1}+1)} \tag{2.27}$$

The identified first order continuous time transfer function is shown in Eq.(2.28) where c is the numerator coefficient (gain) and τ is the denominator coefficient (time constant).

$$\frac{y(s)}{u(s)} = \frac{c}{\tau s+1} \tag{2.28}$$

The transfer function is implemented into the trajectory tracking system introduced in the following section used for robust controller design. For obtaining a robustness against the trajectory, all the discretized trajectory will be identified into the linear regression model in the form of Eq.(2.28).

2.4 Linear Robust Controller Design

Recently, a method to obtain a robust controller with a structured controller (e.g. PI controller) has been suggested by [6]. The robust controller design method used for this study is conducted by following the structured H_∞ controller design which involves solving a nonconvex and nonsmooth optimization problem. The standard or the nominal H_∞ controller design (as phrased in [6]) solves the algebraic Riccati equation [27] or Linear Matrix Inequality (LMI) problem as stated in [6, 34], while the structured H_∞ controller design is obtained through optimization. The structured approach assumes the stabilizing controller to have the same frequency domain representation as the nominal H_∞ controller design [6]. Therefore, the concept of H_∞ control as well as nominal H_∞ controller design will be briefly explained, followed by the structured H_∞ controller design.

2.4.1 H_∞ Control

H_∞ control is one of the established robust controller design methods available today. The method can handle unknown parameters in a plant model as well as parameter uncertainties in a relatively small fluctuation and design a stabilizing controller in its presence [34]. When dealing with H_∞ control, the problem is formulated by introducing a generalized plant model P with a feedback controller and the system is shown in Fig.2.4. The generalized plant model can be defined as a input-output system in Eq.(2.29).

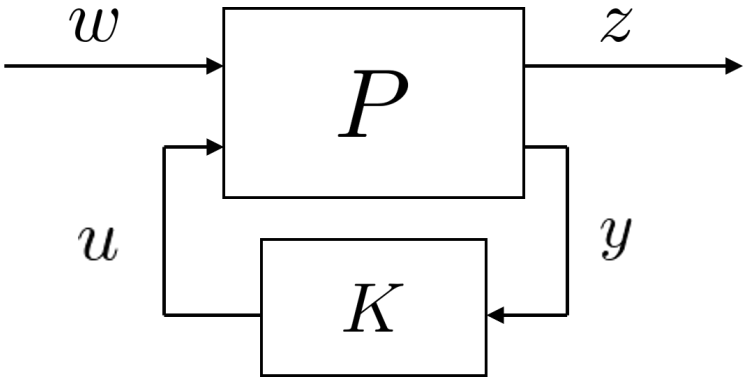

Fig. 2.4 Generalized Plant.

$$\begin{bmatrix} z \\ y \end{bmatrix} = P \begin{bmatrix} w \\ u \end{bmatrix} = \begin{bmatrix} P_{11} & P_{12} \\ P_{21} & P_{22} \end{bmatrix} \begin{bmatrix} w \\ u \end{bmatrix} \tag{2.29}$$

Here, w is a exogenous input representing any outside input originating from outside of the system (i.e. reference input, disturbance, sensor noise, etc), z is a controlled output representing a signal to be minimized by the controller (i.e. deviation, system output, etc). u is the control input and y is the output of the system.

As depicted in Fig.2.4, in the nominal H_∞ controller design the closed-loop generalized plant model is stabilized by the feedback control of $u = Ky$. At the same time, the controller is subjected to minimize the H_∞ norm of transfer function from w to z by T_{zw}. T_{zw} is expressed in the Eq.(2.30) obtained by substituting $u = Ky$ into Eq.(2.29).

$$T_{zw} = P_{11} + P_{12}K(I - P_{22}K)^{-1}P_{21} \tag{2.30}$$

The H_∞ norm of any transfer function is expressed as $\|\cdot\|_\infty$ and therefore $\|T_{zw}\|_\infty$ is expressed by Eq.(2.31).

$$\begin{aligned} \|T_{zw}(P,K;s)\|_\infty &= \sup_{0\leq\omega\leq\infty} \bar{\sigma}(T_{zw}(P,K;j\omega)) \\ \overline{\sigma} &= \sqrt{\lambda_{max}(M^*M)} \end{aligned} \tag{2.31}$$

Here, $\overline{\sigma}$ expresses the maximum singular value, $s = j\omega$ for sinusoidal steady-state response, sup represents the supremum or the maximum signal, λ_{max} is the maximum eigen value, M and M^* are the complex matrix and the conjugate transpose of an complex matrix respectively.

As noted in Section 2.4.1, nominal H_∞ controller design uses either the method of algebraic Riccati equation or Linear Matrix Inequality (LMI) problem [34]. Here, the method

of algebraic Riccati equation is briefly explained referenced from [27]. For the generalized plant introduced in Section 2.4, the state-space realization are shown in Eqs.(2.32).

$$\begin{aligned} \dot{x}(t) &= Ax(t) + B_1 w(t) + B_2 u(t) \\ z(t) &= C_1 x(t) + D_{11} w(t) + D_{12} u(t) \\ y(t) &= C_2 x(t) + D_{21} w(t) \end{aligned} \tag{2.32}$$

Here, $w(t) \in \mathbb{R}^{m_1}$ is the disturbance vector, $u(t) \in \mathbb{R}^{m_2}$ is the control input, $z(t) \in \mathbb{R}^{p_1}$ is the tracking error, $y(t) \in \mathbb{R}^{p_2}$ is the output, and $x(t) \in \mathbb{R}^n$ is the states. The equations from Eqs.(2.32) can be organized into a state-space realization shown in Eq.(2.33) when $[w^T \ u^T]^T$ are the control inputs and $[z^T \ y^T]^T$ are the outputs.

$$\dot{x}(t) = Ax(t) + \begin{bmatrix} B_1 & B_2 \end{bmatrix} \begin{bmatrix} w(t) \\ u(t) \end{bmatrix} \tag{2.33}$$

$$\begin{bmatrix} z(t) \\ y(t) \end{bmatrix} = \begin{bmatrix} C_1 \\ C_2 \end{bmatrix} x(t) + \begin{bmatrix} D_{11} & D_{12} \\ D_{21} & 0 \end{bmatrix} \begin{bmatrix} w(t) \\ u(t) \end{bmatrix} \tag{2.34}$$

For simplicity, $B = \begin{bmatrix} B_1 & B_2 \end{bmatrix}, C = \begin{bmatrix} C_1 \\ C_2 \end{bmatrix}$, and $D = \begin{bmatrix} D_{11} & D_{12} \\ D_{21} & 0 \end{bmatrix}$.

Using Doyle's notation from [27], Eq.(2.29) can be expressed into Eq.(2.35) as a transfer function of Eq.(2.32).

$$\begin{aligned} P &= \begin{bmatrix} P_{11} & P_{12} \\ P_{21} & P_{22} \end{bmatrix} = \begin{bmatrix} D_{11} & D_{12} \\ D_{21} & D_{22} \end{bmatrix} + \begin{bmatrix} C_1 \\ C_2 \end{bmatrix} (sI - A)^{-1} \begin{bmatrix} B_1 & B_2 \end{bmatrix} \\ &= \left[\begin{array}{c|c} A & B \\ \hline C & D \end{array}\right] \end{aligned} \tag{2.35}$$

The following assumptions are made for deriving a stabilizing controller K referenced from [27].

A1. (A, B_2, C_2) are stabilizable and detectable.

A2. vertically long column of D_{12} and horizontally long row of D_{21} is full rank.

A3. with the unitary transformation of w and z and scaling of u and y, the D_{12} and D_{21} is defined by Eq.(2.36) matrix without the loss of generality.

$$D_{12} = \begin{bmatrix} 0 \\ I \end{bmatrix}, \quad D_{21} = \begin{bmatrix} 0 & I \end{bmatrix} \tag{2.36}$$

Additionally, D_{11} is divided into the following subsections.

$$D_{11} := \begin{array}{c} \\ (p_1 - m_2)\updownarrow \\ m_2 \updownarrow \end{array} \begin{array}{c} \overset{(m_1-p_2)}{\longleftrightarrow} \quad \overset{p_2}{\longleftrightarrow} \\ \begin{bmatrix} D_{1111} & D_{1112} \\ D_{1121} & D_{1122} \end{bmatrix} \end{array} \tag{2.37}$$

A4. P_{12} from Eq.(2.29) defined in Eq.(2.38) has a full rank column.

$$\operatorname{rank} \begin{bmatrix} A - j\omega I & B_2 \\ C_1 & D_{12} \end{bmatrix} = n + m_2 \tag{2.38}$$

A5. P_{21} from Eq.(2.29) defined in Eq.(2.39) has a full rank row.

$$\operatorname{rank} \begin{bmatrix} A - j\omega I & B_1 \\ C_2 & D_{21} \end{bmatrix} = n + p_2 \tag{2.39}$$

Next, the following matrices are defined for obtaining the Hamiltonian matrix used for the solution to the algebraic Riccati equation:

$$R := D_{1\bullet}^* D_{1\bullet} - \begin{bmatrix} \gamma^2 I_{m1} & 0 \\ 0 & 0 \end{bmatrix} \tag{2.40}$$

$$\tilde{R} := D_{\bullet 1} D_{\bullet 1}^* - \begin{bmatrix} \gamma^2 I_{p1} & 0 \\ 0 & 0 \end{bmatrix} \tag{2.41}$$

Here, $D_{1\bullet} := [D_{11}\ D_{12}]$, $D_{\bullet 1} := [D_{11}\ D_{12}]^T$, and $\gamma \in \mathbb{R}$ is a prescribed value from the equation $\|T_{zw}(P,K;s)\|_\infty < \gamma$. Solution to the algebraic Riccati equation are obtained by the following Hamiltonian matrix X_∞ and Y_∞ assuming a stabilizing solution.

$$X_\infty := \begin{bmatrix} A & 0 \\ -C_1^* C_1 & -A^* \end{bmatrix} - \begin{bmatrix} B \\ -C_1^* D_{1\bullet} \end{bmatrix} R^{-1} \begin{bmatrix} D_{\bullet 1}^* B_1 C \end{bmatrix} \tag{2.42}$$

$$Y_\infty := \begin{bmatrix} A* & 0 \\ -B_1 B_1^* & -A \end{bmatrix} - \begin{bmatrix} C^* \\ -B_1 D_{\bullet 1}^* \end{bmatrix} \tilde{R}^{-1} \begin{bmatrix} D_{\bullet 1}^* B_1 C \end{bmatrix} \tag{2.43}$$

By using Eq.(2.42) and Eq.(2.43), the "state feedback" and "output injection" matrices as defined in [27] is defined in Eqs.(2.44) and (2.45).

$$F := \begin{matrix} (p_1-m_2)\updownarrow \\ p_2\updownarrow \\ m_2\updownarrow \end{matrix} \begin{bmatrix} F_{11} \\ F_{12} \\ F_2 \end{bmatrix} := -R^{-1}[D_{1\bullet}^* C_1 + B^* X_\infty] \tag{2.44}$$

$$H := \begin{matrix} \overset{(p_1-m_2)}{\leftrightarrow} & \overset{m_2}{\leftrightarrow} & \overset{p_2}{\leftrightarrow} \end{matrix} \begin{bmatrix} H_{11} & H_{12} & H_2 \end{bmatrix} := -[B_1 D_{\bullet 1}^* + Y_\infty C^*]\tilde{R}^{-1} \tag{2.45}$$

Under the assumption that Theorem I (see Appendix A.1) from [27] is met, all rational internally stabilizing controller K satisfying $\|N\|_\infty < \gamma$ for arbitrary $N \in RH^\infty$ can be expressed by Eq.(2.46).

$$K := M_{11} + M_{12}(I - NM_{22})^{-1} N M_{21} \tag{2.46}$$

Where M is defined by the following matrix:

$$M := \begin{bmatrix} M_{11} & M_{12} \\ M_{21} & M_{22} \end{bmatrix} = \left[\begin{array}{c|cc} \hat{A} & \hat{B_1} & \hat{B_2} \\ \hline \hat{C_1} & \hat{D_{11}} & \hat{D_{12}} \\ \hat{C_2} & \hat{D_{21}} & 0 \end{array}\right] \tag{2.47}$$

$$\hat{D_{11}} := -D_{1121} D_{1111}^* (\gamma^2 I - D_{1111} D_{1111}^*)^{-1} D_{1112} - D_{1112} \tag{2.48}$$

Here, $\hat{D_{12}} \in \mathbb{R}^{m_2 \times m_2}$ and $\hat{D_{21}} \in \mathbb{R}^{p_2 \times p_2}$ are any matrices satisfying the following:

$$\begin{aligned} \hat{D_{12}} \hat{D_{12}^*} &:= I - D_{1121}(\gamma^2 I - D_{1111}^* D_{1111})^{-1} D_{1121}^* \\ \hat{D_{21}} \hat{D_{21}^*} &:= I - D_{1112}(\gamma^2 I - D_{1111}^* D_{1111})^{-1} D_{1112}^* \end{aligned} \tag{2.49}$$

as well as:

$$\begin{aligned} \hat{B_2} &:= (B_2 + H_{12})\hat{D_{12}} \\ \hat{C_2} &:= -\hat{D_{21}}(C_2 + F_{12})Z \\ \hat{B_1} &:= -H_2 + B_2 D \hat{-}\hat{} 1_{12} \hat{D_{11}} \\ \hat{C_1} &:= F_2 Z + \hat{D_{11}} \hat{D_{21}^{-1}} \hat{C_1} \\ \hat{A} &:= A + HC + \hat{B_2} \hat{D_{12}^{-1}} \hat{C_1} \\ Z &:= (I - \gamma^{-2} Y_\infty X_\infty)^{-1} \end{aligned} \tag{2.50}$$

The controller K assumed in Eq.(2.46) can be simplified assuming $N = 0$. Eq.(2.51) is referred to as the central solution often used for controller design and has the same structure as Eq.(2.30).

$$K = M_{11} = \hat{D_{11}} + \hat{C}_1(sI - \hat{A})^{-1}\hat{B}_1 \tag{2.51}$$

As can be seen from Eq.(2.51), the dimension of the central solution is equal to the dimension of the plant model. In the general plant model, not only is the dimension of the plant model considered but the weighting function is considered as well. Therefore, the dimension of the controller is the total sum of plant model as well as the weighting function. The dimension for the controller increases depending on the system, making implementation and understanding of the controller difficult. Due to the nature of the controller having a high dimension, for a more practical controller placing a structural constraint on the controller (e.g. PI controller) is preferred.

2.4.2 Structured H_∞ Controller Design

Structured H_∞ controller design makes the controller to have same structure as a practical *PI* (e.g. *P*, *PI*, *PID*, etc) controllers making ease of implementation while keeping a low-order transfer function for better understanding which increases practicality [26, 52]. Here, the method of structured H_∞ controller design using nonsmooth optimization is briefly explained referenced from [6]. The controller design is conducted by following the nominal H_∞ controller design where for a closed-loop system of T_{zw} (input signal w to output signal z) the objective is to minimize the H_∞-norm (corresponds to maximum singular value $\bar{\sigma}(T_{zw}(j\omega))$[67]) such that the controller K stabilizes plant model P internally [26]. The controller K is assumed to have the same frequency domain representation as Eq.(2.30) but with constraint placed on the control structure. With the structural constraint $K \in K_{pi}$ (i.e. for PI controller) and the order of the controller being k ($A_K \in \mathbb{R}^{k\times k}$), Eq.(2.30) is expressed as Eq.(2.52).

$$K = C_K(sI - A_K)^{-1}B_K + D_K \tag{2.52}$$

K is obtained through optimization and the formulation for the optimization problem is summarized as follows:

$$\begin{aligned} \min. \quad & \|T_{zw}(P,K;s)\|_\infty = \sup_{0\le\omega\le\infty} \bar{\sigma}(T_{zw}(P,K;j\omega)) \\ \text{s.t.} \quad & K \text{ stabilizes } P \text{ internally} \\ & K \in K_{pi} \end{aligned} \tag{2.53}$$

The optimization problem of Eq.(2.53) is solved through steepest descent method [18] where the H_∞ norm is evaluated directly using the Hamiltonian bisection algorithm [17, 24] with the subgradients obtained through Clarke's subdifferential [20] and used to compute the step length of the steepest descent method. The method in [6] is unique in that it applies Clarke's subdifferential to a closed-loop transfer function to be used by the steepest decent method. Furthermore, the method is extended to the simultaneous optimization of a finite family of closed-loop transfer functions. Therefore, the method of applying Clarke's subdifferential to nonzero transfer function as well as to a closed loop transfer function and the steepest descent method will be briefly noted followed by a brief explanation for stabilizing a finite family of closed-loop transfer functions.

The H_∞ norm of a nonzero stable transfer function $G(s)$ is expressed in Eq.(2.54) where Eq.(2.54) is attained at frequency ω.

$$\|G\|_\infty = \sup_{\omega\in\mathbb{R}} \bar{\sigma}(G(j\omega)) \tag{2.54}$$

Here, $G(j\omega) = U\sum V^H$ is the singular value decomposition. Let the first column of U be u and the first column of V by v and by doing so, $u = G(j\omega)v/\|G\|_\infty$ can be expressed. Here, the linear function $\phi = \phi_{u,v,\omega}$ is expressed as Eq.(2.55).

$$\begin{aligned} \phi(H) &= \mathrm{Re}(u^H(j\omega)v) \\ &= \|G\|_\infty^{-1}\mathrm{ReTr}vv^H G(j\omega)^H H(j\omega) \\ &= \|G\|_\infty^{-1}\mathrm{ReTr}G(j\omega)^H uu^H(j\omega) \end{aligned} \tag{2.55}$$

Here, ϕ is continuous across all stable transfer function space H_∞ and $\|\cdot\|_\infty$ is the infinity norm. To be more general, Q_u has a column whose orthonormal basis of the eigenspace of $G(j\omega)G(j\omega)^H$ is related to the leading eigen value of $\lambda_1(G(j\omega)G(j\omega)^H) = \sigma(G(j\omega))^2$. Additionally, Q_v has a column whose orthonormal basis of the eigenspace of $G(j\omega)^H G(j\omega)$ is related to the leadin eigen value of $\lambda_1(G(j\omega)G(j\omega)^H) = \sigma(G(j\omega))^2$. Here, $Y \succeq 0$ defines Y is a semidefinite problem. For all Hamiltonian matrix $Y_v \succeq 0, Y_u \succeq 0$ where $\mathrm{Tr}(Y_v) = 1, \mathrm{Tr}(Y_u) = 1$, the subgradient of $\|\cdot\|_\infty$ regarding G is expressed as Eq.(2.56).

$$\begin{aligned}\phi(H) &= \|G\|_\infty^{-1}\mathrm{ReTr}Q_v Y_v Q_v^H G(j\omega)^H H(j\omega) \\ &= \|G\|_\infty^{-1}\mathrm{ReTr}G(j\omega)^H Q_u Y_u Q_u^H H(j\omega)\end{aligned} \tag{2.56}$$

With $G(s)$ being a rational function and assuming finitely existing frequencies $\omega_1, \cdots, \omega_p$ where the supremum of $\|G\|_\infty^{-1} = \bar{\sigma}(G(j\omega_v))$ is attained, all subgradients of $\|\cdot\|_\infty$ regarding G is expressed as Eq.(2.57).

$$\phi(H) = \|G\|_\infty^{-1}\mathrm{Re}\sum_{v=1}^{p}\mathrm{Tr}G(j\omega)^H Q_v Y_v Q_v^H H(j\omega_v) \tag{2.57}$$

Here, Q_v has a column whose orthonormal basis of the eigenspace of $G(j\omega)G(j\omega)^H$ is related to the leading eigen value of $\|G\|_\infty^2$ where $Y_v \succeq 0, \sum_{v=1}^{p}\mathrm{Tr}(Y_v) = 1$. For further details, refer to [20, 5].

Next, assuming smooth operator G can be mapped onto the space H_∞ for all stable transfer function G, the Clarke's subdifferential at x can be calculated for the composite function $f(x) = \|\mathrm{G}\|_\infty$. Clarke's subdifferential is calculated by Eq.(2.58).

$$\partial f(x) = \mathrm{G}'(x)^*[\partial\|\cdot\|_\infty(\mathrm{G}(x))] \tag{2.58}$$

Here, $\partial\|\cdot\|_\infty$ is the subgradient of the H_∞ norm, $\mathrm{G}'(x)^*$ is the adjoint of $\mathrm{G}(x)$ mapping the dual of H_∞ onto $\mathbb{R}^n$ where $\mathbb{R}^n$ is identified with its dual. The following will proceed to compute the adjoint $\mathrm{G}'(x)^*$ for a closed-loop transfer functions. The generalized plant model in Section 2.4.1 will be used to obtain the closed-loop transfer function here.

For the generalized plant model shown in Eq.(2.29), the closed-loop transfer function is obtained as Eq.(2.30). Here, the derivative $T_{zw}^{'}(K)$ of $T_{zw}^{'}$ at K is shown in Eq.(2.59).

$$T_{zw}^{'}(K)\delta K := P_{12}(I - KP_{22})^{-1}\delta K(I - P_{22}K)^{-1}P_{21} \tag{2.59}$$

Here, δK is an element of the same matrix space as K. By using the chain rule from [20], the subgradients Φ_Y of f at K can be expressed as Eq.(2.60).

$$\Phi_Y := T_{zw}^{'}(K)^*\phi_y \in M_{m2,p2} \tag{2.60}$$

Here, $\phi = \phi_Y$ is the subgradient of $\|\cdot\|_\infty$ of $T_{zw}^{'}(K)$ meeting the requirements of $Y \succeq 0, \mathrm{Tr}(Y) = 1$. The adjoint $T_{zw}^{'}(K)^*$ acts on ϕ_Y through Eq.(2.61).

$$\begin{aligned}\langle T_{zw}^{'}(K)^{*}\phi_Y, \delta K\rangle =& \langle T_{zw}^{'}(K)^{*}\phi_y \delta K, \phi_Y\rangle \\ =& \|T_{zw}(K)\|_{\infty}^{-1}\mathrm{ReTr}\{(I-P_{22}(j\omega)K(j\omega))^{-1} \\ & P_{21}(j\omega)T_{zw}(K,j\omega)^{H}QYQ^{H}P_{12}(j\omega) \\ & (I-K(j\omega)P_{22}(j\omega))^{-1}\delta K(j\omega)\}\end{aligned} \tag{2.61}$$

Here, $\langle a,b\rangle$ represents the inner product of a and b. For the full derivation of Eq.(2.61), refer to [6] and thus will be omitted. Finally, the Clarke's subdifferential $f(K) := \|T_{zw}(k)\|_{\infty}$ at K consists of all subgradients Φ_Y ($Y \succeq 0, \mathrm{Tr}(Y) = 1$) and is expressed as Eq.(2.62).

$$\begin{aligned}\Phi_Y =& \|T_{zw}(K)\|_{\infty}^{-1}\mathrm{Re}\{(I-P_{22}(j\omega)K)^{-1}P_{21}(j\omega)T_{zw}(K,j\omega)^{H}QYQ^{H}P_{12}(j\omega) \\ & (I-KP_{22}(j\omega))^{-1}\}^{T}\end{aligned} \tag{2.62}$$

When Eq.(2.62) is expressed in finite number of frequencies from $\omega_1, \cdots, \omega_q$, Clarke's subdifferential $f(K) := \|T_{zw}(k)\|_{\infty}$ at K consists of all subgradients Φ_Y ($Y = (Y_1, \cdots, Y_q), Y_v \succeq 0, \sum_{v=1}^{q}\mathrm{Tr}(Y) = 1$) and can be derived by Eq.(2.63).

$$\begin{aligned}\Phi_Y =& \|T_{zw}(K)\|_{\infty}^{-1}\sum_{v=1}^{q}\mathrm{Re}\{(I-P_{22}(j\omega_v)K)^{-1}P_{21}(j\omega_v)T_{zw}(K,j\omega_v)^{H}QY_vQ^{H}P_{12}(j\omega_v) \\ & (I-KP_{22}(j\omega_v))^{-1}\}^{T}\end{aligned} \tag{2.63}$$

Eq.(2.63) is a general form which can be applied to static, dynamic, structured, or matrix fraction represented controllers. Using Eq.(2.63), the optimization problem Eq.(2.53) can be solved through steepest descent method. Consider now the objective function shown in Eq.(2.53) of minimizing $f(x) = \|\mathrm{G}(x)\|_{\infty}$ where x is K or the regrouped controller data and G maps $\mathbb{R}^n$ smoothly into space H_{∞} of stable transfer function. The necessary condition for reaching a optimal solution is $0 \ni \partial f(x) = \mathrm{G}^{'}(x)^{*}\partial\|\cdot\|_{\infty}(\mathrm{G}(x))$. Thus, the problem is considered to be in the form of Eq.(2.64).

$$d = -\frac{g}{\|g\|}, \;\; g = \mathrm{argmin}\{\|\phi_Y\| : Y = (Y_1, \cdots, Y_q), Y_v \succeq 0, \sum_{v=1}^{q}\mathrm{Tr}(Y) = 1)\} \tag{2.64}$$

Eq.(2.64) shows that the optimum solution is obtained when $0 \ni \partial f(x)$ or if $0 \notin \partial f(x)$ at x then x is changed dependent on the direction d of the steepest descent at x. Here, $\phi_Y = \Phi_Y$ derived from Eq.(2.63). By vectorizing $y = vec(Y), Y = (Y_1, \cdots, Y_q)$, then Φ_Y can now be

expressed as matrix vector product of $\Phi_Y = \Phi y$. Eq.(2.64) can now be interpreted as a semi-definite programming of Eq.(2.65) referenced from [6].

$$\begin{aligned} \min. \quad & t \\ \text{s.t.} \quad & \begin{bmatrix} t & y^T\Phi^T \\ \Phi y & tI \end{bmatrix} \succeq 0 \\ & Y_i \succeq 0, i = 1, \cdots, q \\ & e^T y = 1 \end{aligned} \tag{2.65}$$

Here, $e^T y = 1$ represents $\sum_i \mathrm{Tr}(Y_i) = 1$ and the direction d of the steepest descent method from Eq.(2.64) can be expressed as $d = -\Phi y / \|\Phi y\|$ where (t, y) is the solution of Eq.(2.65) with $y \neq 0$. The algorithm is summarized by the following:

Step 1. **Evaluate Gradient:**
if $0 \ni \partial f(x)$, then terminate. if not, then go to step 2.

Step 2. **Solve Steepest Descent Problem:**
solve Eq.(2.65) to obtain direction d of the steepest descent method at x.

Step 3. **Perform Line Search:**
perform line search to obtain steepest step of $x^+ = x + td$.

Step 4. **Iterate:**
rewrite x as x^+ and repeat from step 1.

When using this approach, the optimization can fail to converge due to the nonsmoothness of f. Modifications of the steepest descent method are discussed in [6] and details will be omitted due to the modification being outside the scope of this dissertation.

Using the steepest descent method to solve Eq.(2.65), Eq.(2.53) is extended to minimizing the H_∞ norm for a finite family of closed-loop transfer functions $T_{zw}^{(k)}$ where k represents the k-th plant model. Consider first a Laplace transformed transfer function of Eq.(2.32) from input w to output z having the dimension of $p_1 \times m_1$ dimension, the transfer function matrix of T_{zw} is expressed as Eq.(2.66).

$$T_{zw} = \begin{bmatrix} p_{11} & \cdots & p_{1j} & \cdots & p_{1m_1} \\ \vdots & \ddots & & & \vdots \\ p_{i1} & & \ddots & & p_{im} \\ \vdots & & & \ddots & \vdots \\ p_{p_1 1} & \cdots & p_{p_1 j} & \cdots & p_{p_1 m_1} \end{bmatrix} \tag{2.66}$$

Here, p_{ij} represents the input from the j-th element of w to the output from the i-th element of z. Now for a k-th plant model ($k \in \mathbb{N}$) of $T_{zw}^{(k)}$, the transfer function matrix of $T_{zw}^{(k)}$ is expressed as Eq.(2.67) where n represents arbitrary integer $1 \leq n \leq k$.

$$
\begin{aligned}
T_{zw}^{(1)} &= \begin{bmatrix} p_{111} & \cdots & p_{1j1} & \cdots & p_{1m_11} \\ \vdots & \ddots & & & \vdots \\ p_{i11} & & \ddots & & p_{im1} \\ \vdots & & & \ddots & \vdots \\ p_{p_11} & \cdots & p_{p_1j1} & \cdots & p_{p_1m_11} \end{bmatrix} \\
&\vdots \\
T_{zw}^{(n)} &= \begin{bmatrix} p_{11n} & \cdots & p_{1jn} & \cdots & p_{1m_1n} \\ \vdots & \ddots & & & \vdots \\ p_{i1n} & & \ddots & & p_{imn} \\ \vdots & & & \ddots & \vdots \\ p_{p_11n} & \cdots & p_{p_1jn} & \cdots & p_{p_1m_1n} \end{bmatrix} \\
&\vdots \\
T_{zw}^{(k)} &= \begin{bmatrix} p_{11k} & \cdots & p_{1jk} & \cdots & p_{1m_1k} \\ \vdots & \ddots & & & \vdots \\ p_{i1k} & & \ddots & & p_{imk} \\ \vdots & & & \ddots & \vdots \\ p_{p_11k} & \cdots & p_{p_1jk} & \cdots & p_{p_1m_1k} \end{bmatrix}
\end{aligned}
\tag{2.67}
$$

Eq.(2.53) is solved using *hinfstruct* MATLAB function [26] where stability and performance is obtained when $||T_{zw}(P,K;s)||_\infty < 1$ as is shown in [72]. Eq.(2.67) was used for the multiple model approach [2] to obtain a common PI gain for k set of plant models P_k which has been used by Ref. [70]. Structured H_∞ controller design proposed here will therefore be robust for multiple LTI models linearized at different flight conditions obtained through linearizing a nonlinear model.

The constructed system for the H_∞ controller design is shown in Fig.2.5. The system has r being the reference trajectory, e being the tracking error, u being the control input, d being the disturbance, and y being the output. The SITF in Fig.2.5 is the transfer function of the converted trajectory for the nth segment in the trajectory. The controller structure is defined as Eq.(2.68) where k_p, k_i are the tunable parameters of K and the integral controller uses

a pseudo integrator ($\varepsilon = 0.02$) for this study. The control period for tracking the reference input was fixed at 50[hz] (0.02 [s]) by referring to [52].

$$K = k_p + k_i \frac{1}{s+\varepsilon} \tag{2.68}$$

W_e and W_u blocks are the weighting functions used for shaping the transfer function from r to e and r to y respectively. In Fig.2.5, T_{zw} from Eq.(2.53) has a following signals where w denotes the reference and disturbance inputs ($w = [r\ d]^T$) and z denotes outputs from W_e and W_u respectively ($z = [z_e\ z_u]^T$). Δe and Δu represents the uncertainty variables where in this study Δe is a fictitious uncertainty placed only to close the loop and $\Delta u = 0$ which considers no uncertainties (Δe and Δu where introduced by referring to Ref.[70, 52, 67]). It should be noted that in this study, weighting functions W_e and W_u placed on the system were used as tuning parameters and tuned through trial and error for the H_∞ norm to be as close to 1 as possible for high tracking performance (tuning method referred to Ref.[70]). Symbol W_e was placed on the sensitivity function to minimize the error for increasing tracking performance. Symbol W_u was placed on the complementary sensitivity function to minimize the command input by referring to Ref. [56]. Performance and stability are obtained by tuning K by solving Eq.(2.53) to meet the following equations as shown in [34].

$$\begin{aligned} \|W_e S\|_\infty &< 1 \\ \|W_e T\|_\infty &< 1 \end{aligned} \tag{2.69}$$

The proposed system incorporates the trajectory information via SITF during the robust controller design which is expressed as a form of a mixed sensitivity problem. In a mixed sensitivity problem [49], the general equation between the sensitivity function S and complementary sensitivity function T holds as the following:

$$S + T = \frac{1}{1+PK} + \frac{PK}{1+PK} = 1 \tag{2.70}$$

Eq.(2.70) is the general equation representing the trade-off between performance and stability. Since the proposed method incorporates SITF into the system (Fig.2.5), Eq.(2.70) is then expressed as a form of a mixed sensitivity problem with the following relation shown in Eq.(2.71).

$$S + T = \frac{1}{1+PK} + \frac{PK}{1+PK} = \text{SITF} \tag{2.71}$$

Since general robust controller design is conducted by expressing the design requirements of Eq.(2.69) in terms of weighting functions $\frac{1}{W_e}$ and $\frac{1}{W_u}$, the proposed system will be evaluated

in terms of $\frac{1}{W_e}$ and $\frac{1}{W_u}$ as well. The proposed method can be defined as a form of a mixed sensitivity problem compared to the conventional method using the general mixed sensitivity problem. Therefore, in order to separate the transfer function from reference input to tracking error between the proposed and conventional method, for the proposed method Eq.(2.72) will be used.

$$T_{r2e} = \frac{S}{SITF} \tag{2.72}$$

The same will be applied to the transfer function from reference input to the plant output and for the proposed method Eq.(2.73) will be used.

$$T_{r2y} = \frac{T}{SITF} \tag{2.73}$$

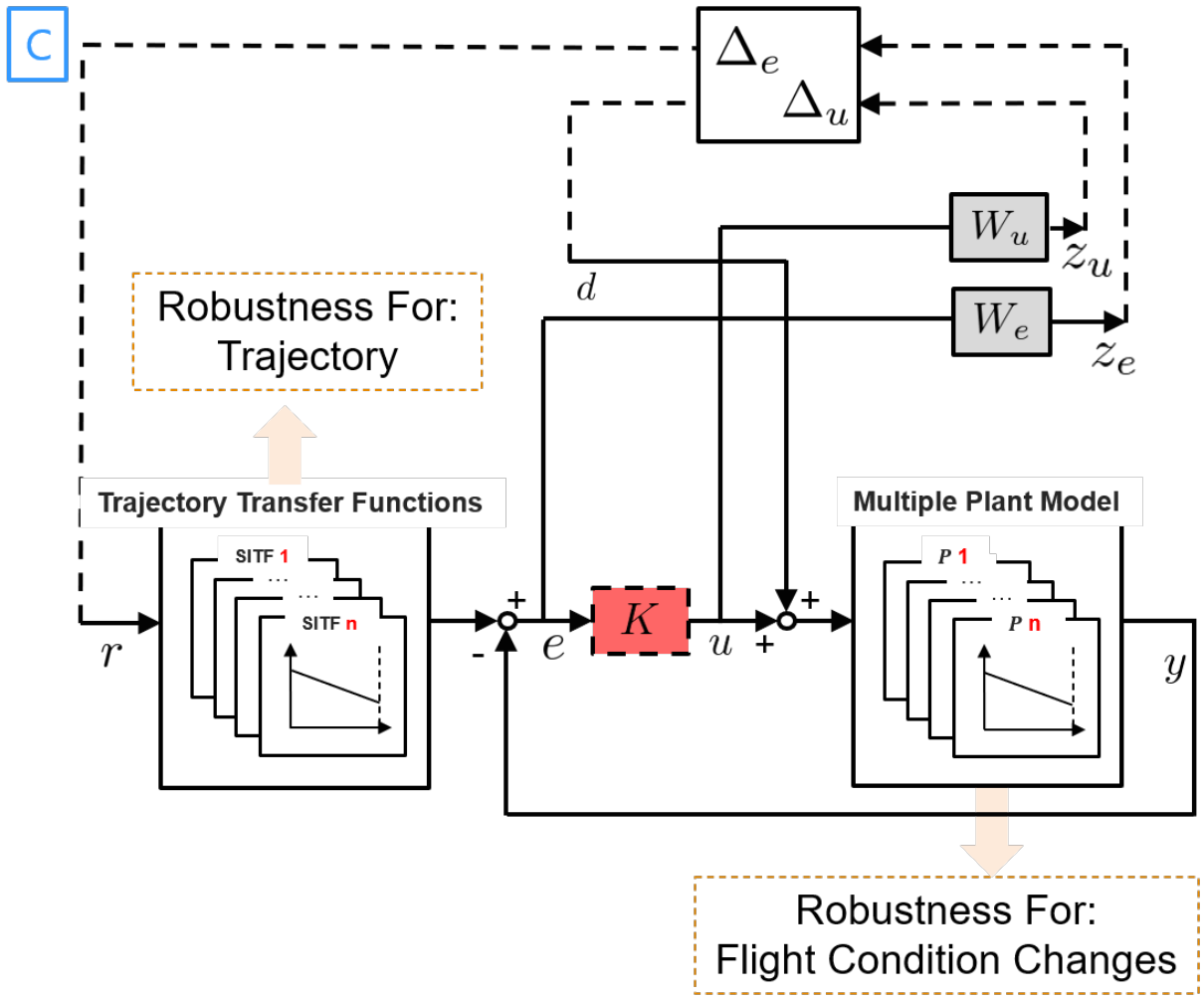

Fig. 2.5 Proposed System for Robust Controller Design Method.

2.5 Advantages and Limitations

Primary advantages of the proposed method over the conventional method of designing the trajectory and robust controller separately are given as follows:

1) Trajectory and robust controller are obtained simultaneously which can reduce the risk of redesign since the stability and performance for the controller is guaranteed to the obtained control-oriented optimal trajectory.

2) Robustness against the trajectory obtained from the optimal solution is obtained since trajectory information is incorporated into the robust controller design through system identification.

3) Flexibility in designing a trajectory specific to the tolerable maximum tracking error given by the user since maximum tracking error is placed as nonlinear inequality constraint in the NLP problem.

The proposed method has some limitations. First, the global optimal solution cannot be necessarily found since the NLP problem is solved with a gradient-based optimizer (SQP) and converges usually to a local optimum. Therefore, the problem is sensitive to the initial conditions as well as scaling of the design variables. Second, in order to satisfy the nonlinear inequality constraint of tolerable maximum tracking error, sufficient knowledge and tuning of the weighting functions for the transfer function from r to e and r to y in the frequency domain is desired and without proper tuning, the maximum tracking error cannot be achieved. The second drawback can often be circumvented by designing the transfer function from r to e to have higher performance at low frequencies (low frequencies are minimized compared to high frequencies) since trajectory usually has moderate changes and relaxed performance at higher frequencies since usually high frequencies are prone to noise. Additionally, the transfer function from r to y should be designed with minimizing the high frequencies since control input should be minimized to high frequency disturbances.

Chapter 3

Performance Comparison to Designing Trajectory and Controller Separately

Following the development of the novel method in the previous Chapter, applicability of the proposed method are identified by conducting the performance comparison to the conventional method of obtaining a trajectory and controller separately to two example problems. In Section 3.1, applicability of the proposed method to a benchmark aerospace related optimal control problem is demonstrated through solving a modified rocket launch problem. In Section 3.2, applicability of the proposed method to a optimal control problem outside of the aerospace field is demonstrated through solving a modified Zermelo's problem.

3.1 Modified Rocket Launch Problem

In order to test the proposed method (Simultaneous) for applicability to aerospace related problems, the rocket launch problem [19] used commonly for optimal control example will be used to compare against the conventional method of obtaining the controller separately from the trajectory (Separated). The problem was modified to incorporate friction to the dynamic model [37] since the model was not controllable in the sense that when making an LTI model, matrix A in Eq.(B.1) did not have full rank where $\det|[B,AB]| = 0$. The state variables are horizontal velocity u, vertical velocity v, horizontal distance x, and vertical distance y. The problem is a rocket launching from the ground to reach the target altitude y_f of 50 and v_f of 0 while maximizing final horizontal velocity u_f with the control input β and is depicted in Fig.3.1. The SISO system tracks the reference v generated at each iteration of SQP and has a feedback loop for obtaining maximum error e_{max} against the output v. The e_{max} is then evaluated to meet the nonlinear inequality constraint.

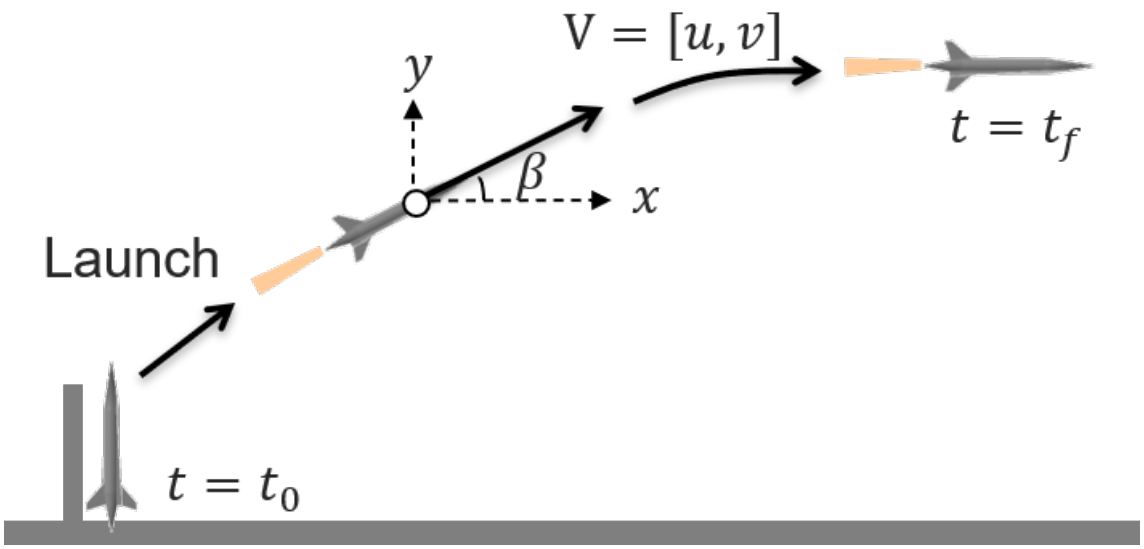

Fig. 3.1 Diagram of Rocket Launch Problem.

3.1.1 Nonlinear Trajectory Design

The nonlinear trajectory design will be evaluated for improving the objective function while meeting the e_{max} nonlinear inequality constraint placed on the NLP probem. The dynamic equations used for trajectory optimization and closed loop nonlinear simulation are shown in Eqs.(3.1). Here, k_1=0.2 and k_2=0.1 both represent the vertical and horizontal air friction respectively. The closed loop nonlinear simulation tracks the reference v with a feedback loop from the output v. Symbol a represents the constant acceleration and was fixed at 2.

$$\begin{aligned} \dot{u} &= a\cos\beta - k_1 v \\ \dot{v} &= a\sin\beta - k_2 v \\ \dot{x} &= u \\ \dot{y} &= v \end{aligned} \tag{3.1}$$

Formulation of the optimal control problem is as follows:

$$
\begin{aligned}
\text{find} \quad & \text{state variables} : X = [u, v, x, y] \\
& \text{control variables} : \beta \text{ [deg]} \\
\text{min.} \quad & -u_f \\
\text{s.t.} \quad & \text{state equations shown in Eqs.(3.1) of Section3.1.1} \\
& -90 \leq \beta \leq 90 \text{ [deg]} \\
& e_{max} \leq 0.99 \quad \text{(Unused in Separated method)} \\
& X_0 = [0, 0, 0, 0] \\
& v_f = 0 \\
& y_f = 45 \\
& t_f = 10 \\
& a = 2
\end{aligned}
\tag{3.2}
$$

The problem was discretized using direct single shooting method explained in Section 2.2.1. The problem was discretized into 10 sub-segments and the transfer function was identified for each sub-segment in the trajectory at every iteration. At each iteration, for the Simultaneous method the maximum tracking error was calculated through closed loop nonlinear simulation and for the Separated method, optimal trajectory was obtained without considering the e_{max} as the nonlinear inequality constraint.

3.1.2 Linear Robust Controller Design

Both controllers obtained in the Separated and Simultaneous method through robust controller design will be evaluated for stability, performance, and robustness against flight condition changes of β as well as to the identified trajectories. The linear time invariant (LTI) model was obtained by linearizing the equations $\dot{u}$ and $\dot{v}$ in Eq.(3.2) at two constant launch angle conditions. The LTI model was constructed by linearizing the equations for the dynamic equation at constant β of 20 [deg] and 80 [deg] through perturbation method. The state equations are linearized about the steady state condition in the form of Eq.(B.1) (subscripts for matrix A and B denotes the linearized β).

$$
\begin{aligned}
\dot{x} &= A_i x + B_i u \\
y &= Cx
\end{aligned}
\tag{3.3}
$$

where the new state variables obtained through perturbation are the following:

$$\begin{aligned} x &= [\Delta u \;\; \Delta v]^T \\ y &= [v] \\ u &= [\Delta\beta] \end{aligned} \tag{3.4}$$

The LTI models linearized through the perturbation are shown in Eq.(3.5).

$$A = \begin{bmatrix} -k_1 & 0 \\ 0 & -k_2 \end{bmatrix}, \quad B = \begin{bmatrix} -2\sin\beta_0 \\ 2\cos\beta_0 \end{bmatrix} \tag{3.5}$$

The LTI models for $\beta = 20$ and $\beta = 80$ [deg] are shown in Eq.(3.6) to (3.8).

$$A_{20} = \begin{bmatrix} -0.2 & 0 \\ 0 & -0.1 \end{bmatrix}, \quad B_{20} = \begin{bmatrix} -0.69 \\ 1.8 \end{bmatrix} \tag{3.6}$$

$$A_{80} = \begin{bmatrix} -0.2 & 0 \\ 0 & -0.1 \end{bmatrix}, \quad B_{80} = \begin{bmatrix} -1.9 \\ 0.35 \end{bmatrix} \tag{3.7}$$

$$C = \begin{bmatrix} 0 & 1 \end{bmatrix} \tag{3.8}$$

The system used for the Separated method in designing the robust controller is shown in Fig.3.2. Here, reference r represents the optimal v and the system feedbacks the v output denoted as y. The system is the same as in the Simultaneous method shown in Fig.2.5 except that the identified trajectory (SITF) is neglected (i.e. explanation of each variables and blocks are omitted, refer to 2.4.1). For the Simultaneous method, since the trajectory was identified at each segment to be incorporated into robust controller design, robustness against the SITF will be evaluated as well. The weighting functions W_e and W_u are shown in Eqs.(3.9) and (3.10) which was tuned through trial and error to increase tracking performance. Robustness against flight condition changes and to the trajectory was evaluated based on the step response of the linearized steady state model (explained in section 3.1.2) and SITF for having high tracking performance.

$$W_e = \frac{s+1}{4s+0.08} \tag{3.9}$$

$$W_u = \frac{s+1}{1.5s+2} \tag{3.10}$$

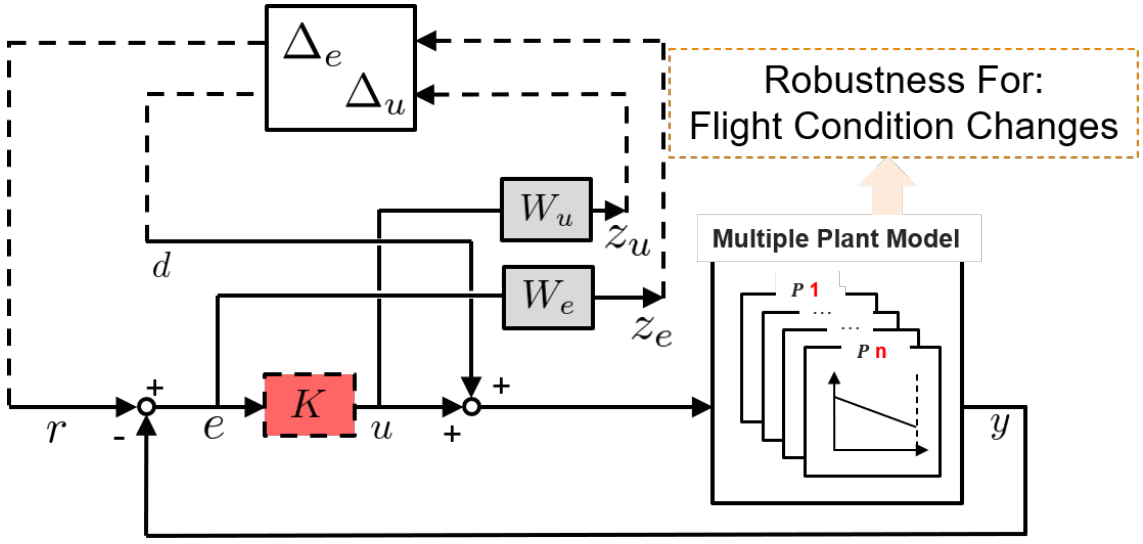

Fig. 3.2 Conventional Robust Controller Design Method (Separated).

3.1.3 Simultaneous Design Results

The linear robust controller is evaluated for stability, performance, and robustness against flight condition changes as well as to the identified trajectories as explained in section 3.1.2. The nonlinear trajectory is evaluated for improvements in the objective function u_f and maximum tracking error e_{max}. The results for the simulation are shown in Fig.3.3 to 3.15. Table 3.1 shows the comparison of the cost function u_f, control gains k_p and k_i, maximum error e_{max} and H_∞ norm for the Simultaneous method compared to the Separated method where the trajectory and controller are designed separately.

Table 3.1 Comparison of Results between Simultaneous and Conventional Methods.

Method	Cost Function u_f	kp	ki	e_{max}	H_∞ Norm
Separated	4.11	1.40	0.31	0.99	0.97
Simultaneous	4.73	1.55	0.28	0.80	0.99

For the linear robust controller design evaluation, both Separated and Simultaneous methods had H_∞ norm of 0.97 and 0.99 respectively which ensures stability and performance.

This is also verified by the poles and gain plot for the sensitivity function S, transfer functions from r to e denoted as T_{r2e}, and transfer functions from r to y denoted as T_{r2y} (transfer functions defined in Section 2.4.2). From Fig.3.3 it can be seen that all poles for the sensitivity function S and T_{r2e} are non-positive for both Separated and Simultaneous method thus both systems has stability. From Fig.3.4, it can be seen that the gain plot of S and T_{r2e} for both systems are below the weighting function $1/W_e$ ensuring performance and from Fig.3.5, the gain plot of the complementary sensitivity function T and T_{r2y} are below the weighting function $1/W_u$ meeting the design requirements. Fig.3.6 represents the step response of each linearized β for both Separated and Simultaneous method. As can be seen from Fig.3.6, each linearized β shows stable response ensuring robustness against flight condition changes to linearized β. Fig.3.7 to 3.11 represents the response of the identified transfer function derived from each segment in the optimized trajectory. v_i represents the v in the trajectory at each discretized ith segment and $v_{i_{max}}$ represents the maximum value in the ith segment. $v_i/v_{i_{max}}$ represents the normalized velocity at each discretized segment and was used as reference step input. Therefore, each identified transfer function represents a segment in the optimal trajectory. As can be seen from Fig.3.7 to 3.11, the proposed method has high tracking performance and has a stable response for both linear models of $\beta = 20$ and $\beta = 80$ [deg] ensuring robustness against the trajectory.

For the nonlinear trajectory design evaluation, from the trajectory obtained through nonlinear trajectory design (Section 3.1.1) shown in Fig.3.13 and 3.15, it can be seen that both Simultaneous and Separated methods have similar trajectory characteristics. Both trajectories gradually decrease β to increase u. Since u is the cosine of β, as β decreases u increases. By placing the maximum error derived from tracking error of the Separated method as a nonlinear constraint, overall β was minimized thus increasing the cost function u and reducing maximum error e_{max}. This can be seen at $t = 8$ of where tracking error decreases from 0.99 to 0.80 in Fig.3.12. The Simultaneous method improved the cost function, had higher tracking performance, and robustness against flight condition changes as well as to the trajectory were obtained.

From the obtained results, the novel method of simultaneous design of trajectory and robust controller was successfully applied to a modified rocket launch problem typically used for optimization examples in terms of the controller having stability, performance, and robustness against flight condition changes. Furthermore, the Simultaneous method showed superior results to the Separated method in terms of maximizing the objective function u_f, minimizing the maximum tracking error e_{max}, and adding robustness against the trajectory.

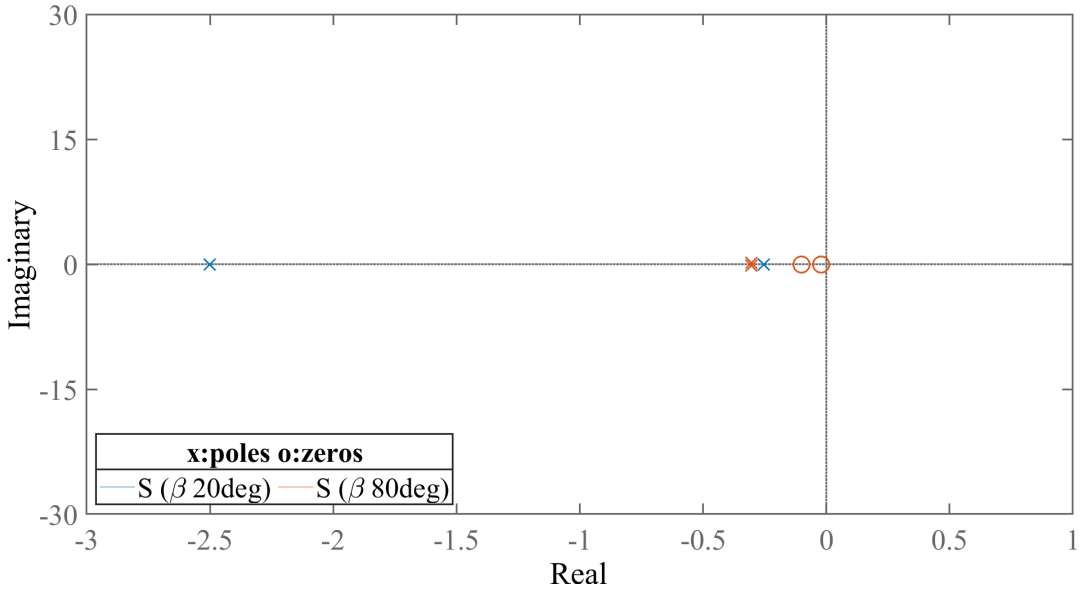

(a) Separated.

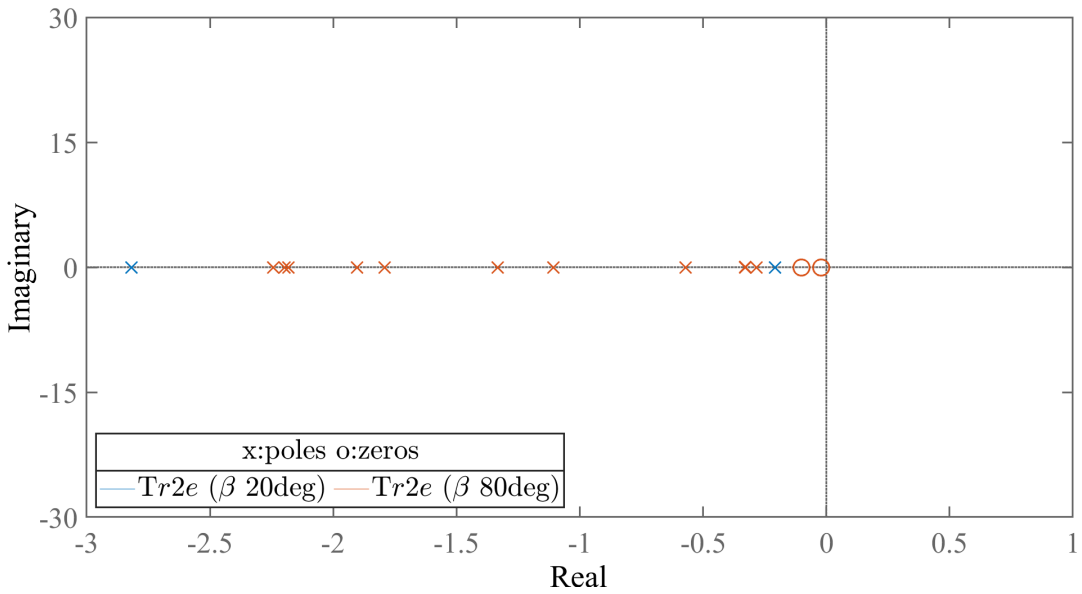

(b) Simultaneous.

Fig. 3.3 Pole/Zero Map for Modified Rocket Problem.

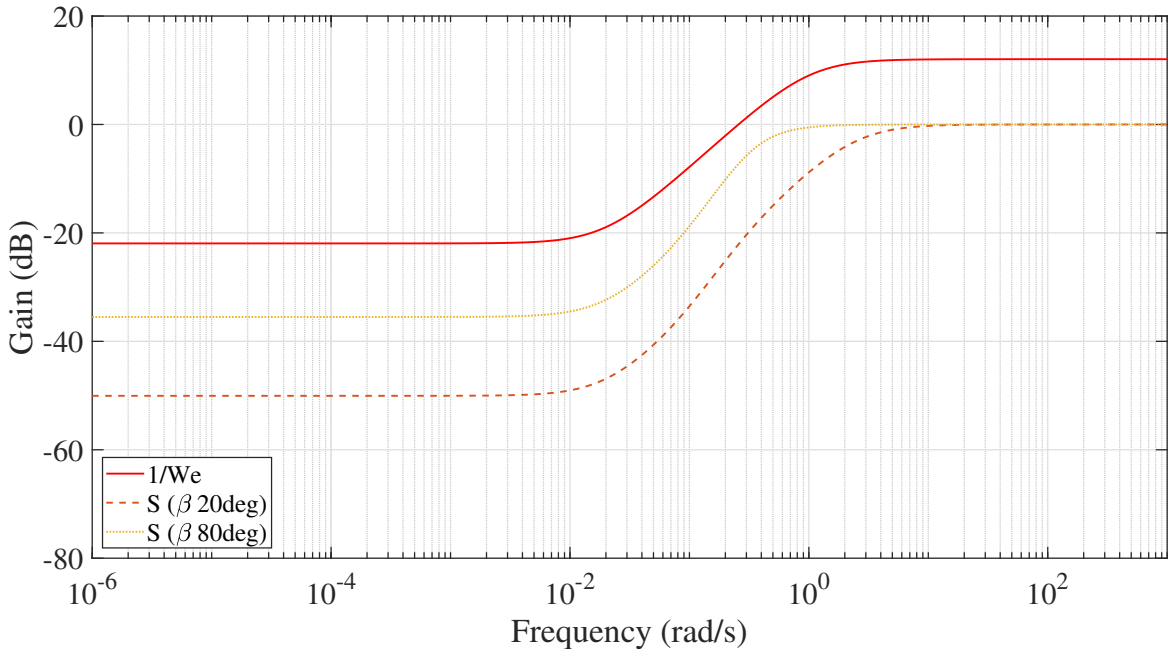

(a) Separated.

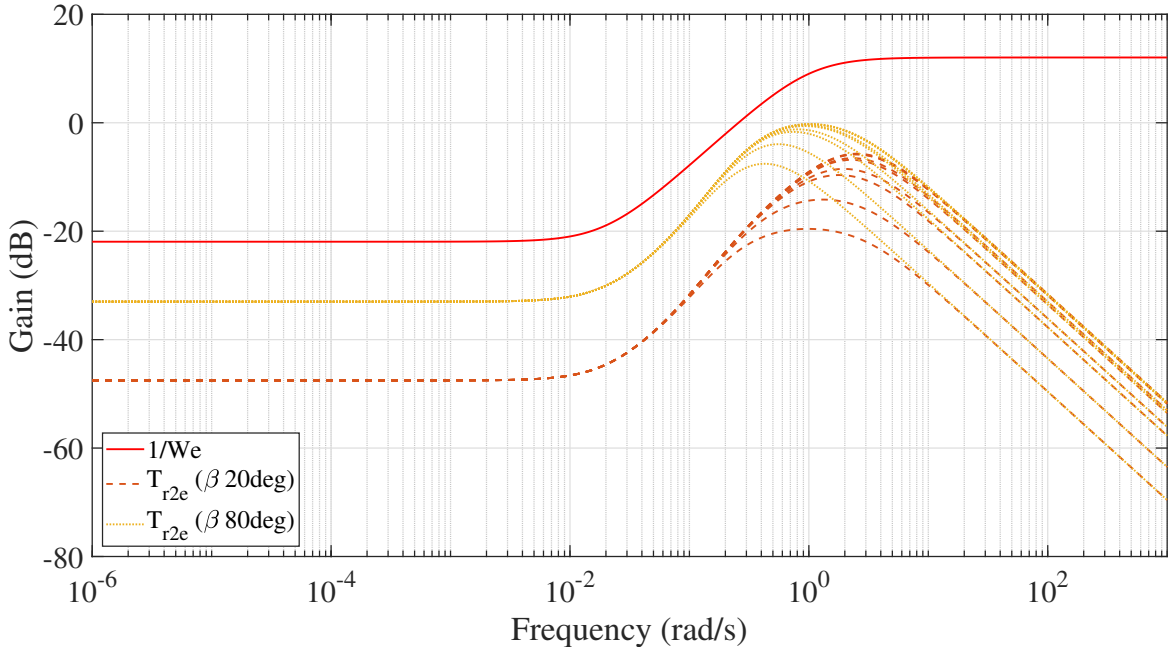

(b) Simultaneous.

Fig. 3.4 Gain Plot of T_{r2e} for Modified Rocket Problem.

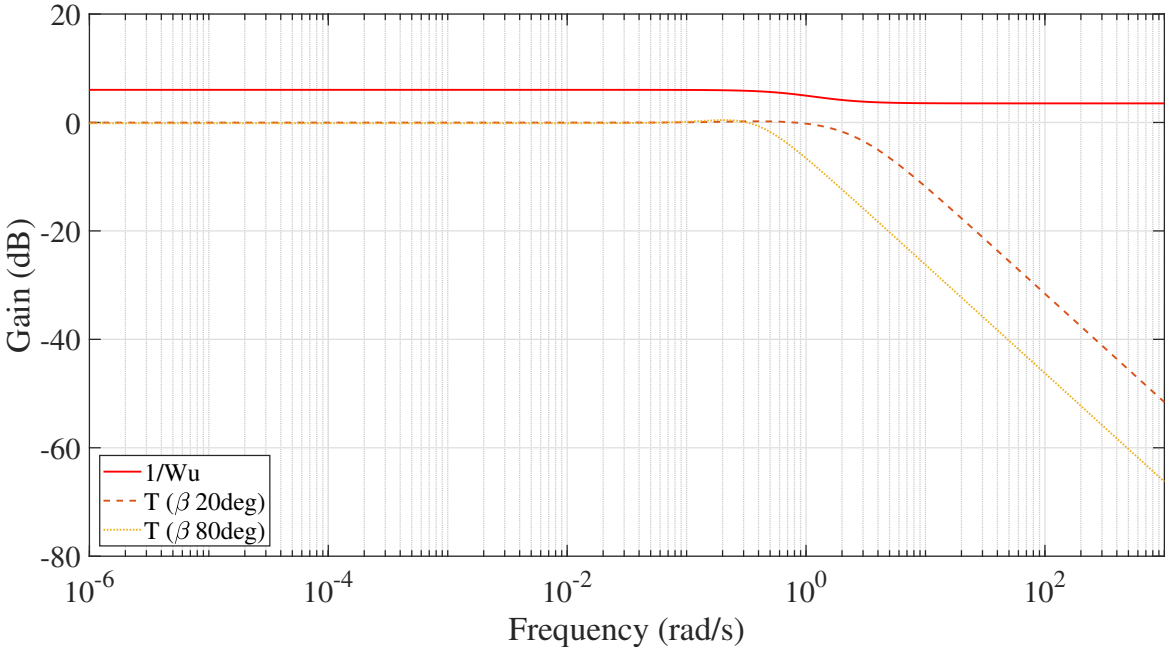

(a) Separated.

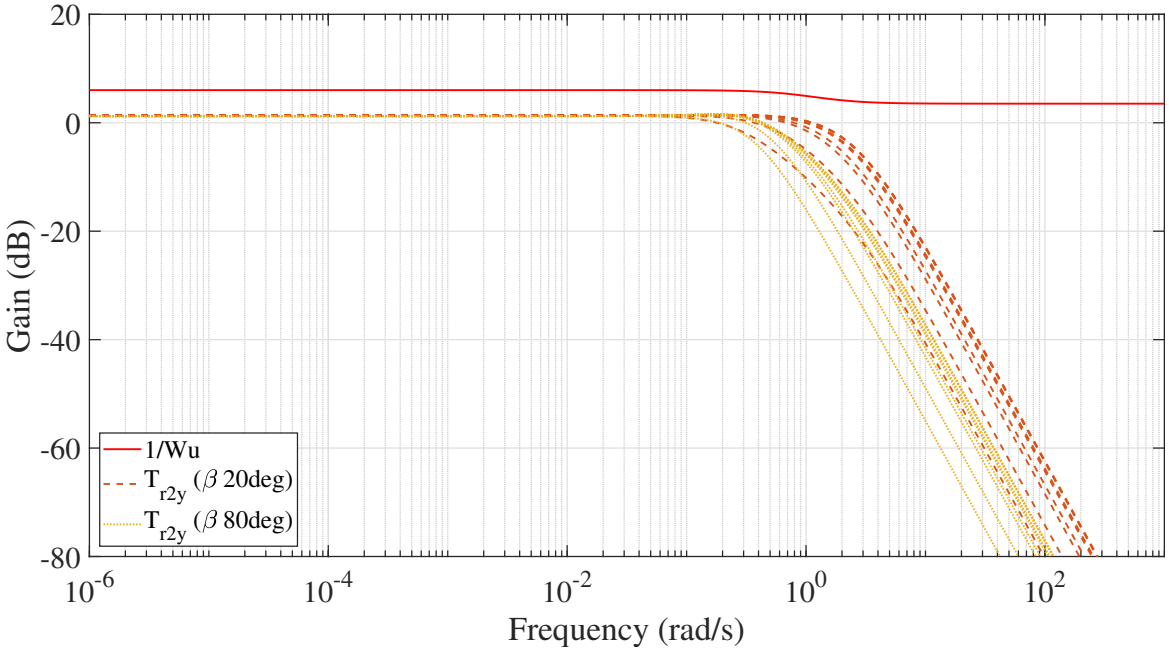

(b) Simultaneous.

Fig. 3.5 Gain Plot of T_{r2y} for Modified Rocket Problem.

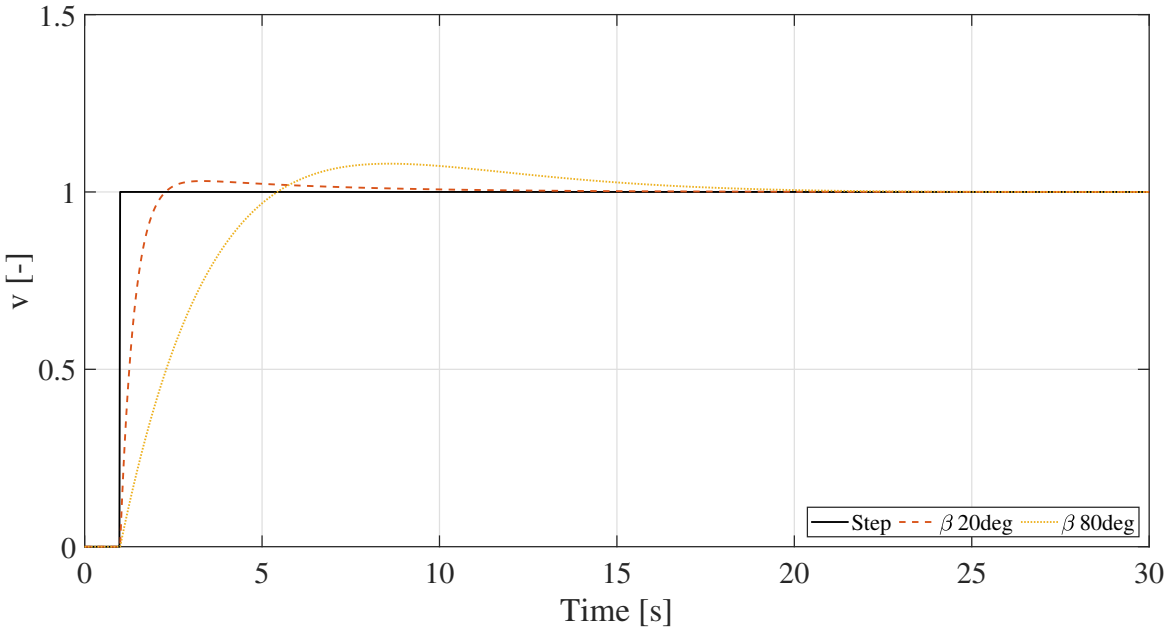

(a) Separated.

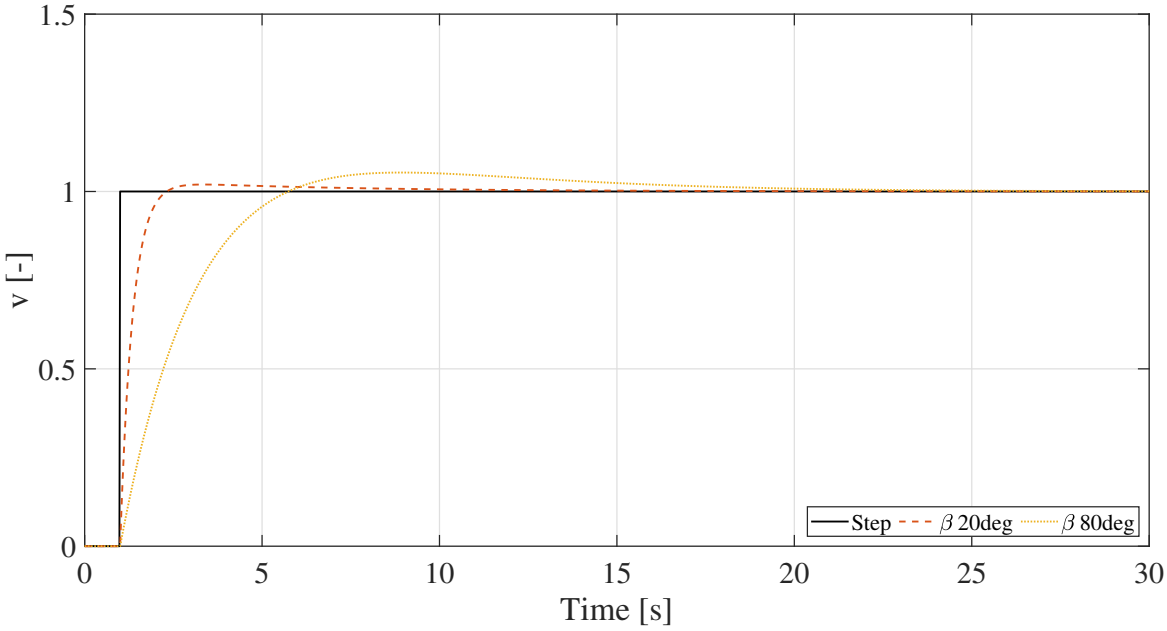

(b) Simultaneous.

Fig. 3.6 Step Response Comparison for Modified Rocket Problem.

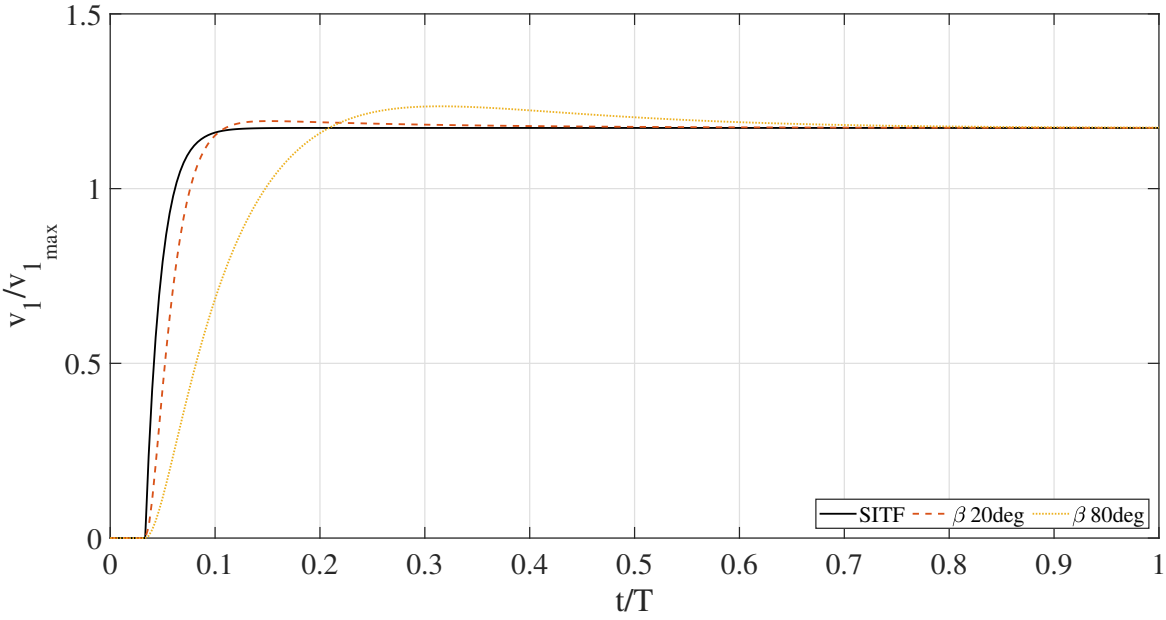

(a) Segment 1 SITF.

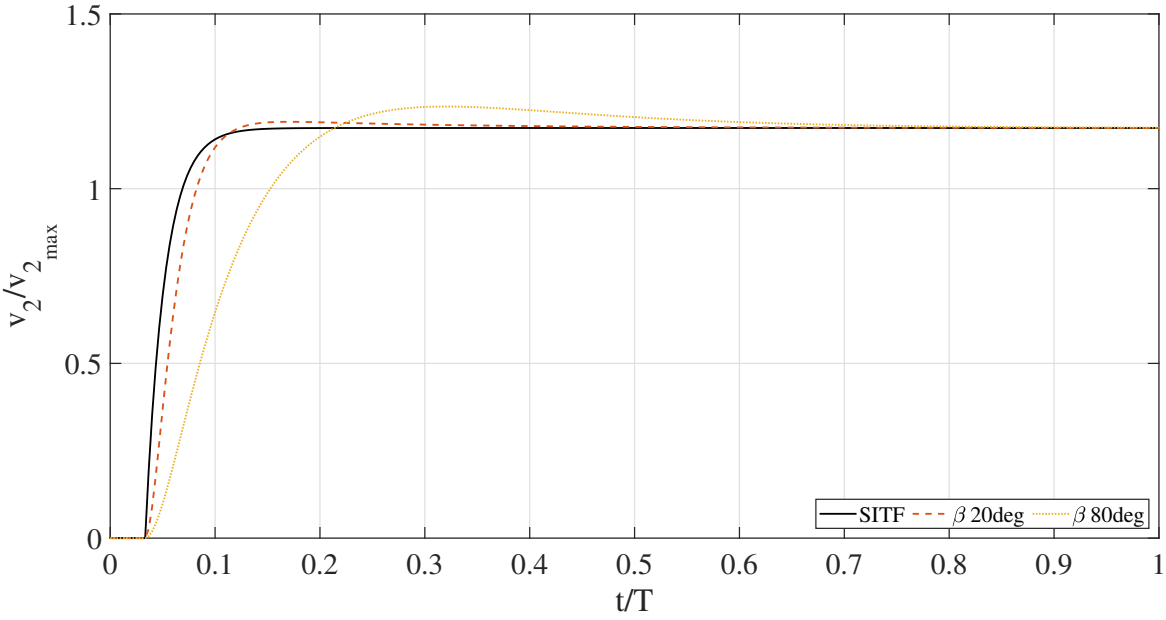

(b) Segment 2 SITF.

Fig. 3.7 Response of SITF Inputs for Modified Rocket Problem (Segment 1 and 2).

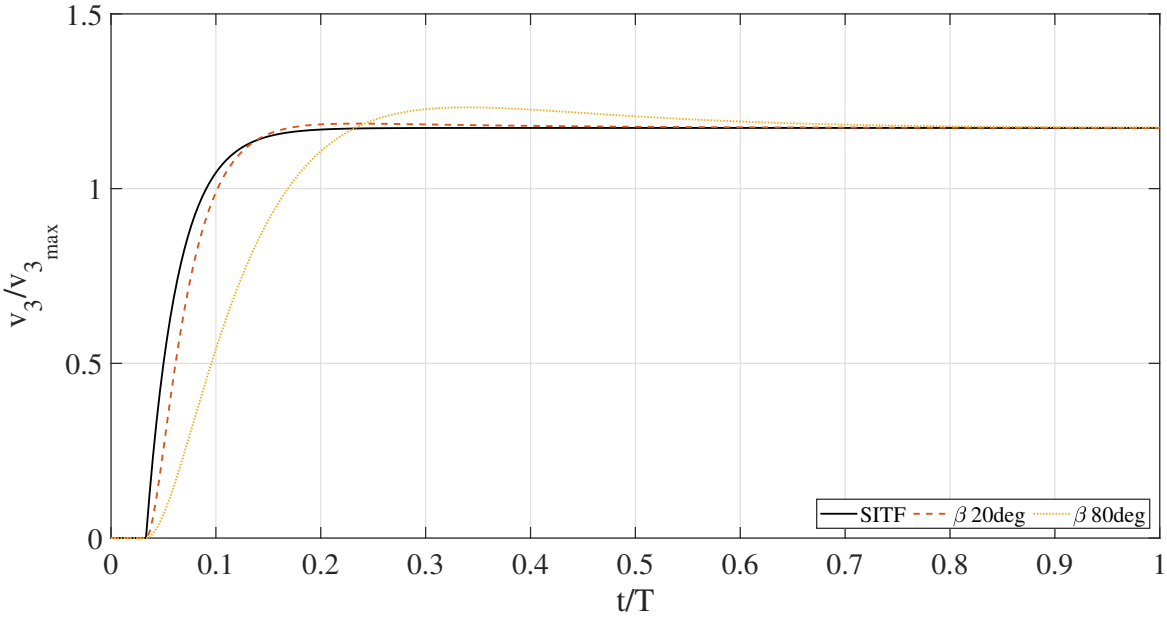

(a) Segment 3 SITF.

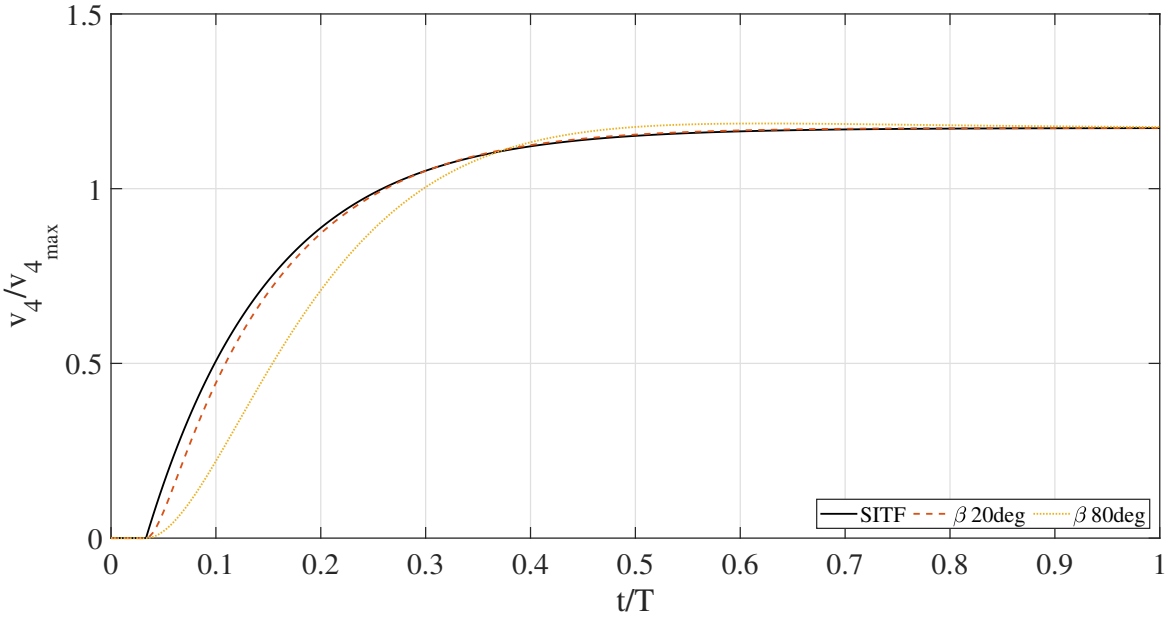

(b) Segment 4 SITF.

Fig. 3.8 Response of SITF Inputs for Modified Rocket Problem (Segment 3 and 4).

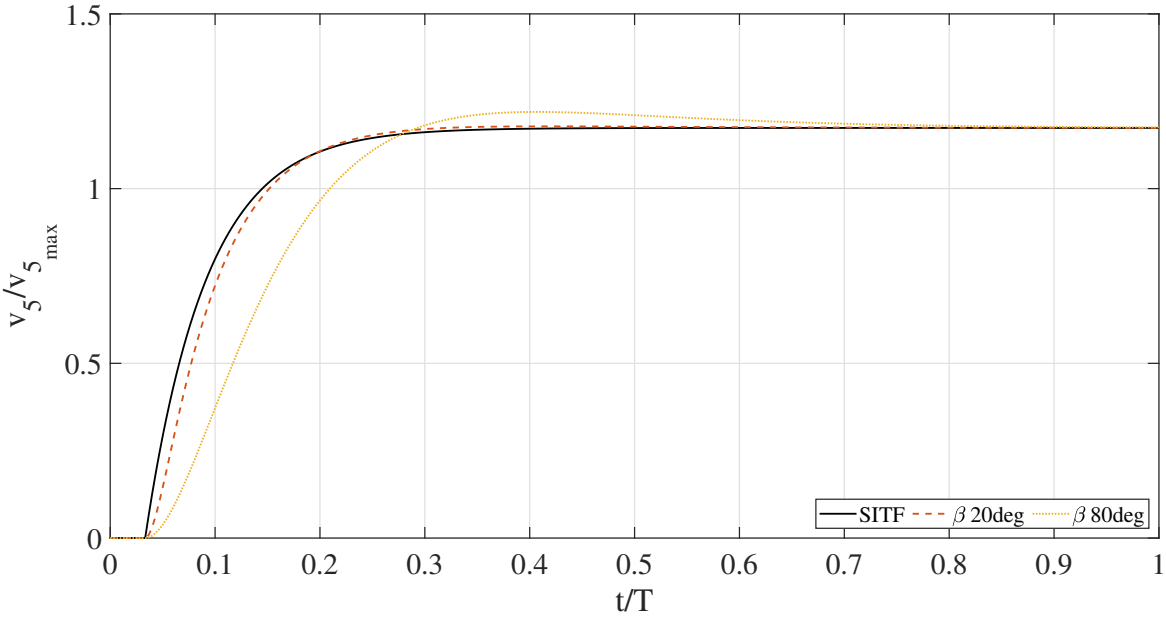

(a) Segment 5 SITF.

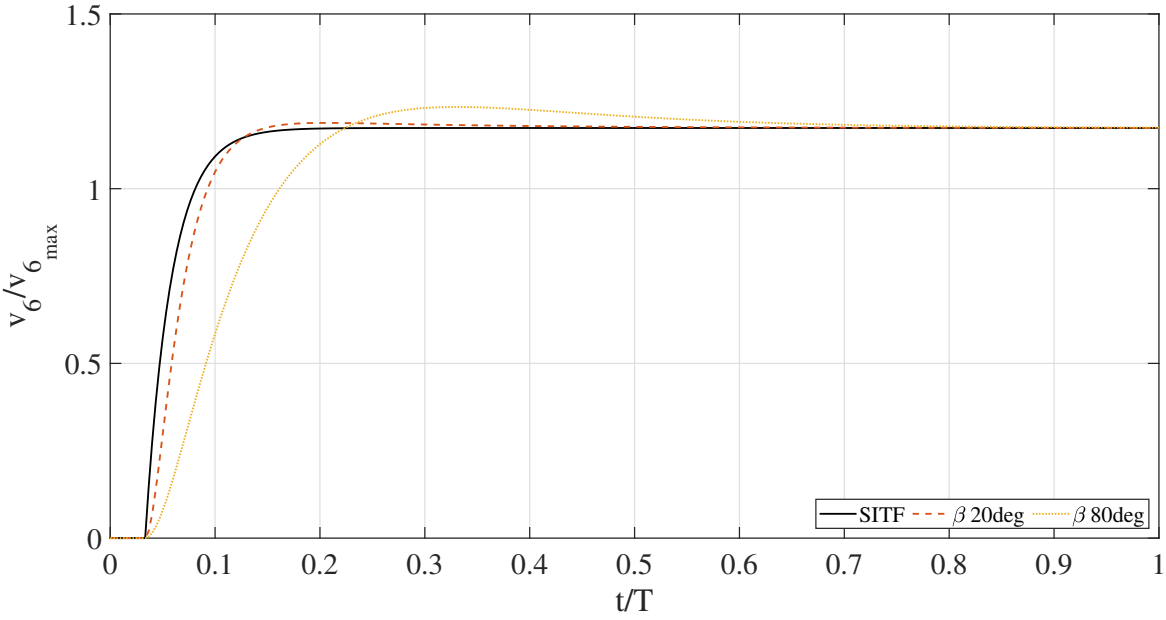

(b) Segment 6 SITF.

Fig. 3.9 Response of SITF Inputs for Modified Rocket Problem (Segment 5 and 6).

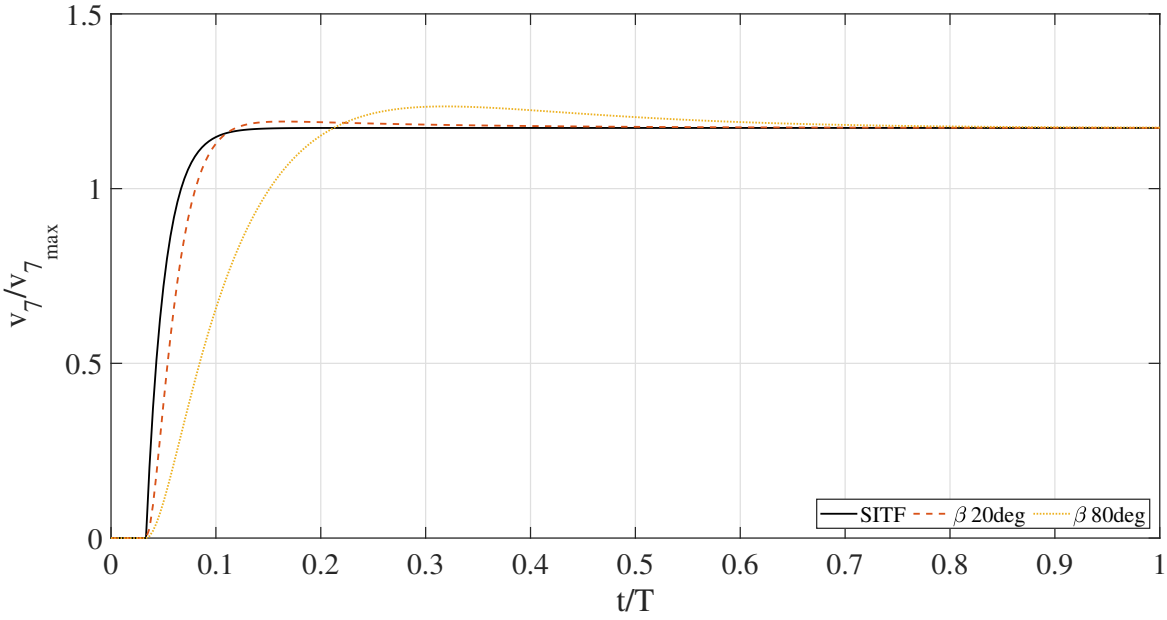

(a) Segment 7 SITF.

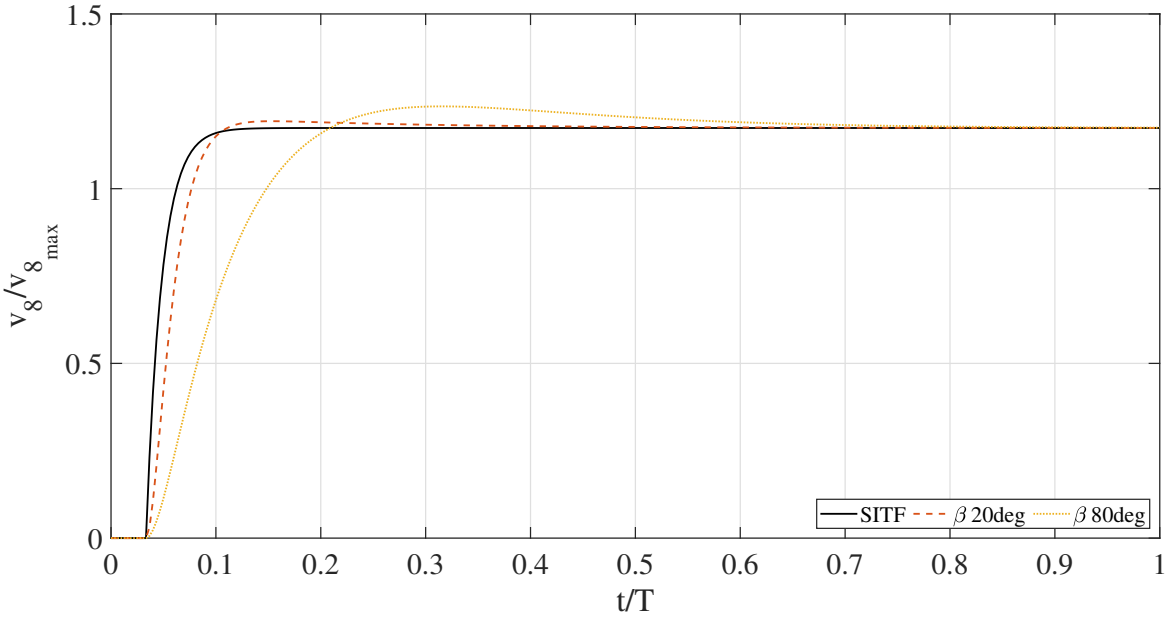

(b) Segment 8 SITF.

Fig. 3.10 Response of SITF Inputs for Modified Rocket Problem (Segment 7 and 8).

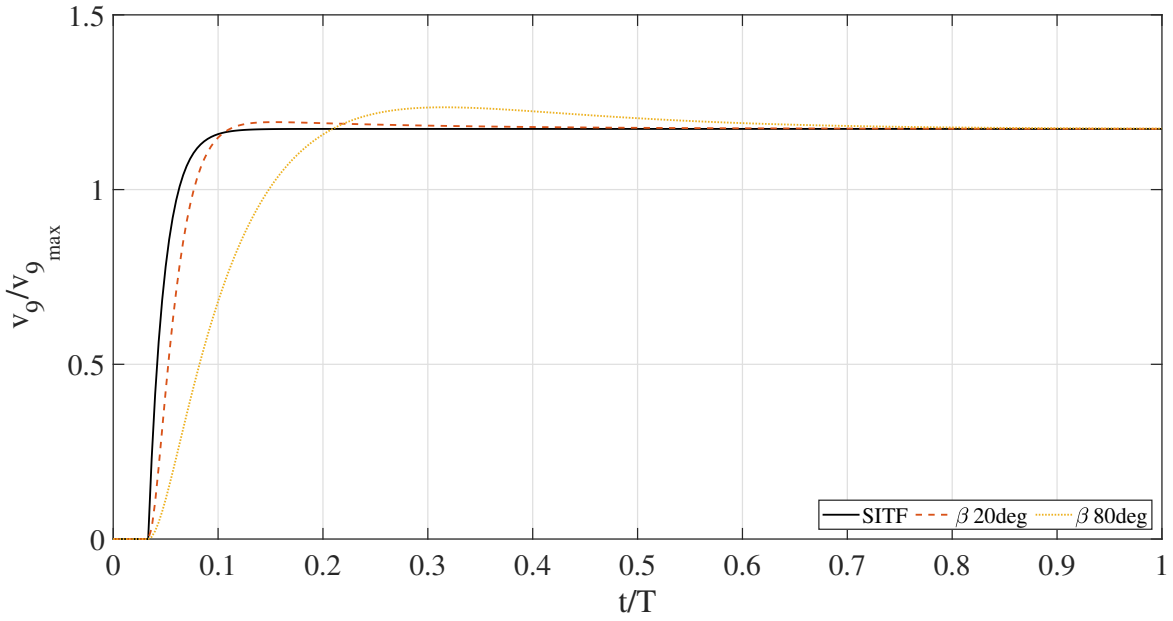

Fig. 3.11 Response of SITF Inputs for Modified Rocket Problem (Segment 9).

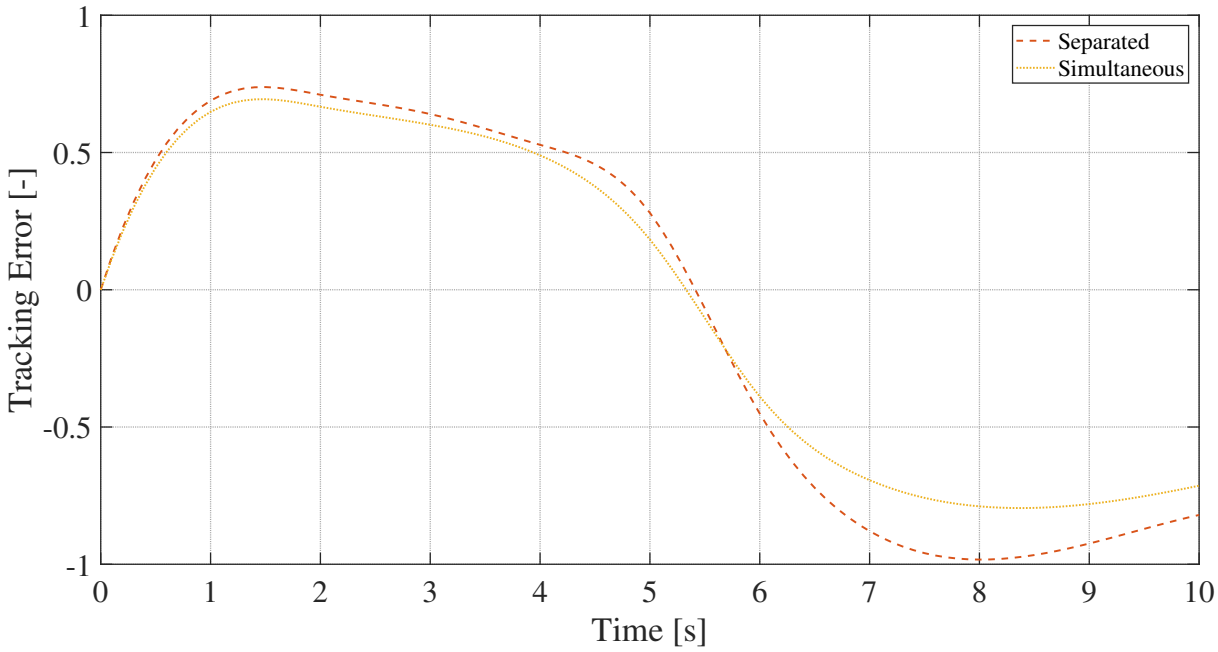

Fig. 3.12 Error Comparison for Tracking v for Modified Rocket Problem.

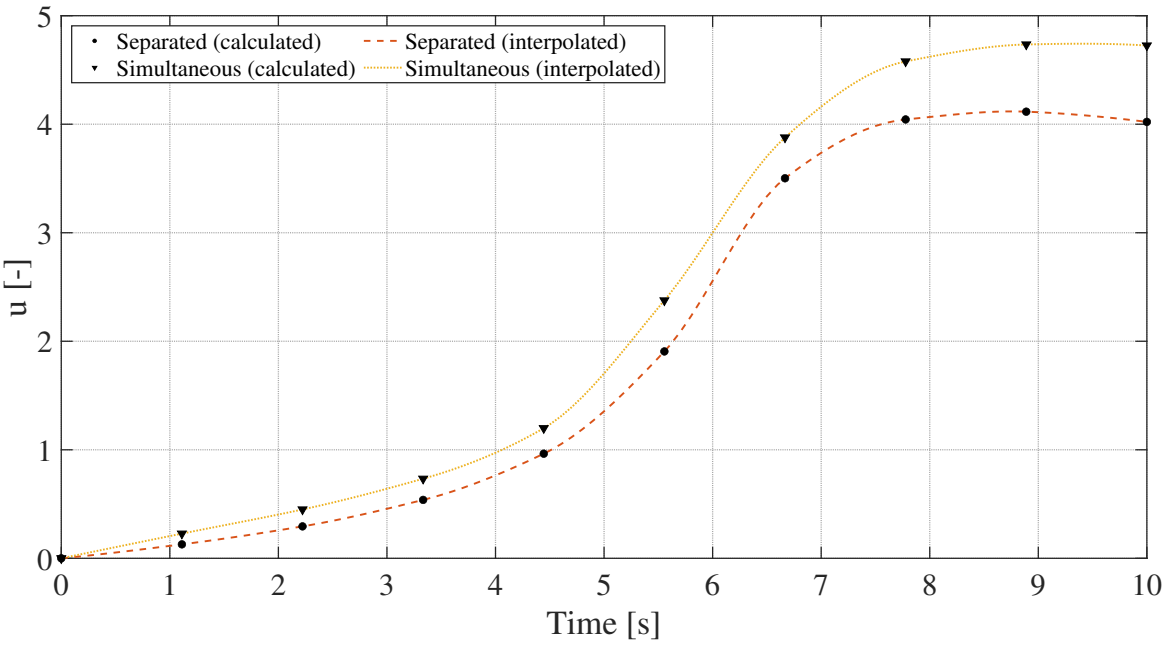

(a) Time History of u.

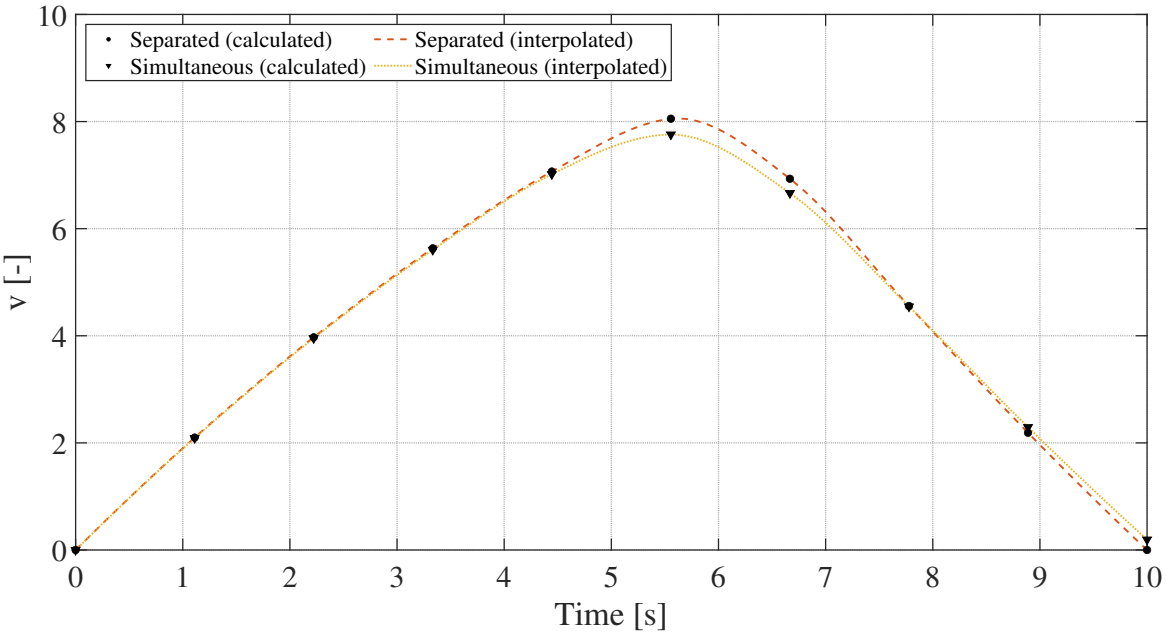

(b) Time History of v.

Fig. 3.13 Comparison between Separated and Simultaneous Methods for Modified Rocket Problem (u and v).

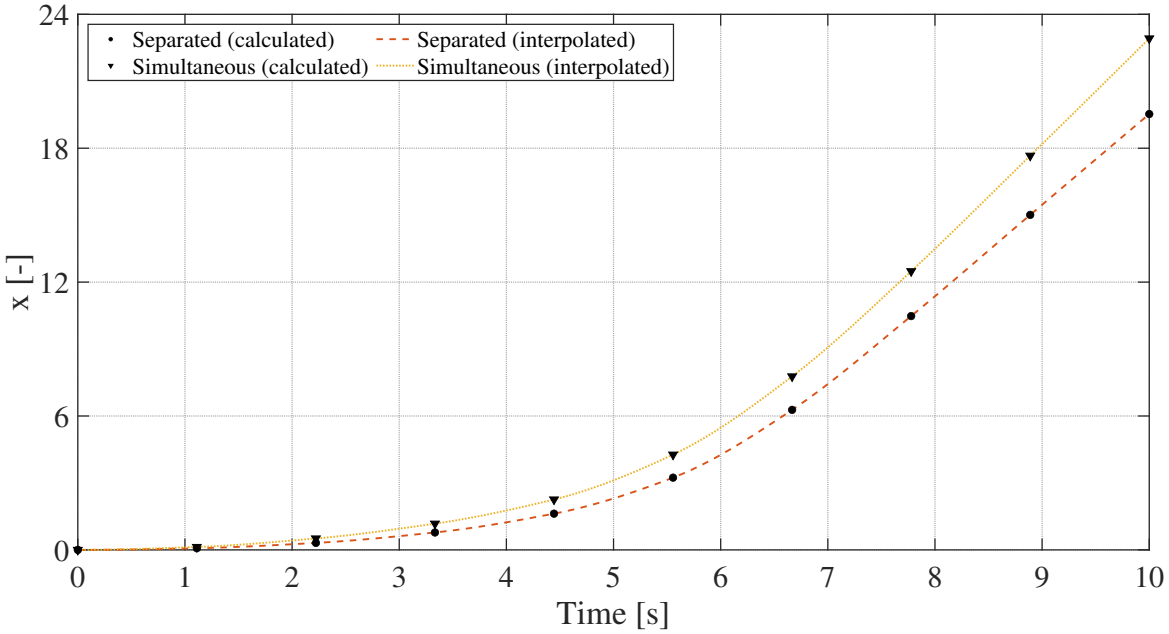

(a) Time History of x.

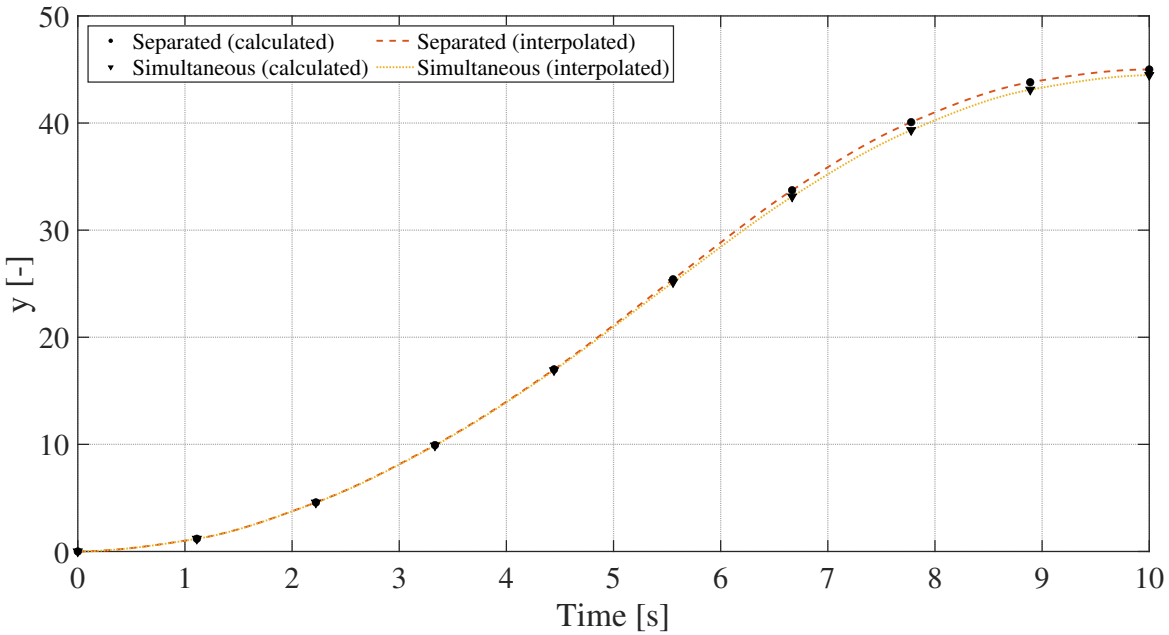

(b) Time History of y.

Fig. 3.14 Comparison between Separated and Simultaneous Methods for Modified Rocket Problem (x and y).

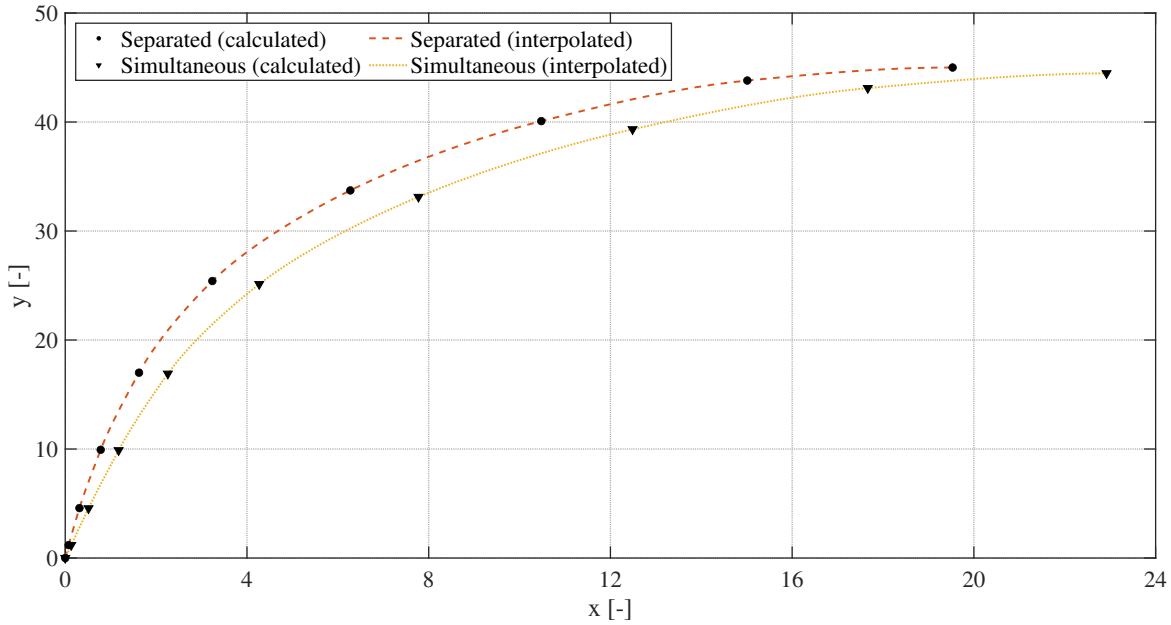

(a) Comparison between x and y.

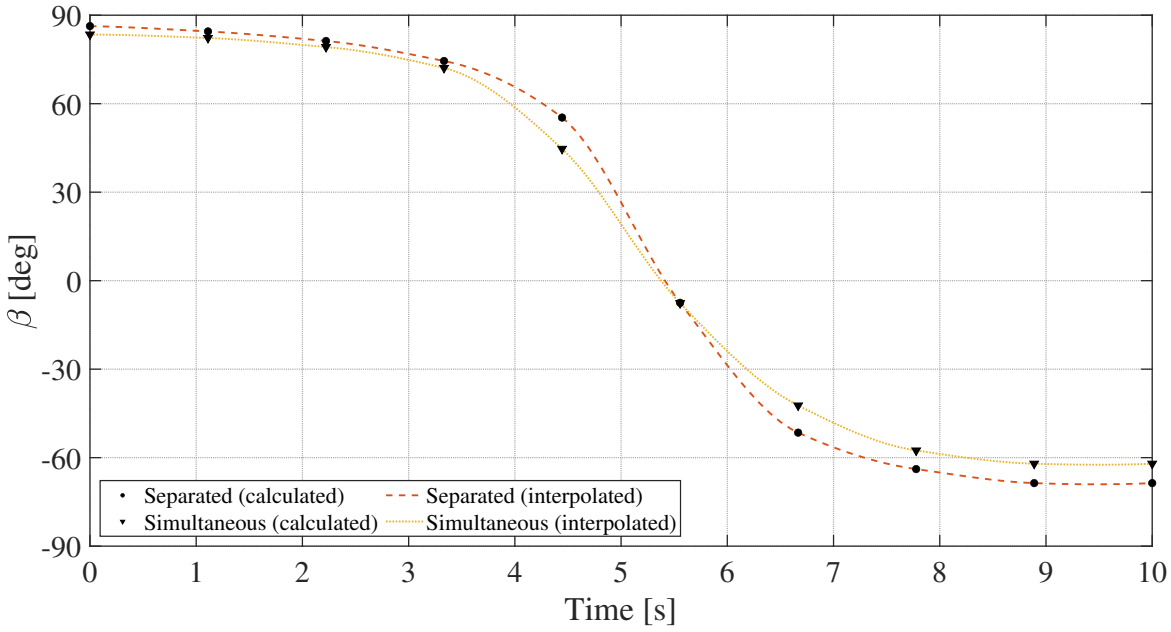

(b) Time History of β.

Fig. 3.15 Comparison between Separated and Simultaneous Methods for Modified Rocket Problem (x to y and β).

3.2 Modified Zermelo‘s Problem

In order to test the Simultaneous method for applicability outside the field of aerospace, Zermelo's problem [19, 10] of navigating a speedboat commonly used for optimal control example will be used to compare against the conventional method of obtaining the controller separately from the trajectory (Separated). The problem was modified to incorporate a parabolic current distribution for adding complexity. The state variables are horizontal distance x and vertical distance y (horizontal velocity $dx = u$, vertical velocity $dy = v$). The problem shown in Fig.3.16 assumes a river with current distribution of $0.2y(y-10)$ in the x-direction and $-0.01x(x-20)$ in the y-direction. The speedboat is accelerating at k to reach the target coordinate y_f of 10 and x_f of 10. Find the optimal steering angle α while maximizing k in a given time $t_f = 3$. The SISO system tracks the reference v generated at each iteration of SQP and has a feedback loop for obtaining maximum error e_{max} against the output v. The e_{max} is then evaluated to meet the nonlinear inequality constraint.

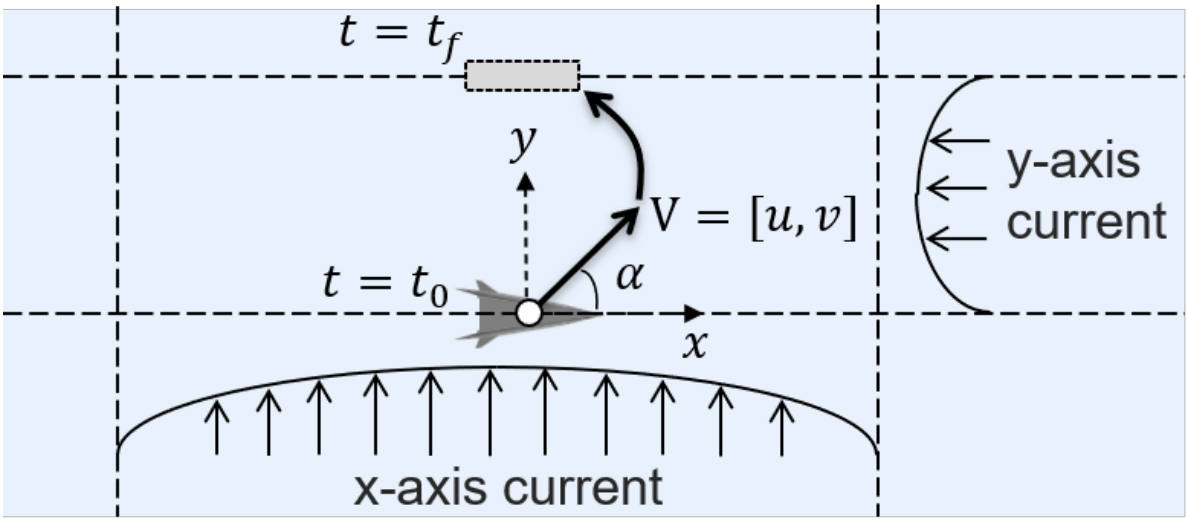

Fig. 3.16 Diagram of Rocket Launch Problem.

3.2.1 Nonlinear Trajectory Design

The nonlinear trajectory design will be evaluated for improving the objective function while meeting the e_{max} nonlinear inequality constraint placed on the NLP probem. The dynamic equations used for trajectory optimization and closed loop nonlinear simulation are shown in Eqs.(3.11). The closed loop nonlinear simulation tracks the reference v with a feedback

loop from the output v. Symbol k represents the constant acceleration which is maximized to represent vehicle parameter optimization.

$$\begin{aligned} \dot{x} &= 0.2y(y-10) + k\cos\alpha \\ \dot{y} &= -0.01x(x-20) + k\sin\alpha \end{aligned} \tag{3.11}$$

Formulation of the optimal control problem is as follows:

$$\begin{aligned} \text{find} \quad & \text{state variables} : X = [x, y] \\ & \text{control variable} : \alpha \text{ [deg]} \\ & \text{vehicle parameter} : k \text{ (acceleration constant)} \\ \text{min.} \quad & -k \\ \text{s.t.} \quad & \text{state equations shown in Eqs.(3.1)} \\ & 0 \leq \alpha \leq 90 \text{ [deg]} \\ & 0 \leq x \leq 40 \\ & 0 \leq y \leq 10 \\ & 1 \leq k \leq 10 \\ & e_{max} \leq 0.665 \quad \text{(Unused in Separated method)} \\ & X_0 = [10, 0],\ X_f = [10, 10] \\ & v_0 = 1 \\ & t_f = 3 \end{aligned} \tag{3.12}$$

The problem was discretized using direct multiple shooting method explained in Section 2.2.1. The problem was discretized into 4 segments with 10 sub-segments and the transfer function was identified for each sub-segment in the trajectory at every iteration for the Simultaneous method. At each iteration, for the Simultaneous method the maximum tracking error was calculated through closed loop nonlinear simulation and for the Separated method, optimal trajectory was obtained without considering the e_{max} as the nonlinear inequality constraint.

3.2.2 Linear Robust Controller Design

Both controllers obtained in the Separated and Simultaneous method through robust controller design will be evaluated for stability, performance, and robustness against flight condition changes of α as well as to the identified trajectories. The linear time invariant (LTI) model

was obtained by linearizing the equations $\dot{x}$ and $\dot{y}$ in Eq.(3.11) at two constant steering angle conditions. The LTI model was constructed by linearizing the equations for the dynamic equation at constant α of 30 [deg] and 60 [deg] as well as constant acceleration $k = 4$ through perturbation method. The state equations are linearized about the steady state condition in the form of Eq.(3.13) (subscripts for matrix A and B denotes the linearized α).

$$\begin{aligned} \dot{x} &= A_i x + B_i u \\ y &= Cx \end{aligned} \tag{3.13}$$

where the new state variables obtained through perturbation are the following:

$$\begin{aligned} x &= [\Delta x \;\; \Delta y]^T \\ y &= [v] \\ u &= [\Delta\alpha] \end{aligned} \tag{3.14}$$

The LTI models linearized through the perturbation are shown in Eq.(3.15).

$$A = \begin{bmatrix} 0 & 2-0.4y_0 \\ -0.02x_0+0.2 & 0 \end{bmatrix}, \quad B = \begin{bmatrix} -4\sin\alpha_0 \\ 4\cos\alpha_0 \end{bmatrix} \tag{3.15}$$

The LTI models for $\alpha = 30$ and $\alpha = 60$ [deg] are shown in Eq.(3.16) to (3.18).

$$A_{30} = \begin{bmatrix} 0 & -1.11 \\ -0.37 & 0 \end{bmatrix}, \quad B_{30} = \begin{bmatrix} -2.00 \\ 3.46 \end{bmatrix} \tag{3.16}$$

$$A_{60} = \begin{bmatrix} 0 & -1.55 \\ -0.42 & 0 \end{bmatrix}, \quad B_{60} = \begin{bmatrix} -3.46 \\ 2.00 \end{bmatrix} \tag{3.17}$$

$$C = \begin{bmatrix} 1 & 0 \\ 0 & 1 \end{bmatrix} \tag{3.18}$$

The system used for the Separated method in designing the robust controller has the same structure as the rocket launch problem shown in Fig.3.2. Here, reference r represents the optimal v and the system feedbacks the v output denoted as y. The system is the same as

in the Simultaneous method shown in Fig.2.5 except that the identified trajectory (SITF) is neglected (i.e. explanation of each variables and blocks are omitted, refer to 2.4.1). For the Simultaneous method, since the trajectory was identified at each segment to be incorporated into robust controller design, robustness against the SITF will be evaluated as well. The weighting functions W_e and W_u are shown in Eqs.(3.19) and (3.20) which was tuned through trial and error to increase tracking performance. Robustness against flight condition changes and to the trajectory was evaluated based on the step response of the linearized steady state model (explained in section 3.1.2) and SITF for having high tracking performance.

$$W_e = \frac{s+2}{5s+0.06} \tag{3.19}$$

$$W_u = \frac{s+1}{1.6s+4} \tag{3.20}$$

3.2.3 Simultaneous Design Results

The linear robust controller is evaluated for stability, performance, and robustness against flight condition changes as well as to the identified trajectories as explained in section 3.1.2. The nonlinear trajectory is evaluated for improvements in the objective function k and maximum tracking error e_{max}. The results for the simulation are shown in Fig.3.17 to 3.26. Table 3.2 shows the comparison of the cost function k, control gains k_p and k_i, maximum error e_{max} and H_∞ norm for the Simultaneous method compared to the Separated method where the trajectory and controller are designed separately.

Table 3.2 Comparison of Results between Simultaneous and Conventional Methods.

Method	Cost Function k	kp	ki	e_{max}	H_∞ Norm
Separated	4.74	1.07	0.85	0.665	0.93
Simultaneous	4.82	1.09	0.83	0.663	0.99

For the linear robust controller design evaluation, both Separated and Simultaneous methods had H_∞ norm of 0.93 and 0.99 respectively which ensures stability and performance. This is also verified by the poles and gain plot for the sensitivity function S, transfer functions from r to e denoted as T_{r2e}, and transfer functions from r to y denoted as T_{r2y} (transfer functions defined in Section 2.4.2). From Fig.3.17 it can be seen that all poles for the sensitivity function S and T_{r2e} are non-positive for both Separated and Simultaneous method thus both systems has stability. From Fig.3.18, it can be seen that the gain plot of S and T_{r2e} for both systems are below the weighting function $1/W_e$ ensuring performance and

from Fig.3.19, the gain plot of the complementary sensitivity function T and T_{r2y} are below the weighting function $1/W_u$ meeting the design requirements. Fig.3.20 represents the step response of each linearized β for both separated and Simultaneous method. As can be seen from Fig.3.20, each linearized β shows stable response ensuring robustness against flight condition changes to linearized β. Fig.3.21 to 3.23 represents the response of the identified transfer function derived from each segment in the optimized trajectory. v_i represents the v in the trajectory at each discretized ith segment and $v_{i_{max}}$ represents the maximum value in the ith segment. $v_i/v_{i_{max}}$ represents the normalized velocity at each discretized segment and was used as reference step input. Therefore, each identified transfer function represents a segment in the optimal trajectory. As can be seen from Fig.3.21 to 3.23, the proposed method has high tracking performance and has a stable response for both linear models of $\alpha = 30$ and $\alpha = 60$ [deg] ensuring robustness against the trajectory.

For the nonlinear trajectory design evaluation, from the trajectory obtained through nonlinear trajectory design (Section 3.2.1) shown in Fig.3.24 and 3.25, it can be seen that both Simultaneous and Separated methods have similar trajectory characteristics. Both trajectories accelerate against the y-direction current since the initial starting α was fixed at 0 [deg]. From there, the speedboat gradually increases α to increase vertical distance. However, since the current is strongest at $y = 5$ and as the speedboat approaches $y = 5$ at around $t = 1.5$, it gradually steers the to $\alpha = 0$ [deg] due to the $x_f = 10$ constraint. From there, to gain vertical distance, the speedboat increases α again around $t = 1.8$ to reach $y = 10$ target. When comparing the Separated and Simultaneous method, by placing the maximum error for the simultaneous method derived from tracking error of the Separated method as a nonlinear constraint, k was increased while decreasing the maximum error from 0.665 to 0.663 at $t = 0.6$. This was due to the increase in k since k is multiplied to α as shown in Eq.(3.11) and thus resulted in greater control reducing maximum error. This can be seen at around $t = 0.6$ of Fig.3.24a where it can be seen that for the Simultaneous method, v has a larger curve compared to the Separated method and the maximum error e_{max} decreases from 0.665 to 0.663 in Fig.3.26. The Simultaneous method improved the cost function, had higher tracking performance, and robustness against flight condition changes as well as to the trajectory was obtained.

From the obtained results, the novel method of simultaneous design of trajectory and robust controller was successfully applied to a modified Zermelo's problem outside of the aerospace field in terms of the controller having stability, performance, and robustness against flight condition changes. Furthermore, the Simultaneous method showed superior results to the Separated method in terms of maximizing the objective function k, minimizing the maximum tracking error e_{max}, and adding robustness against the trajectory.

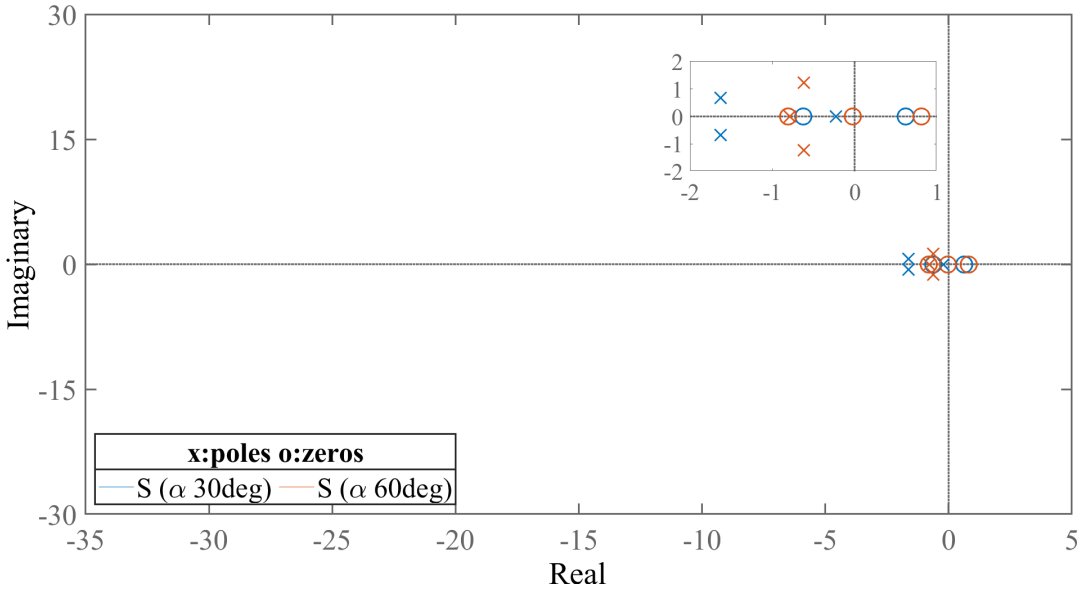

(a) Separated.

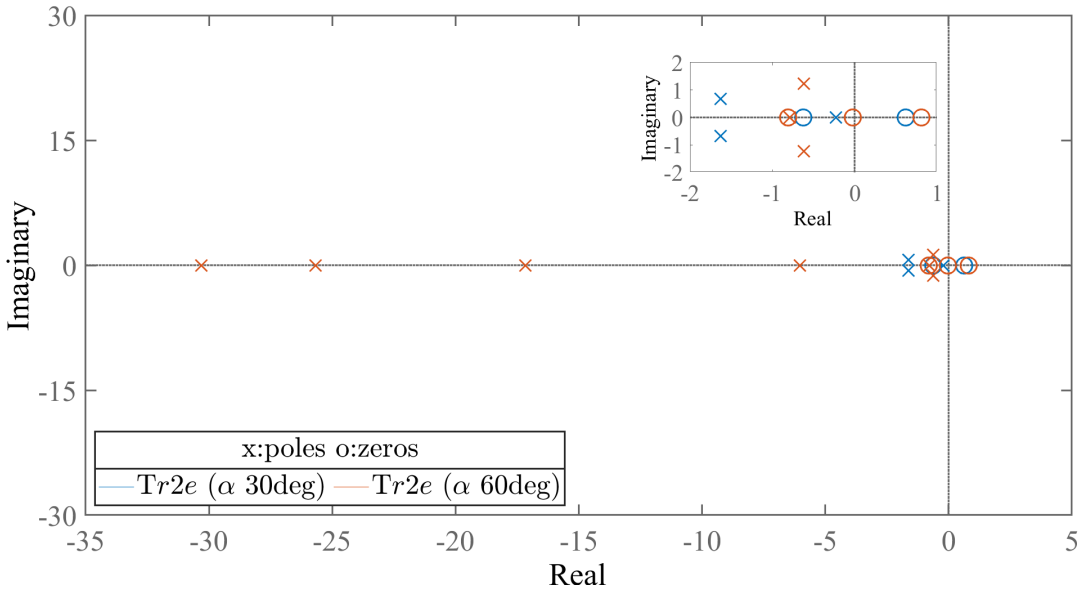

(b) Simultaneous.

Fig. 3.17 Pole/Zero Maps for Modified Zermelo’s Problem.

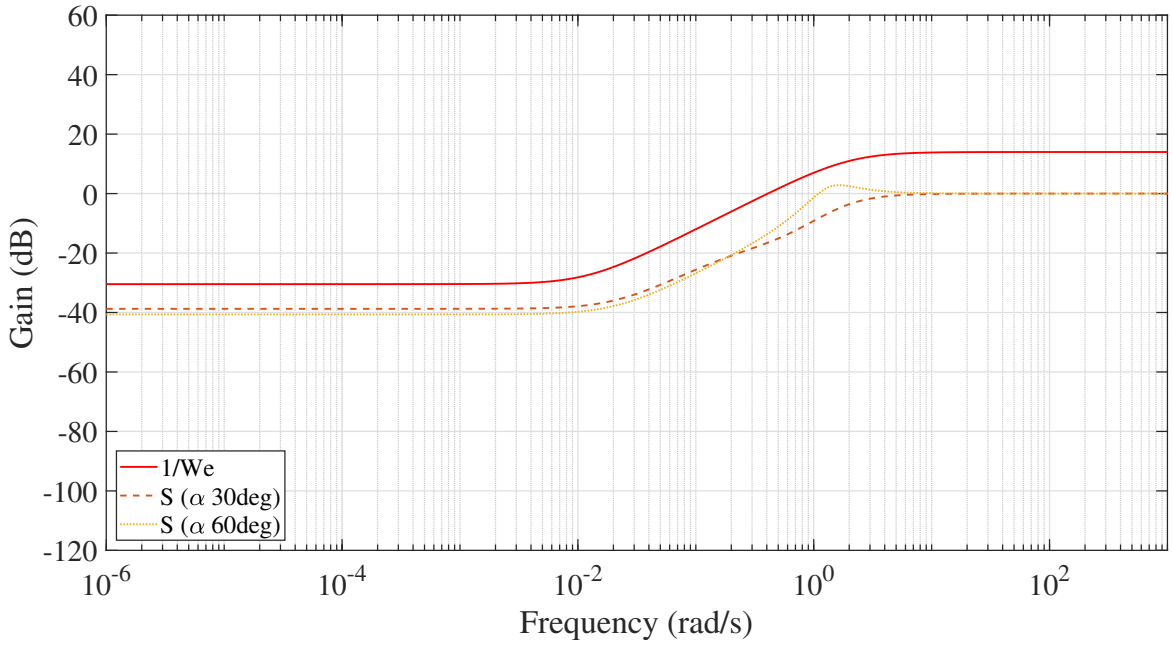

(a) Separated.

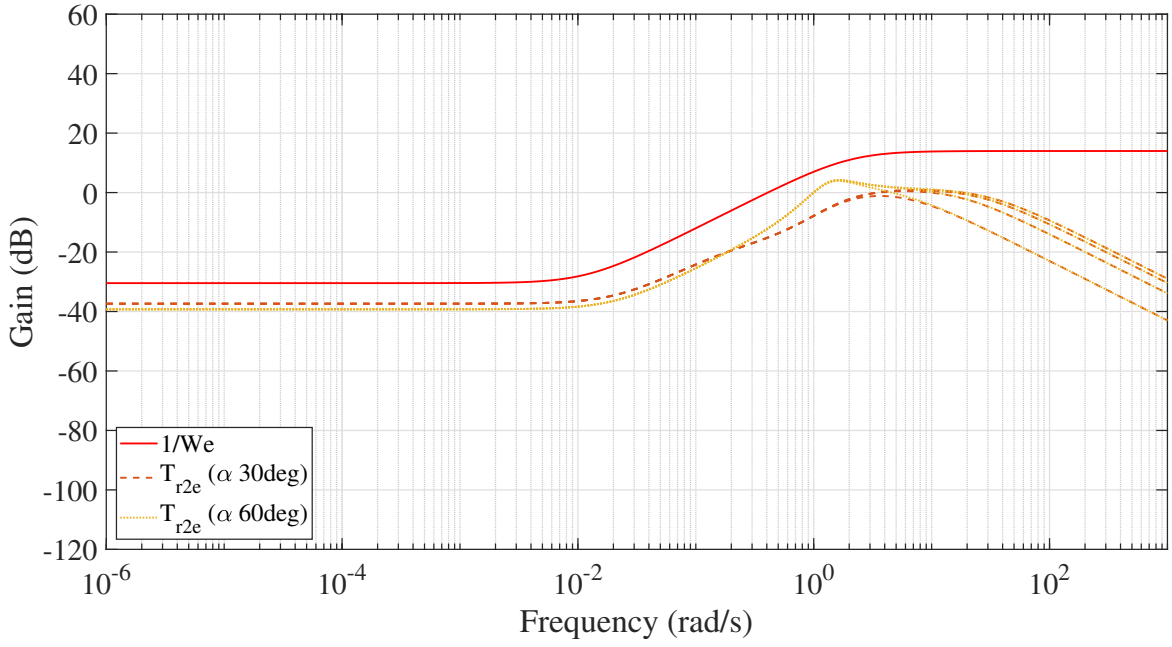

(b) Simultaneous.

Fig. 3.18 Gain Plot of T_{r2e} for Modified Zermelo's Problem.

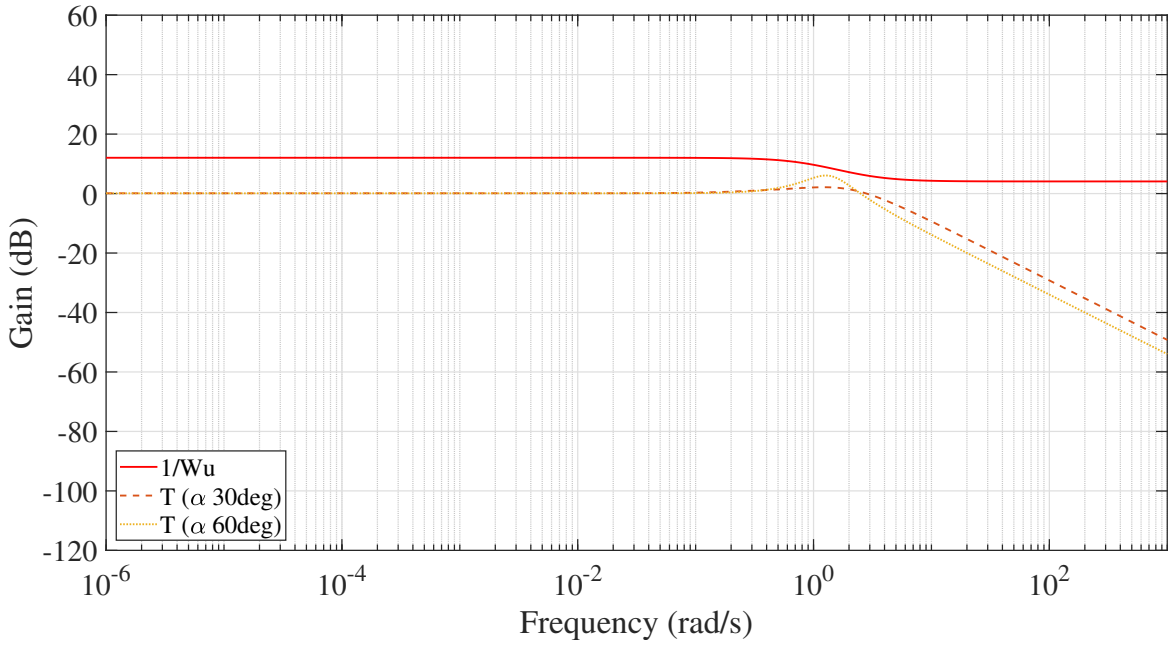

(a) Separated.

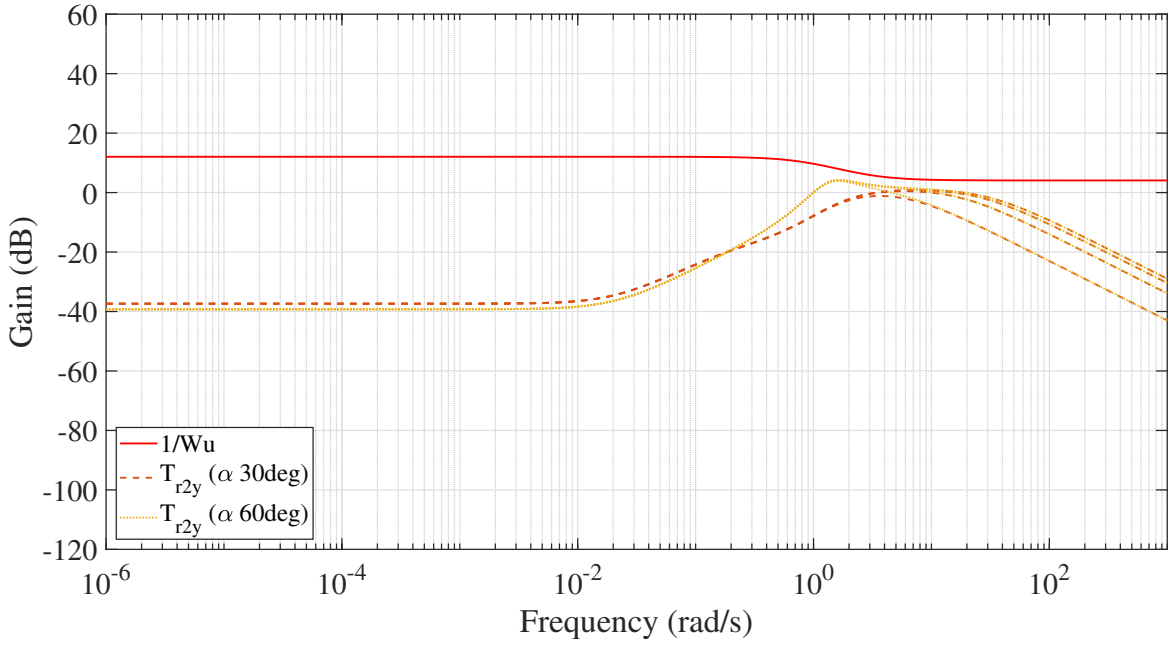

(b) Simultaneous.

Fig. 3.19 Gain Plot of T_{r2y} for Modified Zermelo’s Problem.

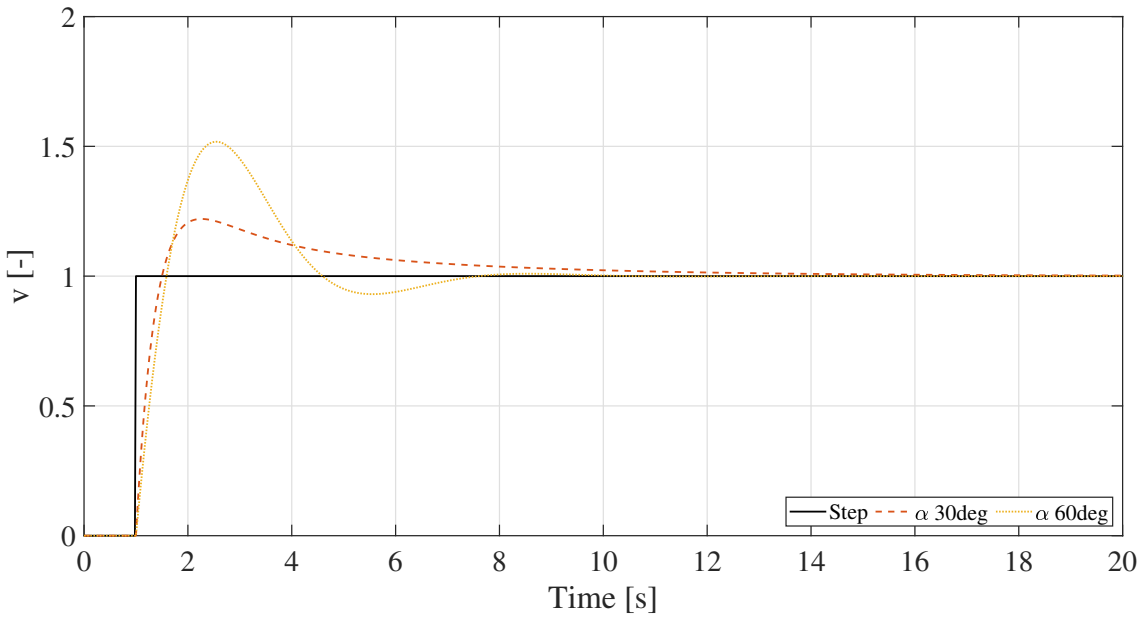

(a) Separated.

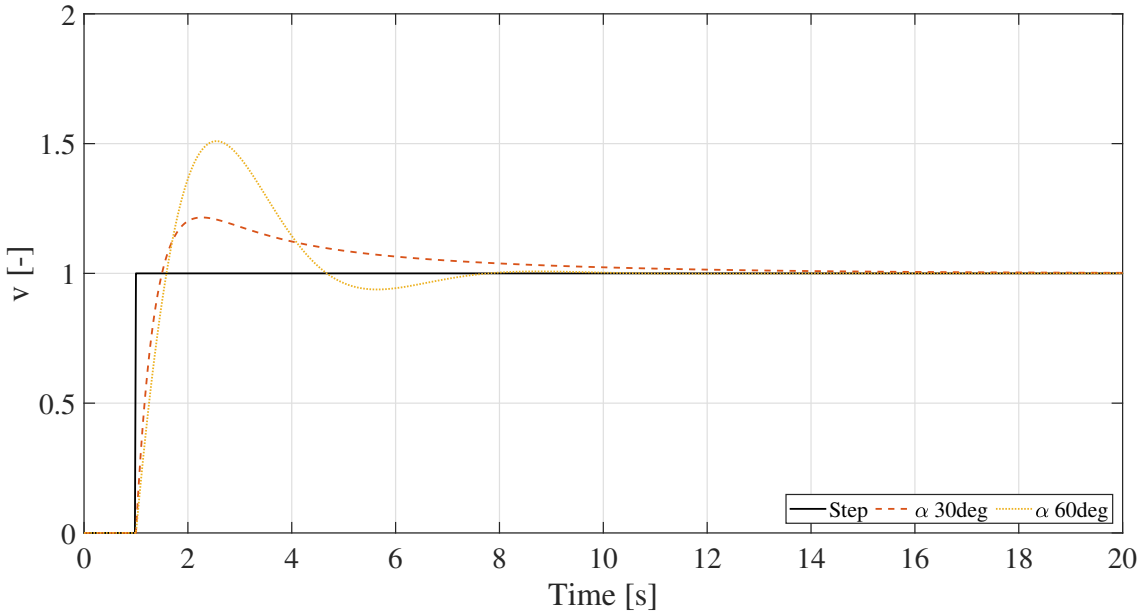

(b) Simultaneous.

Fig. 3.20 Step Response Comparison for Modified Zermelo's Problem.

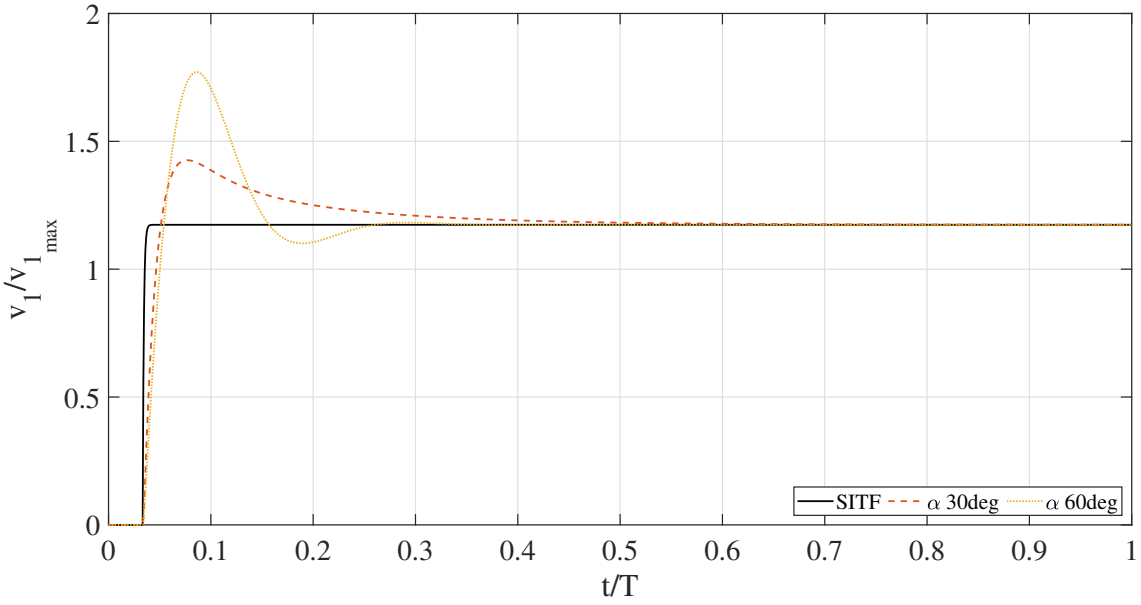

(a) Segment 1 SITF.

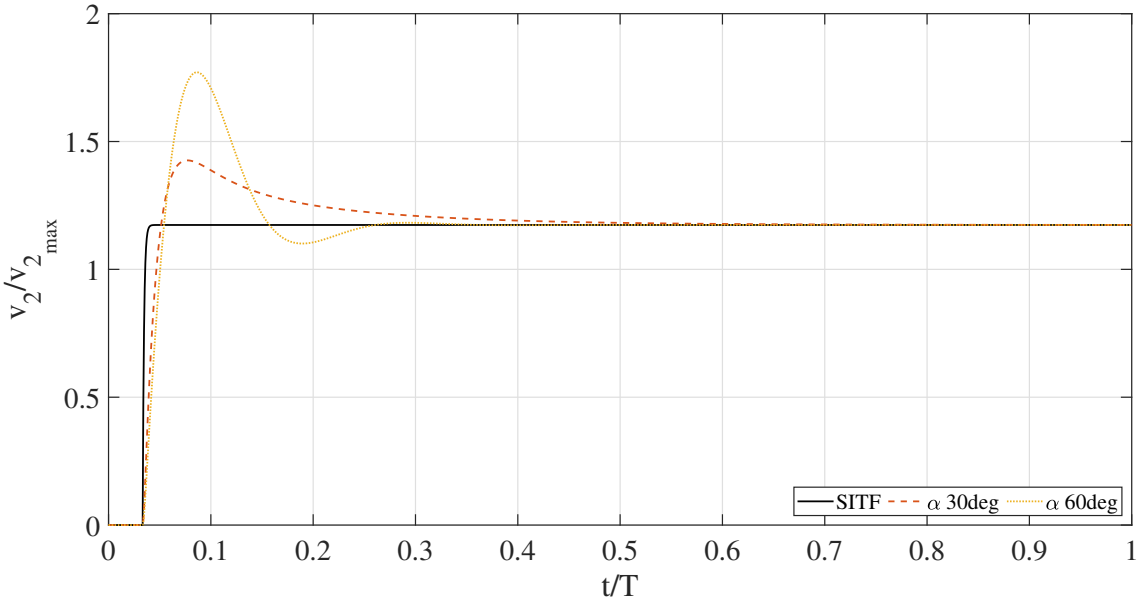

(b) Segment 2 SITF.

Fig. 3.21 Response of SITF Inputs for Modified Zermelo’s Problem (Segment 1 and 2).

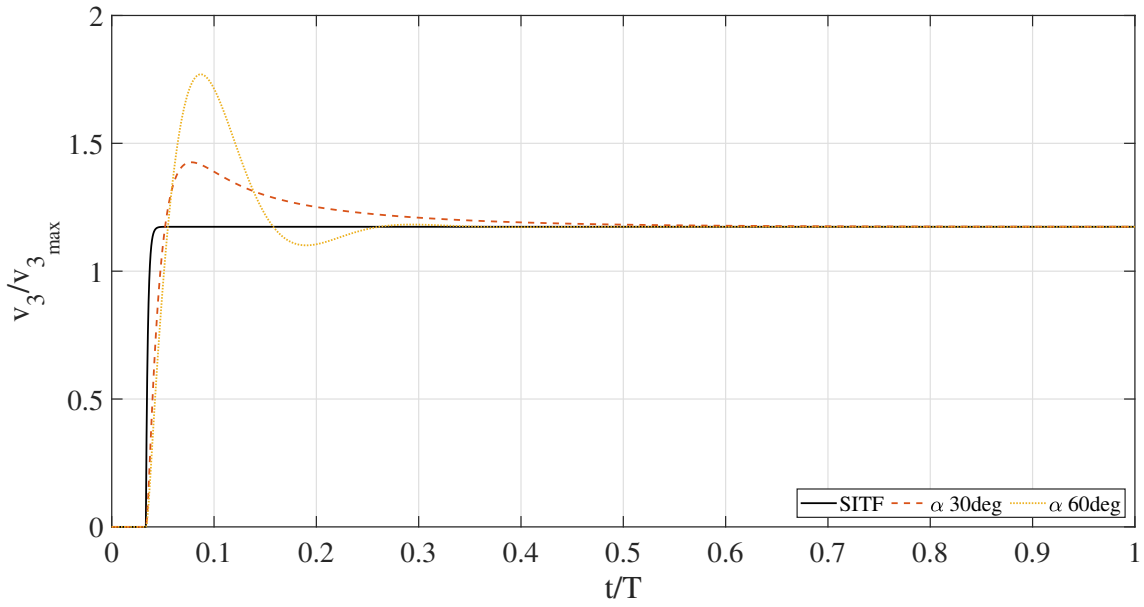

(a) Segment 3 SITF.

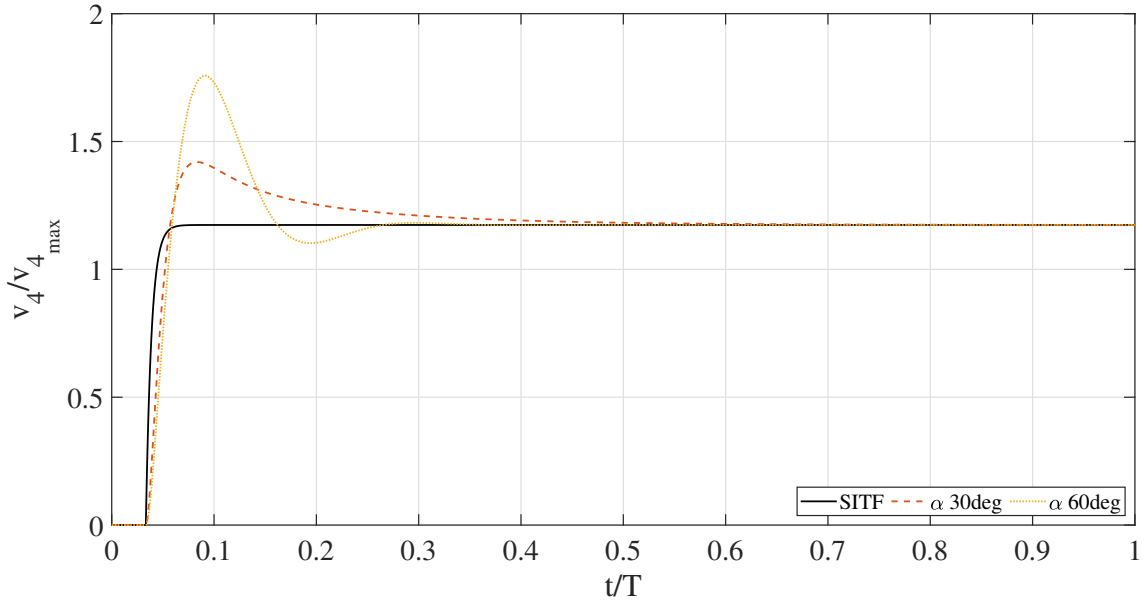

(b) Segment 4 SITF.

Fig. 3.22 Response of SITF Inputs for Modified Zermelo's Problem (Segment 3 and 4).

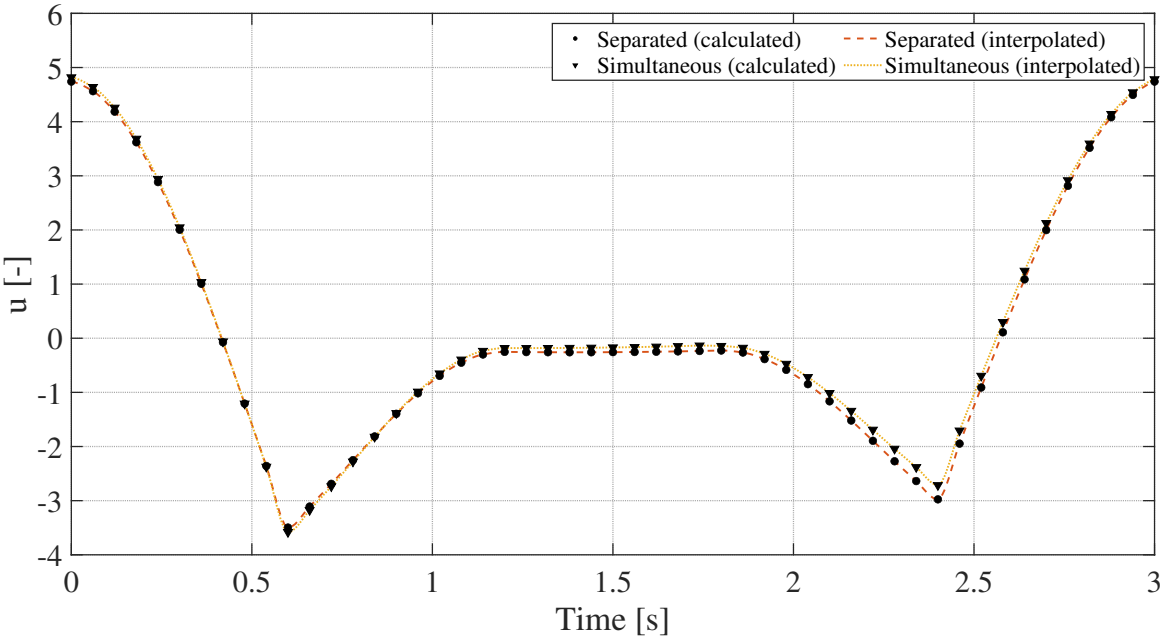

(a) Time History of u.

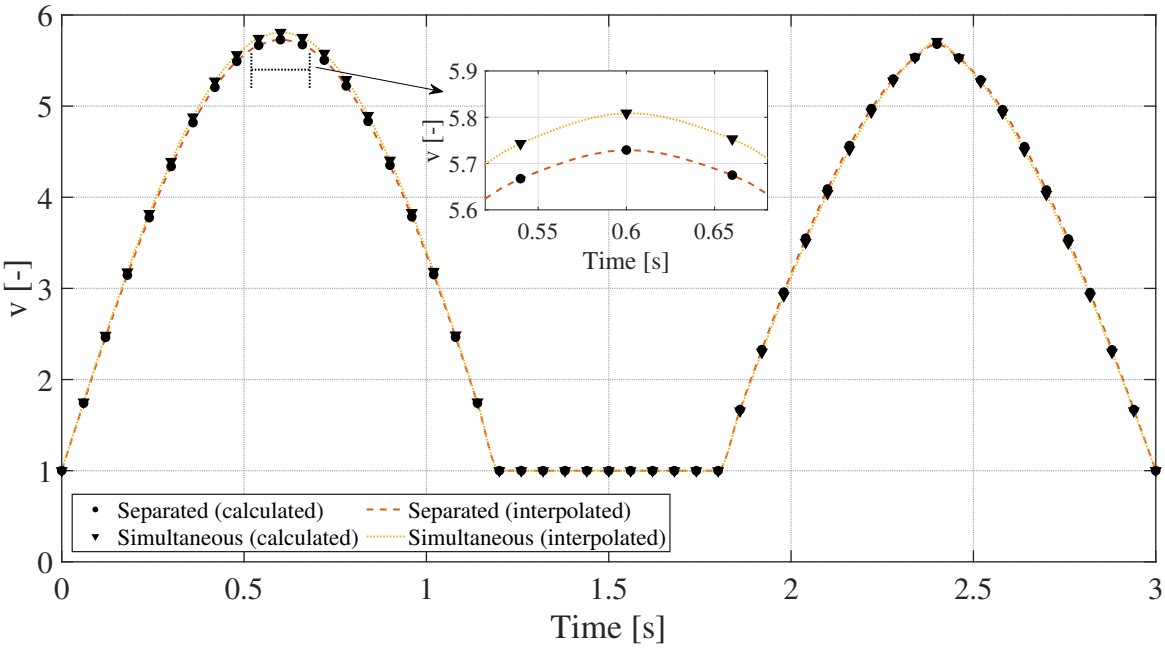

(b) Time History of v.

Fig. 3.23 Comparison between Separated and Simultaneous Methods for Modified Zermelo’s Problem (u and v).

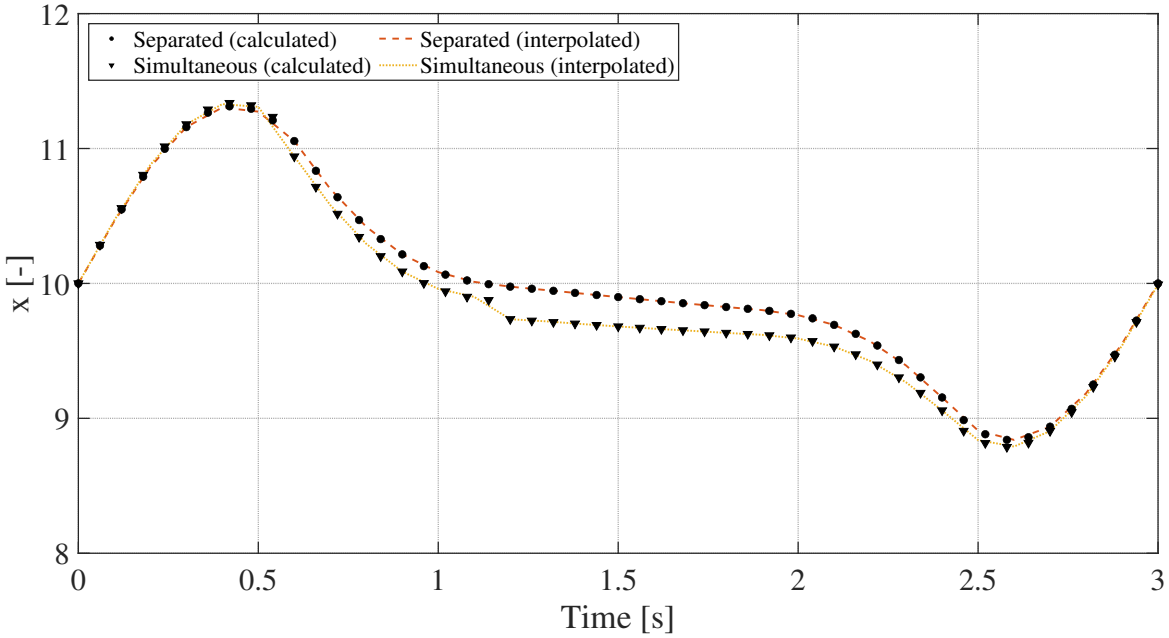

(a) Time History of x.

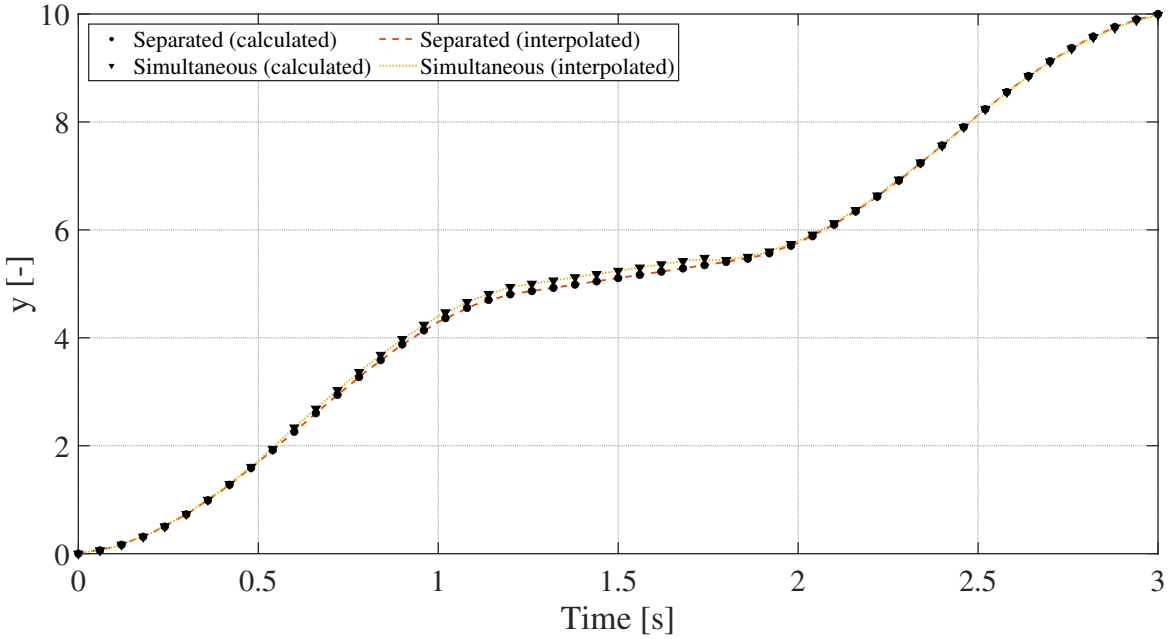

(b) Time History of y.

Fig. 3.24 Comparison between Separated and Simultaneous Methods for Modified Zermelo's Problem (x and y).

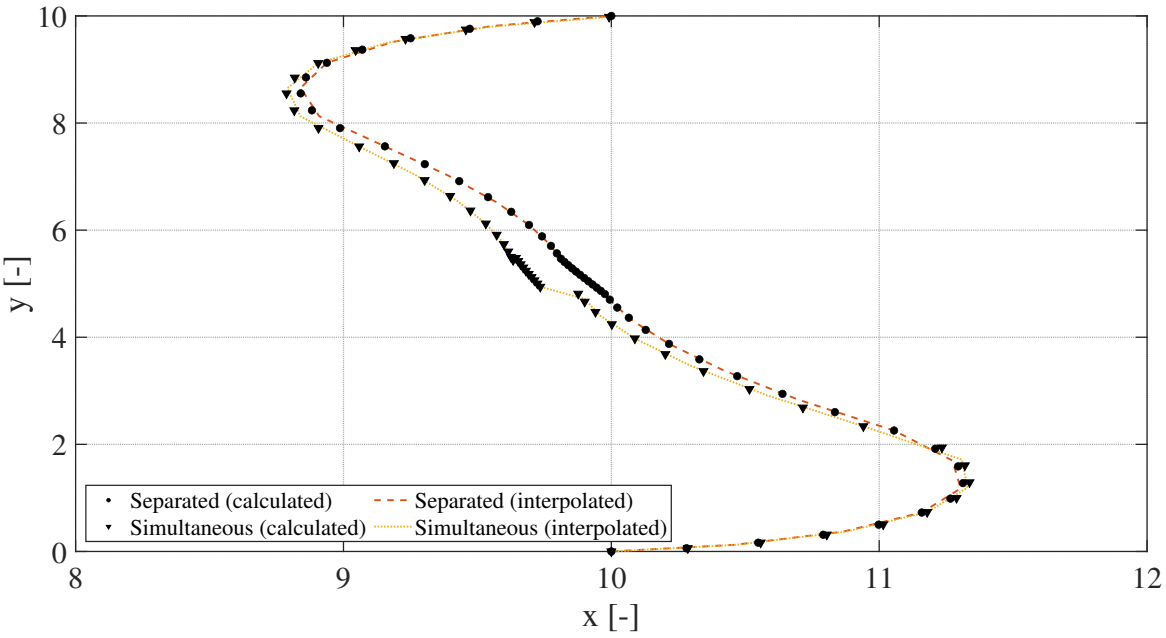

(a) Comparison between x and y.

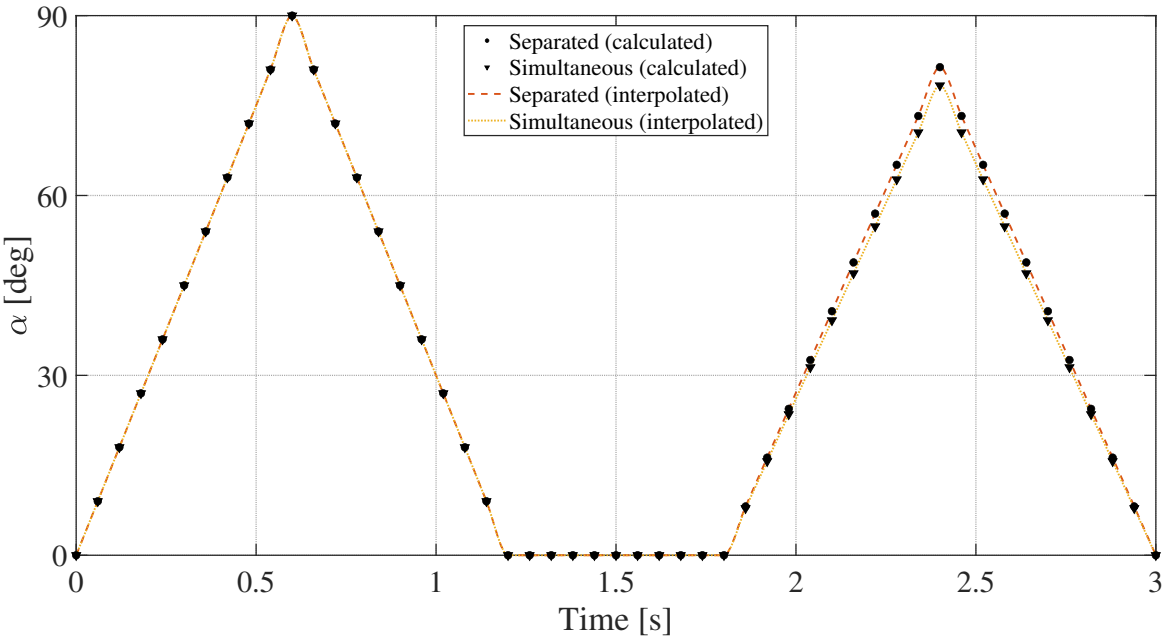

(b) Time History of α.

Fig. 3.25 Comparison between Separated and Simultaneous Methods for Modified Zermelo’s Problem (x to y and α).

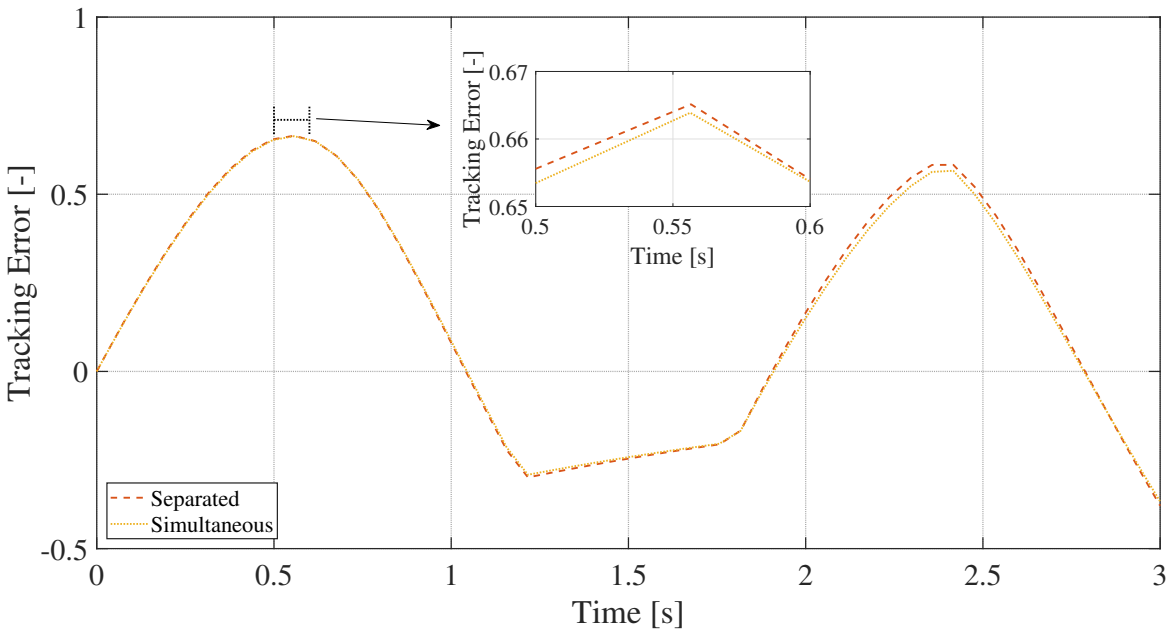

Fig. 3.26 Error Comparison for Tracking v.

3.3 Conclusion of Chapter 3

From the obtained results, the novel method of simultaneous design of trajectory and robust controller were successfully applied to a benchmark aerospace related optimal control problem as well as for a example problem outside the field of aerospace. The designed robust controller had stability and performance with robustness against flight condition changes. The proposed method showed superior results to conventional design method of separately designing the trajectory and robust controller from the viewpoint of improving the objective function, reducing the maximum tracking error placed as the nonlinear inequality constraint, and adding robustness against the trajectory.

Chapter 4

Application to Hypersonic Experimental Aircraft Problem

In this chapter, in order to satisfy the second objective of solving the Hypersonic Experimental Aircraft problem, a simultaneous optimization of trajectory and robust controller design of a experimental launch vehicle with pre-cooled turbojet (PCTJ) engines is conducted via the proposed method. The PCTJ engine is a hypersonic airbreathing engines, and it can be operated with high specific impulse value up to Mach 6 with the precooling system located prior to its core engine. Optimization is executed to maximize flight time while subject to minimizing tracking error to a specified value.

4.1 Hypersonic Experimental Aircraft Problem

The Hypersonic Experimental Aircraft problem is a problem to design a trajectory and controller under flight constraints which maximizes hypersonic cruise duration as well as descent time to increase downrange since the aircraft will be gliding with no thrust and has to touchdown as close to the airstrip as possible for recovery. The experiment consists of 4 phases of launch, suborbital flight, hypersonic cruise, and decent depicted in Fig.4.1. The aircraft will be attached to the fuselage of the NAL735 rocket booster and launched to 100[km] in altitude (i.e. image of launch shown in Fig.4.2). The aircraft will detach from the booster at 100[km] to start its suborbital flight to reach around 50[kPa] of dynamic pressure for cruise test condition shown in Table.4.1 derived by refering to [42]. Then, the aircraft will start pitch up to perform a hypersonic cruise experiment of Mach 5 at 25[km]. Upon finishing the cruise experiment, the aircraft will start its descent for landing.

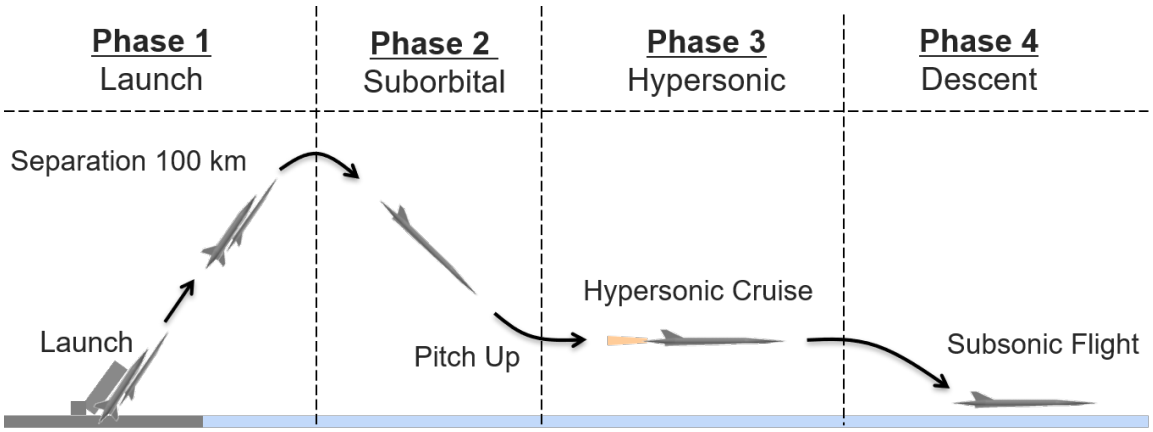

Fig. 4.1 Hypersonic Flight Experiment Concept.

Table 4.1 Hypersonic Engine Test Conditions [42].

Mach Number M	$M \geq 4$
Dynamic Pressure Q [kPa]	$49 \leq Q \leq 51$
Angle of Attack α [deg]	$0 \leq \alpha \leq 6$

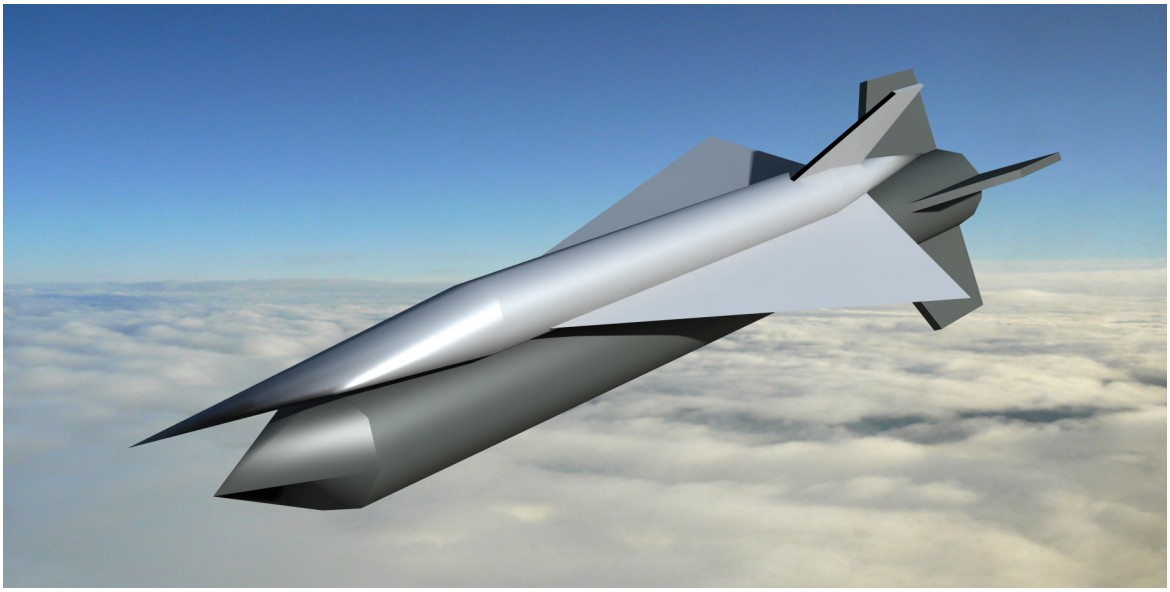

Fig. 4.2 NAL-735 with Hypersonic Experimental Aircraft Configuration.

To solve the Hypersonic Experimental Aircraft problem, the simultaneous method was applied along with CFD analysis shown in Fig.4.3. The initial conditions of vehicle geometry, mass, and propulsion parameters were predefined and CFD analysis were conducted to obtain the aerodynamic coefficients for the designed Hypersonic Experimental Aircraft model to be incorporated into the simultaneous method. The state variables are downrange d, altitude h, velocity v, and flight path angle γ. For the Hypersonic Experimental Aircraft descent problem, analysis for the sizing of the elevon were carried out in order to identify the effect elevon size has on flight time. The elevon sizing was taken as a optimization variable A. The trajectory optimization uses a three state nonlinear Eqs.(4.14) stated in the section 4.2 while the nonlinear simulation to obtain e_{max} uses five state Eqs.(4.15). The formulation of the nonlinear problem is similar to the rocket launch example problem where the maximum error e_{max} is placed as nonlinear constraint taken from separated method from where the optimal trajectory and controller are designed separately. The SISO system is identical to the system shown in Fig.2.5. The system tracks the reference γ generated at each iteration of SQP and has a feedback loop for obtaining maximum error γ_{max}. The γ_{max} is then evaluated to meet the nonlinear inequality constraint. Finally, the control period for tracking the reference input was fixed at 50[hz] (0.02 [s]) by referring to [52] and represents the optimal speed to move the actuators.

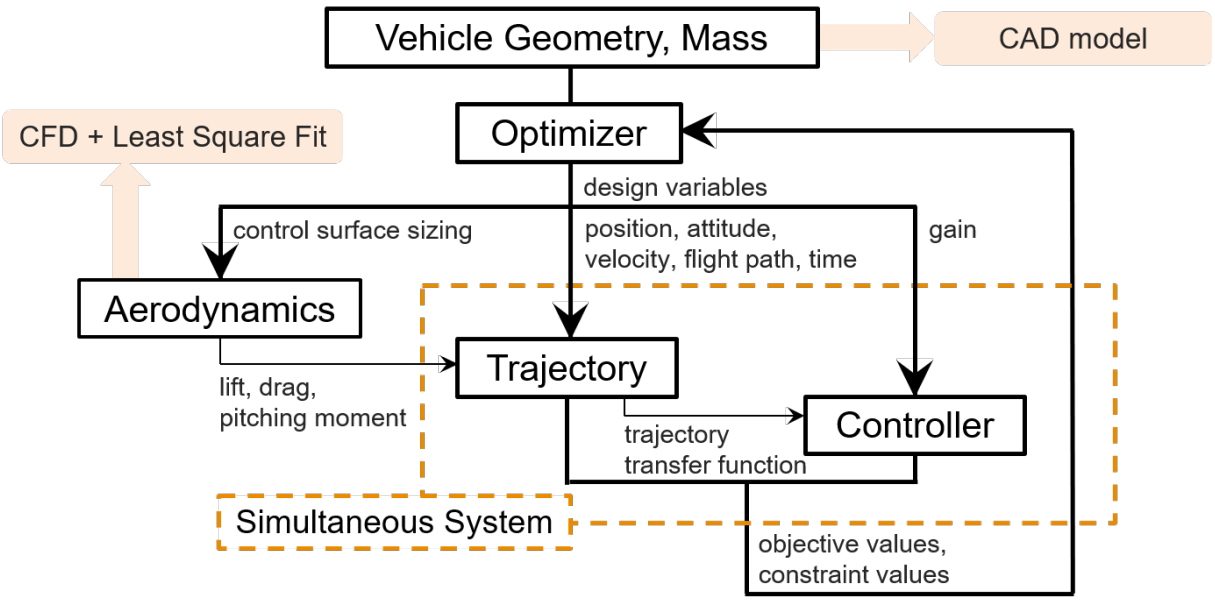

Fig. 4.3 System Overview for the Hypersonic Experimental Aircraft Problem.

4.1.1 Hypersonic Experimental Aircraft

The Hypersonic Experimental Aircraft (Fig.4.4 to 4.6 shows the overview, side, and top view respectively) has been constructed with a waverider applied as its wing (waverider wing) which utilizes shock created on the lower surface to obtain high L/D during hypersonic cruise. Specifications are shown in Table 4.2 and design method of a conical waverider is shown in Appendix C. The maximum elevon sizing was presumed to be maximum of 7.5% and minimum of 2.5% total length of the wing for this analysis (Fig.4.7). The waverider wing is defined as a wing which utilizes the shock wave attached to its leading edge forming a compressed lower surface thus increasing L/D. Previous studies conducted so far through the use of CFD validate the aerodynamic efficiency and the results suggest a relatively high L/D at their given design conditions [36]. The model has been evaluated at low speed of Mach 0.3 where CFD results stated sufficient lift was produced for low speed flight [36].

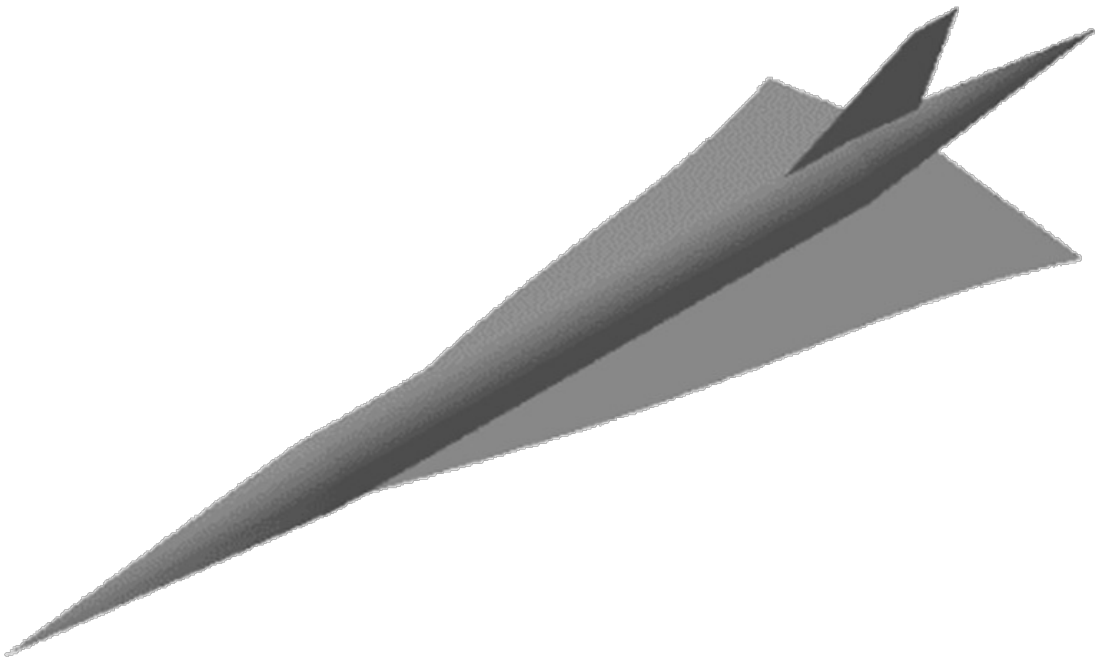

Fig. 4.4 Hypersonic Experimental Aircraft Overall View.

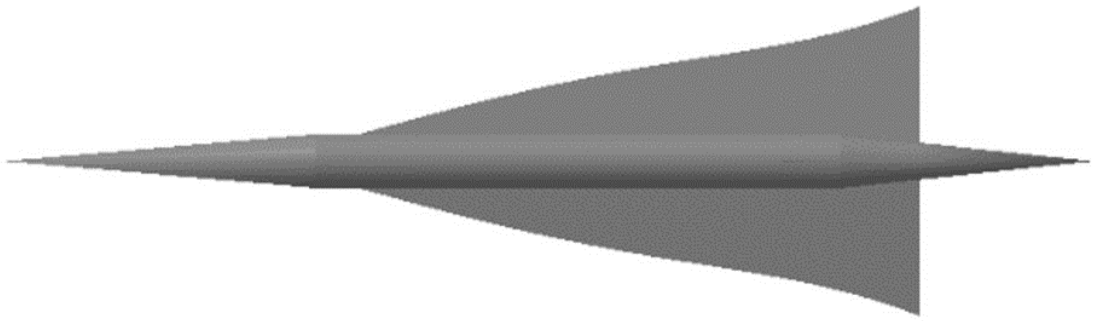

Fig. 4.5 Hypersonic Experimental Aircraft Top View.

Fig. 4.6 Hypersonic Experimental Aircraft Side View.

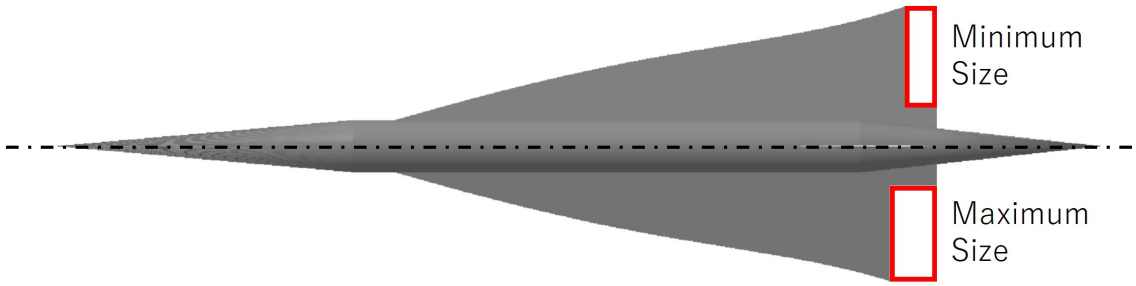

Fig. 4.7 Elevon Area Comparison.

Table 4.2 Aircraft Specification

Total Length [m]	9.6
Total Weight [kg]	803
Wing Span [m]	3.2
Wing Length [m]	5.8
Reference Wing Area [m^2]	8.3
Center of Gravity [m]	60% from nose

4.1.2 NAL-735 Solid Rocket Booster Model

For the Hypersonic Experimental Aircraft problem, the aircraft will be attached to the fuselage of the NAL-735 solid rocket booster [69, 64]. NAL-735 was developed on the base of the SB-735 motor which is the side rocket booster of Japanese satellite launcher M3SII with modifications specifically for launch experiments such as front and rear connection and separation mechanisms for aircraft attachment [58]. The booster has a dimensions of 0.735[m] in diameter, 10[m] in length, and maximum gross weight of 5886[kg] and empty weight of 2370 [kg] [69] producing around 250[kN] of thrust. Specifications are summarized in Table 4.3. A CAD representation of NAL-735 based on Ref.[59] is shown in Fig.4.8 to (4.9) of overall view and side and top view respectively. The launch angle γ_0 was obtained through trial and error of finding the set of γ_0, burnout time and flight time to apogee of reaching 100[km] in altitude at Mach 5. Launch conditions for the Hypersonic Experimental Aircraft problem are summarized in Table.4.4.

Table 4.3 NAL-735 Solid Rocket Booster Specification.

Total Length [m]	10 [69]
Total Weight [kg]	5886 [69]
Fuselage Diameter [m]	0.735 [69]
Nozzle Cant Angle [deg]	2.9 [69]
Control Surface Area [m^2]	3.6 [69]
Thrust [kN]	250 [64]
Isp	266 [59]
Max Burnout Time [s]	50 [64]

Table 4.4 NAL-735/Hypersonic Experimental Aircraft Configuration Launch Conditions.

Launch Angle [deg]	46
Burnout Time [s]	36
Time to Apogee [s]	131
Target Altitude [km]	100
Target Mach	5
Gross Weight at Launch [kg]	6689

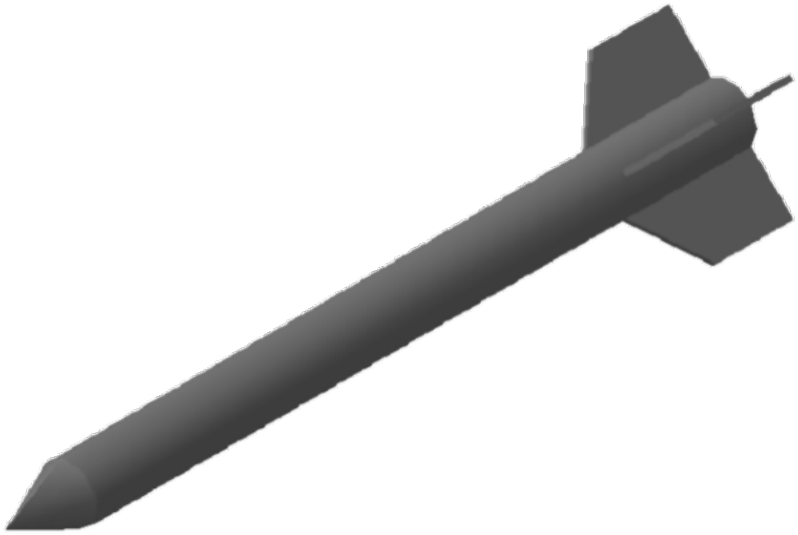

Fig. 4.8 NAL-735 Overall View.

Fig. 4.9 NAL-735 Side and Front View.

The dynamic equations used to model the trajectory of the Phase 1 launch is shown in Eq.(4.1). The equation is the widely-known Tsiolkovsky's equation for the velocity V increment of a rocket in free space [73, 21, 35].

$$V = -gI_{sp}\ln(1-\lambda) \tag{4.1}$$

Where $g = 9.8[m/s^s]$ represents the gravity constant, I_{sp} is the specific impluse, and λ represents the ratio between burned fuel at a certain time denoted as $m(t)$ to the initial weight of the rocket m_0 expressed as Eq.(4.2).

$$\begin{aligned} \lambda &= \frac{[m_0 - m(t)]}{m_0} \\ &= \frac{Bt}{m_0} \\ B &= \frac{dm}{dt} \\ &= \frac{F}{I_{sp}g} \end{aligned} \tag{4.2}$$

Under the assumption that the Lift and Drag are relatively small compared to the gravity constant and thrust T is always parallel to V from Eq.(4.1), the equation of motion for $\dot{\gamma}$ is expressed by Eq.(4.3).

$$\dot{\gamma} = \frac{-g\cos\gamma}{V} \tag{4.3}$$

By solving for Eq.(4.3), it is possible to obtain analytical solution for a gravity assisted turn for a rocket. Under the assumption of the Tsiolkovsky's equation of constant B and applying Eq.(4.1) to Eq.(4.3) and taking the integral, Eq.(4.4) is obtained.

$$\ln \frac{\tan(\frac{\pi}{4} - \frac{r}{2})}{\tan(\frac{\pi}{4} - \frac{r_0}{2})} = \frac{1}{\tau_0}[k_2(\lambda) - k_2(\lambda_0)] \tag{4.4}$$

Here, $T = 25000, m_0 = 6689, \tau_0 = T/m_0$. $k_2(\lambda_0) = 0$ and $k_2(\lambda)$ is expressed as Eq.(4.5) obtained from least square fit between λ and $k_2(\lambda)$ values shown in [35].

$$k_2(\lambda) = 0.92\ln(\lambda) + 4.3 \tag{4.5}$$

$$\tag{4.6}$$

Eq.(4.4) is solved for γ by Eq.(4.5).

$$\gamma = \frac{\pi}{2} - 2\tan^{-1}\left[e^{\frac{1}{\tau_0}(k_2(\lambda) - k_2(\lambda_0)) + \ln(\tan(\frac{\pi}{4} - \frac{\gamma_0}{2}))}\right] \tag{4.7}$$

The state variables for the constant acceleration phase is shown in Eq.(4.8) where the subscript (1a) denotes the constant acceleration phase. Downrange x and altitude y was obtained from Euler integration [7] of u and v with time interval $d = 0.1$ and $N = t_b/d$ where $t_b = 36$ for burnout time. Initial values are $x_0 = 0$ and $y_0 = 0$.

$$\begin{aligned}
u^{(1a)}) &= \dot{x}^{(1a)} = V^{(1a)}\cos(\gamma^{(1a)}) \\
v^{(1a)}) &= \dot{y}^{(1a)} = V^{(1a)}\sin(\gamma^{(1a)}) \\
x^{(1a)}) &= x_{n+1}^{(1a)} = x_0^{(1a)} + du_n^{(1a)}, \;\; 0 \le n \le N-1 \\
y^{(1a)}) &= y_{n+1}^{(1a)} = y_0^{(1a)} + dv_n^{(1a)}, \;\; 0 \le n \le N-1 \\
\gamma^{(1a)} &= \frac{\pi}{2} - 2\tan^{-1}\left[e^{\frac{1}{\tau_0}(k_2(\lambda)-k_2(\lambda_0))+\ln(\tan(\frac{\pi}{4}-\frac{\gamma_0}{2}))}\right]
\end{aligned} \tag{4.8}$$

For the trajectory of the rocket after constant acceleration or after fuel burn, the rocket performs inertial flight and the dynamics are easily obtained by Eq.(4.9) and subscript $(1b)$ denotes the inertial flight phase. Flight time to apogee was obtained to meet the launch conditions listed in Table.4.4 where $t = 131$.

$$\begin{aligned}
u^{(1b)} &= V_f^{(1a)}\cos(\gamma^{(1b)}) \\
v^{(1b)} &= V_f^{(1a)}\sin(\gamma^{(1b)}) - gt \\
x^{(1b)} &= x_f^{(1a)} + V^{(1b)}t_2\cos\gamma^{(1b)} \\
y^{(1b)} &= y_f^{(1a)} + V^{(1b)}t_2\sin\gamma^{(1b)} - \frac{1}{2}gt^{2^{(1b)}} \\
\gamma &= \tan^{-1}\left(\frac{u^{(1b)}}{v^{(1b)}}\right)
\end{aligned} \tag{4.9}$$

Where $x_0^{(1b)} = x_f^{(1a)}, y_0^{(1b)} = y_f^{(1a)}, u_0^{(1b)} = u_f^{(1a)}, v_0^{(1b)} = v_f^{(1a)}, \gamma_0^{(1b)} = \gamma_f^{(1a)}$ to ensure continuity of the trajectory. The state variables for Phase 1 are summarized in Eq.(4.10).

$$\begin{aligned}
x^{(1)} &= \left[x^{(1a)}, x^{(1b)}\right] \\
y^{(1)} &= \left[y^{(1a)}, y^{(1b)}\right] \\
u^{(1)} &= \left[u^{(1a)}, u^{(1b)}\right] \\
v^{(1)} &= \left[v^{(1a)}, v^{(1b)}\right] \\
\gamma^{(1)} &= \left[\gamma^{(1a)}, \gamma^{(1b)}\right]
\end{aligned} \tag{4.10}$$

4.1.3 Aerodynamic Model

The aerodynamic model was derived by an unstructured three-dimensional CFD solver developed by JAXA known as FaSTAR [32] (Fast Aerodynamic Routine). A three-dimensional flow-field around the model was calculated numerically. Numerical analysis was conducted solving the three-dimensional compressible Navier-Stokes equation using finite-volume method. The CFD conditions are summarized in Table 4.5. The viscous model effects were estimated using SA-noft2 [8] and HLLEW [57] scheme for advection was used to accurately capture shockwaves and discontinuities. Time integration was performed using MUSCL [74] method with second-order spatial accuracy. The calculated Mach numbers are summarized in Table 4.6. The total length of the aircraft was used as the reference length.

An automatic hexahedra grid generator Hexagrid [33] developed by JAXA was used to create three-dimensional grids. Based on the input geometry (STL format), Hexagrid generates unstructured mesh based on Cartesian mesh. A grid containing approximately 40 million cells in an 81 cubic meter domain was created for each model (Fig 4.10).

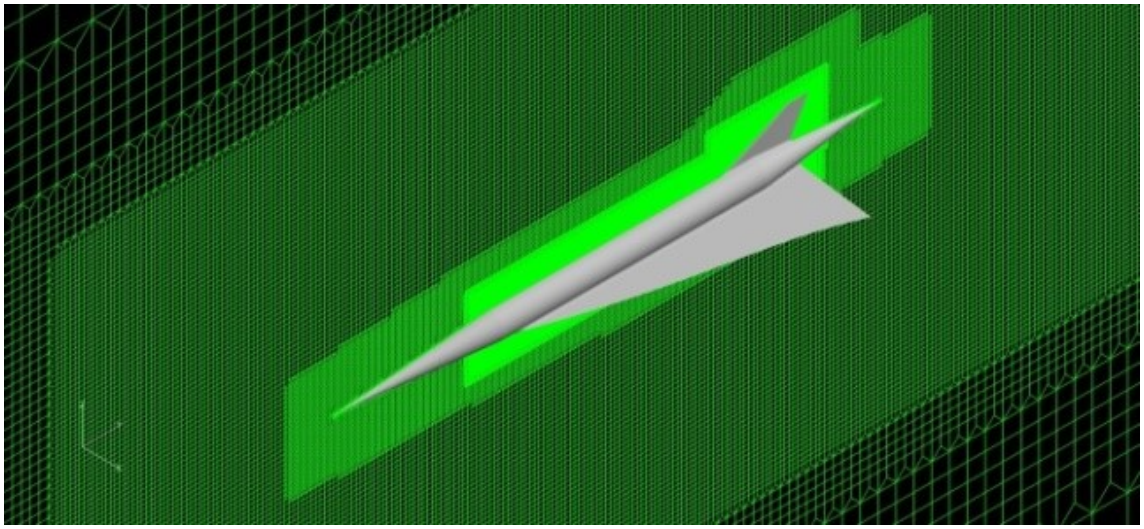

Fig. 4.10 Unstructured Mesh Generated by Hexagrid [33].

Table 4.5 CFD Conditions.

Governing Equation	Navier-Stokes
Turbulence Model	SA-noft2 [8]
Numerical Scheme	HLLEW [57]
Volumetric Accuracy	MUSCL [74]
Time Integration	LU-SGS [66]

Table 4.6 Sample Points.

Mach	0.3, 0.8, 2, 5
α [deg]	0, 5, 10
δ_e [deg]	-15, 0, 15
A	0.025, 0.075

Interpolation of the aerodynamics to obtain the surrogate model of C_L, C_D and C_m was conducted using least square method. The sample points used to generate the surrogate model is summarized in Table 4.6. The least square method is used to interpolate for C_L, C_D and C_m as function of α, Mach, δ_e, and elevon sizing A shown in Eqs.(4.11) to (4.13) used for lift, drag, and moment calculation in Eqs.(4.14) to (4.15). The simulation uses U.S. Standard Atmosphere Model for the air density and static temperature [1].

$$C_L = 0.0196 + 0.0792A - 0.0157M + 0.0243\alpha + 0.0053\delta_e \tag{4.11}$$

$$\begin{aligned} C_D = {} & 0.0146 + 0.2008A - 0.0052M + 0.0006\alpha + 0.0001\delta_e \\ & + 0.0026\alpha A - 0.0004\alpha M + 0.0001\alpha\delta_e \\ & - 0.0211MA - 0.0001M\delta_e + 0.0004\alpha^2 + 0.0006M^2 \end{aligned} \tag{4.12}$$

$$C_m = 0.0011 - 0.0252A + 0.0008M - 0.0008\alpha - 0.0012\delta_e \tag{4.13}$$

4.2 Nonlinear Trajectory Design

The nonlinear trajectory is evaluated for the objective function value, maximum tracking error e_{max}, and the optimized elevon sizing. The dynamic equations used for trajectory optimization considers moments by placing a static margin constraint. The longitudinal equation of motion used to define the 3 state aircraft dynamics with assumption of a round non-rotating earth as well as various variables are given by the nonlinear Eqs.(4.14) where T_N: thrust = 0 for the descent trajectory phase.

$$\begin{aligned}
\dot{d} &= V\cos(\gamma) \\
\dot{h} &= V\sin(\gamma) \\
\dot{V} &= \frac{T_N\cos(\alpha)-D}{m_0} + g\sin(\gamma) \\
\dot{\gamma} &= \frac{L+T_N\sin(\alpha)}{m_0 V} - \left(\frac{g}{V}-\frac{V}{r}\right)\cos(\gamma)
\end{aligned} \tag{4.14}$$

The closed loop nonlinear simulation implements the derivative of pitch rate and angle of attack. After a trajectory is generated at each iteration of the optimization, γ will be set as reference trajectory to be tracked to obtain e_{max}. The longitudinal equation of motion used to define the 5 state aircraft dynamics with assumption of a round non-rotating earth are given by the nonlinear Eq.(4.15) where T_N is 0 for the descent trajectory phase.

$$\begin{aligned}
\dot{d} &= V\cos(\gamma) \\
\dot{h} &= V\sin(\gamma) \\
\dot{V} &= \frac{T_N\cos(\alpha)-D}{m_0} + g\sin(\gamma) \\
\dot{\gamma} &= \frac{L+T_N\sin(\alpha)}{m_0 V} - \left(\frac{g}{V}-\frac{V}{r}\right)\cos(\gamma) \\
\dot{\alpha} &= q-\dot{\gamma} \\
\dot{q} &= \frac{M_{cg}}{I_{yy}}
\end{aligned} \tag{4.15}$$

where the aerodynamic force is obtained by the following:

$$\begin{aligned}
L &= \frac{1}{2}\rho v^2 S C_L \\
D &= \frac{1}{2}\rho v^2 S C_D \\
M_{cg} &= \frac{1}{2}\rho v^2 S\bar{c}(C_m + C_{mq}\frac{q\bar{c}}{2V})
\end{aligned} \tag{4.16}$$

Here, the pitching moment is calculated taking in the effect of changes to α and pitch rate. C_L, C_D, and C_m are obtained through CFD while the pitch damping derivative C_{mq} is obtained by the following equation taken from [28]:

$$C_{mq} = -2\alpha_w V_H \frac{l_t}{\bar{c}} \tag{4.17}$$

Here, α_w is the derivative of C_L with respect to α for the entire aircraft. It should well noted that this is a rough estimation since normally the derivative for the horizontal tail wing is used. V_H is the tail volume taken from the CG to the end of elevon. l_t is the distance from CG to trailing edge of the elevon since the aircraft has elevon for control surface which is attached to the wings.

The static margin (SM) was calculated using the following equation:

$$\text{SM} = \frac{x_{ac} - x_{cg}}{c_{ref}} \tag{4.18}$$

$$x_{ac} = x_{cg} - c_{ref} \frac{C_{m\alpha}}{(C_{L\alpha} + C_D)\cos\alpha + (C_{D\alpha} + C_L)\sin\alpha} \tag{4.19}$$

The formulation for the nonlinear optimal control problem is shown in Eq.(4.20). The structural limit of ± 5[G] was placed as strict requirement to produce a trajectory with less stress structural load. The aircraft is assumed to withstand ± 10[G] referring to previous supersonic experimental aircraft NEXST-1[43].

$$
\begin{aligned}
\text{find} \quad & \text{state variables} : X = [d\ [\text{m}], h\ [\text{m}], v\ [\text{m/s}], \gamma\ [\text{deg}]] \\
& \text{control variables} : \alpha,\ \delta_e\ [\text{deg}] \\
& \text{throttle} : \delta_t \\
& \text{phase duration} : t_f^{(2)},\ t_f^{(3)},\ t_f^{(4)}\ [\text{s}] \\
& \text{elevon sizing} : A\ [\text{m}^2] \\
\text{min.} \quad & -[t_f^{(4)} - t_0^{(3)}] \\
\text{s.t.} \quad & \text{state equations shown in Section V.B in Eqs.(4.14)} \\
& -5 \leq \text{load}\ \ [\text{G}] \leq 5 \\
& 0 \leq \alpha\ \ [\text{deg}] \leq 10 \\
& -15 \leq \delta_e\ \ [\text{deg}] \leq 15 \\
& 0 \leq \delta_t \leq 1 \\
& -2 \leq \dot{\alpha}\ \ [\text{deg/s}] \leq 2 \\
& \text{static margin} \geq 0.01 \\
& e_{max}\ \ [\text{deg}] \leq 20 \\
& 0.025 \leq A \leq 0.075
\end{aligned}
\tag{4.20}
$$

The constraints particular to each phase is summarized below. The constraint structure when applying phases to the trajectory is explained in Section 2.2.1, Eq.(2.9). The optimization variables and objective function are identical for all phases.

Phase 1. **Rocket Launch:**
As stated in 4.1.2, the launch phase was derived analytically to meet the initial conditions of Phase 2. The constraints particular for Phase 1 is stated in Eq.(4.21).

The subscript (1) denotes the rocket launch phase.

$$\begin{aligned} \text{s.t.} \quad & X_0^{(1)} = [0,0,0,45] \\ & X_f^{(1)} = [216,100,1400,0] \\ & t_0^{(1a)} = 0 \text{ [s]} \\ & t_f^{(1a)} = 36 \text{ [s]} \\ & t_0^{(1b)} = 36 \text{ [s]} \\ & t_f^{(1b)} = 131 \text{ [s]} \\ & m_0^{(1)} = 6689 \text{ [kg]} \end{aligned} \tag{4.21}$$

Phase 2. **Suborbital Flight:**

The particular constraints placed for the suborbital flight after separation from NAL-735 is stated in Eq.(4.22). The subscript (2) denotes the suborbital flight phase.

$$\begin{aligned} \text{s.t.} \quad & X_0^{(2)} = [216170,102110,1400,0] \\ & X_f^{(2)} = [d,23000,1500,0] \\ & Q^{(2)} \leq 50 \text{ [kPa]} \\ & \alpha_0^{(2)} = 0 \text{ [deg]} \end{aligned} \tag{4.22}$$

Phase 3. **Hypersonic Cruise:**

The particular constraints placed for the hypersonic cruise after pitching up from suborbital flight is stated in Eq.(4.23). The subscript (3) denotes the hypersonic cruise phase.

$$\begin{aligned} \text{s.t.} \quad & X_0^{(3)} = [d,23000,1500,0] \\ & X_f^{(3)} = [d,23000,1500,0] \\ & -0.2 \leq \gamma^{(3)} \text{ [deg]} \leq 0.2 \\ & 49 \leq Q^{(3)} \text{ [kPa]} \leq 51 \end{aligned} \tag{4.23}$$

Phase 4. **Descent Flight:**

The particular constraints placed for the descent flight after pitching up from hypersonic cruise is stated in Eq.(4.24). The subscript (3) denotes the hypersonic

cruise phase.

$$\begin{aligned} \text{s.t.} \quad & X_0^{(4)} = [d, 23000, 1500, 0] \\ & X_f^{(4)} = [d, 1000, 102, 0] \\ & Q^{(4)} \leq 50 \text{ [kPa]} \end{aligned} \tag{4.24}$$

The problem was discretized using direct multiple shooting method. The problem was discretized into 10 segments and the transfer function was identified for each segment in the trajectory every iteration. At each iteration, the maximum tracking error e_{max} was calculated through nonlinear simulation using Eqs.(4.15).

4.3 Linear Robust Controller Design

The linear robust controller is evaluated for stability, performance, and robustness for flight condition changes as well as to the identified trajectories. The linear time invariant (LTI) model is obtained by linearizing the Eqs.(4.14) at different trim conditions in a reference trajectory. In order produce a reference trajectory, a optimal trajectory obtained through the separated method which does not consider tracking error e as nonlinear inequality constraint was simulated. Therefore, the problem formulation for the nonlinear optimal control problem is the same as Eq.(4.20) except e is not considered. The analysis was conducted for Phase 4 descent where flight Mach number changes occur rapidly in the descent trajectory (i.e. from hypersonic speed of Mach 5 to subsonic speed of Mach 0.3). The reference trajectory obtained through nonlinear optimization is shown in Fig.4.11 and Fig.4.12.

The reference trajectory from Fig.4.11 and Fig.4.12 considers only the longitudinal dynamics since control laws are typically designed for longitudinal and lateral-directional dynamics, as these dynamics are decoupled under most flight conditions [29]. This has also been the case for a Generic Hypersonic Vehicle presented in [78]. Furthermore, in this study only the flight path angle will be tracked for simplicity. Linearizing Eqs.(4.14) was conducted by first considering the steady-state flight condition at each Mach number (Mach 5 to Mach 0.8). The steady-state flight condition are summarized in Table B.1. Perturbation is considered relative to steady-state flight with small angle assumptions to trigonometric functions of perturbed angles ($\sin\Delta\theta = \Delta\theta$ and $\cos\Delta\theta = 1$).

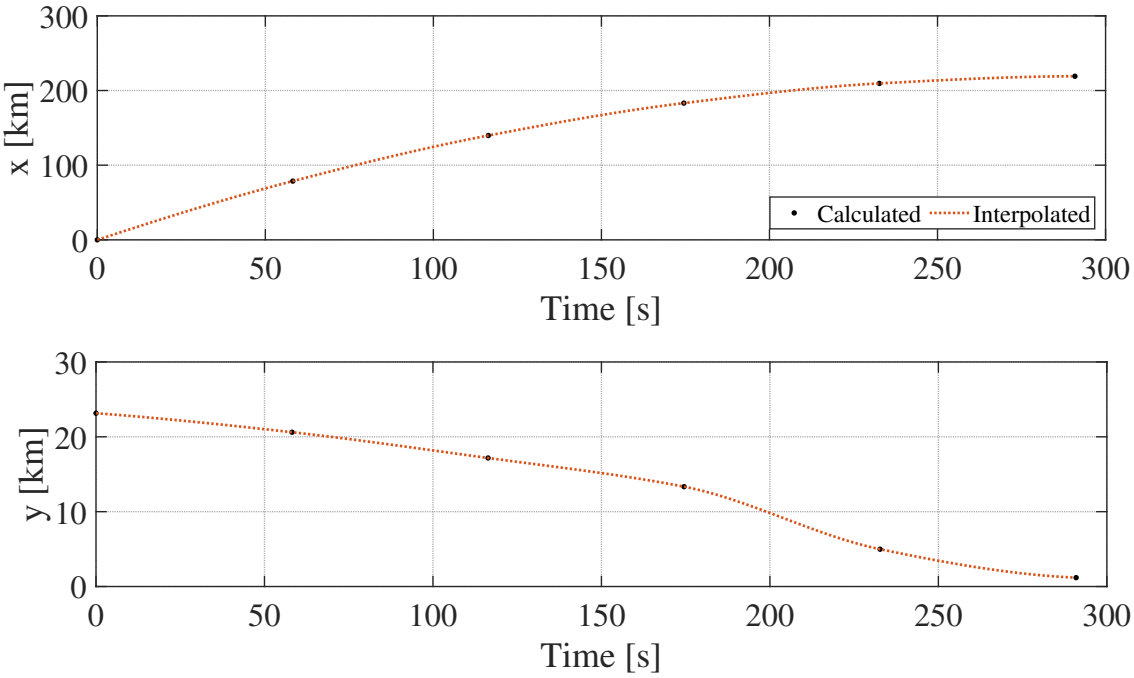

Fig. 4.11 Time History of Downrange and Altitude in the Reference Trajectory.

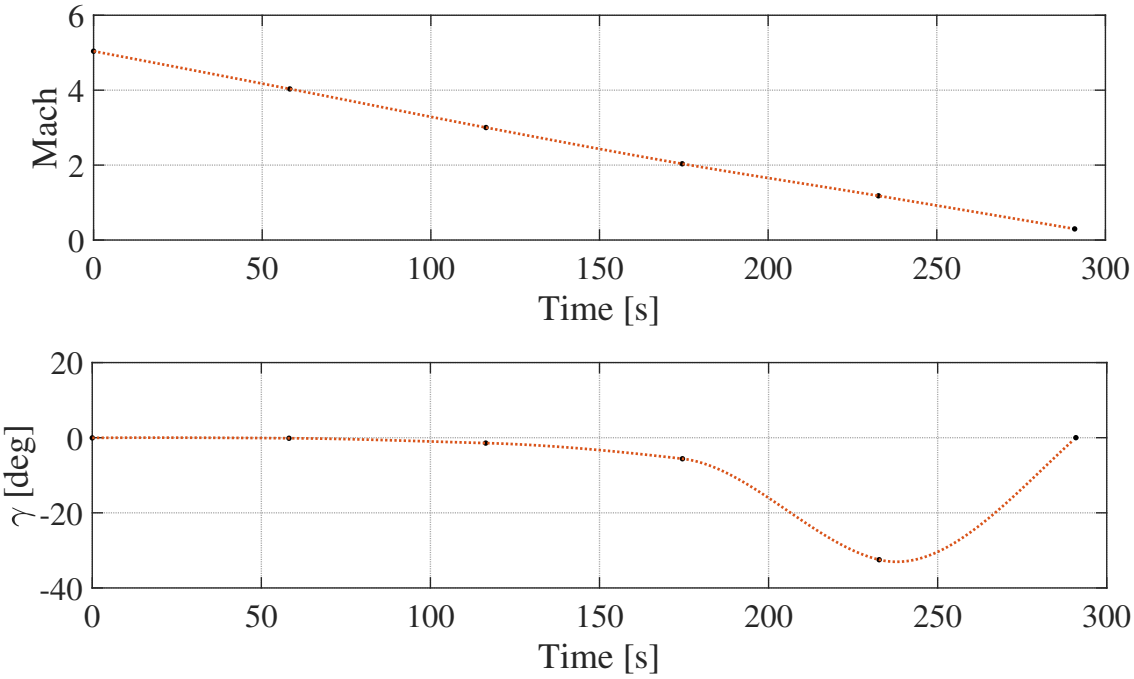

Fig. 4.12 Time History of Mach Number and γ in the Reference Trajectory.

Table 4.7 Descent Trajectory Linearized Point.

Mach	Altitude [km]	AoA [deg]	γ [deg]	Thrust [N]	δ_e [deg]
5	25	5	0	3100	1.4
4	21	4	0	2700	0.8
3	17	4	0	3990	0.7
2	13	3	0	3880	0.1
0.8	3	3	0	3450	-1.0

The state equations are linearized about the steady state condition and is written in the form of Eq.(B.1) where the new state variables are the following:

$$\begin{aligned} x &= [\Delta\alpha \;\; \Delta h \;\; \Delta\gamma \;\; \Delta q \;\; \Delta V]^T \\ y &= [\gamma] \\ u &= [\Delta\delta_e] \end{aligned} \tag{4.25}$$

The LTI models for Mach 5 to 2 are shown in Eq.(4.28) where (subscripts for matrix A and B denotes the linearized Mach number).

$$A_5 = \begin{bmatrix} -0.5197 & 3.897\times10^{-6} & 0 & 1 & -4.111\times10^{-6} \\ 0 & 0 & 1500 & 0 & 0 \\ 0.5197 & -3.897\times10^{-6} & 0 & 0 & 4.111\times10^{-6} \\ -69.03 & 3.933\times10^{-4} & 0 & -9.146 & 5.024\times10^{-5} \\ -106.4 & 9.788\times10^{-4} & -9.800 & 0 & -4.585\times10^{-3} \end{bmatrix} \tag{4.26}$$

$$A_4 = \begin{bmatrix} -0.5513 & 3.458\times10^{-6} & 0 & 1 & -7.339\times10^{-5} \\ 0 & 0 & 1200 & 0 & 0 \\ 0.5513 & -3.458\times10^{-6} & 0 & 0 & 7.339\times10^{-5} \\ -58.57 & 2.055\times10^{-4} & 0 & -9.701 & 7.835\times10^{-4} \\ -74.95 & 8.088\times10^{-4} & -9.800 & 0 & -4.509\times10^{-3} \end{bmatrix} \tag{4.27}$$

$$A_3 = \begin{bmatrix} -0.7286 & 5.714\times10^{-6} & 0 & 1 & -3.013\times10^{-5} \\ 0 & 0 & 900 & 0 & 0 \\ 0.7286 & -5.714\times10^{-6} & 0 & 0 & 3.013\times10^{-5} \\ -57.91 & 3.298\times10^{-4} & 0 & -12.789 & -1.907\times10^{-3} \\ -83.98 & 1.066\times10^{-3} & -9.800 & 0 & -1.907\times10^{-3} \end{bmatrix} \tag{4.28}$$

$$A_2 = \begin{bmatrix} -0.8554 & 5.665\times10^{-6} & 0 & 1 & -6.232\times10^{-6} \\ 0 & 0 & 600 & 0 & 0 \\ 0.8554 & -5.665\times10^{-6} & 0 & 0 & 6.232\times10^{-5} \\ -45.24 & 1.596\times10^{-4} & 0 & -14.99 & -1.203\times10^{-3} \\ -53.96 & 9.246\times10^{-4} & -9.800 & 0 & -1.554\times10^{-2} \end{bmatrix} \tag{4.29}$$

$$A_{0.8} = \begin{bmatrix} -1.406 & 1.139\times10^{-5} & 0 & 1 & -4.529\times10^{-6} \\ 0 & 0 & 240 & 0 & 0 \\ 1.406 & -1.139\times10^{-5} & 0 & 0 & 4.529\times10^{-5} \\ -29.65 & 8.571\times10^{-5} & 0 & -24.55 & -3.293\times10^{-3} \\ -40.46 & 8.611\times10^{-4} & -9.800 & 0 & -4.536\times10^{-3} \end{bmatrix} \tag{4.30}$$

$$B_5 = \begin{bmatrix} -0.1116 \\ 0 \\ 0.1116 \\ -98.58 \\ -9.674 \end{bmatrix}, \quad B_4 = \begin{bmatrix} -0.1183 \\ 0 \\ 0.1183 \\ -83.64 \\ -7.285 \end{bmatrix}, \quad B_3 = \begin{bmatrix} -0.1560 \\ 0 \\ 0.1560 \\ -82.70 \\ -9.196 \end{bmatrix} \tag{4.31}$$

$$B_2 = \begin{bmatrix} -0.1828 \\ 0 \\ 0.1828 \\ -64.61 \\ -6.510 \end{bmatrix}, \quad B_{0.8} = \begin{bmatrix} -0.2995 \\ 0 \\ 0.2995 \\ -42.34 \\ -5.587 \end{bmatrix} \tag{4.32}$$

$$C = \begin{bmatrix} 0 & 0 & 1 & 0 & 0 \end{bmatrix} \tag{4.33}$$

The maximum error to be placed as the nonlinear inequality constraint was evaluated by the step response of the transfer functions from r to e obtained from Eq.(4.26) to (4.33) as shown in Fig.4.13. The controller gains were obtained through robust controller design using the same structure as Fig.3.2 where $K_p = -2.5$ and $K_i = -1.9$ respectively with elevon area assumed to be 0.05.

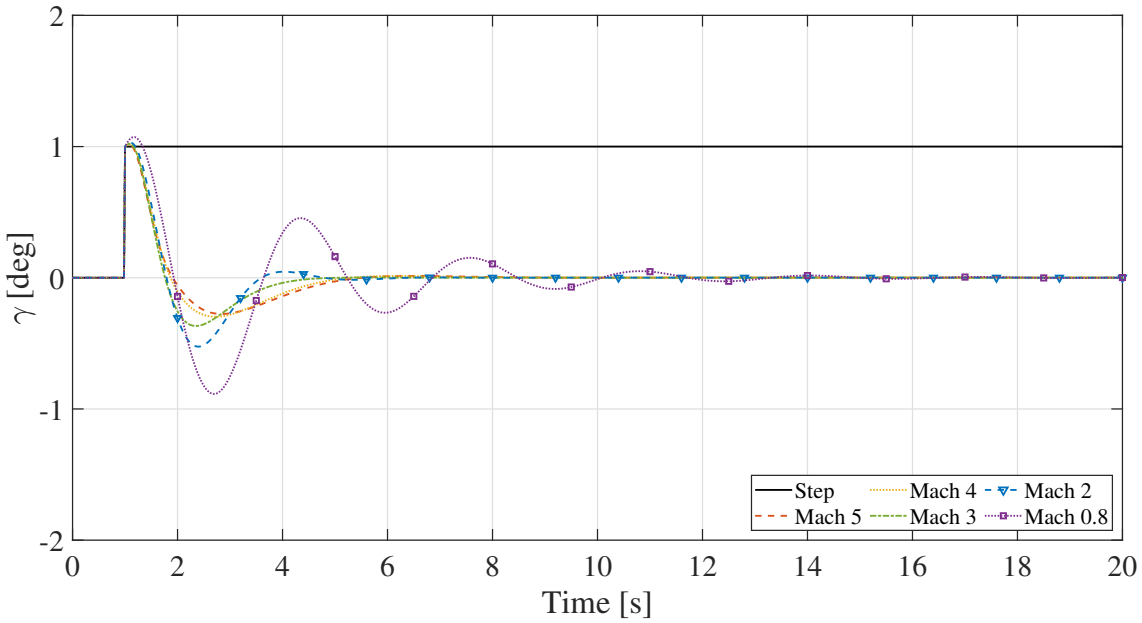

Fig. 4.13 Step Response of transfer functions from r to e for Hypersonic Aircraft Problem.

From Fig.4.13, it can be seen that maximum undershoot was around 0.9[deg] for Mach 0.8 followed by 0.5[deg] for Mach 2. For this analysis, maximum error is presumably to occur during pitch-up in Phase 2. The Mach number decreasing to subsonic from Mach 5 was unlikely and therefore maximum undershoot for Mach 2 at 0.5[deg] was selected. With the assumption of the flight path angle during suborbital flight being close to -40[deg], the maximum error to be placed as the nonlinear inequality constraint was fixed at ± 20[deg] ($\pm 40 \times 0.5$). From here, the gain where the maximum error occurs can be calculated $20\log(e/r) = 20\log(20/40) = -14$[dB]. Therefore, the weighting functions were tuned to have a average close to -14[dB] in the low frequencies below 10^0 and gradually weaken the tracking performance in the high frequencies above 10^0 since high frequencies are sensitive to noise. The weighting functions W_e and W_u used for analysis are shown in Eq. (4.34) and

(4.35). Using the same W_e and W_u, the performance of the designed controller is evaluated in Section 5.3.

$$W_e = \frac{1000s^2 + 6000s + 3}{6000s^2 + 375s + 3.75} \tag{4.34}$$

$$W_u = \frac{25s + 1}{50s + 200} \tag{4.35}$$

4.4 Simultaneous Design Results

The linear robust controller is evaluated for stability, performance, and robustness for flight condition changes as well as to the identified trajectories as explained in section 3.1.2. The nonlinear trajectory is evaluated for the objective function value, maximum tracking error e_{max}, and the optimized elevon sizing. The results for the controller design are shown in Fig. 4.14 to 4.22 and trajectory results are shown in Fig.4.23 to 4.32. Table 4.8 summarizes the critical factors from the results.

For the linear robust controller design evaluation, by using the simultaneous method the H_∞ norm of T_{zw} was 0.94 which ensures stability and performance. This is also verified by the poles and gain plot for the transfer functions from r to e denoted as T_{r2e} and transfer functions from r to y denoted as T_{r2y} (transfer functions defined in Section 2.4.2). From Fig.4.14, it can be seen that all poles for T_{r2e} are non-positive thus the system has stability. From Fig.4.15, it can be seen that the gain plot of T_{r2e} are below the weighting function $1/W_e$ ensuring performance and from Fig.4.16, the gain plot of T_{r2y} are below the weighting function $1/W_u$ meeting the design requirements. Fig.4.17 represents the step response of each linearized Mach number. As can be seen from Fig.4.17, each linearized LTI model shows stable response ensuring robustness for flight condition changes to linearized Mach number. Fig.4.18 to 4.22 represents the step response of the identified trajectory transfer function SITF derived from each segment in the optimized trajectory. Symbol γ_i represents the γ in the trajectory at each discretized ith segment and $\gamma_{i_{max}}$ represents the maximum value in the ith segment. Symbol $\gamma_i/\gamma_{i_{max}}$ represents the normalized velocity at each discretized segment and was used as reference step input. γ greater than 0.1 [deg] was incorporated into the robust controller design since small γ will be similar to a steady state flight. Therefore, each identified transfer function from γ_1 to γ_{15} represents a segment in the optimal trajectory. As can be seen from Fig.4.18 to 4.22, each identified transfer function has high tracking performance and has a stable response for the linear models of Mach 5 to Mach 0.8 ensuring robustness for trajectory. This is due to the proposed method implementing each γ in the discretized segment is into the H_∞ controller design.

For the nonlinear trajectory design, optimal sizing of the elevon, objective function value, and the maximum tracking error constraint will be evaluated. From the obtained trajectory shown in Table.4.8, it can be seen the sizing of the elevon A was 0.048 which showed decrease from the initial guess of 0.05. This was due to the tracking error nonlinear inequality constraint where tracking error increased during pitch up maneuver near the start of Phase 3 shown in Fig.4.24. Since dynamic pressure was close to 0 upon separation at $t = 0$ in Fig.4.26, any error accumulated during the time until pitch up could not be minimized resulting in a trajectory where sudden peak in dynamic pressure occurred as altitude decreased depicted in Fig.4.23. This resulted in the sizing of the elevon to decrease since the trajectory did not need an increase in C_m to increase tracking control but decreased to keep the control from overshooting. Adding to this, the optimization process was to increase flight duration so in order to minimize C_D, the size of the elevon were reduced where C_D increase steadily during Phase 4 descent seen in Fig.4.27. The trajectory cruises at 23[km] at the start of the descent to gradually decrease velocity so as not to violate the dynamic pressure constraint since the dynamic pressure is around 50 [kPa] at $t_0^{(4)}$ shown in Fig.4.23 and Fig.4.26. Since the aircraft is gliding with no additional thrust as shown in Fig.4.30 where throttle and fuel are zero, the aircraft gradually increases α to maintain sufficient lift while keeping the drag at minimum seen in Fig.4.25. As a result, the trajectory overall has relatively high L/D for a hypersonic aircraft of around 4. From Fig.4.31, it can be seen that the suborbital flight starts at 224[s] and at 274[s] the aircraft performs a pitch up maneuver. Additionally, the static margin and pitch rate constraints were satisfied as can be seen from Fig.4.29. From the obtained tracking performance, hypersonic flight time resulted in 101[s] and 292[s] for descent time covering 152[km] and 163[km] in downrange respectively. With the Phase 4 flight time, the downrange capable of being covered for the return flight back was 163[km] of the 732[km] total downrange of the entire experiment. Finally, with the proposed method maximum tracking error resulted in 5.5[deg] as can be seen in Fig.4.32 well below the tolerable maximum tracking error meeting the design requirement.

With the proposed method, a control-oriented optimal trajectory satisfying the maximum tracking error constraint of 20[deg] was achieved with the maximum tracking error being 5.5[deg]. Additional optimal sizing of the elevon decreased from initial 0.05 to 0.048 in order to increase performance during pitch-up as well as to reduce drag. Furthermore, robustness for flight condition changes to Mach number as well as to the trajectory was successfully obtained and validated through pole placement, frequency response, and step response. For the Hypersonic Experimental Aircraft problem, it was identified that a total of 101[s] of hypersonic engine test was possible as well as the flight capability of flying 163[km] back to the airstrip during descent.

Table 4.8 Comparison of Results between Integrated and Separated Methods.

Phase 3 Flight Time $[s]$	Phase 4 Flight Time $[s]$	Elevon Sizing $[\%]$	kp	ki	e_{max} [deg]	H_∞ Norm	Phase 4 Downrange [km]
101	292	0.048	-3.05	-1.44	5.51	0.94	163

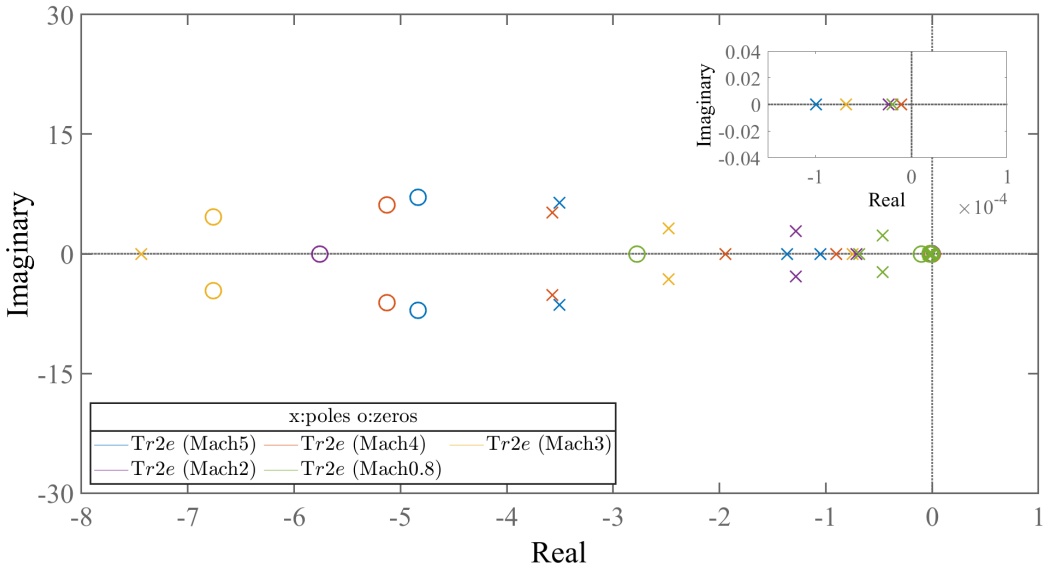

Fig. 4.14 Pole/Zero Map for Hypersonic Aircraft Problem.

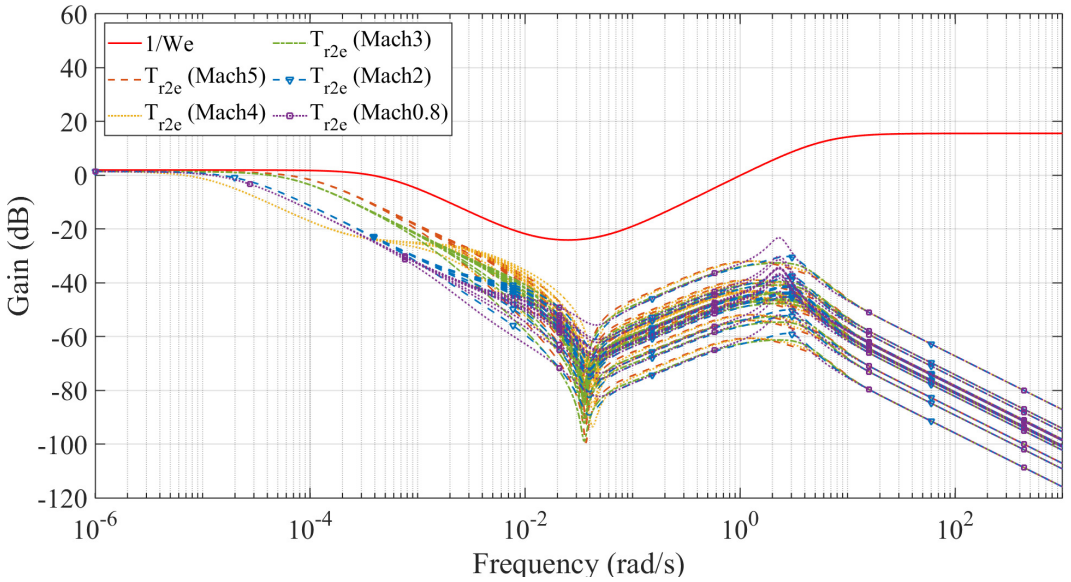

Fig. 4.15 Gain Plot of T_{r2e} for Hypersonic Aircraft Problem.

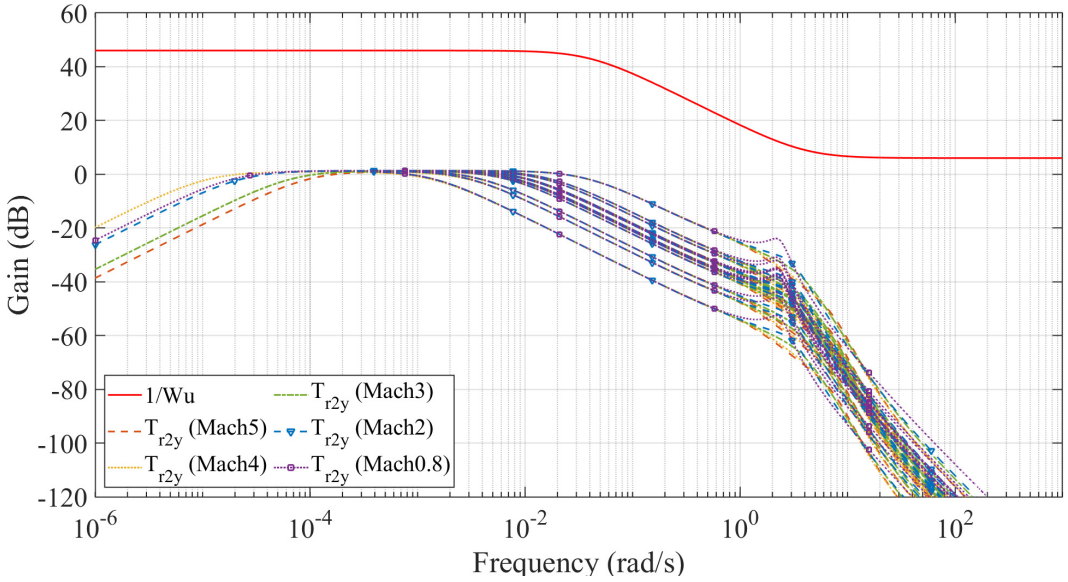

Fig. 4.16 Gain Plot of T_{r2y} for Hypersonic Aircraft Problem.

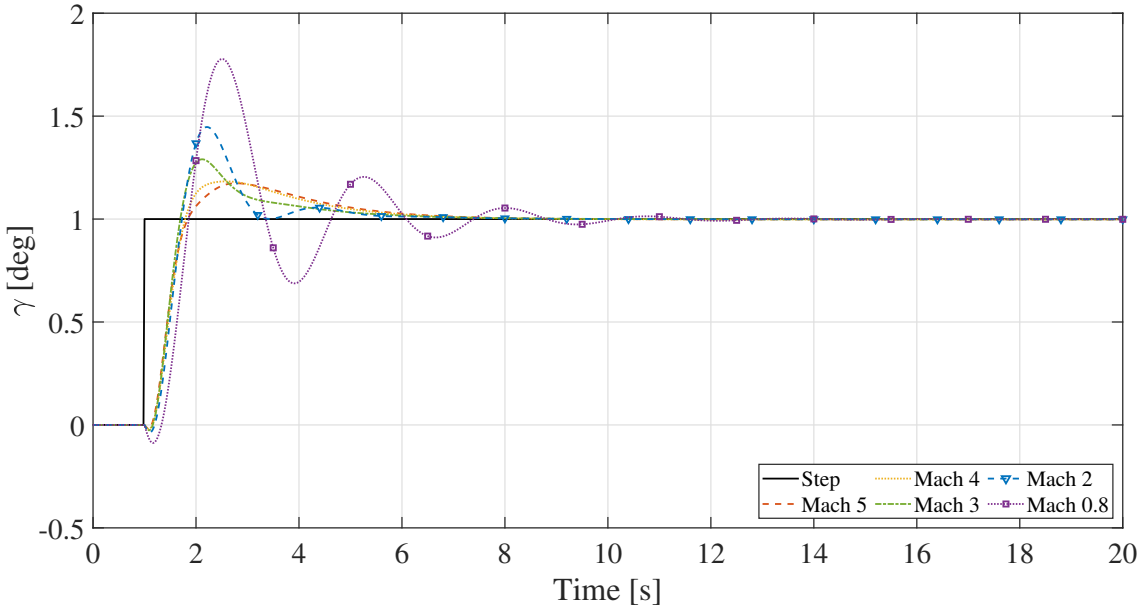

Fig. 4.17 Step Response for Hypersonic Aircraft Problem.

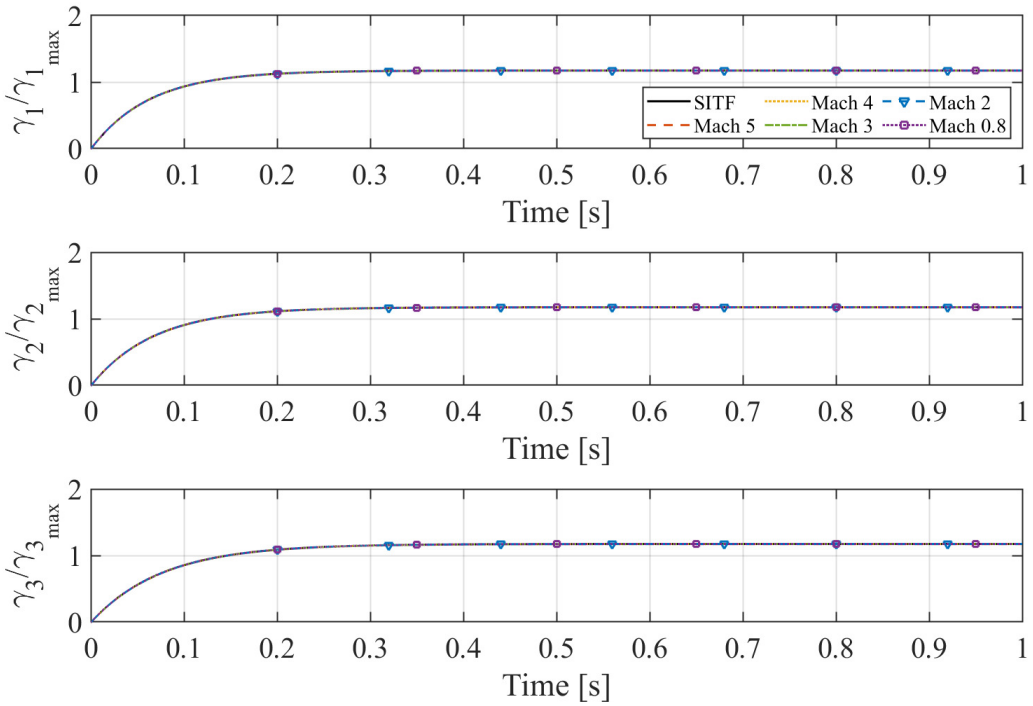

Fig. 4.18 Response to SITF Inputs Against Mach Variance for Hypersonic Aircraft Problem (Segment 1,2,3).

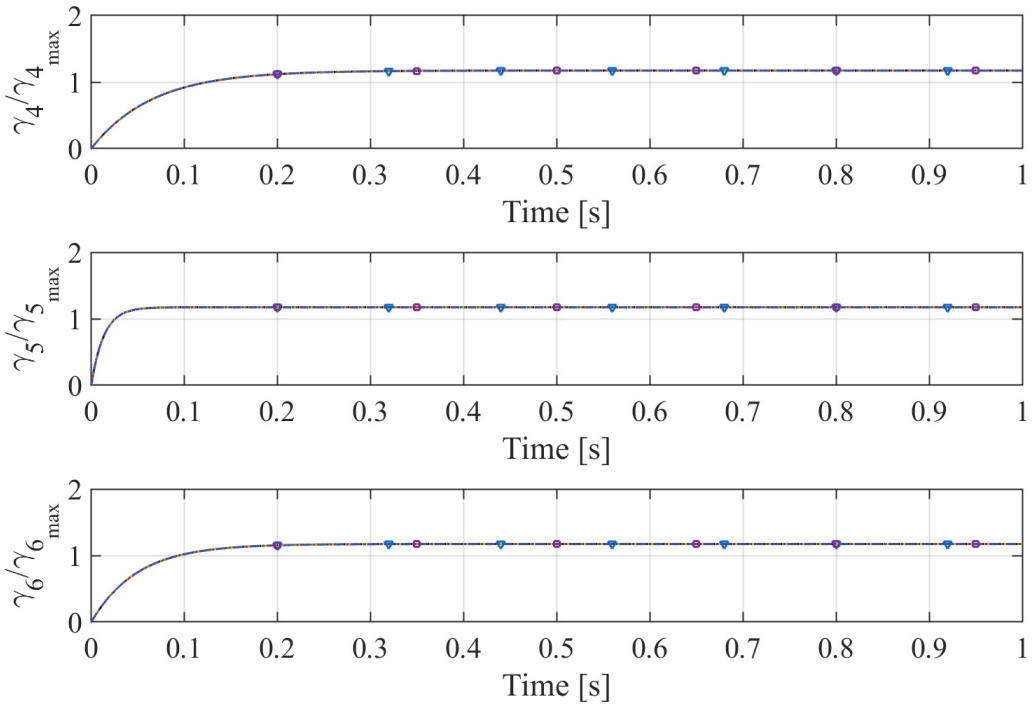

Fig. 4.19 Response to SITF Inputs Against Mach Variance for Hypersonic Aircraft Problem (Segment 4,5,6).

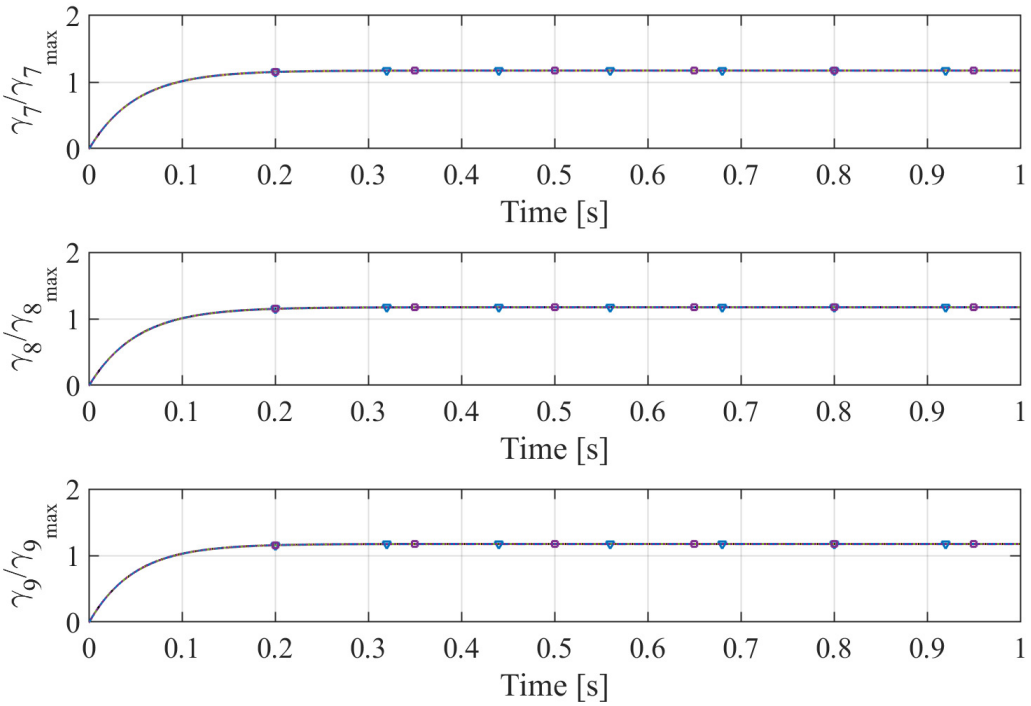

Fig. 4.20 Response to SITF Inputs Against Mach Variance for Hypersonic Aircraft Problem (Segment 7,8,9).

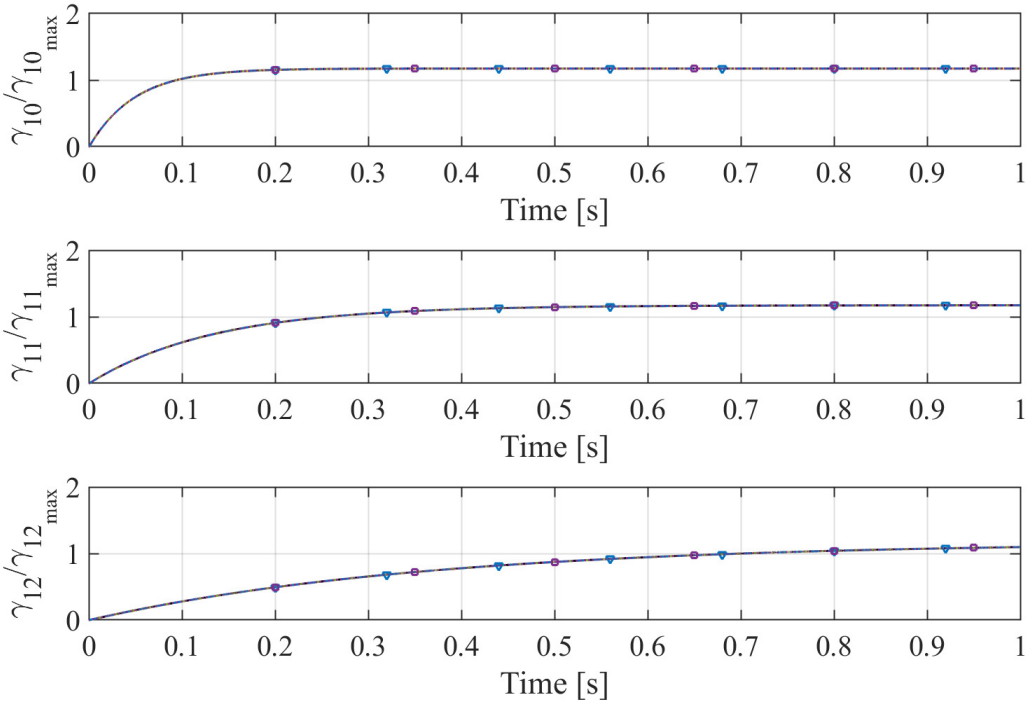

Fig. 4.21 Response to SITF Inputs Against Mach Variance for Hypersonic Aircraft Problem (Segment 10,11,12).

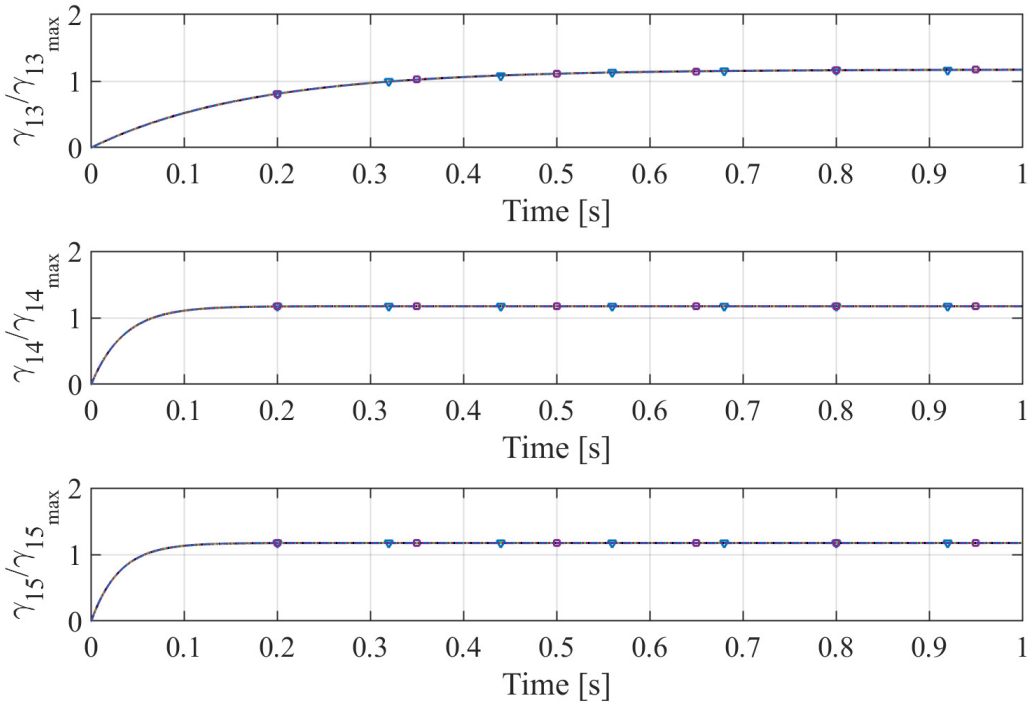

Fig. 4.22 Response to SITF Inputs Against Mach Variance for Hypersonic Aircraft Problem (Segment 13,14,15).

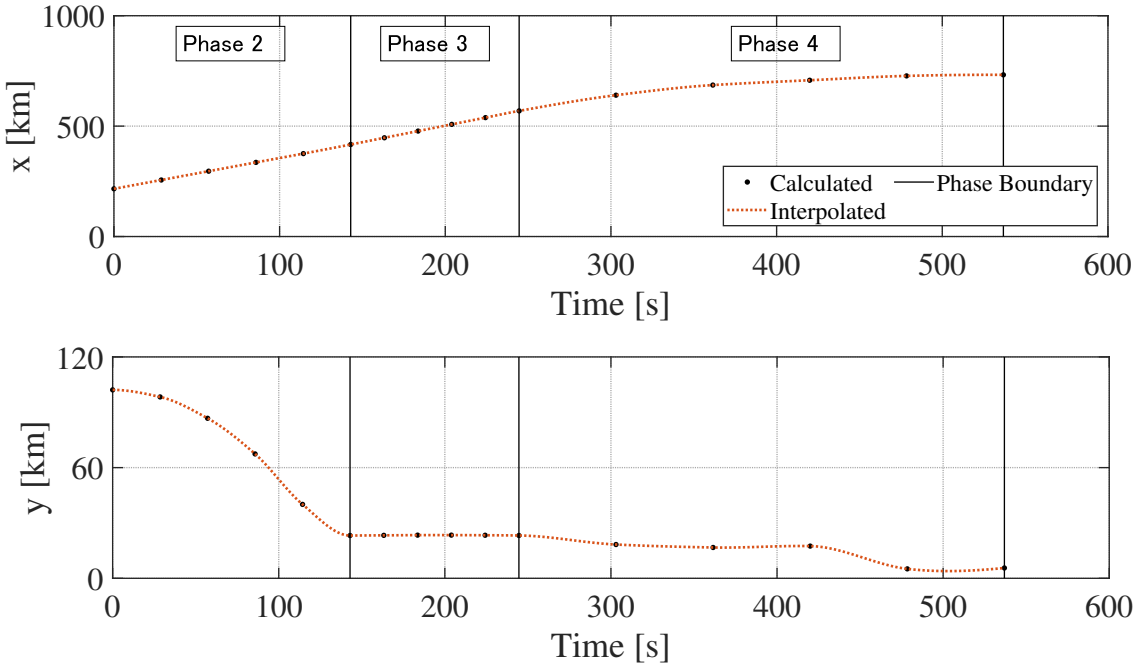

Fig. 4.23 Time History of Downrange and Altitude in the Optimal Trajectory.

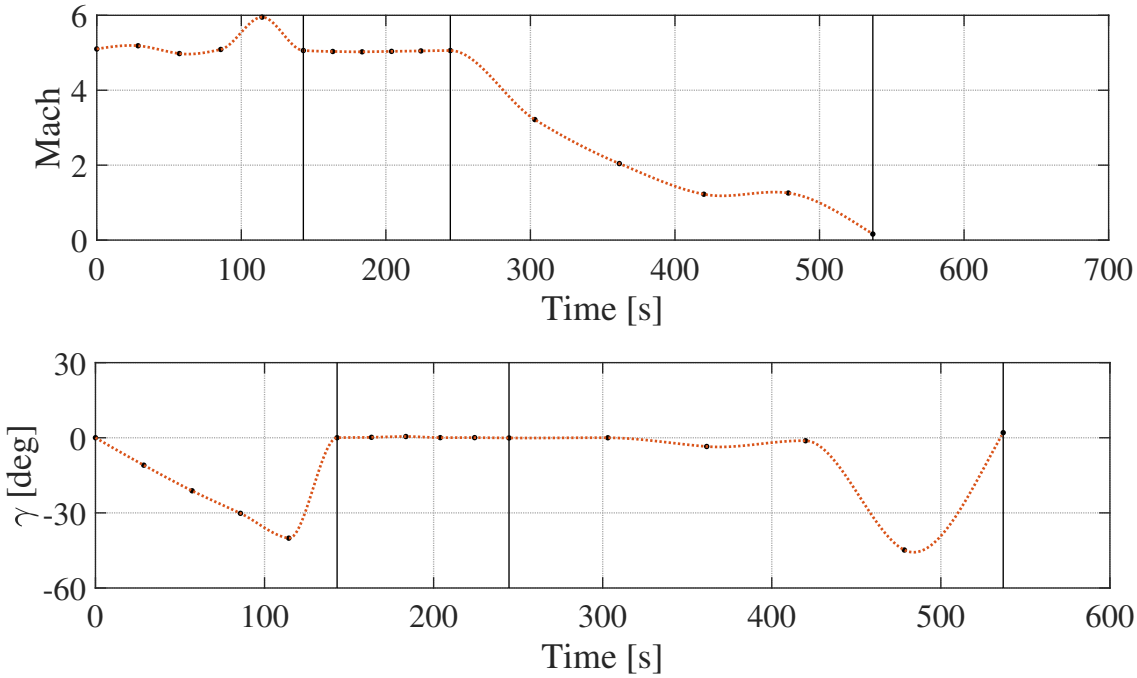

Fig. 4.24 Time History of Mach Number and γ in the Optimal Trajectory.

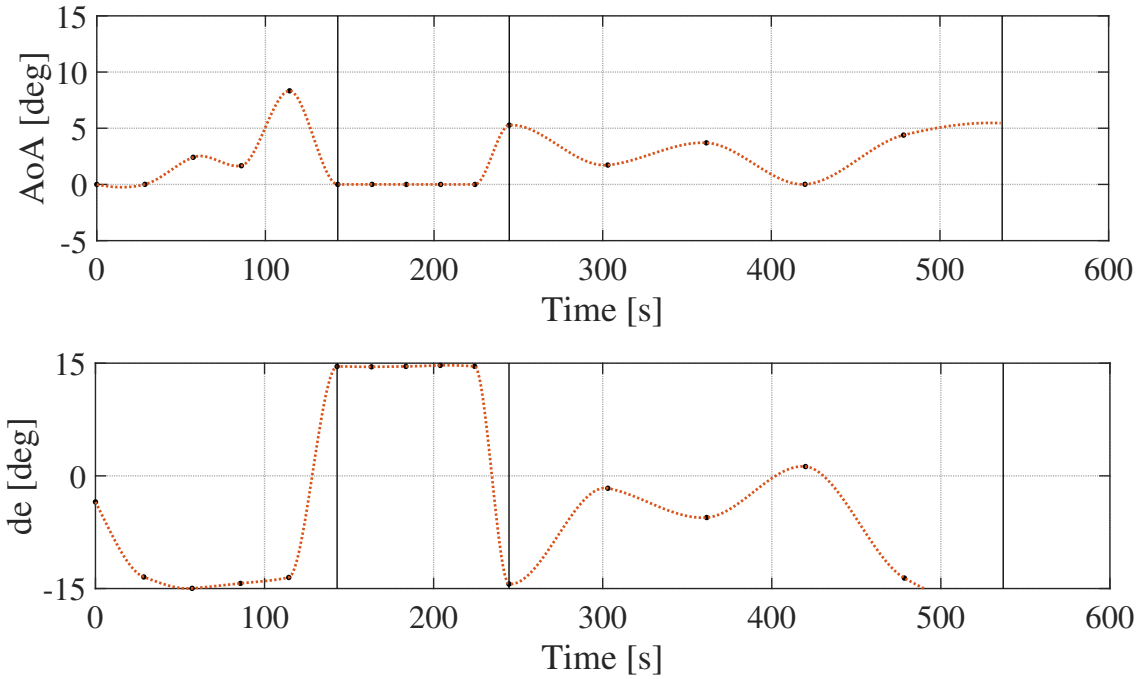

Fig. 4.25 Time History of Angle of Attack and δ_e in the Optimal Trajectory.

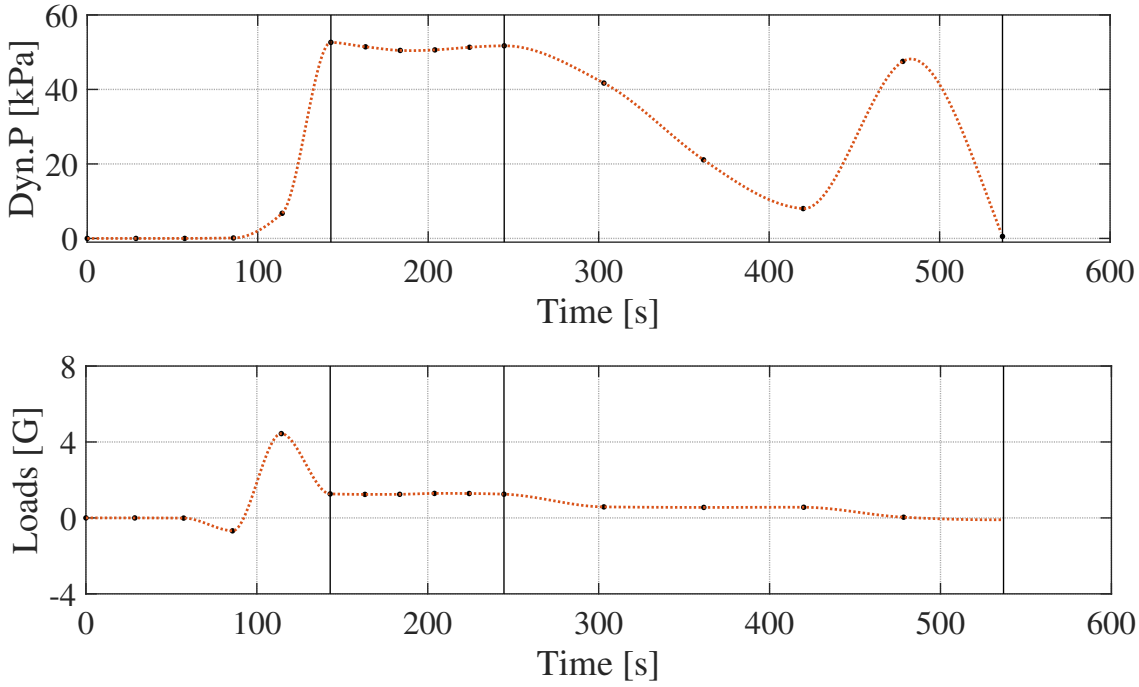

Fig. 4.26 Time History of Dynamic Pressure and Load in the Optimal Trajectory.

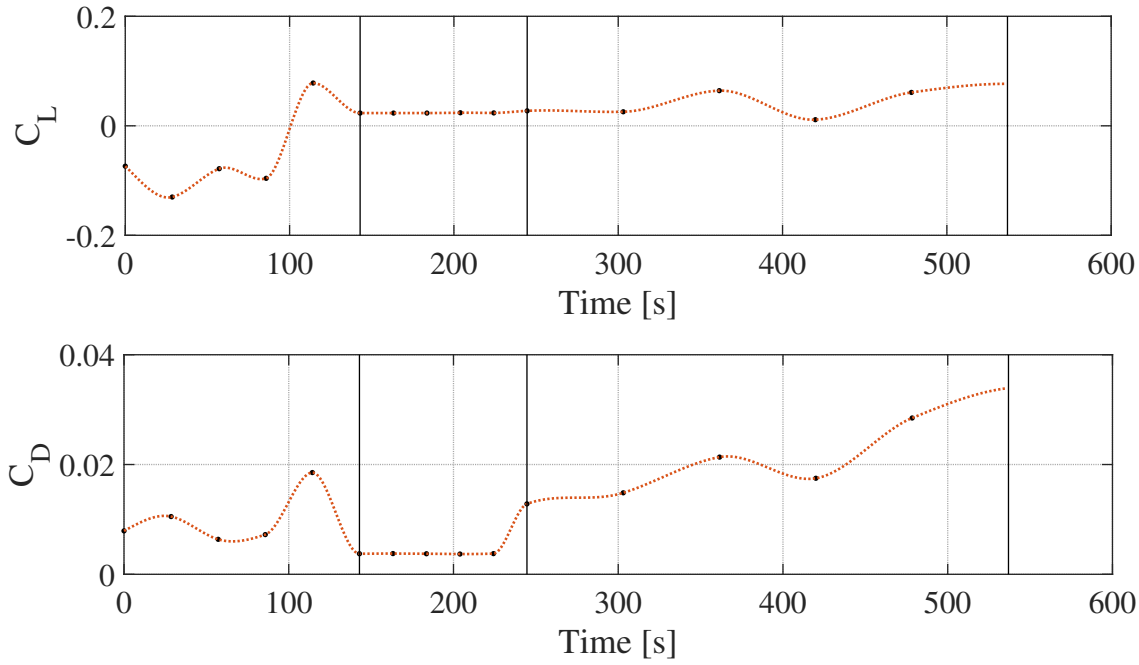

Fig. 4.27 Time History of C_L and C_D in the Optimal Trajectory.

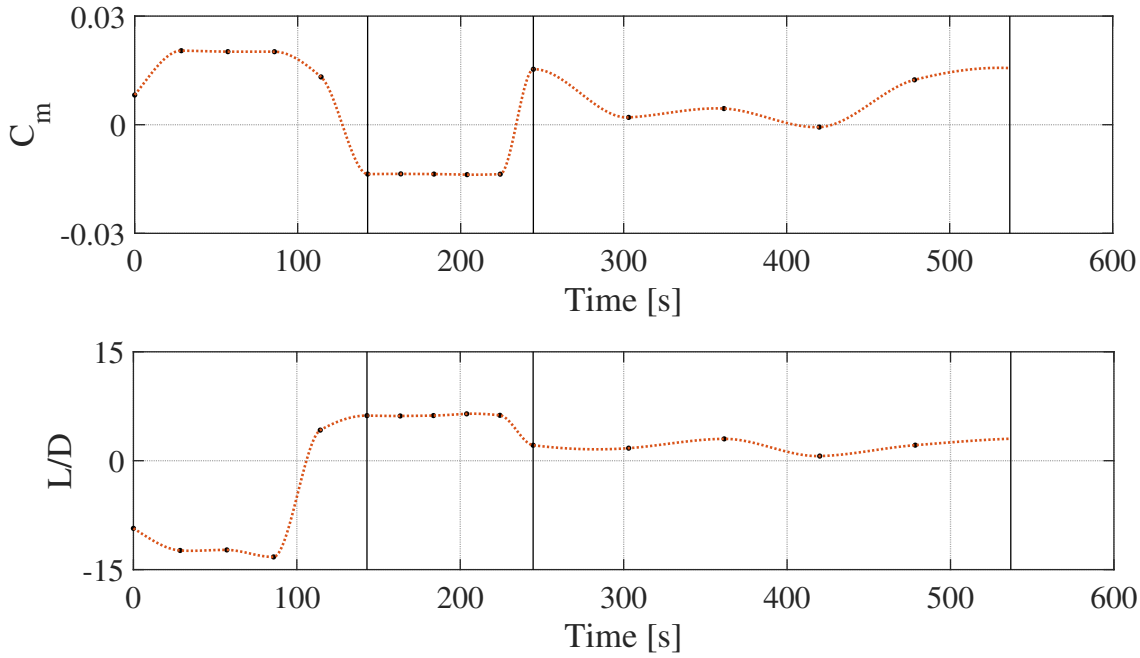

Fig. 4.28 Time History of C_m and L/D in the Optimal Trajectory.

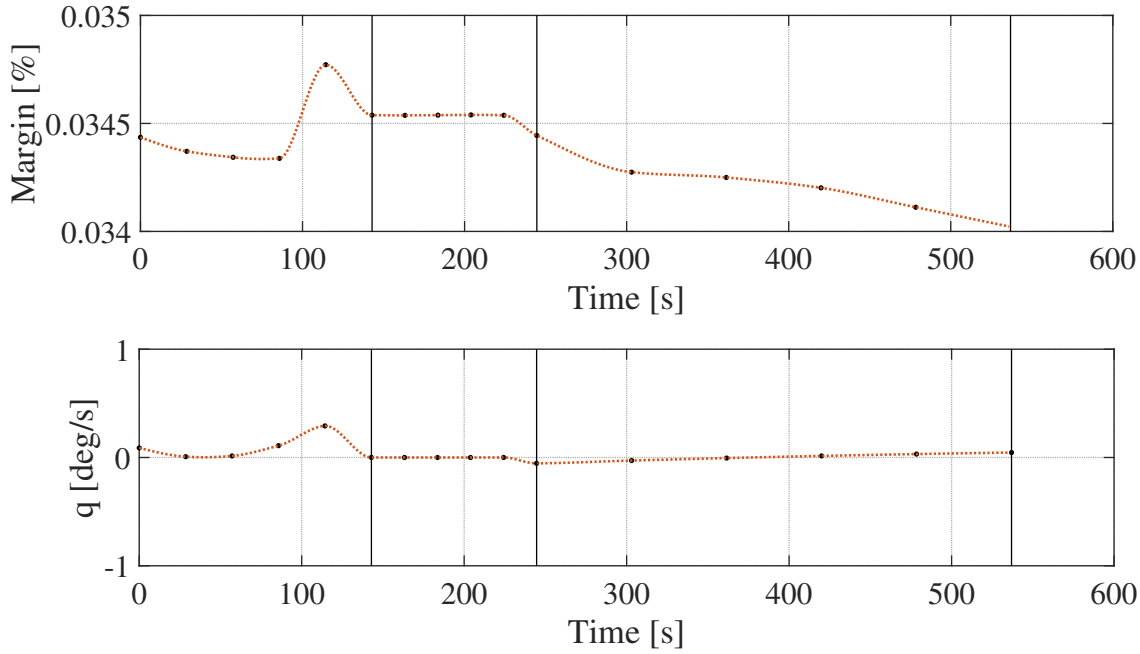

Fig. 4.29 Time History of Static Margin and Pitch Rate in the Optimal Trajectory.

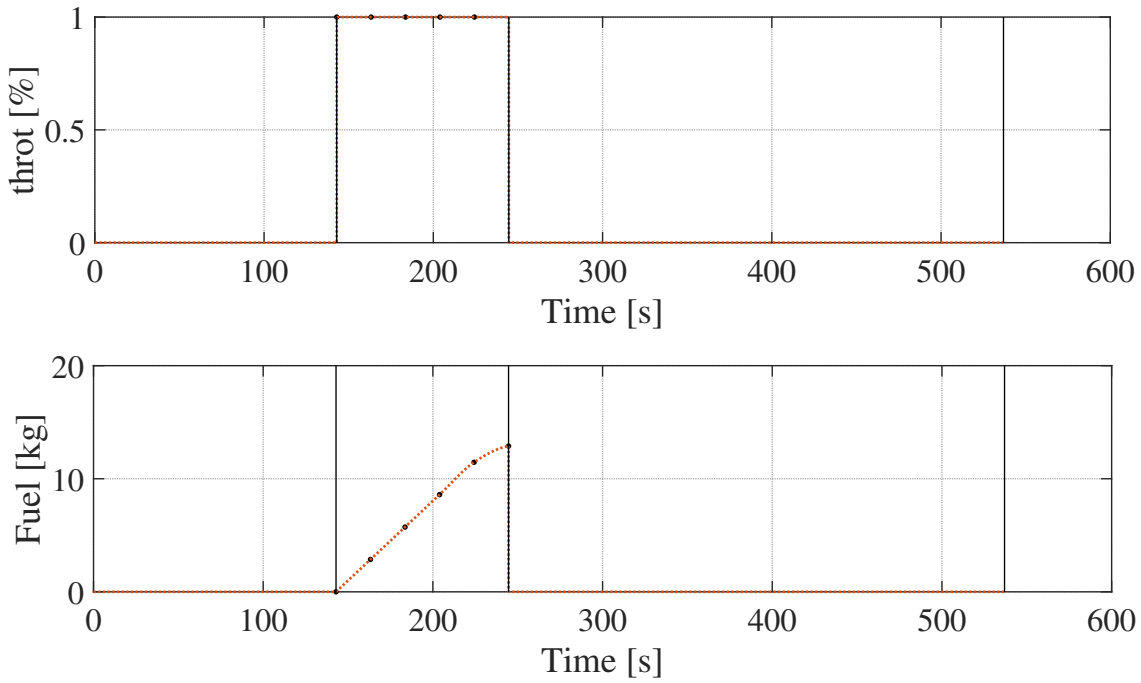

Fig. 4.30 Time History of Throttle and Fuel Consumption in the Optimal Trajectory.

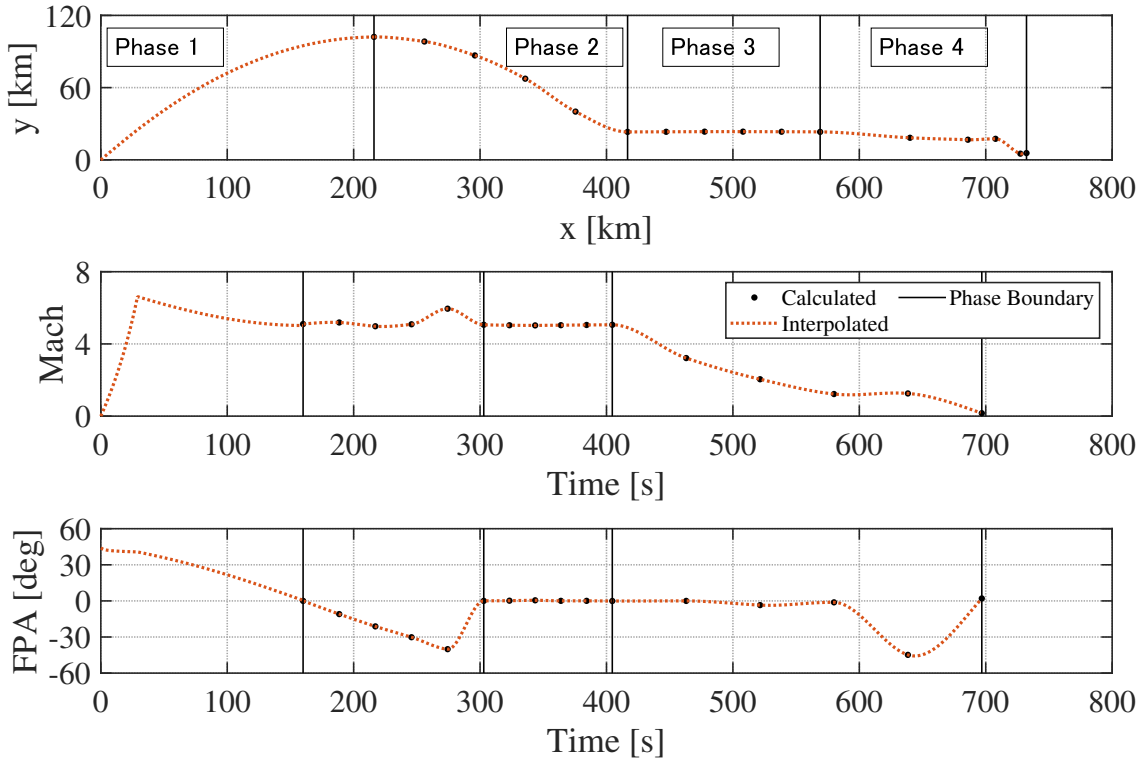

Fig. 4.31 All Phases in the Optimal Trajectory.

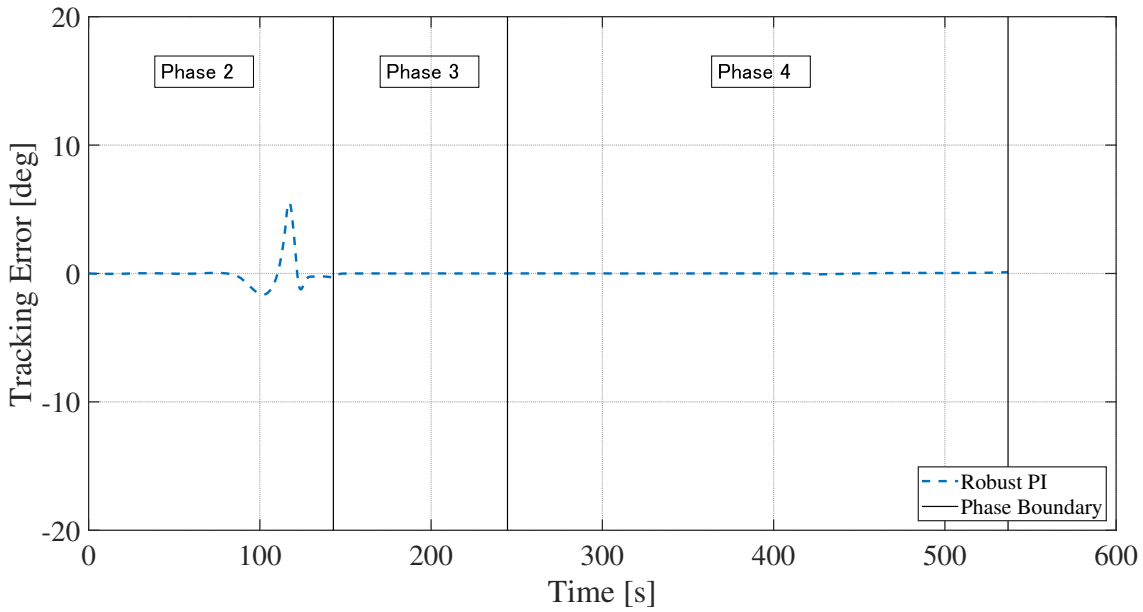

Fig. 4.32 Tracking Error Time History for Tracking Reference γ.

4.5 Conclusion of Chapter 4

The novel method of simultaneous design of trajectory and robust controller was successfully applied to the Hypersonic Experimental Aircraft problem in terms of the controller having stability, performance, and robustness for flight condition changes as well as to the trajectory. Furthermore, a control-oriented trajectory and optimal sizing of the elevon were obtained satisfying the flight constraints while maximizing flight duration for performing hypersonic engine test and descent flight. From the analysis, a possible Mach 5 engine test duration as well as return to airstrip downrange capability limit were identified.

Chapter 5

Monte Carlo Simulation of Hypersonic Experimental Aircraft Problem

In this chapter, in order to complete the second objective a Monte Carlo simulation is conducted to evaluate the trajectory and robust controller obtained in the previous chapter for robustness against state uncertainties present during separation from the rocket booster. The system is evaluated focused primarily on the tracking performance of maintaining the maximum tracking error under the specified value (i.e from Section 4.3) in the dispersed trajectory. The system is also evaluated on the mission success rate along with statistics of achieving each mission requirement. With the acquired data, mission success rate is identified along with valuable insights to increase control performance is discussed.

5.1 Monte Carlo Simulation

In order to test the robustness of the obtained control-oriented trajectory and robust controller against state uncertainties during separation of the rocket and aircraft, performing a Monte Carlo simulation is one possible method. Monte Carlo simulation is frequently used for launch vehicles during stage separation or during a phase [31, 50, 41, 9, 44, 71, 59]. This is due to the stage separation having many uncertainties such as aerodynamic forces, direction and attitude of the vehicle, sensor errors, and etc. Monte Carlo simulation applied to trajectory analysis is a method of generating a variance of trajectories via random selection of uncertainties. It can be used whenever the states or dynamics are not completely deterministic as well as when the outcome is too complicated to model [31].

5.2 Mission Requirements and Uncertainty Model

The evaluated mission requirements is taken from Table 4.1 in Section 4.1 and is summarized in Table 5.1. The primary focus of the Monte Carlo simulation is to verify the mission success rate on maximum tracking error e since the robust controller was designed where only robustness against flight condition changes and to the optimal trajectory were considered. With the primary focus on tracking performance, the hypersonic engine test conditions and cruising requirements were placed as well. The dynamic pressure requirement for the hypersonic engine test condition is relaxed since the system only takes the flight path angle as reference and velocity controller was omitted for simplicity. Therefore, it was assumed that velocity will decrease with the current controller thus resulting in dynamic pressure decrease. Also, regarding the dynamic pressure during the descent from hypersonic to subsonic, the dynamic pressure can exceed if sufficient deceleration is not attained. Therefore, a spoiler is presumed to be equipped on the aircraft creating 3 times the C_D value compared to C_D obtained through least square fit in Eq.4.12. Adding to the engine test condition, the Hypersonic Experimental Aircraft is designed for cruising. Therefore, cruising condition of flight path angle as well as altitude was placed along with the controller tracking performance preset in Section 4.3.

The uncertainties taken into account for the Monte Carlo simulation is summarized in Table 5.2 which was taken from previous supersonic experiment NEXST-1 of the same vehicle size and separating from NAL735 rocket booster [41]. Variance is assumed to be three times the standard variance σ and the nominal values were taken from the optimal trajectory obtained in the previous section. The uniform distribution law was chosen to reflect equal uncertainty occurrence inside the variance. A total of 200 simulation cases were performed where the number of simulation cases were referenced from guidance and control evaluation on supersonic experimental aircraft D-SEND#2 [44].

Table 5.1 Evaluated Hypersonic Experimental Aircraft Engine Test Conditions.

Mission Item	Evaluated Mission Requirements
Maximum Tracking Error e [deg]	$\lvert e\rvert \leq 20$
Cruise Mach Number $M^{(3)}$	$4.0 \leq M^{(3)}$
Dynamic Pressure $Q^{(3)}$ [kPa]	$40 \leq Q^{(3)} \leq 55$
Angle of Attack $\alpha^{(3)}$ [deg]	$0 \leq \alpha^{(3)} \leq 6$
Flight Path Angle $\gamma^{(3)}$ [deg]	$-0.5 \leq \gamma^{(3)} \leq 0.5$
Altitude $h^{(3)}$ [km]	$22 \leq h^{(3)}$

Table 5.2 Uncertainties at Separation from NAL735 Rocket Booster.

Parameter	Nominal	Variance ($\pm 3\sigma$)	Distribution Law
Altitude [km]	102	± 300	Uniform
Velocity [m/s]	1416	± 60	Uniform
Flight Path Angle [deg]	0	± 3	Uniform
Angle of Attack [deg]	0.35	± 3	Uniform

5.3 Results

The system is evaluated on the robust controller meeting the tolerable maximum tracking error being robust against disturbing factors on the states during separation as well as mission success rate statistics of achieving each mission requirement. Table 5.3 summarizes the results of the Monte Carlo simulation statistics on each mission requirements. Table 5.4 summarizes the results of the Monte Carlo simulation on mission requirements from Table 5.1. The trajectory results obtained from the dispersion is shown from Fig.5.1 to 5.8. Fig.5.9 depicts the tracking error history for all trajectory dispersion. Finally, Fig.5.10 to 5.12 shows the error distribution on each mission requirements.

From the Monte Carlo simulation results of tracking the optimal trajectory, the designed controller having robustness against disturbing factors on the states are evaluated. As can be seen from Table 5.3, the maximum tracking error for all cases had an average error of 8.7[deg] which meets the requirement of less than 20[deg]. The range in which the maximum tracking error fluctuated was maximum value of 19.1[deg] and minimum value of 4.8[deg] respectively. It can be seen that tracking error had standard deviation of 4.5[deg] which states the tracking performance varied depending on the trajectory dispersion as can be seen in Fig.5.9. The tracking error fluctuated mainly due to the aircraft pitching up or pitching down uncontrollably upon separation from the rocket booster depending on the uncertainty values. This can be seen in Fig.5.3 where there is an trend on the angle of attack pitching up to maximum of 35[deg] if the initial angle of attack upon separation was positive and the angle of attack pitching down up to minimum of -30[deg] if the initial angle of attack was negative respectively. This was due to the dynamic pressure being nearly zero since the altitude was at 100[km] where air density thin depicted in Fig.5.4. With the dynamic pressure being zero, even with the aircraft having C_L, C_D, and C_m values shown in Fig.5.5 and Fig.5.6, no lift, drag, or pitching moment were produced as can be seen in Fig.5.7. This resulted in the aircraft pitching up or down uncontrollably until sufficient dynamic pressure was available for the elevon to have any effect. Due to this, if the angle of attack increased or decreased close to 35[deg] or -30[deg] upon separation from the rocket booster, a spike

in lift and drag occurred at $t = 120$[s] during pitch up at around 23[km] which caused the tracking performance of the flight path angle controller to fluctuate during pitch up from $\gamma = -30$[deg] which can be seen in Fig. 5.2. The fluctuation causes the velocity to decrease and thus decreases the dynamic pressure. Furthermore, the decrease in dynamic pressure contributed to a overshoot for tracking γ and caused a spike in load with maximum of around 16[G] depicted in Fig.5.4 which exceeds the assumed 10[G] structural limit. Therefore, to reduce fluctuation in dynamic pressure as well as loading is to introduce thrusters for pitch control during suborbital flight where there is no dynamic pressure. Expansion of a thruster controller to the current control system is possible with the proposed method. Due to the decrease in dynamic pressure, minor fluctuation in downrange and altitude was present as can be seen in Fig.5.1. Nevertheless, robustness against uncertainties at separation from the NAL735 rocket booster was obtained since the designed robust controller met the tracking performance requirement of ± 20[deg] for all cases.

Additionally, the designed controller meeting the mission requirement for achieving engine test condition is evaluated. From Table 5.3, it can be seen that cruise mach number, angle of attack, and altitude mission requirements are met for all 200 cases. Error distribution of the three can be found on Fig.5.10 to 5.11. Notable aspect of the three are that the cruising altitude had a variance from 22.3[km] to 26.6[km]. This was due to the tracking error caused by the angle of attack deviation as explained in the previous paragraph. From Table 5.3, it can be seen that the dynamic pressure has a 71.5[%] success rate. The dynamic pressure decreases due to the flight dispersion of the flight path angle as previously stated. Nevertheless, as can be seen from Fig.5.10, dynamic pressure ranged from 40[kPa] to 50[kPa] thus the mission requirements were identified for having a 71.5[%] success rate.

From the results obtained, robustness against state uncertainties present during separation was obtained with a 71.5[%] mission success rate for conducting hypersonic engine test with the Hypersonic Experimental Aircraft. Additionally, a valuable insight to incorporate thrusters to have control of pitch during suborbital flight was obtained which can be achieved through the expansion of the proposed method utilizing the structured H_∞ controller design method.

Table 5.3 Monte Carlo Simulation Statistics on Engine Test Conditions.

Statistics	Cruise Mach	Dynamic Pressure [kPa]	AoA [deg]	γ [deg]	Altitude [km]	Maximum Error [deg]
Maximum	5.02	52.4	3.12	0.518	26.6	19.1
Minimum	4.27	29.5	2.38	0.497	22.3	4.79
Average of Maximum μ	4.71	42.5	2.70	0.499	24.2	8.70
Std. Dev. of Maximum σ	0.194	6.19	0.199	0.0566	1.20	4.53
Individual Success Rate [%]	100	71.5	100	93.5	100	100

Table 5.4 Monte Carlo Simulation Results on Mission Success Rate.

Category	Cases	Probability P [%]
Mission Success	143	71.5
Mission Failure : Dynamic Pressure	57	28.5
Total	200	$P_{\text{fail}} = 28.5$

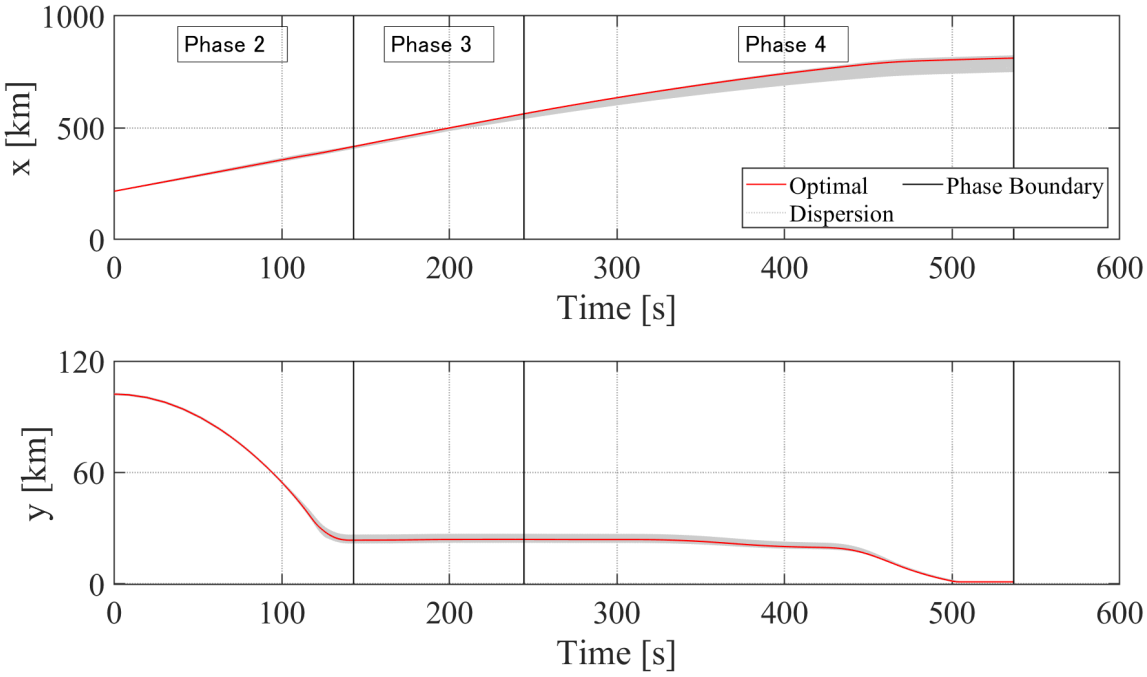

Fig. 5.1 Time History of Downrange and Altitude from Monte Carlo Simulation.

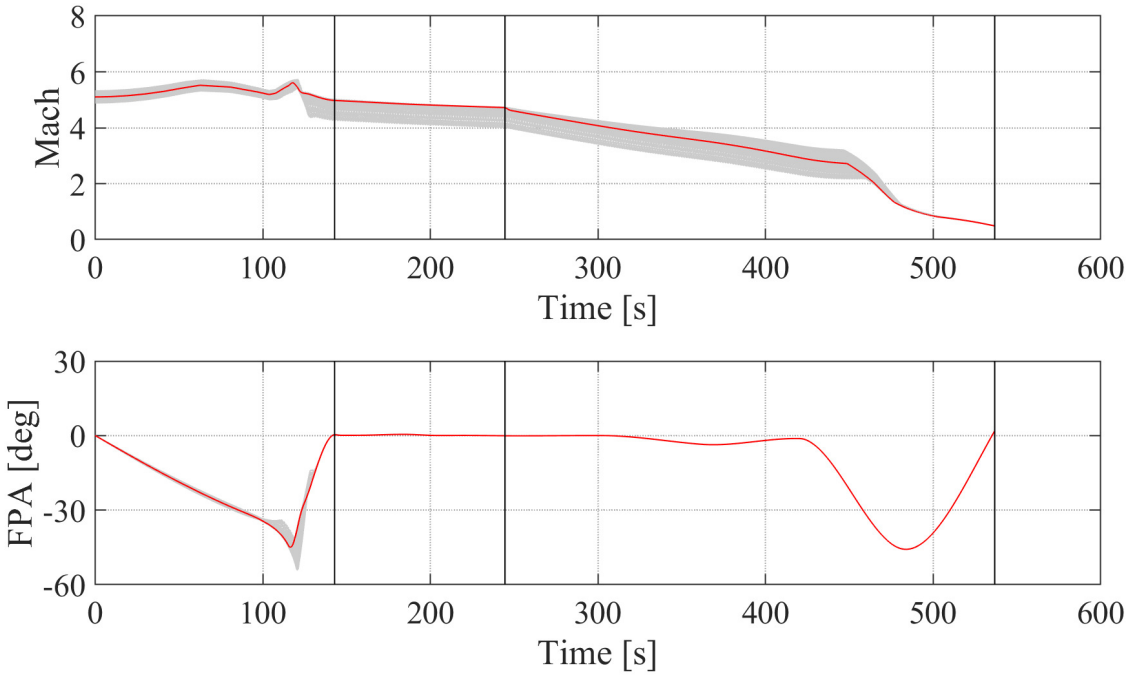

Fig. 5.2 Time History of Mach Number and γ from Monte Carlo Simulation.

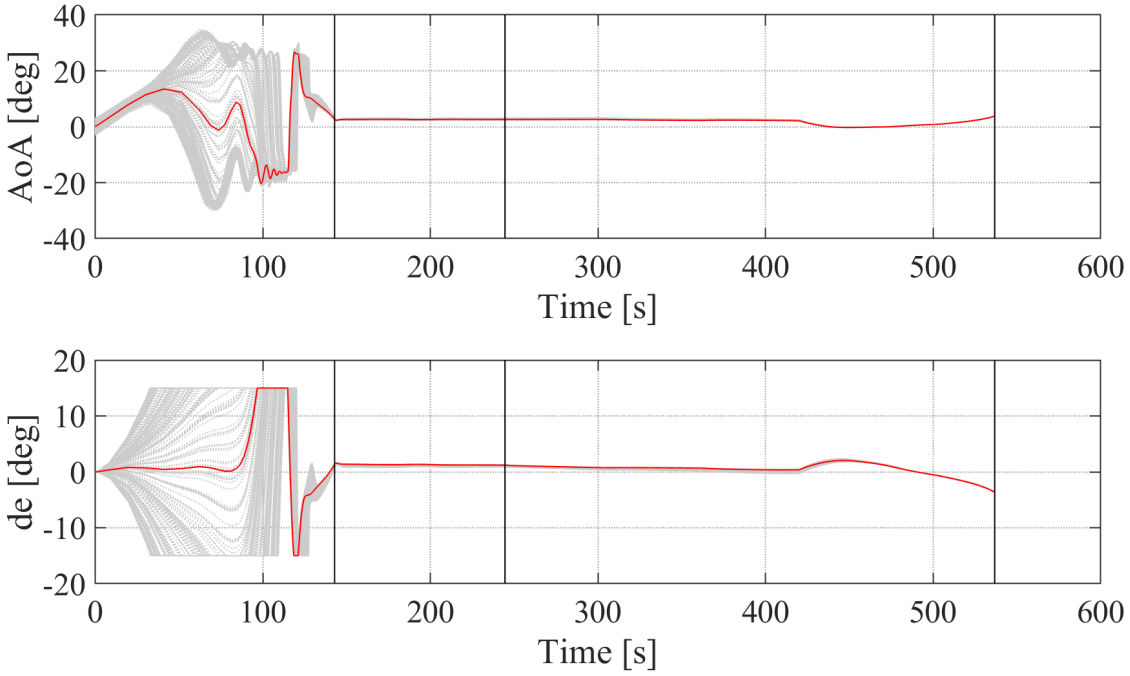

Fig. 5.3 Time History of Angle of Attack and δ_e from Monte Carlo Simulation.

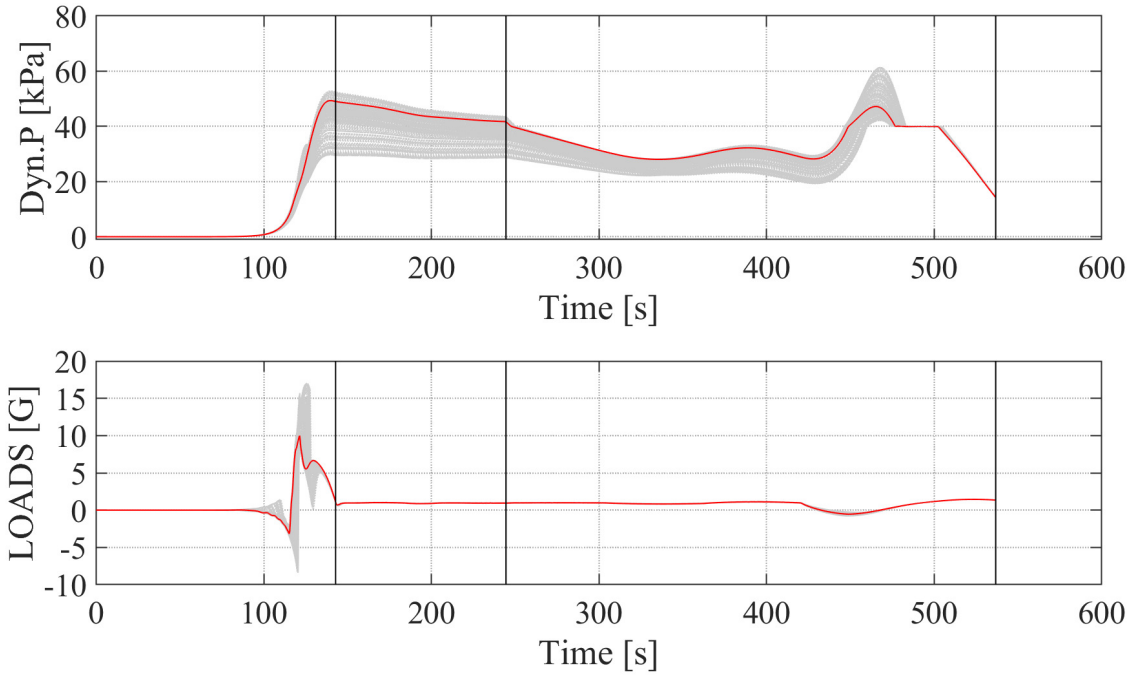

Fig. 5.4 Time History of Dynamic Pressure and Load from Monte Carlo Simulation.

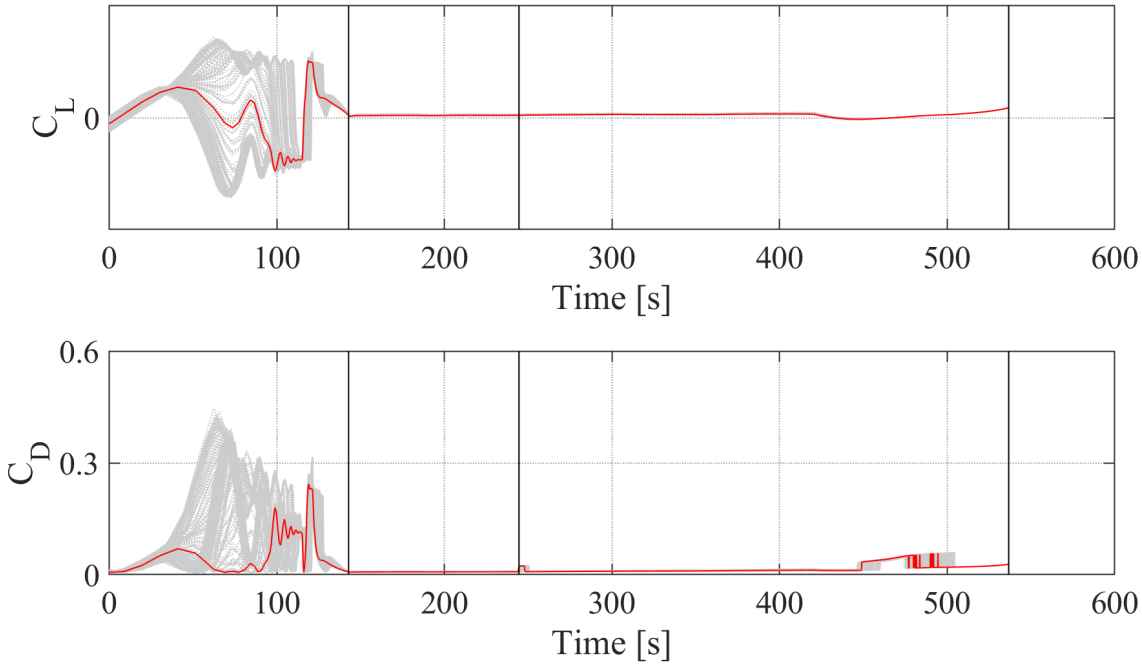

Fig. 5.5 Time History of C_L and C_D from Monte Carlo Simulation.

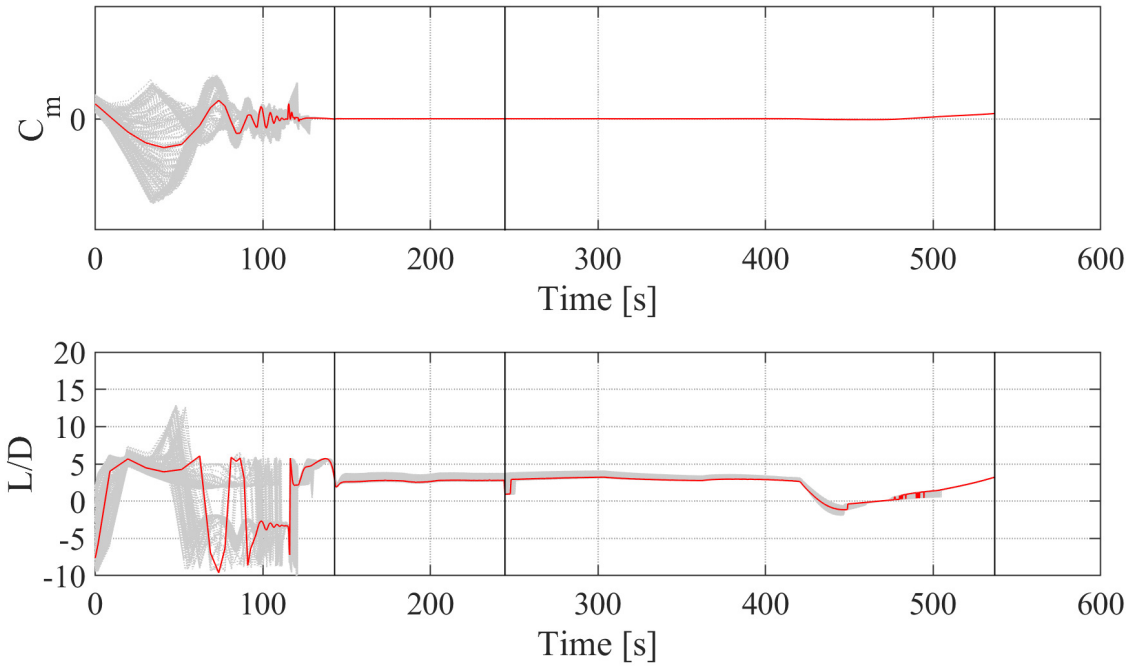

Fig. 5.6 Time History of C_m and L/D from Monte Carlo Simulation.

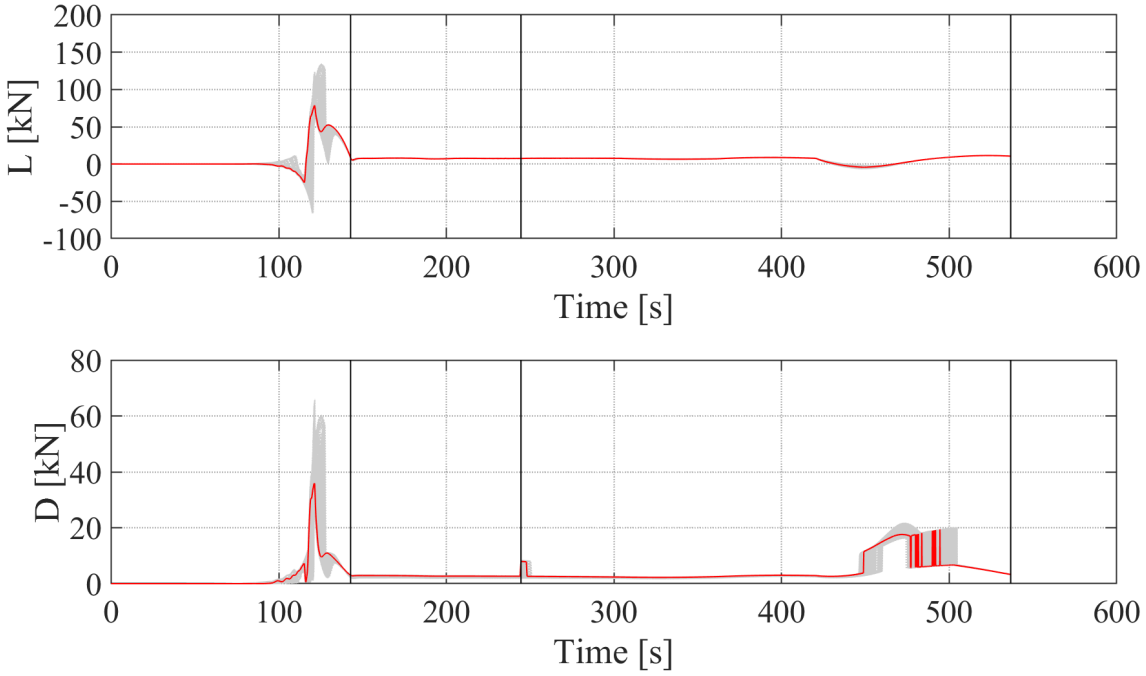

Fig. 5.7 Time History of Lift and Drag from Monte Carlo Simulation.

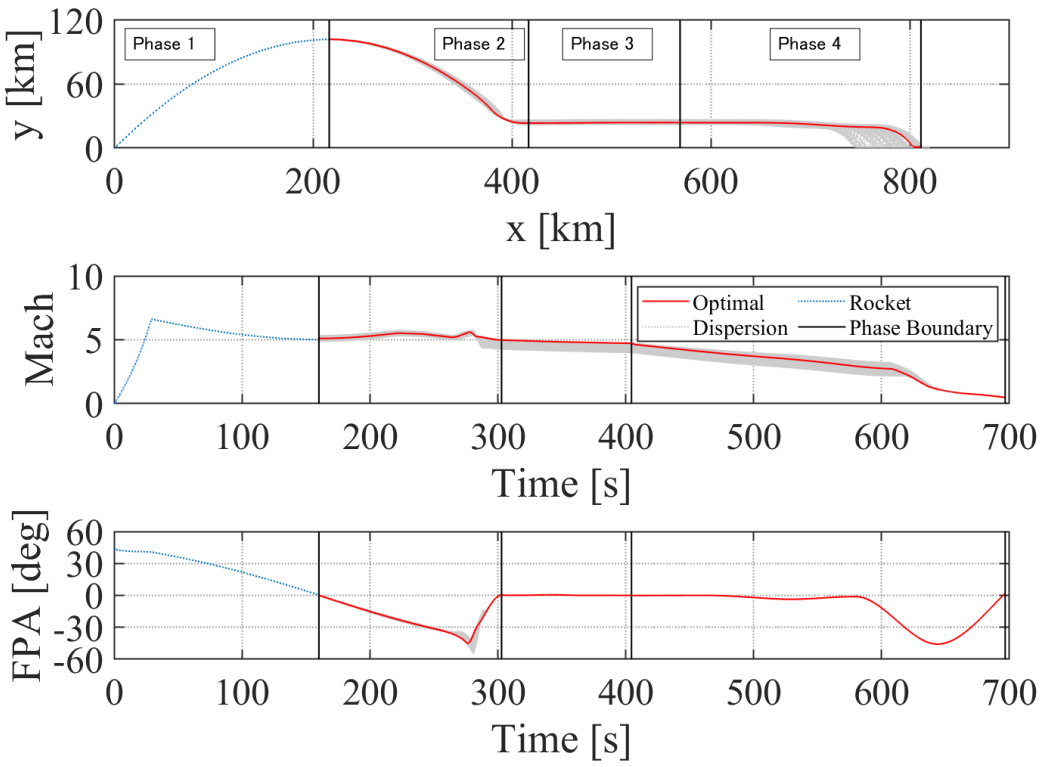

Fig. 5.8 All Phases from Monte Carlo Simulation.

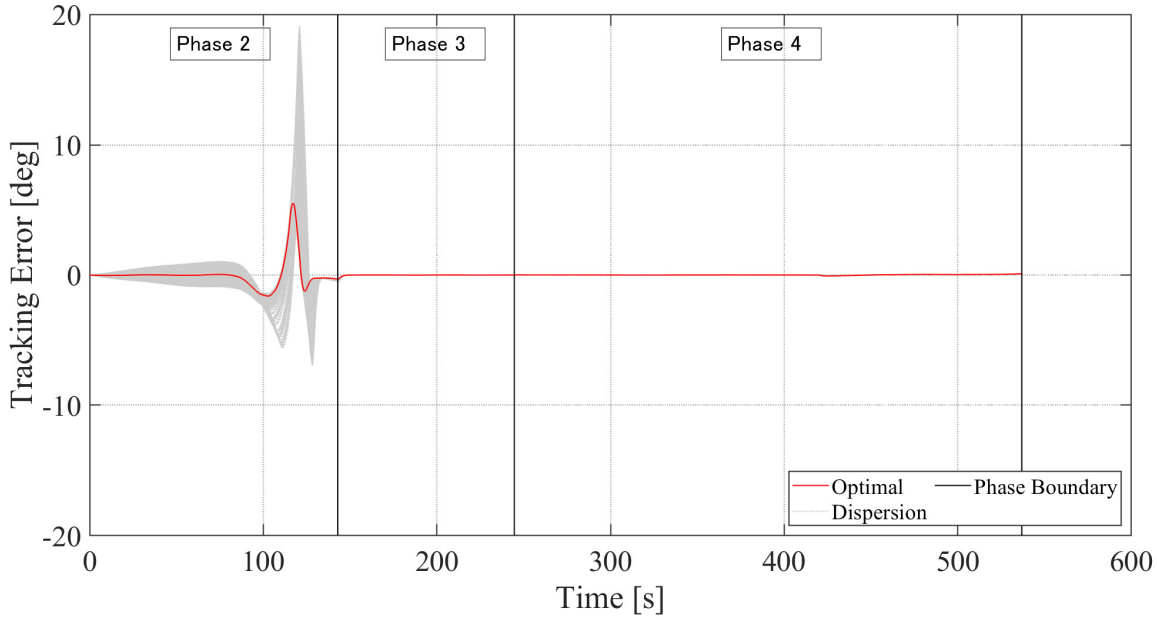

Fig. 5.9 Error Comparison for Tracking γ from Monte Carlo Simulation.

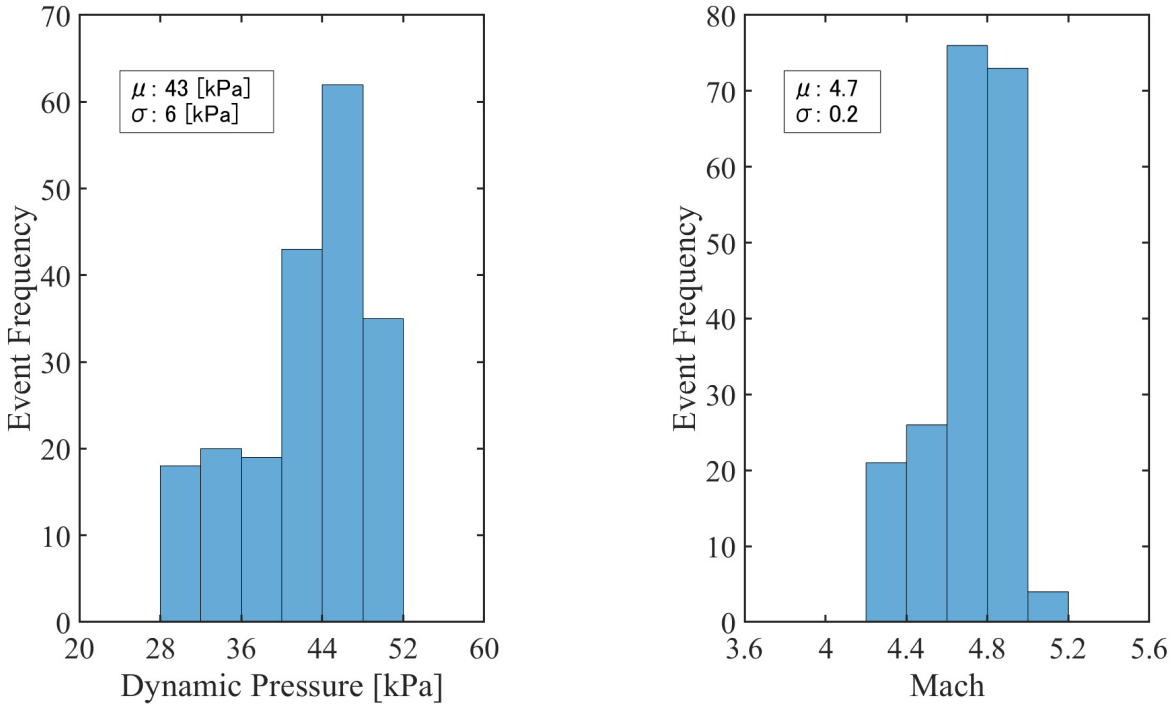

Fig. 5.10 Error distribution of Dynamic Pressure and Mach Number.

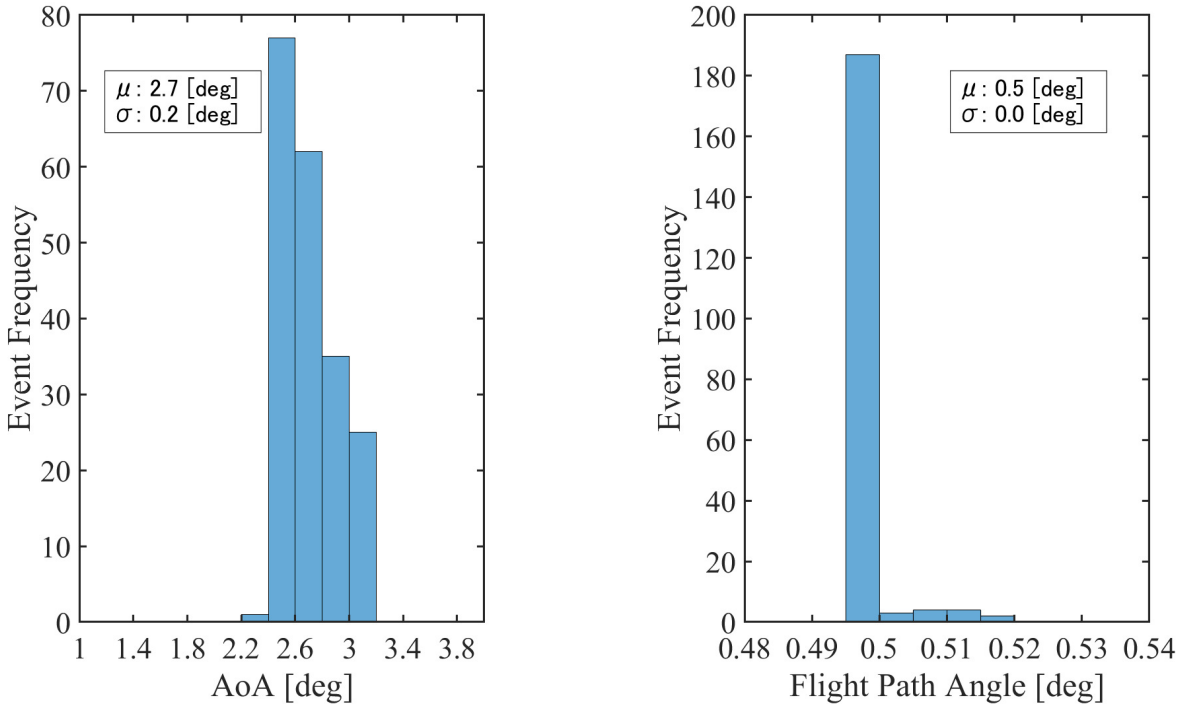

Fig. 5.11 Error distribution of Angle of Attack and Flight Path Angle.

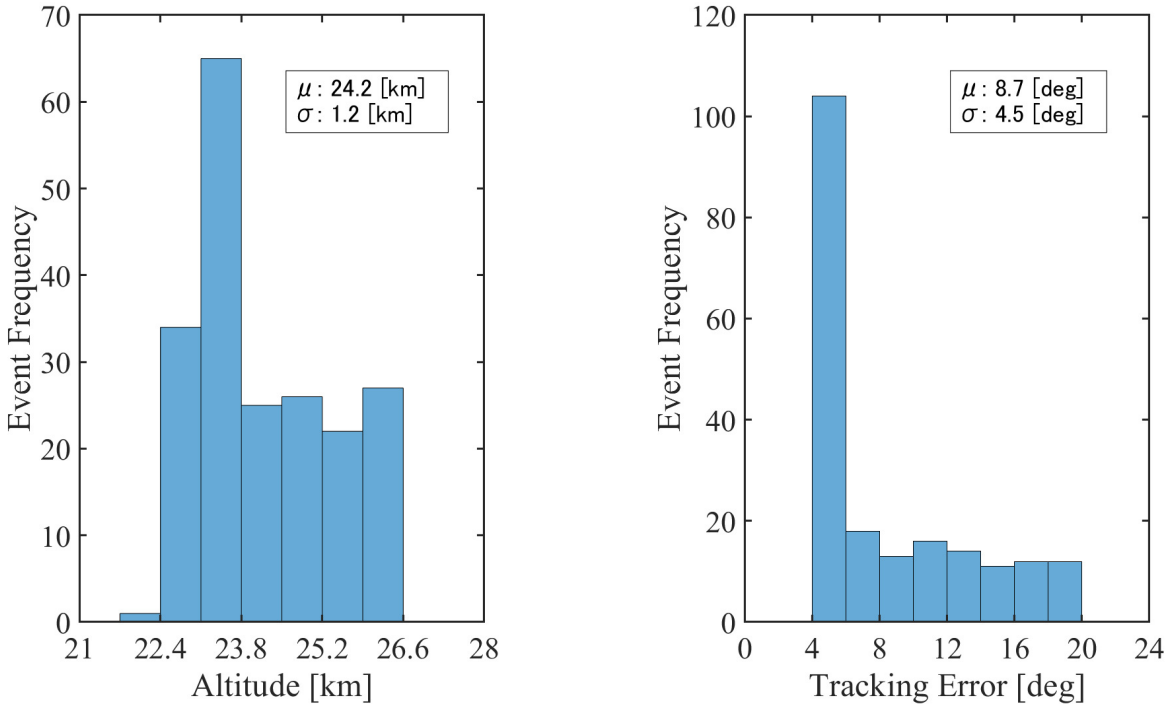

Fig. 5.12 Error distribution of Altitude and Tracking Error.

5.4 Conclusion of Chapter 5

Robustness against state uncertainties present during separation was obtained as well as the mission success rate for conducting hypersonic engine test with the Hypersonic Experimental Aircraft. The primary cause in decreasing the success rate was identified to be the velocity decrease during pitch up from suborbital flight causing a decrease in dynamic pressure. It was also identified that significant spike in loading occurs due to the deviation from the reference trajectory since no air is present for producing enough dynamic pressure during suborbital flight. A valuable insight was obtained to incorporate thrusters to have control of pitch during suborbital flight where sufficient air density is not obtained and elevon does not function which can be done through the expansion of the proposed method.

Chapter 6

Summary

6.1 Conclusion

Within the growing commercial market for high speed travel and to meet the expectations of the rising demand for intercontinental travel, hypersonic transport aircraft in pursuit for faster and reliable flight system promotes the possibility in realizing the opportunity. In particular, hypersonic aircrafts with airbreathing engines are expected to handle the flight profile of aircraft-like operability where the aircraft will takeoff horizontally from an airstrip, climb to cruising altitude, cruise at hypersonic speeds, and descent to perform landing maneuvers. An essential effort for realizing such hypersonic aircraft is to conduct their trajectory and control analysis early in the stage of development so as to clarify key concepts to meet specific mission requirements and to facilitate the development of key technologies accordingly due to the strong coupling between the reference trajectory and robust controller. This is a major concern in designing hypersonic aircraft as well as with aerodynamics, thermodynamics, structural dynamics, and etc. Trajectory and controller decides the behavior in which to specify the constraints placed among the disciplines and should be considered as early as possible. In order to handle these difficulties, the present study proposed a novel method of simultaneous trajectory and controller design for obtaining a control-oriented trajectory and robust controller for minimizing tracking error to promote mission success. Proposals were given regarding a numerical technique for integrating the discretized trajectory segments into the robust controller design through system identification and providing robustness against flight condition changes and to the obtained optimal trajectory.

For the first objective concerning **development of simultaneous design method of trajectory and robust controller**, in Chapter 1 a novel method to simultaneously design the trajectory and robust controller by converting the trajectory into a transfer function at each discretized segment of the trajectory and incorporating each identified transfer function

to the H_∞ controller design was proposed. At each iteration of the SQP, the tracking error is obtained through closed-loop system of tracking the trajectory generated at each iteration and evaluated to meet the nonlinear inequality constraint placed on the NLP problem. In Chapter 2, the proposed method is validated by successfully applying to 2 well-known optimal control problems of which one is aerospace related and another being outside the field of aerospace for showing applicability outside of aerospace field. For each example problem, the results were compared to the conventional method where the trajectory and robust controller are obtained separately and showed results where tracking error was reduced for the simultaneous method thus generating a control-oriented trajectory.

For the second objective concerning **application to hypersonic experimental aircraft with control surface sizing**, in Chapter 4 the proposed method was applied to the simultaneous design of trajectory and robust controller for the Hypersonic Experimental Aircraft. Hypersonic aircrafts are known to have a strong coupling between trajectory and controller performance. Therefore, by using the novel method along with optimal sizing of the control surface, a reference trajectory and robust controller was obtained for the Hypersonic Experimental Aircraft as well as optimal control surface sizing to increase tracking performance. The obtained results ensured both a control-oriented trajectory and a controller robust against flight condition changes as well as to generated optimal trajectory. In Chapter 5, the obtained trajectory and controller was evaluated via Monte Carlo simulation of the uncertainties present during separation from the rocket booster. From the statistical results, the tolerable maximum tracking constraint was maintained for all cases and mission success rate was identified for meeting engine test and cruise requirements. A valuable insight was obtained to incorporate a thruster controller on the system to have control of pitch during suborbital flight where sufficient air density cannot be obtained. This can be achieved through expanding the control system design in the current framework of the proposed method.

By performing a simultaneous trajectory and controller design for obtaining a control-oriented trajectory and robust controller, this dissertation provided an insight into the benefits of integrating the design process and showing a potential simultaneous trajectory and robust controller design methodology for the Hypersonic Experimental Aircraft. The obtained results and experience can serve as guidelines to future trajectory and controller designs of unmanned aircraft as well as to initiate a step towards the process of maturing technical readiness of the system for actual flight tests.

6.2 Novelties of the Present Research

For the sake of clarity, major novelties in the present research (i.e. the attempts that cannot be found in previous researches) are enumerated below:

1) A method of simultaneous trajectory and controller design was developed for obtaining a control-oriented trajectory and robust controller for minimizing tracking error.

2) The advantages over the conventional method of designing the trajectory and controller separately were identified in terms of improving objective function and tracking performance applicable to aerospace related and for fields outside of aerospace.

3) Simultaneous design of trajectory and controller along with sizing of the control surface for the Hypersonic Experimental Aircraft was conducted.

4) Flexibility in expanding control system design to fit individual problems in the framework of the proposed method.

6.3 Recommendations for Future Work

Based on the knowledge and lessons learned from the development of the the simultaneous design of trajectory and robust controller as well as application to Hypersonic Experimental Aircraft, in future studies the work carried out in this dissertation can be improved or utilized by the following aspects in no particular order:

1) To improve the convergence of the optimization, a surrogate model may be created before the simulation of identifying tracking error performance to predefined set of reference trajectories. This may decrease calculation time since tracking error through nonlinear simulation is calculated beforehand. Additionally, higher fidelity aerodynamics model is necessary to improve maturity of the obtained results since the aerodynamic interpolations were derived through least square fit. Such improvements can be obtained by using Kriging's method or by radial basis network interpolation while increasing the amount of data points.

2) The current design philosophy is to conduct heuristic weighting function tuning through loop shaping of the sensitivity and complementary sensitivity function for better understanding of the controller characteristics. Thus, extensive knowledge on frequency domain tuning is required for obtaining satisfactory results. Therefore, the current proposed method can be adjusted to be more user friendly by adding automatic tuning of the weighting functions under a design objective of the individual problem.

3) Uncertainties in the aerodynamics was not modeled in the current dissertation since emphasis was placed on obtaining a controller robust to flight condition changes. This was due to time restriction on deriving the aerodynamic characteristics only by CFD for the Hypersonic Experimental Aircraft model and no wind tunnel experiments were conducted to validate the uncertainties present. Furthermore, the actuator uncertainties were not incorporated due to the complexity in modeling and further research is needed to evaluate the effect modeling error has on the solution. Both aerodynamic and actuator uncertainties are possible to be incorporated into the proposed method since H_∞ controller design was used for the robust controller design.

4) Expanding the problem formulation used in the current Hypersonic Experimental Aircraft problem is needed to mature the technical readiness since the problem was simplified due to time restrictions. Critical factors to be investigated are expanding the current control system design to incorporate thruster controller for increasing mission success rate, incorporate directional and roll dynamics to perform a a three dimensional analysis, perform a design analysis on TPS for thermal protection, and compare the controller performance to a gain scheduled controller.

5) Investigation of the trajectory of the booster while and after should be conducted since improvements the current Monte Carlo simulation assumed that state separation uncertainties existed on the aircraft itself and not effecting the trajectory of the rocket. Particular attention should be paid to the interaction between the rocket booster and aircraft and acquiring more insightful knowledge is indispensable for continuing on with further research.

Appendix A

Case Study on Designing Reference Trajectory

A case study is conducted to evaluate the flight trajectory of the Hypersonic Experimental Aircraft for sensitivities to tracking performance. Furthermore, the flight trajectory with the smallest fuel consumption over downrange ratio was analysed through parametric study with the flight path angle γ being the parametric variable. The Hypersonic Experimental Aircraft model was constructed using CFD and a surrogate model was created to interpolate the coefficients to the aircraft dynamics. A controller was constructed with the angle of attack and thrust being the control input to the aircraft model. From the results, the flight path angle of -4deg had the smallest fuel consumption over downrange ratio and the tracking performance decreased as the flight path angle became steeper due to the controller saturating from the angle of attack limit.

A.1 Overview

Although many CFD has been conducted for the evaluation of cruise and low speed flight for the Hypersonic Experimental Aircraft [40, 39], simulation of actual flight trajectory to sensitivities in tracking performance as well as fuel consumption had not been conducted. The aircraft model is still in need of thorough validation of its aerodynamics, however a preliminary test on flight control is needed since the coupling between trajectory and controller is prevalent for hypersonic aircrafts [65]. Due to this, the tracking performance is assumed to be effected by the reference trajectory. Additionally, although the total amount of fuel needed has not been finalized, limiting the fuel consumption is critical since liquid hydrogen is used for fuel. Liquid hydrogen has a very high specific energy (MJ/kg) however, a

very low energy density (MJ/L). This makes it hard to store large quantity of liquid hydrogen in fuel tanks and fuel shortage may occur [54]. Therefore, evaluation on the trajectory minimizing the fuel consumption over downrange ratio is necessary in the preliminary analysis of the flight trajectory as well.

The objective of this case study is to construct a controller for the Hypersonic Experimental Aircraft satisfying the constraints placed on the flight trajectory. Additionally, the constructed controller was evaluated for sensitivities to tracking error with respect to the parametric reference γ input as well as to identify the smallest fuel consumption over downrange ratio.

A.2 Reference Trajectory Generator

The flight profile was referenced from Fig.4.1 of Phase 4 where the aircraft starts its decent after the hypersonic cruise experiment. For this case study, it was assumed that the aircraft would decent from hypersonic cruising altitude of 25[km] to altitude of 6[km] for subsonic flight. The reference for tracking in this case would be the reference trajectory given by the parametric γ. The parametric γ evaluated in this research are $\gamma = -2, -4, -6, -8, -10$ [deg]. The γ inputs are given as a Bessel function and tuned to meet the target altitude of 6[km].

$$t^2\ddot{\gamma} + t\dot{\gamma} + (t^2 - n^2)\gamma) = 0 \tag{A.1}$$

Where t is time in seconds, γ is flight path angle [deg], $n = 15$ and is the integer order.

For the simulation, a longitudinal flight control system controlling the altitude and velocity was constructed shown in Fig.A.1. Here, γ_{target} represents the target flight path angle

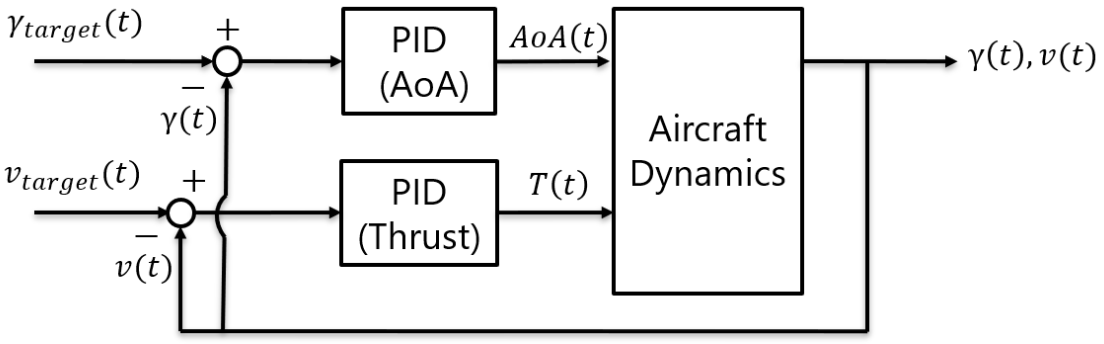

Fig. A.1 Controller for Tracking Reference Trajectory.

and v_{target} represents the target Mach number respectively. Two controller were designed each controlling the angle of attack (AoA) and thrust of the PCTJ engine. The parameters

for the gain used in the PID controllers were set so as to have high tracking performance. The aircraft dynamics used for the analysis are the nonlinear dynamics identical to Eq.(4.14). The controller gains tuned for high tracking performance are summarized in Table A.1. The aerodynamics and engine models used in the simulation are interpolated using a radial basis function network (RBFN)[23] method shown in Fig.A.2. For the aerodynamic data, the sample points are summarized in Table A.2 with the same numerical analysis conditions as shown in Table 4.5 in Chapter 4 and defined as a function of Mach and angle of attack. The solver FaSTAR developed by JAXA was used as well as the automatic grid generator Hexagrid developed by JAXA as used in Chapter 4. Lastly, thrust has a maximum output of 1600[N] at Mach 5 and 2000[N] at below Mach 0.8 which was derived referencing the data provided by JAXA and defined as a function of thrust and altitude. The simulation was conducted in a MATLAB/SIMULINK environment using U.S. Standard Atmosphere model for the air density and static temperature. The initial conditions for the simulation are summarized in Table A.3 where the simulation starts after the hypersonic cruise test. Additionally, the trajectory constraints while the aircraft is descending is summarized in Table A.4. The termination condition for the simulation was the derivative for the state variables in Eq.(4.14) of $\dot{h}, \dot{v}, \dot{\gamma} \leq 1 \times 10^{-2}$ and subsonic cruise velocity after descent was ± 0.4.

Table A.1 Angle of Attack and Thrust Controller Gains.

kp_{AoA}	ki_{AoA}	kd_{AoA}	kp_{thrust}	ki_{thrust}	kd_{thrust}
200	0	900	1000	-2	10

Table A.2 Aerodynamic Sample Points.

Mach Number	0.3, 0.8, 2, 4, 5, 6
Angle of Attack [deg]	-10, -8, -6, -4, -2, 0, 2, 4, 6, 8, 10

Table A.3 Initial Conditions for Phase 4.

Altitude h [km]	25
Mach Number	5
AoA [deg]	1.4
Pitching Moment	0
Thrust [N]	1535
Control Start t_{on} [s]	$500 \leq t_{on} \leq 3600$

Table A.4 Trajectory Constraints.

Load F_z [G]	$-5.5 \leq F_z \leq 5.5$
Dyn. Pressure Q [kPa]	$Q \leq 51$
AoA [deg]	$-10 \leq \alpha \leq 10$
Thrust [N]	Mach $5 \leq 1600$
	Mach $0.8 \leq 2000$

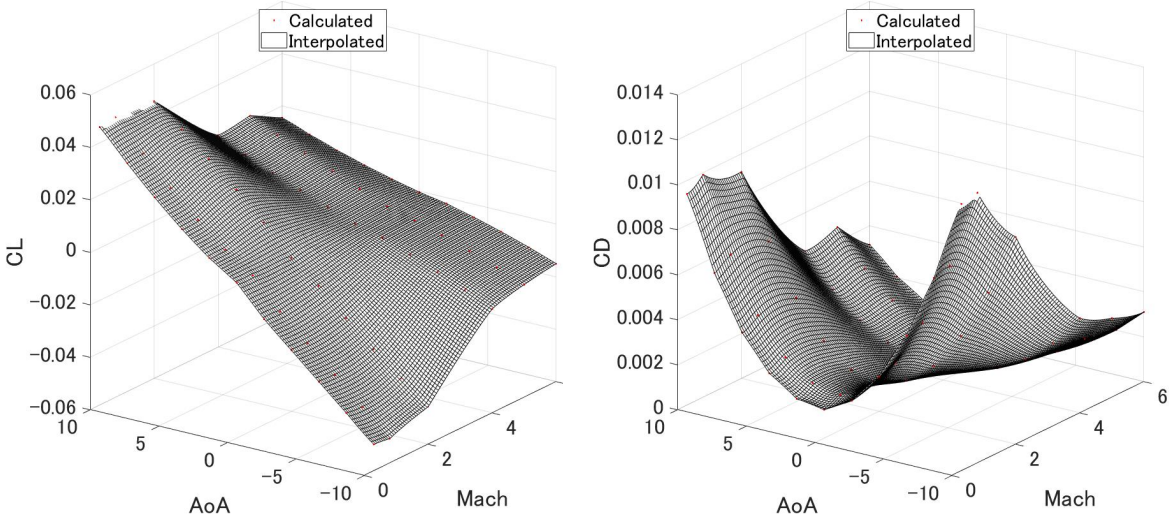

(a) C_L Surrogate Model. (b) C_D Surrogate Model.

Fig. A.2 Aerodynamic Interpolation Surface.

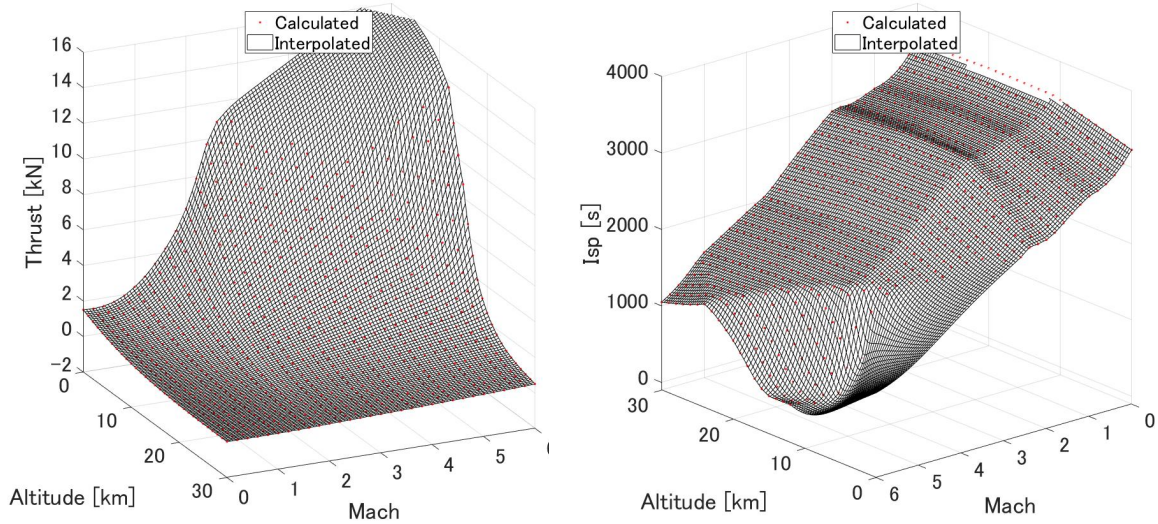

(a) Thrust Surrogate Model. (b) I_{sp} Surrogate Model.

Fig. A.3 Engine Characteristics Interpolation Surface.

A.3 Results and Discussion

Results for flight path angle of -4[deg] and -10[deg] are shown in Fig.A.5 and Fig.A.6 respectively. Fig.A.4 shows the downrange with respect to altitude and flight path angle with respect to fuel consumption over downrange. From Fig.A.5, it can be seen that satisfactory controller performance is achieved for $\gamma = -4$[deg]. From Fig.A.6, it can be seen that for $\gamma = -10$[deg] the load factor constraint is violated. From Fig.A.5 and Fig.A.6, simulation converges after descent maintaining cruising altitude and velocity but $\gamma = -10$[deg] took longer to converge due to the tracking performance for tracking γ decreasing as the flight path for descent became steeper. Here, the blue line represents the system output, orange line is reference input, black line is steady-state flight before the descent, green line is descent duration for $\gamma = -4$, and red line is constraint placed on the trajectory. Tracking performance decreased for $\gamma = -10$[deg] due to the AoA restriction of ± 10[deg] placed as an constraint to prevent stall and the insufficient lift caused tracking performance to decrease. Additionally, the velocity decreased since the velocity controller detects the velocity error from the input Mach command thus increasing the thrust however, insufficient thrust occurred due to the high angle of attack creating more drag. This drag creates a velocity overshoot which forces the thrust controller to create more thrust consuming more fuel.

From the results, it can be concluded that fuel consumption over downrange had a minimum value at $\gamma = -4$[deg] due to the decrease in tracking performance as the flight path became steeper which then caused the velocity overshoot. Therefore, flight path angle should be minimized as much as possible while meeting trajectory constraint.

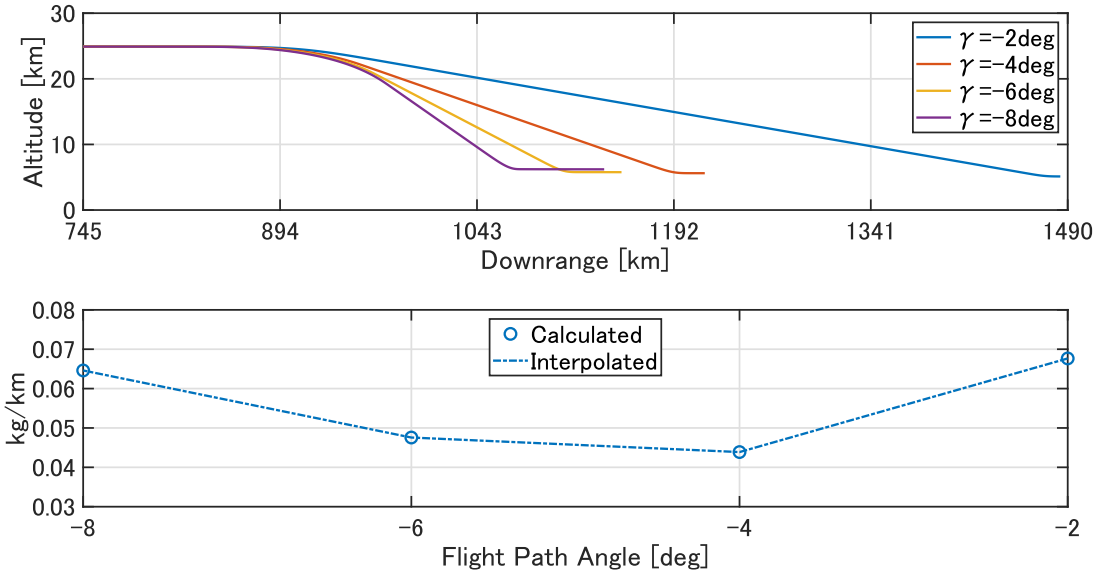

Fig. A.4 Comparison Between h to Downrange and Fuel Consumption over Downrange to γ

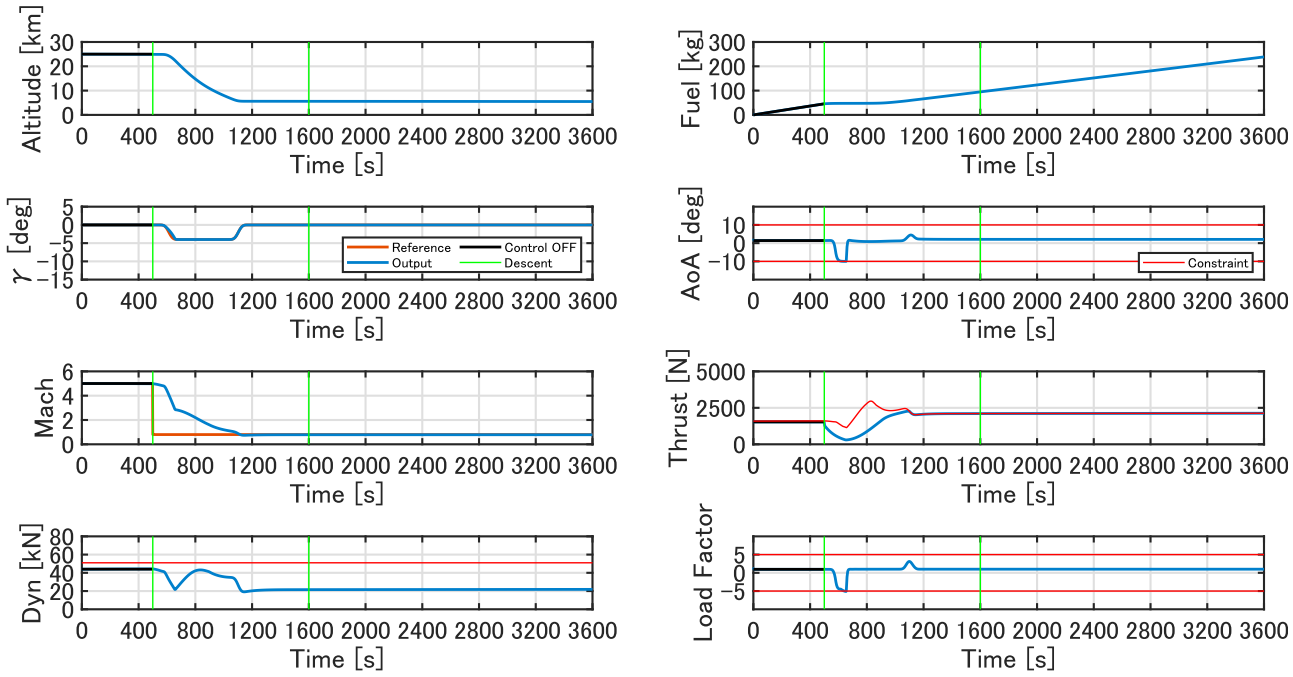

Fig. A.5 Simulation Results of $\gamma = -4$[deg].

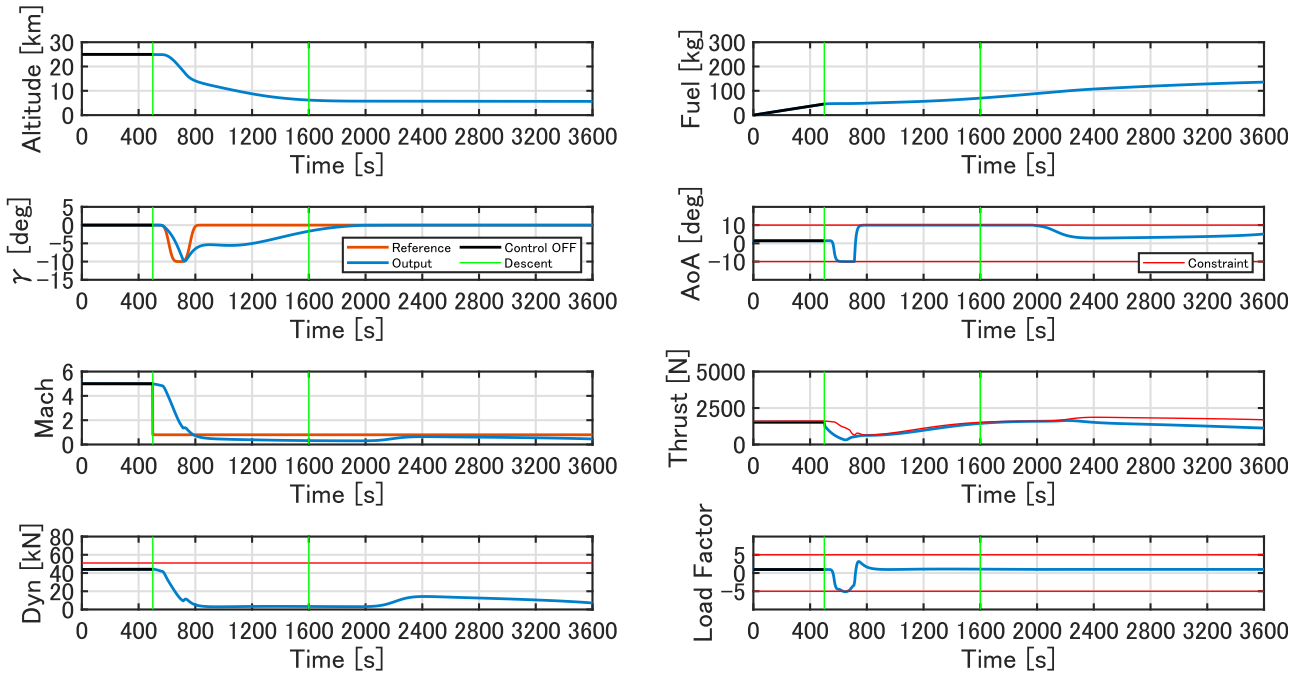

Fig. A.6 Simulation Results of $\gamma = -10$[deg].

Appendix B

Case Study on Designing Robust Controller

A case study is conducted to design a robust controller for the Hypersonic Experimental Aircraft and evaluated for stability and performance as well as robustness against flight condition changes in the assumed descent trajectory phase taken from the previous case study in Chapter A. The nonlinear dynamic equations were linearized using perturbation from steady state flight at each flight Mach number of the descent trajectory. From the results, robust controller was obtained meeting the control performance and a controller robust to flight Mach number of 5 to 2 was constructed for the Hypersonic Experimental Aircraft in the descent trajectory phase. Furthermore, it was identified that the controller performs differently at each Mach number where the overshoot becomes greater as the Mach number increases and performance decreases significantly.

B.1 Overview

To obtain a controller to stabilize the system in the presence of varying flight mach numbers, one possible method is to introduce a robust controller [6]. Recently, there has been numerous papers in H_∞ controller design applied to aerospace vehicles[55, 22] by also placing a structured constraint on the controller. Therefore, theoretically the same can be applied to a hypersonic aircraft model to make the controller robust to varying mach number through H_∞ controller design while inflicting a structured constraint on the controller. This makes the controller to have same structure as a conventional PID making ease of implementation while keeping a low-order transfer function for faster calculation time. However, a structured H_∞

controller design approach has not been conducted for the current second stage Hypersonic Experimental Aircraft model.

The objective of this paper is to design a structured H_∞ controller design for the Hypersonic Experimental Aircraft model in the descent trajectory phase to be robust to varying flight mach numbers and to evaluate the obtained controller to have stability and desired control performance.

B.2 Robust Controller Design

For this case study, the robust controller design was conducted by referencing the $\gamma = -4$[deg] trajectory generated from the previous case study from A for the Hypersonic Experimental Aircraft. In order to conduct a robust controller design, a set of linear time invariant (LTI) models were needed for the reference trajectory. The LTI models were obtained by linearizing Eq.(4.14) at different flight conditions in the reference descent trajectory. The reference descent trajectory had satisfactory tracking performance while minimizing the fuel consumption over downrange. The LTI model was constructed by linearizing the equations for the flight range of Mach 5 to Mach 2 in the descent trajectory phase. Linearization of Eq.(4.14) was conducted by first considering the steady-state flight condition at each Mach number (Mach 5 to Mach 2). The steady-state flight condition are summarized in Table B.1 taken from the reference descent trajectory. Additionally, the aerodynamic characteristics at the steady-state flight conditions were obtained by the surrogate model from the previous case study shown in Fig.A.2 and A.3. Second, a perturbed flight is considered relative to steady-state flight. The perturbed variables are summarized in Table B.2. Small angle assumptions to trigonometric functions of perturbed angles were made ($\sin\Delta\theta = \Delta\theta$ and $\cos\Delta\theta = 1$). The state equations are linearized about the steady state condition and is written in equation (B.1) (subscripts for matrix A, B, and C denotes reference Mach number).

$$\begin{aligned} \dot{x} &= A_i x + B_i u \\ y &= C_i x \end{aligned} \tag{B.1}$$

where the new state variables are the following;

$$\begin{aligned} x &= [\Delta h \;\; \Delta V \;\; \Delta\gamma]^\mathsf{T} \\ u &= [\Delta\alpha] \end{aligned}$$

The LTI models for Mach 5 to 2 are shown in equations (B.2) to (B.5).

Table B.1 Steady State Condition

Mach	Altitude [km]	AoA [deg]	γ [deg]	Thrust [N]	$C_{L\alpha}$
5	25	1.6	0	1600	0.785
4	25	2.2	0	620	0.745
3	15	0.9	0	2600	1.3
2	11	1.0	0	4000	1.867

Table B.2 Perturbation Variables

State Variable	Perturbed State
Altitude r [km]	$r+\Delta r$
velocity v [m/s]	$v+\Delta v$
Angle of Attack a [deg]	$a+\Delta a$
Flight Path Angle γ [deg]	$\gamma+\Delta\gamma$
Thrust T [N]	$T+\Delta T$

$$A_5 = \begin{bmatrix} 0 & 0 & 1.490\times10^{3} \\ 3.016\times10^{-4} & -0.029 & -9.800 \\ -1.116\times10^{-6} & 1.046\times10^{-5} & 0 \end{bmatrix}, \quad B_5 = \begin{bmatrix} 0 \\ -0.077 \\ 0.219 \end{bmatrix} \tag{B.2}$$

$$A_4 = \begin{bmatrix} 0 & 0 & 1188.4 \\ 0.0001 & -0.0013 & -9.800 \\ 0 & 0 & 0 \end{bmatrix}, \quad B_4 = \begin{bmatrix} 0 \\ -0.0296 \\ 0.1657 \end{bmatrix} \tag{B.3}$$

$$A_3 = \begin{bmatrix} 0 & 0 & 885 \\ 0.0004 & -0.0070 & -9.800 \\ 0 & 0 & 0 \end{bmatrix}, \quad B_3 = \begin{bmatrix} 0 \\ -0.0509 \\ 0.8823 \end{bmatrix} \tag{B.4}$$

$$A_2 = \begin{bmatrix} 0 & 0 & 590.2 \\ 0.0007 & -0.0166 & -9.800 \\ 0 & 0 & 0 \end{bmatrix}, \quad B_2 = \begin{bmatrix} 0 \\ -0.0869 \\ 1.4874 \end{bmatrix} \tag{B.5}$$

$$C = \begin{bmatrix} 0 & 0 & 1 \end{bmatrix} \tag{B.6}$$

The calculated LTI model(Theory) was compared against the nonlinear model as well as the *linearize* command in MATLAB to validate its accuracy. A step response of γ=1deg

from the trimmed state was compared for the theory, MATLAB linearized, and nonlinear model. The results are shown in Fig.B.1 to B.4. The results show that LTI model for this analysis show qualitative similarity thus LTI model(Theory) will be used to construct the H_∞ controller.

Using the obtained LTI models varying in flight condition changes of flight Mach number, the robust controller design will be conducted through the structured H_∞ controller design. The structured H_∞ controller design will impose a PID structured constraint. The structured H_∞ controller design proposed here will be robust against flight condition changes of Mach number variance which are the LTI models (equations (B.2) to (B.5)) linearized at different Mach numbers. Stability is achieved by ensuring equation B.7.

$$||T_{zw}(P,K;s)||_\infty := \sup_{0\leq w\leq\infty} |T_{zw}(P,K;jw)| < 1 \tag{B.7}$$

Here, P represents the plant model, T_{zw} denotes the closed-loop transfer function from reference input r to the output of W_e shown in Fig.1.4, $||\cdot||_\infty$ denotes the H_∞ norm, and K represents the controller. For a set of plant models representative of plant variations during the descent trajectory, structured H_∞ controller design is achieved by solving the non-smooth optimization problem by using *hinfstruct* MATLAB function. The function solves the non-smooth optimization problem of the following structure;

$$\begin{aligned} \min. \quad & \|T_{zw}(P,K;s)\|_\infty \\ \text{s.t.} \quad & K \text{ stabilizes } P \text{ internally} \\ & K \in K_{pid} \end{aligned} \tag{B.8}$$

This seeks to minimize T_{zw} with tunable parameters K. For multiple models *hinfstruct* can be used by applying different models in the same manner as equation B.8 and Eq.(2.67) shows the block diagram of structured H_∞ controller design against multiple P models. The constructed system for tracking the reference flight path angle for the Hypersonic Aircraft Model is shown in Fig.1.4. The system is an SISO with the angle of attack (AoA) as its command input and flight path angle (γ) as its output. The reference input is given as the γ. The plant models used for the synthesis are the LTI models from equation (B.2) to (B.5). The controller structure is defined as equation (B.9) where K_p, K_i, K_d,and n are the tunable parameters of K.

$$K = K_p + K_i\frac{1}{s} + K_d\frac{ns}{n+s} \tag{B.9}$$

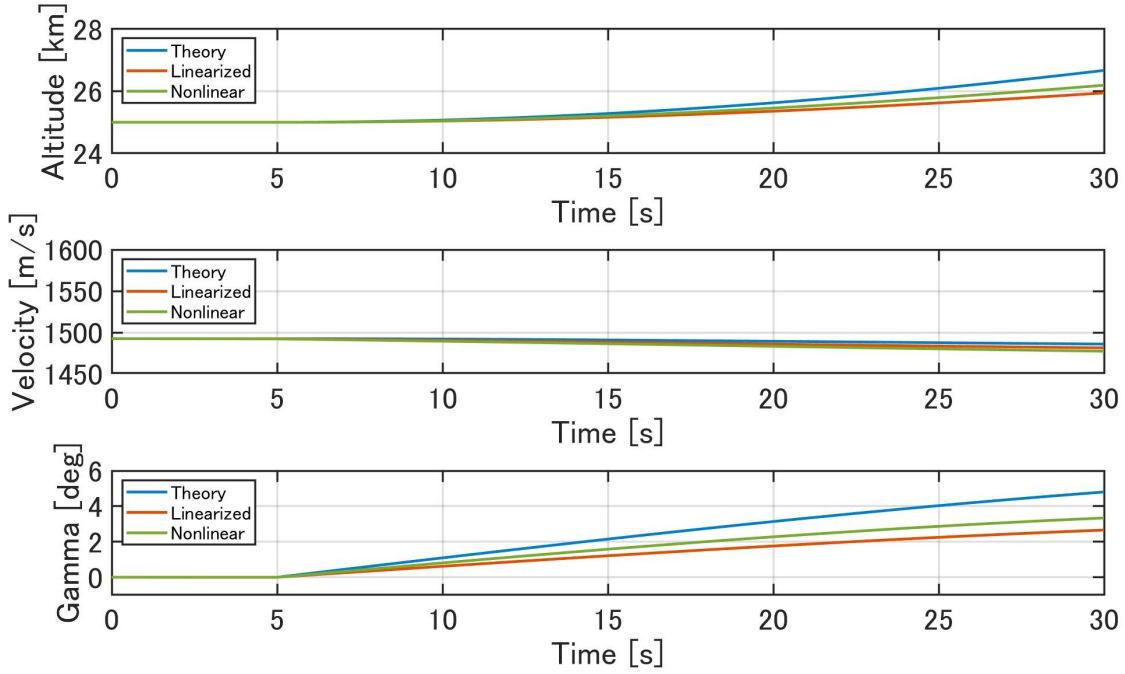

Fig. B.1 Mach 5 Theory, MATLAB linearized, and Nonlinear Dynamics Step Response Comparison.

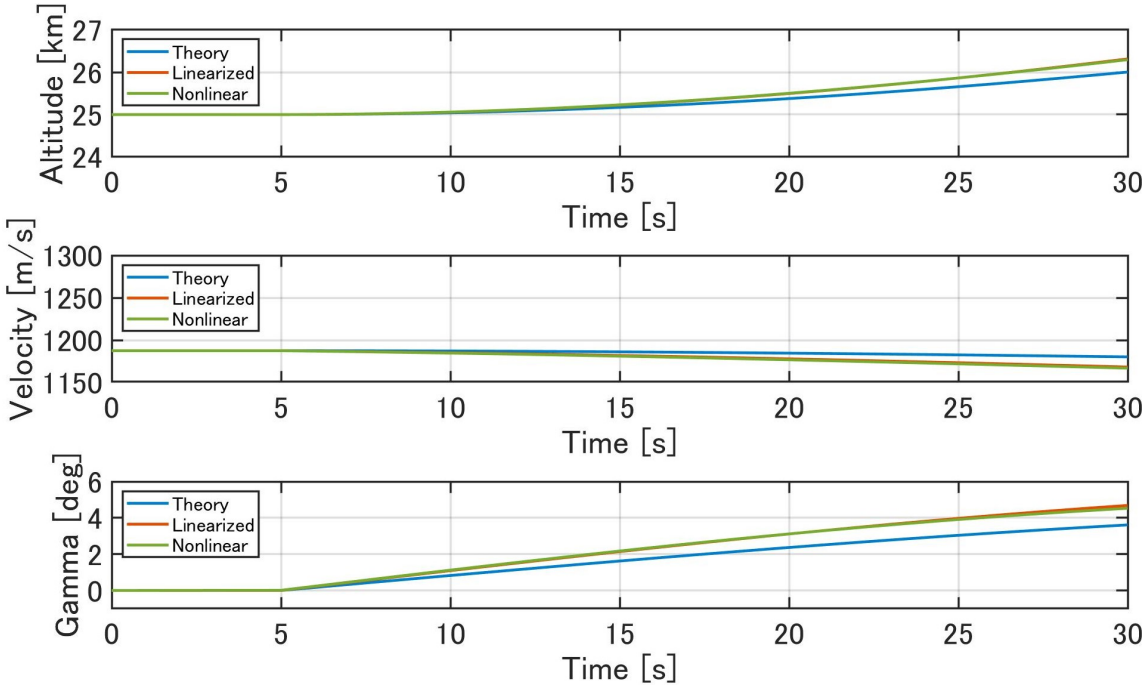

Fig. B.2 Mach 4 Theory, MATLAB linearized, and Nonlinear Dynamics Step Response Comparison.

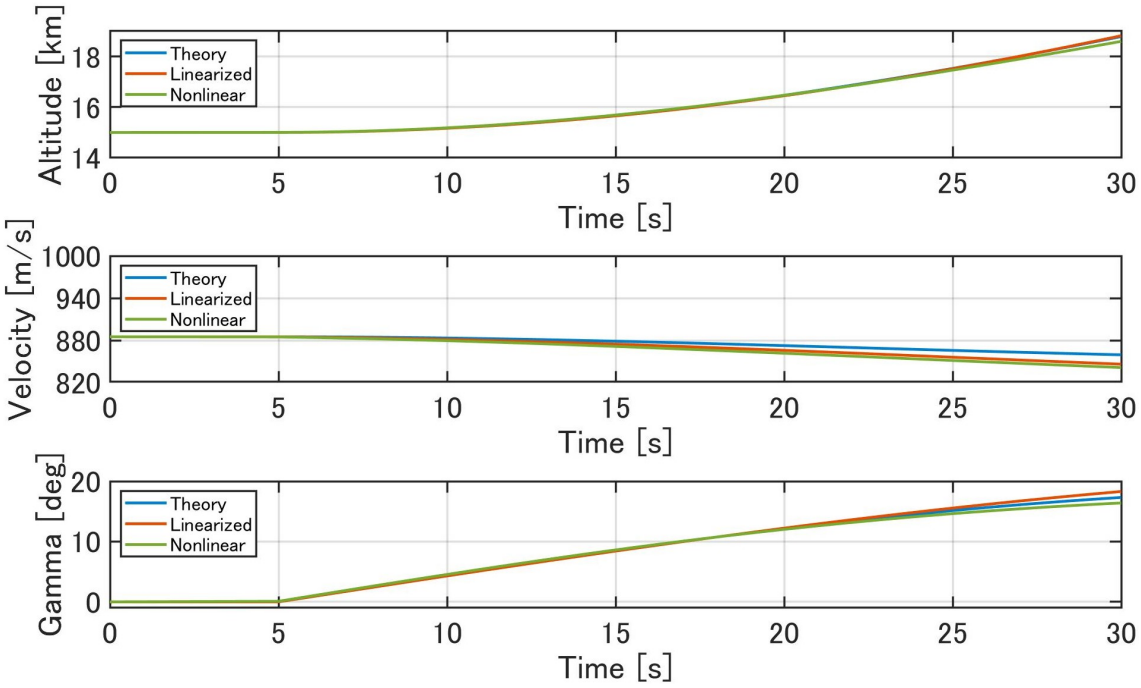

Fig. B.3 Mach 3 Theory, MATLAB linearized, and Nonlinear Dynamics Step Response Comparison.

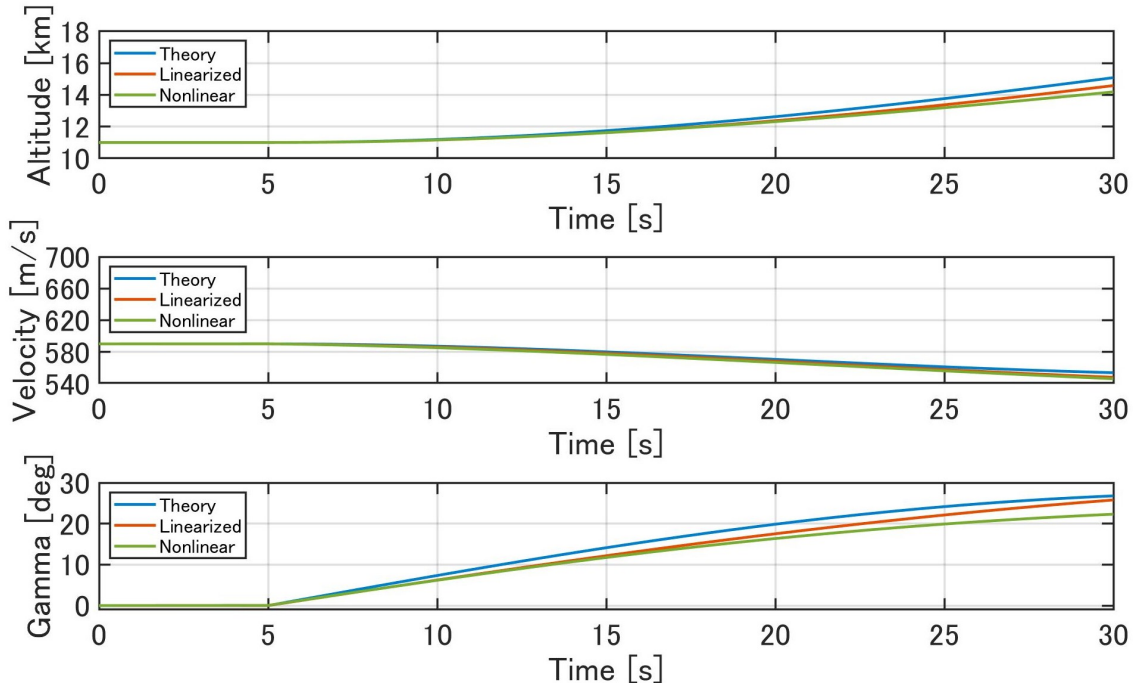

Fig. B.4 Mach 2 Theory, MATLAB linearized, and Nonlinear Dynamics Step Response Comparison.

The weighting function (W_e) placed on the system as shown in Fig.1.4 was set so as for the H_∞ norm to be as close to 1 as possible for high tracking performance. W_e is defined in Eq.(B.10). Since no weight function is placed for the command input, W_e was tuned to meet control performance criterion as discussed in the next section. For the system shown in Fig.1.4, *hinfstruct* minimizes Eq.(B.11) since T_{zw} denotes sensitivity function from w input to z output. From Fig.1.4, Eq.(B.7) can be rewritten to Eq.(B.12).

$$W_e = \frac{1.1s + 1.15}{1.2s + 1.2} \tag{B.10}$$

$$T_{wz} = W_e \frac{1}{1 + PK} \tag{B.11}$$

$$\left\| W_e \frac{1}{1 + PK} \right\|_\infty < 1 \tag{B.12}$$

In order to evaluate the structured H_∞ controller design for having robust stability and desired control performance, a set of evaluation criterion was set. The evaluation criterion (Table B.3) for the desired control performance was set by referring to Ref.[76] and checked with doublet response of ± 1deg γ since in the flight profile, AoA is expected change from pitch up (positive AoA) to pitch down (negative AoA).

Table B.3 Evaluation Criterion

Desired Controller Performance
1) $\|T_{zw}\|_\infty < 1$
2) Poles of T_{ry} function is non-positive
3) Overshoot $\leq 40\%$ of step input
4) 90% rise time ≤ 10 seconds
5) 10% settling time ≤ 30 seconds
6) AoA command input $\leq \pm 10$ degrees
7) Stable Doublet Response with AoA $\leq \pm 10$ degrees

B.3 Results and Discussion

The results are shown in Fig.B.6 to B.7 and Table B.4 summarizes the H_∞ and PID gains derived from the structured H_∞ synthesis and Table B.5 summarizes the poles/zeros of each transfer function. The results will be evaluated base on the criterion set in Table B.3.

Table B.4 shows the obtained H_∞ norm and can be seen to meet criteria 1) since $\|T_{wz}\|_\infty < 1$. From Fig.B.5 it is evident that the frequency response of T_{ry} is below W_e as placed on the sensitivity transfer function shown in equation B.11. Since the design procedure for the structured H_∞ synthesis involves tuning the weights placed on the system to have a H_∞ norm of less than 1, W_e was tuned to be close to 1 for better tracking performance. From Fig.B.5, it can be seen that the W_e constraints were met. The poles for the complementary transfer function T_{ry} (subscript number denotes mach number) are summarized in Table B.5 and can be seen that all poles in the s-plane are non positive which states that the closed loop system is stable for the linear models of mach 5 to 2 thus criteria 2) is achieved.

For the evaluation criterion for desired control performance, Fig.B.6 shows the step response of the linear system in the time domain for Mach 5 to 2 and will be used to validate a stable response. From Fig.B.6, it can be seen that all models converge thus having a stable step response. Mach 2 and 3 has faster settling time compared to Mach 4 and 5. This is due to the $C_{L\alpha}$ of mach 4 and 5 being smaller than Mach 2 and 3 as can be seen from Table B.1. This comes form the nature of hypersonic aircrafts where C_L decreases and C_D increases with higher Mach number. Mach 5 has smaller settling time compared to Mach 4 since $C_{L\alpha}$ is smaller as can be seen from Table B.1. Table B.6 summarises the results for the desired control performance for each Mach number. From Table B.6, all the criteria from criteria 3) to 5) was achieved. Fig.1.5 in Chapter 1 shows the simulation results for doublet response to multiple γ reference inputs. From Fig.1.5, it can be seen that all models converge thus having a stable step response to γ reference inputs between $\pm$1deg thus achieving criteria 7). From Fig.1.5, it is also evident that AoA command input is within $\pm$10deg and criteria 6) is achieved as well. However, as can be seen from the doublet response, the controller performs differently at each Mach number where the overshoot becomes greater as the Mach number increases. With the robust controller robustness against flight condition changes is obtained, but the performance can deviate significantly.

The objective for the case study is to design a robust for the designed Hypersonic Experimental Aircraft model and to evaluate the controller for stability and desired control performance at varying flight mach numbers in the descent trajectory phase. From the results, all the criterion defined in Table B.6 were achieved. Therefore, evaluation results show that the structured H_∞ controller design was achieved and ensures stability at varying mach numbers as well as meeting the desired control performance. Furthermore, it was identified that the controller performs differently at each Mach number where the overshoot becomes greater as the Mach number increases and performance decreases significantly.

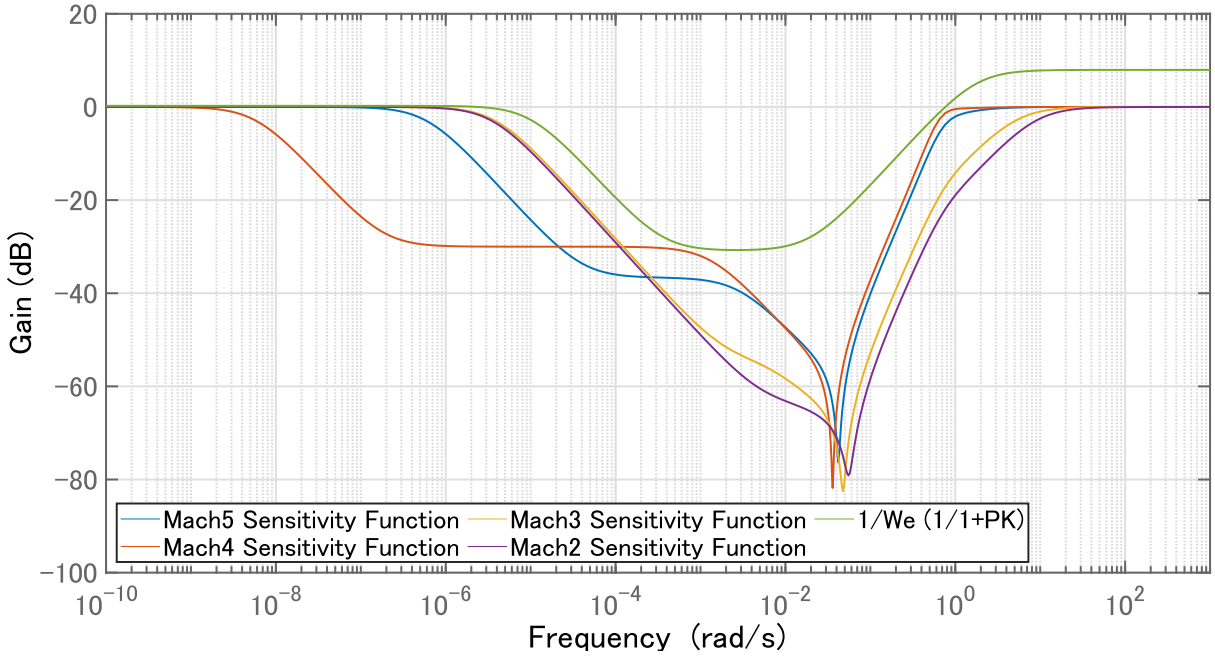

Fig. B.5 Frequency Response of Sensitivity Functions (Mach 5 to 2).

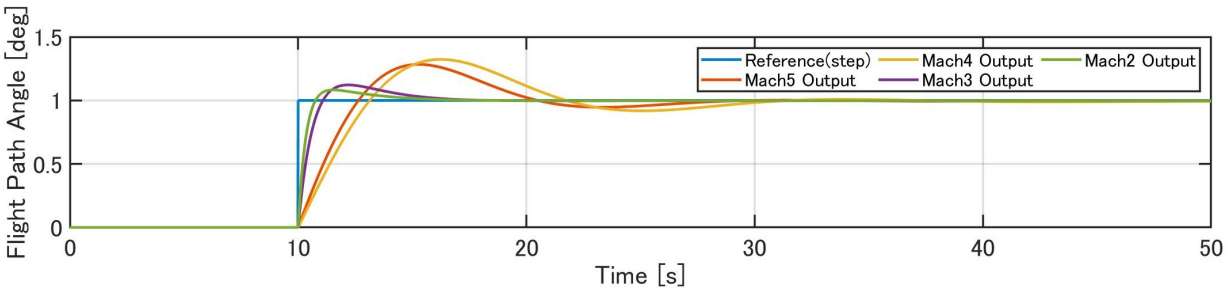

Fig. B.6 Mach 5 to 2 Step Response.

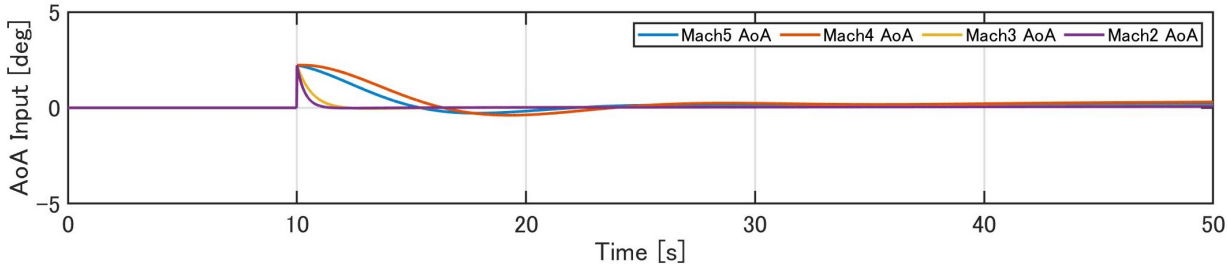

Fig. B.7 Mach 5 to 2 AoA Command Input.

Table B.4 H_∞norm and PID Gain

H_∞norm	K_p	K_i	K_d	n (filter coeff.)
0.917	3.35	4.43	6.03	0.992

Table B.5 Pole/Zero of Transfer Function

Transfer Function	Poles	Zeros
T_{ry5}	-2.5154 -0.2624 + 0.5614i -0.2624 - 0.5614i -0.2228e-9 -0.0029	-0.4157 + 0.5462i -0.4157 - 0.5462i 0 -0.0029
T_{ry4}	-2.0902 -0.2244 + 0.5467i -0.2244 - 0.5467i -0.2577e-13 -0.0013	-0.4157 + 0.5462i -0.4157 - 0.5462i 0 -0.0013
T_{ry3}	-8.4731 -0.3771 + 0.5621i -0.3771 - 0.5621i -0.1636e-10 -0.0070	-0.4157 + 0.5462i -0.4157 - 0.5462i 0 -0.0070
T_{ry2}	-14.0892 -0.1489e-10 -0.0165 -0.3933 + 0.5566i -0.3933 + 0.5566i	-0.3338 + 0.2664i -0.3338 - 0.2664i 0 -0.0166

Table B.6 Desired Controller Performance Criterion Results

Mach	overshoot $\leq 40\%$	rise time $\leq$ 10sec	settling time $\leq$ 30sec	AoA $\leq$ 10deg
5	28%	2.1sec	22.3sec	2.2deg
4	32%	2.4sec	24.8sec	2.2deg
3	12%	0.8sec	10.8sec	2.2deg
2	8%	0.5sec	9.6sec	2.2deg

Appendix C

Conical Waverider Design Method

The waverider wing applied for the Hypersonic Experimental Aircraft depicted in Chapter 4 utilizes a conical waverider design philosophy since waveriders are know for there high lift to drag ratio in hypersonic speeds. Here, the concept of generating a conical waverider is briefly explained.

C.1 Inverse Design Method of Conical Waverider

Waveriders typically take on the shape of a wedge-like configuration (e.g. wedge, conical, osculating, starbody,etc) and consists of a high-pressure lower surface and a low-pressure upper surface in a hypersonic flow field. This pressure difference is the key concept the waverider and is well known to have a lift to drag ratio (L/D) breaking the "L/D barrier" as stated by Kuchemann [48]. Essential for exhibiting high L/D is for the shockwave to be attached on the leading edge to maintain high pressure on the lower surface which can be interpreted as the vehicle riding on the shockwave hence the name waverider.

In order to meet the requirements of an attached shock wave on the leading edge, waveriders are frequently created using the inverse design method [51]. In this method, the generating flowfield which will define the shape of the waverider is first specified with the generating flowfield is simply being supersonic or hypersonic flow past a body (i.e. wedge or cone are typically used and cone will be used in this disseratation). From the obtained flowfield past a cone, the shape of the waverider is prescribed by the lower surface curve (LBC) on the base plane. The lower surface of the waverider is created by starting from the LBC and tracing the streamlines in the generating flowfield upstream until the shock wave is intersected which is identical to defining the leading edge for the waverider. Finally, the shape of the upper surface of the waverider is traced from leading edge to the base plane parallel to the free stream direction. The unique approach taken for the inverse design method

was that the leading edge angle between the upper surface and lower surface is predefined and the design process is iterated to derive the shockwave angle needed to obtain the wedge angle. This was conducted from an engineering standpoint of specifying enough thickness on the leading edge to ensure manufacturing and tolerable thermal capability. The numerical method for the design of a conical waverider is briefly explained by the following:

i) Assume arbitrary wedge angle x[deg], shockwave angle $\beta < 90$[deg], and free stream Mach number M_1.

ii) Calculate turning angle θ using Eq.C.1 referenced from [4] with $\kappa = 1.4$.

$$\tan\theta = 2\cot\beta \frac{M_1 \sin^2\beta - 1}{M_1^2(\kappa + \cos 2\beta)} \tag{C.1}$$

iii) Calculate the Mach number after passing through the oblique shockwave denoted as M_2 using Eq.C.2.

$$M_2 = \frac{M_{n2}}{\sin(\beta - \theta_0)} \tag{C.2}$$

Where M_{n2} and M_{n1} are defined by the following:

$$\begin{aligned} M_{n2} &= \sqrt{\frac{2 + (\kappa - 1)M_{n1}^2}{2\kappa M_{n1}^2 - (\kappa - 1)}} \\ M_{n1} &= M_1 \sin\beta \end{aligned} \tag{C.3}$$

iv) Calculate the velocity of the deflected stream after the oblique shock V from Eq.C.4.

$$V = \frac{2}{(\gamma - 1)M_2^2} + 1 \tag{C.4}$$

The radial and normal components of V, u and v respectively, are obtained by Eq.C.5 using the fact that tangential velocity at the oblique shock wave (i.e. perpendicular to the normal velocity corresponding to M_{n1} and M_{n2}) is the same on both sides of the shockwave.

$$\begin{aligned} u &= V\cos(\beta-\theta) \\ v &= -M_{n2}\sqrt{(\kappa R T_s)} \end{aligned} \tag{C.5}$$

Here, T_s is the initial static temperature after the shockwave calculated using the oblique shock relations and free stream static temperature T_{inf} shown in Eq.C.6.

$$T_s = \frac{T_{inf}(1+0.5(\kappa-1)M_{n1}^2)(2\frac{\kappa}{\kappa-1}M_{n1}^2-1)}{(\kappa+1)^2\frac{0.5}{(\kappa-1)}M_{n1}^2} \tag{C.6}$$

v) Calculate the total enthalpy h_t for obtaining local speed of sound a.

$$h_t = \frac{a_{inf}^2}{(\kappa-1)+0.5u_{inf}^2} \tag{C.7}$$

Here, a_{inf} and u_{inf} are the free stream speed of sound and radial velocity respectively and by using Eq.(C.6) a is calculated by Eq.(C.8).

$$a = \sqrt{(\kappa-1)(h_t-0.5(u^2-v^2))} \tag{C.8}$$

vi) From the obtained equations, integrate the Taylor-Maccoll equation to obtain u and v with respect to θ shown in Eq.C.9 taken from [3]. It should be well noted that the obtained u and v are in spherical coordinates.

$$\begin{aligned} \frac{dv}{d\theta} &= -\frac{(2-\frac{v^2}{a^2})}{(1-\frac{v^2}{a^2})}u - \frac{\cot\theta}{(1-\frac{v^2}{a^2})}v \\ \frac{du}{d\theta} &= v \end{aligned} \tag{C.9}$$

Stop the integration when $v=0$ which signifies the surface of the cone generating the shockwave was reached.

vii) Calculate the turning angle θ_{wedge} at $v = 0$ (equivalent to leading edge wedge angle) and compare to the predefined target wedge angle x and iterate the above process until $\theta_{wedge} = x$. Otherwise repeat from step ii with $\beta = \beta - 0.01$. Upon convergence, the flowfield of the streamline is obtained after the defined oblique shockwave.

viii) After the flowfield has been obtained, the inverse design of the lower surface of the waverider is conducted. Start at the LBC specified by the designer in the base plane and obtain (x_0, y_0) Cartesian coordinates.

ix) Obtain the wedge angle θ from the vertex of the cone to (x_0, y_0). From θ, obtain the corresponding u and v to be converted to Cartesian coordinates u_c and v_c through sin and cos of θ.

x) Obtain the slope $y = \frac{v_c}{u_c}x$ and multiply $dx = 0.1$ to obtain the next coordinate of the streamline (x_n, y_n).

xi) Repeat steps vii to ix until $\theta = \beta$ which is the leading edge of the waverider and thus the lower surface is obtained.

xii) The upper surface is typically drawn to be parallel to the free stream and can be modified by the designer to change the aerodynamic characteristics according to desired requirements [51, 39].

References

[1] (1976, U.S. Government Printing Office). U.s.standard atmosphere.

[2] Ackermann, J. (1985). Multi-model approaches to robust control system design. *IFAC Model Error Concepts and Compensations, USA*.

[3] Anderson, J. (2003). Modern compressible flow third edition. *McGraw-Hill Companies Inc.*

[4] Anderson, J. (2007). Fundamentals of aerodynamics fifth edition. *McGraw-Hill Companies Inc.*

[5] Apkarian, P. and Noll, D. (2005). Controller design via nonsmooth multi-directional search. *SIAM J. on Control and Optimization*.

[6] Apkarian, P., Noll, D., and Pellanda, P. (2006). Nonsmooth h-infinity synthesis. *IEEE Trans. Aut. Control, 51, pp. 71*.

[7] Atkinson, K., Han, W., and Stewart, D. (2009). Numerical solution of ordinary differential equations. *John Wiley and Sons, Inc*.

[8] Aupoix, B. and Spalart, P. R. (2003). Extensions of the spalart-allmaras turbulence model to account for wall roughness. *International Journal of Heat and Fluid Flow, Volume 24, Issue 4,*.

[9] Bahm, C., Baumann, E., Martin, J.and Bose, D., Beck, R., and Strovers, B. (2012). The x-43a hyper-x mach 7 flight 2 guidance, navigation, and control overview and flight test results. *AIAA CIRA 13th International Space Planes and Hypersonics Systems and Technologies*.

[10] Ben-Asher, J. (2010). Optimal control theory with aerosapce applications. *American Institute of Aeronautics and Astronautics, Inc*.

[11] Blanvillain, E. and Gallic, G. (2015). Hikari: Paving the way towards high speed air transport. *20th AIAA International Space Planes and Hypersonic Systems and Technologies Conference, Scotland*.

[12] Bock, H. and Plitt, K. (1984). A multiple shooting algorithm for direct solution of optimal control problems. *IFAC 9th Triennial World Congress, Budapest, Hungary*.

[13] Boeing Commercial Airplanes (2019). Current market outlook.

[14] Boggs, P. (1996). Sequential quadratic programming. *Acta Numerica, pp.1-000*.

[15] Bortoff, S., Schwerdtner, P., Danielson, C., and Di Cairano, S. (2019). H-infinity loop-shaped model predictive control with heat pump application. *European Control Conference, Italy*.

[16] Boulet, B. and Duan, Y. (2007). The fundamental tradeoff between performance and robustness, a new perspective on loop shaping, classical control revisited part2. *IEEE Control Systems*.

[17] Boyd, S., Balakrishnan, V., and Kabamba, P. (1989). A bisection method for computing the h_∞ norm of a transfer matrix and related problems*. *Mathematics of Control, Signals, and Systems p207-219*.

[18] Boyd, S. and Vandenberghe, L. (2004). Convex optimization. *Cambridge University Press*.

[19] Bryson, A. and Y., H. (1975). Applied optimal control. *Hemisphere Publishing Corporation, Washington D.C.*

[20] Clarke, F. (1978). Nonsmooth analysis and optimization. *Proceedings of the International Congress of Mathematicians*.

[21] Cornelisse, J., Schoyer, H., and Wakker, K. (1979). Rocket propulsion and spaceflight dynamics. *Pitman Publishing Ltd.*

[22] David Sánchez, D., Bennani, S., Cruciani, I., and Aranda, J. (2013). H-infinity control of the vega launch vehicle first stage in presence of roll. *19th IFAC Symposium on Automatic Control in Aerospace Vol.46-19, 1474-6670*.

[23] Forrester, A., Sobester, A., and Keane, A. (2008). Engineering design via surrogate modeling. *John Wiley and Sons*.

[24] Gahinet, P. and Apkarian, P. (1992). Numerical computation of the h_∞ norm revisited. *Proceedings of the 31st IEEE Conference on Decision and Control*.

[25] Gahinet, P. and Apkarian, P. (1994). A linear matrix inequality approach to h_∞ control. *International Journal of Robust and Nonlinear Control, Vol. 4, pp. 421-448*.

[26] Gahinet, P. and Apkarian, P. (2011). Structured h_∞ synthesis in matlab. *In Proceedings IFAC, Milan*.

[27] Glover, K. and Doyle, J. (1988). State-space formulae for all stabilizing controllers that satisfy an h_∞ norm bound and relations to risk sensitivity. *Systems and Control Letters 11 (1988) 167-172*.

[28] Grauer, J., Morelli, E., and Murri, D. (2017). Flight test technique for quantifying pitch rate and angle of attack rate dependencies. *Journal of Aircraft 54(6):1-11*.

[29] Gundlach, J. (2012). Designing unmanned aircraft systems. *American Institute of Aeronautics and Astronautics, Inc*.

[30] Han, S. (1997). A globally convergent method for nonlinear programming. *Journal of Optimization Theory and Applications: Vol.22, No.3*.

[31] Hanson, J. and Beard, B. (2010). Applying monte carlo simulation to launch vehicle design and requirement analysis. *NASA/TP—2010–216447*.

[32] Hashimoto, A., Ishida, T., and Aoyama, T. (AIAA 2016-1358, 2016). Results of three-dimensional turbulent flow with fastar. *54th AIAA Aerospace Sciences Meeting Sciences, AIAA Sci Tech Forum*.

[33] Hashimoto, A., Murakami, K., and Aoyama, T. (2009). Lift and drag prediction using automatic hexahedra grid generation method. *AIAA paper 2009-1365*.

[34] Hirata, M. (2017). Practical robust control (in japanese). *Corona Publishing Co., Ltd., Tokyo*.

[35] Hiroshi, M. (1981 (In Japanese)). Flight dynamics (hikou rikigaku). *Yokendo Publishing Co., Ltd., Tokyo*.

[36] Hiruma, M. (09-14, 2018). Evaluation of altitude control for an airbreathing hypersonic aircraft model. *31st Congress of the International Council of the Aeronautical Sciences, Belo Horizonte, Brazil*.

[37] Hiruma, M., Takase, R., Taguchi, H., and Tsuchiya, T. (2020). Integrated design of trajectory and robust control for hypersonic experimental aircraft. *AIAA International Space Planes and Hypersonic Systems and Technologies Conferences, Canada*.

[38] Hiruma, M., Takase, R., and Tsuchiya, T. (12-14 December 2019). Structured h_∞ control design for the hypersonic experimental aircraft. *Asia-Pacific International Symposium on Aerospace Technology, Gold Coast, Australia*.

[39] Hiruma, M., Tezuka, A., Taguchi, H., and Hongoh, M. (2016). Low speed aerodynamics on the hypersonic experimental aircraft. *60th Space Sciences and Technology Conference, Japan (In Japanese)*.

[40] Hiruma, M., Tezuka, A., Taguchi, H., and Hongoh, M. (25-27 November 2015). Evaluation of waverider derived wing for hypersonic experimental aircraft. *Asia Pacific International Symposium on Aerospace Technology, Cairns, Australia*.

[41] Horinouchi, S., Ohnuki, T., Yoshida, K., Kwak, D., Tokugawa, N., Shindo, S., Machida, S., Murakami, Y., Nakano, E., Takagi, S., Yanagi, R., and Sakata, K. (2006). Results of the supersonic experimental airplane nexst-1 basic design. *JAXA Research and Developement Report, JAXA-RR-05-044 (In Japanese)*.

[42] Kanameda, D., Fujikawa, T., Tsuchiya, T., and Taguchi, H. (25-27 November 2015). Experimental aircraft of hypersonic air-breathing engine launched by solid-propellant rocket. *Asia-Pacific International Symposium on Aerospace Technology, Cairns, Australia*.

[43] Katayanagi, R., Tsushima, K., Futatsudera, N., and Takahashi, R. (2002). Developement of the small supersonic experimental rocket airplane. *Mitsubishi Heavy Industries Technology Report Vol.39, No.1 (In Japanese)*.

[44] Kawaguchi, J., Ninomiya, T., and Suzuki, H. (2012). Guidance and control for d-send#2. *28th ICAS, Australia*.

[45] Kelly, M. (2017). An introduction to trajectory optimization: How to do your own direct collocation. *Siam Review Vol.59, No.4, pp.849-904*.

[46] Khairudin, N. and Keesman, K. (2009). Linear regression technique for state-space models with application to biomedical/biochemical example. *Proceedings of the 6th Vienna International Conference on Mathematical Modelling, Austria*.

[47] Kirches, C. (2011). Fast numerical methods for mixed-integer nonlinear model-predictive control. *Vieweg+Teubner Verlag and Springer Fachmedien Wiesbaden GmbH*.

[48] Kuchemann, D. (2012). The aerodynamic design of aircraft. *American Institute of Aeronautics and Astronautics, Inc*.

[49] Kwakernaak, H. (1993). Robust control and h_∞ optimization tutorial paper. *Automatica, Vol.29 No.2, pp.255-273*.

[50] Lin, M. and Xu, M. (2017). Entire flight trajectory design for temporary reconnaissance mission. *Trans. Japan Soc. Aero. Space Sci. Vol. 60, No. 3, pp. 137–151*.

[51] Lobbia, M. (2004). A framework for the design and optimization of waverider-derived hypersonic transport configurations. *Ph. D. Dissertation of the Department of Aeronautics and Astronautics, The University of Tokyo*.

[52] Marcos, A. and Sato, M. (2017). Flight testing of an structured h-infinity controller: An eu-japan collaborative experience. *IEEE Conference on Control Technology and Applications (CCTA), Hawaii*.

[53] Maurer, H. and Gillessen, W. (1975). Application of mulitple shooting to the numerical solution of optimal control problems with bounded state variables. *Computing 15, 105-126, Springer-Verlag*.

[54] Momenthy, A. (1983). Fuels of the future. *The Space Congress Proceedings, USA*.

[55] Navarro-Tapia, D., Marcos, A., Bennani, S., and C., R. (2018). Linear parameter varying control synthesis for the atmospheric phase vega launcher. *IFAC-PapersOnLine Vol. 51-26, 2405-8963*.

[56] Navarro-Tapia, D., Simplicio, P., Iannelli, A., and Marcos, A. (2017). Robust flare control design using structured h_∞ synthesis: a civilian aircraft landing challenge. *IFAC PapersOnLine 50-1(2017)3971-3976*.

[57] Obayashi, S. and Guruswamy, G. (1995). Convergence acceleration of a navier-stokes solver for efficient static aeroelastic computations. *AIAA Journal Vol. 33, No.6*.

[58] Ohnuki, T., Hirako, K., and Sakata, K. (2006). National experimental supersonic transport project. *25th International Congress of the Aeronautical Sciences*.

[59] Ohnuki, T., Machida, S., Yoshida, K., Oka, N. Kwak, D., Takatoya, T., Tada, A., Honda, M., Mizuno, T., Kawamura, Y., Murakami, Y., Shindo, S., Fujiwara, T., Hirano, H., Nakano, E., Tokugawa, N., Kawakami, H., Ishizuka, T., Matayoshi, N., Okai, K., Hirako, K., and Sakata, K. (2007). The second flight experiment of the supersonic experimental airplane (nexst-1). *JAXA Reasearch and Developement Report, JAXA-RR-06-049 (In Japanese)*.

[60] Ohtsuka, T. (2016). Introduction to nonlinear optimal control (in japanese). *Corona Publishing Co., Ltd., Tokyo*.

[61] Oppenheim, A. and Schafer, R. (2010). Discrete-time signal processing. *Pearson Higher Education*.

[62] Osgood, B. (2019). Lectures on the fourier transform and its applications. *American Mathematical Society*.

[63] Powell, M. (1977). A fast algorithm for nonlinearly constrained optimization calculations. *Proceedings of the Biennial Conference Held at Dundee,*.

[64] Sakata, K. (2001). Supersonic experimental airplane (nexst) for next generation sst technology. *39th Aerospace Sciences Meeting and Exhibit,AIAA-2002-0527, Nevada*.

[65] Schmidt, D. (1992). Problems in control system design of hypersonic vehicles. *IFAC Proceedings Volume 25, Issue 22, Pages 89-96*.

[66] Seokkwan, Y. and Antony, J. (1988). Lower-upper symmetric-gauss-seidel method for the euler and navier-stokes equations. *AIAA Journal, Vol. 26, No. 9, pp. 1025-1026*.

[67] Simplicio, P., Navarro-Tapia, D., Iannelli, A., and Marcos, A. (2018). From standard to structured robust control design: Application to aircraft automatic glide-slope approach. *IFAC PapersOnLine 51-25 (2018) 140–145*.

[68] Subchan, S. (2008). A direct multiple shooting for the optimal trajectory of missile guidance. *17th IEEE International Conference on Control Applications, Texas*.

[69] Tada, A., Murakami, Y., and Takizawa, M. (2007). Flight control system of the nexst-1 experimental vehicle for supersonic aerodynamic measurement. *45th AIAA Aerospace Sciences Meeting and Exhibit, Nevada*.

[70] Takase, R., Suzuki, S., and Masayuki, S. (2019). Design of a fault-tolerant pid flight controller with structured h_∞ synthesis (in japanese). *JSASS 50th Annual Conference, Japan*.

[71] Tartabini, P., Bose, D., Thornblom, M., and Lien, J. (2006). Mach 10 stage separation analysis for the x43-a. *44th AIAA Aerospace Sciences Meeting and Exhibit, Nevada*.

[72] Toffner-Clausen, S. (1996). System identification and robust control. *Springer-Verlag London*.

[73] Tsiolkovsky, K. (1975). Study of outer space by reaction devices. *NASA Technical Translation NASA TT F-15571, Translation of "Issledovaniye mirovykh prostranstv reaktivnli priborami", Moscow Mashinotroyeniye Press, 1967*.

[74] Van Leer, B. (1979). Towards the ultimate conservative difference scheme. v.a second order sequel to godunov's method. *Volume 32, Issue 1 1979*.

[75] Wakabayashi, S., Yoshida, H., Chiga, T., Sato, T., Taguchi, H., Kojima, T., Okamoto, T., Ikeda, Y., Nakaya, S., and Tsue, M. (17-19, September, 2018). Research and development of ramjet engine for high-mach integrated control experiment (himico). *22nd AIAA International Space Planes and Hypersonics Systems and Technologies Conference, Florida*.

[76] Wang, Q. and Stengel, R. (2000). Robust nonlinear control of a hypersonic aircarft. *Journal of Guidance, Control, and Dynamics Vol.23 No.4*.

[77] Whitley, R. and Ocampo, C. (January 2009). Direct multiple shooting optimization with variable problem parameters. *AIAA Aerospace Sciences Meeting Including The New Horizons Forum and Aerospace Exposition, Orlando, Florida*.

[78] Wiese, D., Annaswamy, A., Muse, J., Bolender, M., and Lavretsky, E. (2016). Sequential loop closure based adaptive autopilot design for a hypersonic vehicle. *AIAA Guidance, Navigation, and Control Conference, 2016-1379*.

[79] X-43A Mishap Investigation Board (2003). Report of findings x-43a mishap. *NASA, Vol. 1, Washington, D.C.*

[80] Young, P. and Garnier, H. (2006). Identification and estimation of continuous-time, data-based mechanistic (dbm) models for environmental systems. *Environmental Modelling & Software 21 1055e1072*.

[81] Zheng, W. (1999). A least-squares based algorithm for transfer function identification. *5th International Symposium on Signal Processing and its Applications*.

Acknowledgement

What I have learned over my Ph.D course is nothing short of extraordinary from my first day at my laboratory till the final day. The knowledge and experience I gained through meeting extraordinary people, the complexity and ingenuity of the research in aerospace, the responsibility as a Ph.D candidate at one of the most prestigious university in Japan, it has and will be a ride that I am most proud of to almost calling it achieving eudaimonia. Nothing was obtained without the many personal connections that I was able to make throughout my days. Here, I would like to honor the ones who have impacted me the most.

I would like to express my utmost gratitude to my Ph.D advisors, Professors Tsuchiya and Shinji Suzuki, for supporting me during these past 3+ years. Professor Tsuchiya has provided me the opportunity of a life time of pursuing research in the field of aerospace. Ever since building my first LEGO X-Wing, I loved aircrafts and always wondered what my dream aircraft can look like. I have yet to finalize on the design but to do so I needed the knowledge and experience Professor Tsuchiya was a pioneer in. That is, the conceptual design of aircrafts through optimization. Even though I was only able to gain a glimpse of the world Professor Tsuchiya sees, the research field engulfed me with ideas never that I would have imagined before. I hope that I could be as lively, enthusiastic, and energetic and to someday be able to command an audience as well as he can. Professor Suzuki has also been supportive of my research as well as finding a career in the aerospace industry and has given me the freedom to pursue various projects without objection. He has also provided insightful discussions about the future of the aerospace industry in Japan and am looking forward to actualizing my potential in growing the industry. Professor Suzuki is by far, the most cunning and humorous advisor I know and was an honor to study under Professor Suzuki.

I also have to thank the members of my thesis committee members. Professor Kawaguchi provided me intuitive advice on expanding my research for practicality. Professor Nakasuka gave me helpful advice in addressing the novelties in my research from both broad and detailed perspectives. From Professor Kojiro Suzuki, I received comments that I couldn't recognize beforehand but were critical in completing my research. Dr. Taguchi provided me with some of the remarkable research topics prior to the start of my research as well as to

the end. I have to acknowledge and will not hesitate to say that the research conducted was highly influenced by the future Dr.Taguchi envisioned and could not have hoped for a better research topic than the one provided. Dr. Taguchi is my second advisor for this dissertation in that I have received unimaginable amount of expertise from him regarding hypersonic vehicles and engines. Again, I would like to express my sincere appreciation for their helpful advice and suggestions in general.

I will forever be thankful to the collaborative research group consisting of members from Japan Aerospace Exploration Agency (JAXA) and universities for providing a hands on project. Dr. Taguchi and Professor Tsuchiya is part of this group as well and they gave me valuable comments prior to writing this dissertation through the meetings. I have received countless advice from Mr. Hongoh regarding the concept of waveriders and especially would like to thank him in aiding me to do wind tunnel testing at Kashiwa campus. Also, I would always like to thank Dr. Hirotani for providing pinpoint advice which made significant sense many times during my JAXA trainee days and I would not have been able to grow as much as I did over the years without your help.

A comfortable but energetic laboratory is important to surviving and staying sane in grad school. I was lucky to be a part of such laboratory and without a doubt made my research life bigger and better. I would like to express my sincere gratitude to Project Associate Professor Nakamura for providing me the opportunity to foresee a career in the aerospace industry. The tour to MRJ test facility in Seattle really gave me an insight on how my knowledge and research can be actualized in the industry and gave me confidence to pursue a career as an aerospace engineer. I want to personally thank Assistant Professor Entzinger for his intuitive comments during lab meetings and really appreciate the time and effort to comprehend my research to give me valuable advice. Finally, I would like to take the opportunity to thank my colleagues from bachelors, masters, to Ph.D at my laboratory for supporting me intensively. Special thanks goes to Ryoichi Takase for his support on robust controller design methods and with him Yuji Shimizu for actualizing my potential in SSBU with ZSS. I would like to thank Mr. Yoshikawa for opening my field of view on control theory as much as he did with opening the door to the world of board games. Also, Naoto Morita my fellow colleague for always teaching me with his overfull knowledge on aircraft design and optimization.

Last but not least, nothing would have been possible from the start of my research if it weren't for my family especially parents. My research belongs to them as much as it belongs to me and would like to express my thank you from the bottom of my heart for providing me with a once in a life time opportunity in endeavoring into the unknown.

Sincerely,
Masaharu Hiruma